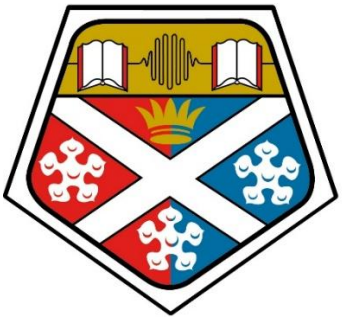

University of Strathclyde Glasgow

Optimisation of Brewer's Spent Grain Biochar Synthesis for Remediation of Emerging Contaminants from Water

Jordan Peter Mooney

Thesis submitted for the degree of Doctor of Philosophy

Department of Chemical and Process Engineering

University of Strathclyde

2025

Declaration of Authenticity and Author's Rights

This thesis is the result of the author's original research. It has been composed by the author and has not been previously submitted for examination which has led to the award of a degree.

Jordan Peter Mooney

June 2025

Acknowledgements

The completion of this work would not have been possible without the support and guidance from many people.

Firstly, I would like to thank my supervisor Prof Ashleigh Fletcher. Her knowledge, guidance and support has been invaluable throughout my time at the University of Strathclyde. Our weekly chats never failed to reinvigorate and inspire me to be my best academic self. Thank you for believing in me and trusting me over the course of this journey.

I would also like to thank Dr Yi-Chieh Chen, Dr Leung Tang, Mrs Mara Knapp and Dr Jake Sheriff for their help undertaking data collection, analysis and training at various stages of this work. I would also like to thank the laboratory technicians, Mr Ian Airdrie, Mr Christopher Jones and Mr Liam Kirkwood for their diligence, expertise and wit, helping me survive those long hours in the lab.

I wish to thank the entirety of the Fletcher research group but especially Dr David Ashworth and Mr Aidan Harvey for always being available to discuss ideas with, provide criticism but most importantly for keeping me sane on this long journey. I would also like to thank Mr Mathis Bornand for his hard work and assistance in the lab during his Erasmus traineeship.

Finally, I wish to express my profound thanks to my parents without whom none of this would have been possible. Not only for supporting me financially but for their patience and understanding at the setbacks and my frustrations. They've always believed in me, even perhaps when I didn't myself and I will forever be grateful for their unconditional love and encouragement.

Abstract

Emerging contaminants are a class of pollutants in water of growing prominence due to their endocrine disrupting properties, persistence in the environment and potential adverse effects on humans and the environment. Adsorbents such as activated carbons and biochars are used in wastewater treatment applications, however new synthesis precursors and pathways are constantly required to develop new functional adsorbents in environmentally and economically sustainable ways. Brewer's Spent grain has been identified as a precursor material of interest, due to its low cost, homogeneity and high carbon and nitrogen content capable of being upcycled into biochars. However, no systematic optimisation process or full characterization of biochars from brewer's spent grain has been carried out. Here we show the optimisation of brewer's spent grain biochar through utilisation of design of experiments and fully characterise the optimal adsorbent composition, textural properties, and adsorption behaviour with the surrogate pollutant methyl orange dye. Through screening design of experiments, we found that hold temperature and hold time were the only factors of statistical significance, but washing with the chemical activating agent hydrochloric acid was required to alter the surface chemistry of the materials. The optimal synthesis conditions for the biochar were at 900°C and a hold time of 2.5 hours giving a yield of 7.6%, a surface area of 1433 $m^2 g^{-1}$, small mesopore and large micropore sizes and a variety of aromatic, oxygen and nitrogen containing functional groups on the surface. Notably, silica present within the feedstock is mobilised to the surface after pyrolysis, presenting another possible site for adsorption. Methyl orange dye adsorption on the surface followed the Temkin isotherm model, indicating heterogenous adsorption behaviour. Thermodynamic studies indicated an initial physisorptive mechanism with enthalpy of -51.9 kJ mol^{-1} followed by a chemisorptive mechanism after an uptake of approximately 270 mg g^{-1}. These results demonstrate the suitability of brewer's spent grain biochars for use in water remediation applications, creating a circular economic pathway to upcycle the waste material from the brewing industry. These materials present an environmentally friendly and cost-effective method of biochar production as compared to other non-renewable precursor derived biochars such as those derived from peat and coal. It also presents a local waste route to Scotland as compared to imported biomass waste, further advancing sustainability initiatives.

Contents

List of Abbreviations

A	Absorbance
ANOVA	Analysis of Variance
a_E	Elovich desorption constant
A_m	Cross section of adsorbate molecule
AOPs	Advanced Oxidation Processes
AR	As received
ASTM	American Society for Testing Materials
ATR	Attenuated Total Reflectance
b_E	Elovich initial adsorption rate
b_0	Offset term
b_1	Coefficient of the effect of x_1
BET	Brunauer Emmett Teller
BJH	Barrett Joyner Halenda
BSG	Brewer's Spent Grain
b_T	Temkin constant
C	Concentration
c	BET constant
C_0	Initial concentration
C_b	Equilibrium product in solution concentration
CCC	Central Composite Circumscribed
CCD	Central Composite Circumscribed
CCF	Central Composite Face-Centred
CCI	Central Composite Inscribed
C_e	Equilibrium concentration
CHN	Carbon Hydrogen Nitrogen
C_{Int}	Boundary layer thickness constant
C_{Max}	Maximum measurable concentration
C_t	Concentration at time t
C_θ	Standard state of solution
D	Design matrix
D_{DR}	Dubinin Radushkevich constant
D^+	Pseudo inverse of design matrix
D^{-1}	Inverse of design matrix
DoE	Design of Experiments
DOF	Degrees of Freedom
D_p	Penetration depth
DR	Dubinin Radushkevich
D^T	Transpose of design matrix
E	Energy
$E_{Binding}$	Binding energy of electron
EDA	Electron Donor-Acceptor
EDS	Energy dispersive X-ray Spectroscopy
EDX	Energy dispersive X-ray
$E_{Kinetic}$	Kinetic energy of electron
E_{Photon}	Energy of incident photon
EPSRC	Engineering and Physicical Sciences Research Council
$E_{Recorded}$	Measured binding energy
FTIR	Fourier Transform Infrared Spectroscopy
Ge	Germanium

h	Planck's constant
HOMO	Highest occupied electron orbital
I	Background subtracted peak area
IPD	Intra particle diffusion
IR	Infrared
IUPAC	International Union of Pure and Applied Chemistry
k	Number of factors
k_1	Pseudo first order rate constant
k_2	Pseudo second order rate constant
k_{ads}	Rate constant of adsorption
K_b	Equilibrium constant for individual type of site
k_{des}	Rate constant of desorption
K_F	Freundlich characteristic constant
K_F^{θ}	Standard Freundlich equilibrium constant
k_{int}	Intra particle diffusion rate
K_L	Langmuir equilibrium constant
K_L^{θ}	Standard Langmuir equilibrium constant
K_T	Temkin equilibrium constant
K_T^{θ}	Standard Temkin equilibrium constant
l	Path length
LED	Light emitting diode
LUMO	Lowest unoccupied electron orbital
m	Degree of fractionation
m_A	Mass of adsorbent
MF	Microfiltration
MNP	Micro (nano)plastics
MO	Methyl orange
MOFs	Metal organic frameworks
MOPs	Metal organic polyhedral
MQA	Maximum quantity adsorbed
n	Molar adsorbate uptake
n_0	Micropore molar uptake
N_A	Avogadro's constant
N	Number of sites occupied
n_c	Crystal refractive index
NEXUS	Newcastle University XPS users' service
n_F	Freundlich heterogeneity constant
NIST	National Institute for Standards and Technology
n_m	Monolayer capacity
N_m	Total number of adsorption sites
NMs	Nanomaterials
N_s	Sample refractive index
n_T	Temkin characteristic constant
OX	Optimised biochar X
P	Pressure
P^0	Saturation vapour pressure
P/P^0	Relative pressure
PFAS	Per and Polyfluoroalkyl Substances
PFO	Pseudo first order
PFOA	Perfluorooctanoic acid
PFOS	Perfluorooctanesulphanoic acid
pH_f	Final pH
pH_i	Initial pH
PSE	Pseudo standard error
PSO	Pseudo second order

PZC	Point of zero charge
q	Mass uptake
q_e	Uptake at equilibrium
q_m	Mass uptake monolayer capacity
q_s	Maximum uptake on an individual type of site
q_t	Uptake at time t
q_θ	Standard state of solid
R	Universal gas constant
R^2	Coefficient of determination
RO	Reverse Osmosis
S	Surface area
$F_{Sensitivity}$	Sensitivity factor
SED	Secondary electron detector
SEM	Scanning electron microscopy
SiChar	Silicon biochar
SX	Screening biochar X
SXW	Washed screening biochar X
T	Temperature
t	Time
TGA	Thermogravimetric analysis
$t_{\alpha, DOF}$	t-table value
UF	Ultrafiltration
UV-Vis	Ultraviolet Visible
V	Volume of solution
v	Volume adsorbed
v_i	Initial volume
v_m	Volumetric monolayer capacity
V_{Water}	Volume of water
w/w	Weight by weight
x	Factor
XPS	X ray photoelectron spectroscopy
y	Response variable

α	Significance level
α_{CCC}	Axial factor level for CCC designs
α_{CCI}	Factorial factor level for CCI designs
$\Delta_{ad}H^\circ$	Isosteric heat of adsorption
ΔG	Gibb's free energy
ΔG^θ	Standard Gibb's free energy
ΔG_{max}^θ	Maximum Standard Gibb's free energy
ΔH_A	Heat of adsorption
ΔH_L	Heat of liquefaction
ΔH	Change in enthalpy
ΔH^θ	Standard change in enthalpy
ΔH_{max}^θ	Maximum change in enthalpy
ΔS	Change in entropy
ΔS^θ	Standard change in entropy
ε	Absorptivity
θ	Fraction of occupied sites
φ	Angle of incidence
λ	Wavelength of light
ν	Frequency of light
Φ	Work function

List of Figures

List of Tables

1 Introduction

1.1 Water Resources

Water is the fundamental building block of life here on Earth. While water covers approximately 71% of the surface of the globe, less than 2.5% of the water present on Earth is freshwater (1). Of this fresh water, 98.8% is locked away as ground water or as glaciers and icecaps, unavailable currently as a resource to humans. This final 0.03% of the Earth's water makes up all the surface water on Earth: every lake, river and swamp; piece of ground ice and flake of permafrost; all of the water in the atmosphere, and is the primary component of every living thing on Earth.

This tiny fraction of the Earth's water is arguably humanity's greatest and oldest resource, with the first great civilisations born upon the banks of the great river valleys of the ancient world in Mesopotamia, and the Nile, Indus and Yellow river valleys. Human history is a story of our relationship with water, not only as a drinking water source for us and livestock but as an irrigation source for crops and later transportation routes for early industrial societies. We rely on water resources that are absolutely imperative to almost all aspects of modern life, but our unsustainable management of freshwater reserves threatens to cause ever greater strain on this limited resource.

In 2022, 2.2 billion people lived without safely managed drinking water and 3.5 billion without safely managed sanitation (2), according to the United Nations. While these numbers have decreased since 2015, there is a long way to go in solving many of the issues surrounding clean water and sanitation. International tensions caused by conflicts involving water shortages have already broken out in many areas affected by water scarcity. Many conflicts have arisen over water resources, such as recently in Kyrgyzstan and Tajikistan in 2021, where a disagreement over the management of shared irrigation water resulted in open conflict (3), also between Egypt and Ethiopia over damming of the Nile river (4) which Arab media has reported as a threat to 150 million Egyptian and Sudanese citizen's lives (5). These examples illustrate the need for international cooperation and good management of our existing water resources.

These problems are but symptoms of some of the greatest challenges being faced by humanity today: climate change, population growth and rapid industrialisation. All three of these issues disproportionally affect the global south and less economically developed

countries, which also have the poorest quality of water due to lack of water treatment infrastructure (6). Increasing industrialisation and population growth are the main causes of another cause of strain on current water resources: anthropogenic pollution. The United Nations World Water development report 2017 estimates that more than 80% of global wastewater is discharged without sufficient treatment (7). The report also states that, while high income countries on average treat 70% of generated wastewater, this drops to 8% for low-income countries, indicating the need for development of low energy and low-cost technologies to help in the treatment of wastewater streams. As water monitoring and analysis techniques have become more widespread and common, a new designation of pollutants, named emerging contaminants, have been identified. Their increasing prevalence in wastewater streams is a new area of concern requiring new modern solutions to remove them.

1.2 Emerging Contaminants

Emerging contaminants, or substances of emerging concern, are defined by the British Geological Survey as pollutants that are not yet regulated but may be of concern to human or environmental health. They are largely not new chemicals, but their prevalence and use has become more widespread with advancing chemical technologies and increasing standard of living within countries. These chemicals have likely been present in wastewater systems for a long time but their presence has only now been noticed due to advances in monitoring technologies and due to their adverse effects downstream. Emerging contaminants classification is a complicated issue, as they can be grouped by their uses, their physico-chemical or biological properties, or by their impact on the people and the environment (8). Some of the classes of emerging contaminants found to affect Scotland are:

- **Industrial Pollutant**s: A wide range of chemicals that include petroleum derived hydrocarbons from fuels, lubricant and combustion by-products (9); metals such as iron, copper and zinc (10); and other industrial chemicals such as textile dyes (11), and disinfectants and their by-products (12).
- **Pharmaceuticals:** A wide variety of therapeutic chemicals used for both human and animal treatment. Examples include common medicines like paracetamol and ibuprofen; antidepressants, anti-inflammatories, analgesics, and antibiotics (13).

- **Personal Care Products:** This group encompasses many chemicals used in routine human activities such as sunscreen and UV-filtering chemicals (14); antimicrobial chemicals, like Triclosan (15) found in soaps and shampoos; and recreational drugs such as nicotine and its metabolites (16).
- **Hormones and Endocrine Disrupting Chemicals:** Hormones used for therapeutic purposes may fall into the pharmaceutical category listed above and many of the other families of emerging contaminants have endocrine disrupting effects. It does however feel pertinent to mention hormones and endocrine disruptors in their own right. Many synthetic hormones, such as oestradiol and estrone used in contraceptive medicine and hormone replacement therapies, are found in significant concentrations in waterbodies (17). Other non-hormonal endocrine disruptors include phthalates, used in the plastics industry (18); butyl parabens, found in cosmetics (19); and a wide variety of flame retardants (20, 21).
- **Per- and Poly-fluoroalkyl Substances (PFAS):** A family of chemicals identified for their heat resistance and chemical resistance and used in a variety of applications including paints, coatings and most famously for non-stick cookware. While the most prevalent PFAS chemicals such as perfluorooctanoic acid (PFOA) and perfluorooctane sulphonate (PFOS) are now banned in Europe, they are still found in the environment from leaching from products created using them prior to the ban (22). Traditional wastewater treatment plants have significant trouble in remediating PFAS from water (23), which is an ongoing area of research (24, 25).
- **Pesticides:** Pesticides are a blanket term for many chemicals that have the effect of targeting a range of pest species. They can include herbicides, fungicides, insecticides, acaricides, and molluscicides, for use in arable and livestock farming as well as in companion animal veterinary medicine and domestic gardening (26). While effective in their target environment, when removed from their intended surroundings can have unintentional consequences. Pesticides can enter aquatic environments from many routes including runoff from fields, through soil leeching, and via domestic sewer systems.
- **Food Additives:** Many food additives fall under the umbrella of flavourings, preservatives, and antimicrobial agents. Some common food additive emerging contaminants include caffeine (9) and artificial sweeteners like sucralose and aspartame (27).

- **Microplastics:** Microplastics are defined as small plastic particles less than 5 mm, they can be made of many different chemical species. Even smaller, micro (nano)plastics (MNP), defined as being smaller than 100 µm, have been shown to affect nutrient absorption in plants and accumulation in plant organs including fruits and leaves (28). MNP have also been known to accumulate in aquatic organisms as well, leading to issues with reproduction, growth, and behaviour (29). These pollutants can also bioaccumulate and biomagnify up the food chain, potentially transferring to humans and other animal species leading to chronic health conditions (30).
- **Nanomaterials:** This group of materials are split into two subgroups: Nanomaterials (NMs) having one dimension in the range of 1-100 nm and nanoparticles (NPs), which have all of their dimensions in this range. NMs have a wide range of applications including building materials, targeted drug delivery systems and cosmetics. These materials are further broken down into organic NMs such as proteins and carbohydrates; synthetic carbon NMs like fullerenes and carbon nanotubes; and inorganic NMs made of metallic or ceramic compounds such as titanium dioxide used in sunscreens and paints. While organic and carbon NMs are thought to be biodegradable, inorganic NMs are not and can lead to health risks including inflammatory responses and DNA damage in living organisms (31) .

These pollutants are typically found at low concentrations, but are still at levels found to be at concentrations of significance to cause harm or adverse effects in humans or animals. Despite these low levels, many emerging contaminants manage to bypass traditional physical, chemical or biological wastewater treatment procedures due to their unique physicochemical makeup (32). This fact shows a dire need for new technologies capable of removing specific pollutants from water streams.

1.3 Water Remediation Technologies

Many water remediation technologies exist in industry today, with each having advantages and disadvantages based on application, scale and, capital and running costs. Wastewater treatment procedures can broadly be split into 4 categories: physical, chemical, biological, and electrochemical, which are further broken down into different technologies that will be briefly described, and their advantages and disadvantages addressed (33, 34).

1.3.1 Physical Treatment

Physical treatment processes are generally low energy and the simplest forms of wastewater treatment processes. They utilise physico-chemical interactions, such as adsorption, filtering and molecular sieving, to separate water from pollutant molecules, no chemical interactions take place during these processes. The most common examples are adsorption processes, membrane filtration, and reverse osmosis:

- **Membrane Filtration:** Membrane filtration utilises a thin physical barrier, which selectively allows certain molecules to pass through depending on their size. Membrane filtration can be separated into ultrafiltration (UF) and microfiltration (MF), depending on the pore size of the membrane medium, which determines the size of the molecules prevented from passing through (35). Many varieties of membrane media exist, giving them high separation selectivity and efficiency. However, membrane technologies suffer from fouling problems, requiring regular replacement and significant downtime, leading to higher costs of the wastewater treatment process (36). They suffer also from scaling issues and require high pressure to maintain flowrate through the membrane system.
- **Reverse Osmosis:** Osmosis is the phenomena seen when a solvent passes spontaneously from an area of high solvent concentration (low solute concentration) to an area of low solvent concentration (high solute concentration) due to the differences in chemical potential. Reverse osmosis (RO) forces this process in the opposite direction by applying a pressure gradient across a semi-permeable membrane (37). Like membrane filtration described above, the size and selectivity for separation are dependent on the membrane material utilised in the RO process. Unlike membrane filtration process, all of the water does not pass through the membrane but is separated into two streams: the permeate (the purified water, which passes through the membrane) and the concentrate (the remaining water, which does not pass through the membrane and contains all of the blocked pollutant molecules). The concentrate is allowed to flow away from the membrane and is collected and recycled for further treatment. RO systems suffer many of the same set-backs as membrane filtration systems in that they are prone to fouling and have large energy costs associated with the large pumping pressures required (38). RO systems have high initial capital costs (39), and may have high concentrate flowrates depending on the rejection rate of the system.

- **Adsorption:** Water purification utilising adsorbents dates back thousands of years, with documents from the Indus valley civilisation as far back as 450 BC detailing the use of sand and charcoal filters for treatment of drinking water (40). Adsorption processes occur at the surface of the adsorbent material, with target molecules adhering to, and being immobilised on, the surface. Adsorption is an efficient and low energy process, which is well understood with wide applicability for many target pollutants, depending on the adsorption media utilised. Adsorption can be limited by the capacity of the material, selectivity towards target species and ability to be regenerated. Adsorption phenomena will be discussed in greater detail in Chapter 3.

1.3.2 Chemical Treatment

Chemical wastewater treatment methods involve the reaction of chemical species or electron transfer between added chemical media and the target wastewater species. These chemical reactions allow for improved separation of the pollutants from purified water but also conversion of the pollutants into benign or less environmentally hazardous chemical species. Bleaching, coagulation/ flocculation, ion exchange and advanced oxidation process are some of the most common chemical treatment processes:

- **Bleaching:** Bleaching or chlorination is the addition of chlorine (Cl_2) or chlorine dioxide (ClO_2) to water as an oxidising agent (41, 42). These chemicals are effective for the disinfection and germicide of many bacteria, viruses, and parasites. Bleaching, however, has several issues, such as the need for chemical storage and utilisation, as well as unwanted by-products such as chloroform and halogenated hydrocarbons from the chemical interaction of chlorine species with pollutant molecules. Bleaching also incurs high running costs due to the cost of the chemical agents and potential requirements for downstream dechlorination processing.
- **Coagulation/ Flocculation:** Coagulation/ flocculation is a chemical treatment technique used to help in the process of sedimentation in wastewater streams. The chemicals added during the process promote the agglomeration of pollutant molecules into larger particles, which can then sediment and be removed (43). The process utilises two types of chemicals: inorganic hydrolysing metal coagulants (44), such as the aluminium based aluminium sulphate, sodium aluminate or aluminium chloride, or iron-based coagulants such as ferric salts like ferric sulphate

or ferric chloride; and organic polymeric flocculants both of which have drawbacks and advantages (45). Inorganic coagulants require high doses, leading to high costs. Synthetic organic coagulants are non-biodegradable and require further processing to avoid environmental damage after use, while natural organic coagulants have short shelf lives leading to waste. All coagulants lead to significant sludge formation, requiring costly disposal and storage.

- **Ion Exchange:** Ion exchange is the transfer of ions from the ion exchange material such as a resin and the liquid phase (46). It is commonly used in water softening where calcium and magnesium ions in the liquid phase are displaced by sodium ions from within the resin. The resins are also used to exchange more harmful cation pollutant ions such as cadmium, lead (47) and chromium (48) as well as potentially harmful anionic pollutants such as nitrate and perchlorate (49). Ion exchange resins are classified into anionic exchange resins which use anions, cationic exchange resins which exchange cations and amphoteric exchange resins where both ions of positive and negative charges can be substituted. Ion exchange resins are low energy and generally easily regenerated, but have limited pollutant range (only charged pollutants) and can become fouled by adsorption of organic contaminants (50).
- **Advanced Oxidation Processes:** Advanced oxidation processes (AOPs) utilise generation of oxidising agents through various means to help in the chemical treatment of wastewater (51). A few AOPs include:
    - Photocatalysis: The utilisation of light absorption on photocatalytic materials to generate hydroxyl and superoxide ions for oxidation of pollutants. Examples include titanium oxide and zinc oxide (52).
    - Fenton's Process: The use of an iron catalyst and hydrogen peroxide, which degrades into hydroxyl radicals for the oxidation of targeted pollutants (53).
    - Ozonation: The addition of ozone, a powerful oxidising agent which reacts with pollutants through many mechanisms depending on the pH of the aqueous environment (54).
    - Sonolysis: The use of ultrasonic waves to create hydroxyl and hydrogen ions for oxidation and reduction of pollutant molecules. Direct pyrolytic

cleavage of the pollutants due to the sound waves can also occur depending on the target molecules (55).

- Wet Air Oxidation: A high temperature (150-400 °C) and high pressure (2-40 MPa) (56) liquid phase oxidation process used to treat wastewater. At these reaction conditions, reactive species such as hydroxyl radicals are generated for the oxidation of the target pollutant species (57).

Advanced oxidation processes have many advantages including their effective treatment of difficult to remove pollutants and low sludge formation. However, many of the processes can lead to toxic by-products of the oxidation process, which remain untreated. Many of the processes require expensive chemicals or incur high energy costs, which present a barrier to economic feasibility (58).

1.3.3 Biological Treatment

Biological treatment is the utilisation of living creatures, such as fungi, algae or microbes or chemicals derived from living creatures like enzymes to degrade pollutants in water streams (59). Biological treatments can be broadly split into two categories depending on their use of oxygen in the reaction process as aerobic and anaerobic degradation:

- **Aerobic:** These processes require the use of microorganisms to consume organic compounds in an oxygen rich environment into carbon dioxide, water and other metabolites. Examples include activated sludge processes, sequencing batch reactors and rotating biological reactors (60). These are cost effective and highly efficient methods of dealing with organic material in wastewater systems. However, high sludge production, odour issues and temperature and weather perturbations are regular problems encountered by these processes.
- **Anaerobic:** These processes take place in the absence of oxygen, producing value added chemicals such as methane. Technologies include anaerobic digestion and completely stirred tank reactors (60). These technologies have high removal rates, low sludge production and provide a valorisation pathway for the products. However, small changes in process operating conditions and feedstocks can lead to vast differences in products presenting a barrier to scale-up for this process.

1.3.4 Electrochemical Treatment

Electrochemical methods involve the generation of redox reactions at the anode and cathode of an electrochemical cell. Treatment of both organic pollutants through oxidation at the anode and reduction of metal ions at the cathode is possible, giving a wide variety of targeted pollutants through these methods (61). The oxidation of organics can be either direct, occurring at the surface of the electrode and not involving other chemical species or indirect, with participation of oxygen containing species in the aquatic environment to form oxidising ions such as hydroxyl (33). A few electrochemical treatment technologies are discussed below:

- **Electrocoagulation:** Electrocoagulation utilises typically iron or aluminium electrodes to generate coagulant chemicals through sacrificial anode oxidation (62). This process then follows a similar mechanism as coagulation discussed above, but produces less sludge while still maintaining a high removal efficiency.
- **Electroflotation:** This technology utilises the hydrogen and oxygen gas bubbles generated through electrolysis of water. These bubbles create electoflocs, which are agglomerations of pollutants which are carried to the surface creating a bubbly suspension of pollutants which can easily be removed (63). This technology is often utilised in combination with electrocoagulation to increase pollutant removal efficiency.
- **Electrodeposition:** This technique exposes wastewater to direct electrical current, causing organic pollutants to be oxidised at the anode, and positively charged species like metal ions to be reduced at the cathode (64). This process has a high removal efficiency, but incurs high energy costs to maintain the high electric currents, and is inefficient for low concentration pollutant applications (65).
- **Electrocatalysis:** Electrocatalysis involves the use of a catalyst material to reduce the activation energy of redox reactions carried out through passing electrical currents through the wastewater solution (66). Electrocatalytic anodes, such as platinum and ruthenium oxide, can be used for the oxidation of organic contaminants (67).

1.3.5 Summary

In real word applications, these wastewater treatment technologies are used in series to meet consent standards due to their various strengths and target species. In this work,

adsorption was identified as a technology with potential for investigation due to its applicability to target many emerging contaminant species, as the sorbents used are tuneable and exhibit high removal efficiencies. Their low energy demand under operation, minimal chemical use, and economic viability, also make them attractive for use as a sustainable technology.

1.4 Research Approach

This research aims to develop sustainable adsorbents for use in water remediation applications. In order to achieve this goal, several frameworks for achieving sustainability and environmentally grounded concepts have been consulted to ensure that from the outset this work maximises economic, environmental and social utility.

1.4.1 UN Sustainable Development Goals

The United Nations sustainable development goals are a series of aims set out by all United Nations member states agreed as a framework for the improvement of health, to encourage economic growth and to reduce poverty while tackling climate change and becoming better caretakers of our natural environment. This work attempts to address some aspects of several sustainable development goals, the goals and the attempted impact are detailed below.

- **6. Clean Water and Sanitation**: This work aims to develop biochar adsorbents for use in water remediation applications, helping to develop new highly functional and tuneable materials for a use in a variety of applications
- **12. Responsible Consumption and Production**: This work utilises the renewable waste feedstock brewer's spent grain as the biomass precursor for the biochar materials rather than depletable sources like fossil fuels. The work also follows the Green Chemistry Principles of chemical synthesis to further this goal.
- **13. Climate Action**: The synthesis process of this work attempts to minimise energy consumption and waste products wherever necessary in attempt to lower the environmental impact of the synthesis process. Adsorbent technology is also inherently low energy separation technology as compared to other water remediation techniques.
- **14. Life Below Water**: Pollutants in wastewater systems can also affect the physical hydrosphere and biosphere. Adsorption technologies help to reduce the biological

and chemical oxygen demands of our waterways, reducing environmental strain and helping to reduce pollution in marine environments

1.4.2 Circular Economy

The circular economy is a concept with growing interest especially within Scotland. The concept of a circular economy lays out a plan for minimising waste products overall in the goal of a net-zero future. It states that as much as reasonably practical, waste streams and co-products from one process should be utilised as feedstocks by another process to minimise waste to landfill, reduce environmental impact and preserve virgin resources. It also generates additional revenue streams from products previously regarded as waste and reduces feedstock costs for downstream producers. In light of this, it is possible to create value from waste streams to support the development of sorbent materials for use in adsorption processes, addressing a range of applications.

Many families of adsorbents are widely used in research and industry, such as metal organic frameworks (MOFs), zeolites, metal organic polyhedra (MOPs), mesoporous silica, clays, and porous carbon adsorbents such as activated carbons and biochars. It is important to couple an adsorbent system application to the target species at the conditions where the separation process is to take place. Mesoporous materials are highly advantageous for liquid phase separations due to the wide pores allowing for effective diffusion through the matrix, while a high micropore volume is advantageous for gas phase separations where high surface area is most important. Surface chemistry and attraction of an adsorbent to a target species are also important but not the only factors of which researchers should be aware. For example, many MOFs are not stable in water, due to the low energy coordination bonds holding the ligands and metal centres together, making them generally unsuitable for aqueous separations (68). Thermal stability is also a factor to consider, if the adsorption process is to be carried out at elevated temperatures, for example in post-combustion flue gas remediation.

In the interest of environmental impact, cost savings, and process safety, the synthesis route of each adsorbent should be considered before an adsorbent is chosen. By following the principles of green chemistry and engineering, more environmentally conscious, economically sustainable and safer materials can be obtained (69). These green chemistry principles will be discussed in greater detail in Section 1.4.5.

1.4.3 Activated Carbon and Biochar

In this work, activated carbons and biochar materials have been investigated, as they offer unique advantages compared with other porous material adsorbents. Biochars are known to have highly porous structures with large surface areas, a wide variety of surface functional groups and pore size distributions, which are highly tailorable, depending on the synthesis conditions and precursor materials chosen. Biochars are highly thermally stable and stable in aqueous conditions. They can be easily mixed with binders to produce pellets, or ground to powders, depending on the requirements of the application. Biochars have the ability to be disposed of safely and easily at the end of their lifecycle, through composting or combustion, due to their high carbon content.

While many activated carbon materials have been traditionally synthesised from fossil fuel feedstocks, such as coal, peat, or bitumen, a concerted effort to move away from these practices has been undertaken in recent years. Such materials are increasingly synthesised from renewable waste materials or by-products from agriculture, forestry, and the food and drink industries. Materials, such as peanut shells, coconut shells, and waste wood, have begun to be used in recent times. These precursor materials can be bought in large quantities for low prices. Local waste sources can be utilised to further reduce transport costs, making waste precursor materials highly covetable for upcycling into biochar materials.

Biochars can be broadly split into two subcategories: physically activated and chemically activated. Chemically activated carbons are produced through pyrolysis of a precursor material impregnated with a chemical activating agent, such as potassium hydroxide, zinc chloride, phosphoric acid or potassium carbonate, under an inert atmosphere. Physical activation, on the other hand, takes place at relatively higher temperatures in an atmosphere of an oxidising agent, such as superheated steam or carbon dioxide gas. Activated carbons from a single precursor material can have widely different structures, behaviours and interactions with adsorbates, depending on the type of activation and the activating agent(s) used.

1.4.4 Biochar from Brewer's Spent Grain

Brewer's spent grain (BSG), or draff, is a major co-product of the brewing and distilling industry with major potential for valorisation (70). In Scotland alone it is estimated that over 45,000 tonnes of BSG are produced every year, based on BSG being 85% of the total by-

products of breweries (71, 72). The traditional waste route for BSG is as feed for cattle and other ruminants, with the rest being sent to landfill (73). As a nitrogen rich and high carbon content lignocellulosic biomass (74), it has great potential to be upcycled into higher value products.

BSG is a material of increasing interest to industry and academia in recent years with several new avenues for utilisation noted. BSG has applications in a variety of sectors, including upcycling into materials for soil remediation (75, 76), upcycling into fine chemicals, such as sugars (77), phenols (78), and fermentation products like ethanol (79) and lactic acid (80) as well as alternative ingredients in food stuffs like bread (81), muffins (82) and cookies (83). However, many recent studies have been investigating BSG as a precursor material for biochars and activated carbons, for use as adsorbents in remediation studies. BSG is used in its raw form as an adsorbent, however, pyrolysis vastly increases the surface area of the material, increasing its capacity and allowing for greater modification of the surface to target specific pollutants (84-86). Upcycling of BSG into a high-quality adsorbent could be used to tie multiple waste streams together, providing a circular economic pathway for the BSG and providing a renewable, low cost and environmentally conscious solution to water remediation issues.

Table 1.1 and Table 1.2 show a non-exhaustive list of publications converting BSG into biochars, the activating agents used and the pollutant species targeted. While not a biochar, the study “Recycling of Brewer’s Spent Grain as a Biosorbent by Nitro-Oxidation for Uranyl Ion Removal from Wastewater” is included in the table to show how the raw biomass can be utilised as an adsorbent. However, the low surface areas recorded are a barrier to their effective implementation in wastewater treatment systems despite the low processing cost.

A great number of activation methods are employed within the literature. In chemical activation, zinc chloride salt solution, phosphoric acid, hydrogen peroxide and sodium and potassium hydroxide are the most common chemical activator agents used. In physical activation, steam and carbon dioxide are the oxidising gases flown over the BSG during pyrolysis. Some studies use a combination of both chemical and physical methods. A wide range of surface areas can be achieved using the various recipes listed above, it is not simple enough to say one method of BSG biochar production is the best. There is a complex

interplay of the synthesis parameters taking place, giving rise to a variety of surface areas, pore size distributions and surface characteristics in the materials listed above.

The highest surface area found to date was for a char chemically activated with sodium hydroxide, pyrolysed at 800 °C, this had a very large surface area of 3286 $m^2 g^{-1}$ and extreme microporosity, making up 73% of the pore volume (87). Biochars obtained through physical activation methods were also created in this study with steam and carbon dioxide at 800°C, exhibiting surface areas of 636 $m^2 g^{-1}$ and 551 $m^2 g^{-1}$, respectively. Both showed the same extreme character of microporosity, at 65 and 68%, respectively but also contained a significant mesopore volume. The biochars in this study, however, were not subjected to any remediation tests on any target pollutant material but the results here show good promise for being highly effective in liquid phase adsorption systems due to their high surface areas and presence of mesopores within the porous matrix.

In other studies, many target pollutants have been tested: problematic metal ions such as chromium, uranium, cadmium and strontium; organic dyes such as methylene blue, tartrazine yellow and reactive red; emerging contaminants such as the pharmaceutical acetaminophen, the emerging contaminant pesticide pymetrozine, and the common food additive caffeine, have all be investigated to varying effectiveness showing the wide variety of potential applications for biochars derived from BSG.

Table 1.1: Publications utilising BSG as a feedstock for production of biochar materials

Article	Activation type	Activating agents	Synthesis conditions	Surface area ($m^2\ g^{-1}$)	Target species	Ref
Adsorption of caesium on different types of activated carbon	Physical	Steam	800 °C, 30- 45 min, 10-15 mL H_2O	686-758	Caesium	(88)
Acetaminophen removal by calcium alginate/activated hydrochar composite beads: Batch and fixed-bed studies	Physical and chemical	Steam, KOH, N_2	Physical: 220 °C, 10 °C min^{-1}, 16 hrs, Chemical: 800 °C, 10 °C min^{-1}, 1 hr, 1:4 w/w ratio KOH, 150 mL min^{-1} N_2	1872	Acetaminophen	(89)
Removal of the pesticide Pymetrozine from aqueous solution by biochar produced from Brewer's spent grain at different pyrolytic temperatures	Physical	N_2	300-700 °C, 2-4 hrs, 10 °C min^{-1}	6-25	Pymetrozine	(90)
Mild hydrothermally treated brewer's spent grain for efficient removal of uranyl and rare earth metal ions	Physical	Steam, NaOH	100-175 °C, 1-24 hrs	<2	La^{3+}, Eu^{3+}, Yb^{3+} and UO_2^{2+}	(91)
Adsorptive desulphurization of model oil by Ag nanoparticles-modified activated carbon prepared from brewer's spent grains	Chemical	H_3PO_4	300 °C, 20 °C min^{-1}, 30 mins, 0.3M H_3PO_4, 1 hr 300 °C	412	Dibenzothiophene	(92)
Adsorption of food dye using activated carbon from brewers' spent grains.	Chemical	H_2O_2, H_3PO_4	400C, 10 °C min^{-1}, 5 hrs	166-768	Tartrazine yellow dye	(93)
Recycling of Brewer's Spent Grain as a Biosorbent by Nitro-Oxidation for Uranyl Ion Removal from Wastewater	Chemical	H_2O_2, $KMnO_4$, $H_3PO_4/NaNO_2$	No pyrolysis	<2	U(VI)	(94)
Removal of cobalt and strontium by adsorption using Brewer's spent grain formed by pyrolysis	Physical	N_2	450, 650, 850 °C, 5 °C min^{-1}, 1 hr	2-394	Cobalt, strontium, Nickel, manganese, Cadmium and Sodium	(95)

Table 1.2: Publications utilising BSG as a feedstock for production of biochar materials (continued)

Article	Activation type	Activating agents	Synthesis conditions	Surface area (m^2 g^{-1})	Target species	Ref
Production, characterization and application of activated carbon from brewer's spent grain lignin	Chemical	H_3PO_4	1:1, 2:1, 3:1 g g^{-1}, 300, 450, 600 °C	33-692	Nickel, Calcium, Magnesium, Zinc, Iron, Chromium, Aluminium, Silicon, phenols sugars	(96)
Optimization of one-pot H3PO4-activated hydrochar synthesis by Doehlert design: Characterization and application	Chemical	H_3PO_4	10 °C min^{-1}, 100-200 °C, 4-24 hrs	9	Methylene blue dye	(97)
Adsorption kinetics of Cr(VI) ions onto biochar from brewer's spent grain	Chemical	KOH, H_3PO_4	600 °C, 3 hr, KOH: 1:3 ratio, H3PO4: 1:2 ratio	0-7	CR(VI)	(98)
Use of brewing industry waste to produce carbon-based adsorbents: Paracetamol adsorption study	Physical	N_2	400, 500, 550 °C, 20 mL min N_2	238-364	Acetaminophen	(99)
Properties of activated carbon obtained from brewer's spent grains	Physical and chemical	Steam, CO_2, NaOH	Physical: 800 °C with steam and CO_2, Chemical: 800 °C with 1:3 NaOH	551-3286	-	(87)
Activated hydrochar produced from brewer's spent grain and its application in the removal of acetaminophen	Physical and chemical	Steam, KOH	Physical: 220 °C, 10 °C min^{-1}, 16hr Chemical: 1:4 KOH, 800 °C 10 °C min^{-1}, 1 hr	10-1513	Acetaminophen	(100)
Chromium adsorption studies using brewer's spent grain biochar: kinetics, isotherm and thermodynamics	Physical and chemical	ZnCl	500- 700 °C, 30-180 mins, ZnCl concentration 5-20%	284-412	Chromium	(101)
Low-cost adsorbents prepared from brewer's spent grain for pollutants removal	Physical and chemical	H_3PO_4	Physical: 550 °C, 1 hr Chemical: 300 °C, 1.5 hr, 4.22:1 (w/w)	0-147	Methylene blue dye and Reactive red 120 dye, chromium (VI), caffeine, phosphates and ammonium	(102)

1.4.5 Green Chemistry & Engineering Principles

Green Chemistry is the practice of reducing or eliminating the generation of harmful substances at all stages of chemical processes lifecycle: synthesis, use and end of life (103). This concept has led to the adoption of The Twelve Principles of Green Chemistry by many scientists and engineers as a framework to fit their work to the global goal of sustainability. The green chemistry principles encapsulate all three pillars of sustainability: Environmental; Economic and Social with the overall goal of increasing process efficiency, reducing waste products, decreasing hazards to name a few. During the design phase of any chemical process, each of the principles should be considered and strived towards. The green chemistry principles considered in this work are listed as follows:

- **2. Atom Economy**: This principle calls for the incorporation of all reactant material to be part of the final product. This could take the form of running at stoichiometric amounts of reactants, or reduction of excess where possible. In this work this principle will take the form of maximising yield of biochar where possible, reducing the fraction of lignocellulosic biomass which is converted to pyrolytic compounds. These could be considered by-products or co-products which may have uses in other applications, but for this work only the solid biochar adsorbents are considered as the main product. The amount of gas required in the synthesis will also be reduced to an optimum value while maintaining adsorbent characteristic integrity, increasing the atom economy of the process. Consequently, chemical activation has also been ruled out for the initial design of this synthesis due to the increased waste production associated with these methods which is contrary to improving atom economy.
- **3. Less Hazardous Chemical Syntheses**: This principle encourages process safety to be considered in the design of all chemical processes, be this through more benign operating conditions i.e. low temperature and pressure or through minimising intermediates or products harmful to both the environment or human or animal health. In this work, the pyrolysis hold temperature will be minimised while maintaining adsorbent characteristic integrity, this leads to inherently less hazardous syntheses. Once again, the eradication of chemical activators from the synthesis (many of which are irritants and inherently hazardous like strong acids and bases) is partially due to this principle.

- **4. Designing Safer Chemicals**: This principle urges that where possible the design of chemical products should be non-toxic while retaining functionality. In this work, chemical activators, which may be retained by the porous matrix and leech into the environment during use were not considered for the initial design. Biochar materials may pose some hazards as a dust, they are generally seen as benign.
- **5. Safer Solvents and Auxiliaries**: This principle imposes the reduction, or elimination, of harmful solvents in chemical synthesis that may be toxic, flammable or corrosive. This may come in the form of solvent-free systems, use of water only, use of supercritical fluids or ionic liquids. In this work, only water is used as a solvent when necessary.
- **6. Design for Energy Efficiency**: This principle necessitates the minimisation of environmental and economic impact from energy requirements of chemical processes. In this work hold temperature, hold time will be minimised and ramp rate will be maximised in the interest of energy efficiency while maintaining adsorbent performance of the synthesised materials.
- **7. Use of Renewable Feedstocks**: This principle incentivises the transition away from depleting feedstocks such as fossil fuels wherever technically possible. This principle is imperative to the work carried out here, opting for a local high-volume waste product in brewer's spent grain rather than the traditional alternatives for carbonaceous adsorbent feedstocks like coal, virgin wood or peat.
- **10. Design to Degradation**: This principle addresses how the end-of-life plans of a synthesised chemical must be considered in its design. Materials should, where possible, be designed to degrade into benign products once their function is complete. This principle is key to the decision to use biochar materials in opposition to other synthetic adsorbents. MOFs and zeolites both have cases where their degradation products can lead to environmental and health hazards, while biochar materials can be safely combusted or allowed to reintegrate into soil in some applications.

Another framework for the design and implementation of sustainable process are the Principles of Green Engineering (69). While green engineering principles and green chemistry principles both have the same goal of minimising waste, developing safer production methods and helping with the design of inherently sustainable processes, green engineering principles take a broader perspective at the task. Green engineering looks at

the whole life cycle of a product, including procurement, use and end of life plans and is not only interested in chemical syntheses but all types of engineering: from chemical synthesis to manufacturing to architectural design. While there is significant cross-over between the two frameworks, the green engineering principles highlight some new areas of though. The principles of green engineering which are pertinent to this study are listed as follows:

- **2. Prevention Instead of Treatment:** This principle stipulates the design provision that preventing the production of by-products rather than separation from the desired products saves money, time and resources. This principle can also be understood in a process safety context, that in the hierarchy of controls elimination and substitution of a hazard are more desirable that controlling or protecting against a hazard once it has been created. This principle encapsulates principles 2 and 3 from the green chemistry principles and is employed in this work through the maximisation of yield and the optimisation of process parameters to their safest possible configurations while maintaining adsorption characteristic integrity of the synthesised material.
- **3. Design for Separation:** As product separation and purification are highly energy intensive process, this principle is imperative to minimise the energy, time and economic costs involved with these processes. Adsorption process are at their most fundamental a separation process: in this case of pollutants from water. Adsorption is inherently a low energy process, able to perform spontaneously at low temperature and pressure unlike many other liquid separation processes such as distillation. Physisorptive adsorption process even expel heat into their surroundings due to their inherent thermodynamic properties. In the development of materials for adsorption processes, this work furthers this principle as an alternative process to high energy separation process.
- **4. Maximise Mass, Energy, Space and Time Efficiency:** This principle mandates not only the maximisation of atom efficiency and energy efficiency as per principles 2 and 6 of green chemistry, but also for the efficiency of time and space. As discussed above, the synthesis process will be optimised to minimise temperature to save energy and maximise yield, reduce gas flowrates and not use chemical activation agents to increase atom economy while maintaining operational integrity as an adsorbent media. However, time efficiency will also be maximised by increasing ramp rate and reducing hold time in the reactor. Space efficiency, while not

optimised in this work is inherently lower through the choice to investigate adsorbent technologies which have an inherently lower plant footprint than bulky technologies such as some biological treatment apparatus.

- **6. Conserve Complexity:** This principle supports the need for simplicity in processes, as complicated materials require greater costs on reactants, energy and time as well as greater care in end of life recycling. In this work, the choice to omit chemical activators in the initial design stage is due to this principle. The choice to proceed with a single step pyrolysis process, rather than multistep processes seen in literature is also due to this principle.
- **7. Durability Rather than Immortality:** While this principle encapsulates some of what is covered by principle 10 of the green chemistry principles it goes slightly further than just calling for designers to consider the end of life plans for a material. This principle stipulates that all materials should be designed with an inherent life span, as materials which persist beyond their useful lifespan present problems by accumulating in the environment. An example of this are single use non-recyclable plastics, which after use take significant effort to properly dispose of and as a result are accumulating in land-fill sites across the world. The principle is followed in this work by choosing activated carbons, a biodegradable adsorbent material which can be combusted or composted depending on the application after their lifespan as an adsorbent material has expired. This is counter to other adsorbent materials like MOFs or zeolites which may degrade into harmful by-products or persist in the environment after their commercial lifespan has passed.
- **10. Integrate Local Material and Energy Flows:** This principle advocates for the utilisation of feedstocks and energy local to the site of production to minimise energy, environmental impact, costs and uncertainties caused by global supply chains. This work implements this principle by utilising the local, inexpensive feedstock BSG for the biomass component of the adsorbents rather than exotic biochar precursors such as coconut which must be imported from across the world.
- **12. Renewable Rather than Depleting:** This principle promotes the use of renewable feedstocks rather than finite resources wherever possible in a chemical process. This is not only due to the inherent sustainability positives in utilising a regenerative feedstock but as finite non-renewable precursor stocks dwindle, the price is likely to rise increasing operational costs and procurement issues. In this

work BSG is utilised as the biomass feedstock in opposition to finite biochar precursors like coal and peat.

Within all of these frameworks, there is a common theme that the use of materials should be minimised, and this approach has been adopted within this study to create the bio-based sorbents. By choosing a design of experiments approach, it is possible not only to reduce the raw materials used but also the energy invested in its processing, while also permitting the full parameter space to be mapped.

Using design of experiments to screen and optimise carbonaceous adsorbents is an area of emerging focus within the literature, and has been shown to be an effective way of understanding the synthesis parameters of a material and the responses in material characteristics (104). While work investigating the pyrolysis of brewer's spent grain for adsorbent manufacture has been shown, only surface level work utilising a design of experiments approach has been carried out (96). Brewer's spent grain derived activated carbon has been shown to be an effective material for the adsorption in liquid phase applications as shown in Table 1.1 and Table 1.2. The integration of three perspectives: the implementation of the design of experiments method and green chemistry guiding principles; the utilisation of brewer's spent grain as a precursor material; and the application of the derived biochar materials as a renewable and environmentally conscious liquid phase adsorbent constitutes the distinctive contribution of this research.

1.5 Design of Experiments

1.5.1 Basics of Design of Experiments

Design of experiments (DoE) is a statistically informed method of experimental planning, utilising information from wider literature and preliminary experiments and is initiated prior to commencing a study. It is preferable to a traditional "one factor at a time" experimental procedure due to much more information being elucidated by performing less experiments in many cases, saving both time and money spent in the laboratory.

Some basic terminology imperative to understanding the process of DoE is detailed below:

- **Factor**: An experimental variable under investigation, e.g. Temperature, pH or residence time. Factors are split into three subtypes:
    - **Design Factors**: One which is controlled during the DoE process.

    - **Constant Factors**: Factors which are kept at the same value for all experiments in the design.
    - **Nuisance Factors**: Which are further subdivided into uncontrolled (e.g. ambient temperature), controlled (e.g. raw material batch) and noise (e.g. instrument variation).
- **Factor Level**: The value of a factor, e.g. 300 K, 4 hours, pH 7
- **Response**: A measured parameter e.g. yield, surface area
- **Effect of a Factor:** The average response when a factor is changed from a low level to a high level
- **Interaction Between Factors**: These occur when the effect of a factor on a response depends on the level of another factor. These interactions can be synergistic, antergistic or have no effect.

Design of experiments has 3 main use cases:

1. **Screening**: The process of determining the factors of significance to a response variable
2. **Optimisation**: The process of finding the best set of conditions for a chosen response variable
3. **Robustness Testing**: The process of assessing the variability of a response at selected experimental conditions

In this work only screening and optimisation DoE were investigated and so only they will be discussed in the rest of this chapter.

1.5.2 Full Factorial Designs

Full factorial designs consist of all of the combinations of each factor at each factor level. They allow for the estimation of all main effects and all interactions between factors. The number of experiments in a full factorial design can be found from Equation 1.1 below.

$$Number\ of\ experiments = levels^{k} \tag{1.1}$$

Where *k* is the number of factors.

For a typical screening experiment with 2 factor levels the number of experiments doubles with every additional factor added. For this reason, full factorial designs are suitable for screening factors when the total number of factors is low. Factors are denoted as x_1, x_2, x_3

etc. while response variables, for a given set of factor levels, are denoted as y_1, y_2, y_3 etc. In a 2-level factorial design the levels are denoted as (+) and (-) representing the factor level at the maximum and minimum of the factor range.

Table 1.3 shows the 8 factor combinations for a 2 level, 3 factor (denoted as 2^3) full factorial design and Figure 1.1 displays the factor combinations, levels and responses as a 3D diagram.

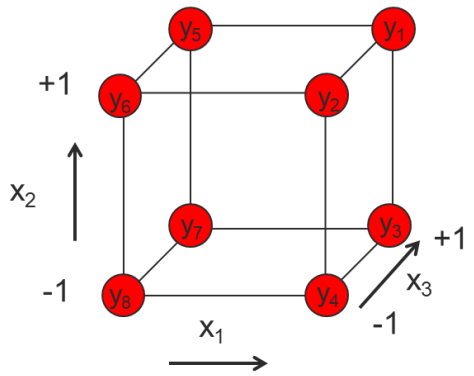

Figure 1.1: 3^2 full factorial design factor combinations diagram

Table 1.3: 3^2 full factorial design factor combinations

Experiment	x_1	x_2	x_3	Response
1	+	+	+	y_1
2	+	+	-	y_2
3	+	-	+	y_3
4	+	-	-	y_4
5	-	+	+	y_5
6	-	+	-	y_6
7	-	-	+	y_7
8	-	-	-	y_8

The model equation of this design would take the form shown below in Equation 1.2.

$$y = b_0 + b_1x_1 + b_2x_2 + b_3x_3 + b_{12}x_1x_2 + b_{13}x_1x_3 + b_{23}x_2x_3 + b_{123}x_1x_2x_3 \qquad (1.2)$$

Where b_0 is the offset term, b_1 is the coefficient of the effect of x_1, b_{12} is the interaction coefficient for factor x_1 and x_2 and b_{123} is the coefficient of the 3-factor interaction term of x_1, x_2 and x_3.

The effect of a parameter can be estimated as the average response as the factor moves from a low to a high-level while. For example, to estimate the effect on x_1 as described in Table 1.1 above, we would average the change in the responses while the other factors stay constant i.e. from y_5 to y_1, y_6 to y_2, y_7 to y_3, and y_8 to y_4. This is demonstrated in Figure 1.2 below.

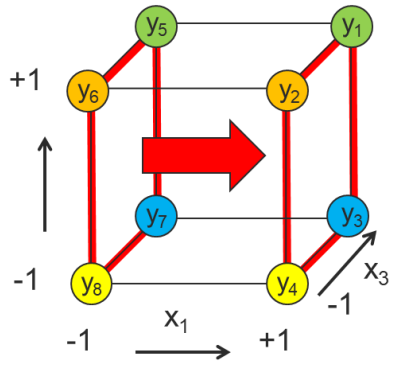

Figure 1.2: Estimation of effects of x_1 schematic

This could be written as:

$$Effect\ of\ x_1 = \frac{(y_1 - y_5) + (y_2 - y_6) + (y_3 - y_6) + (y_4 - y_8)}{4}$$

$$Effect\ of\ x_1 = \frac{y_1 + y_2 + y_3 + y_4 - y_5 - y_6 - y_7 - y_8}{4}$$

More generally this can be written as:

$$Effect\ \text{of}\ x_i = \frac{\sum y_{(+)} - \sum y_{(-)}}{2^{k-1}} \tag{1.3}$$

Where *i* is the factor.

Or:

$$Effect\ \text{of}\ x_i = \frac{\sum y_j\, x_{i,j}}{2^{k-1}} \tag{1.4}$$

Where *j* is the experiment number.

The effect is the average response between the highest value (-) to (+); in the above example, this would be a step of 2 (the distance from -1 to 1). To determine the coefficients of the model (which are the effects when the step size is 1, i.e. the value of the response

when the factor is 1 and all other factors are 0) we must divide by the step value, which in this example is 2.

So,

$$b_i = \frac{\sum y_i \, x_{i,j}}{2^k} \tag{1.5}$$

To determine the level of an interaction term, the levels of the components of the interaction should be multiplied together. The offset term is the value of the response when all factors are set to 0, it is always included at (+) for every experiment to allow for its calculation. For the 2^3 full factorial design, this is demonstrated in Table 1.4 below.

Table 1.4: 2^3 full factorial design factor combinations and interactions levels

Experiment	Offset	x_1	x_2	x_3	x_1x_2	x_1x_3	x_2x_3	$x_1x_2x_3$	Response
1	+	+	+	+	+	+	+	+	y_1
2	+	+	+	-	+	-	-	-	y_2
3	+	+	-	+	-	+	-	-	y_3
4	+	+	-	-	-	-	+	+	y_4
5	+	-	+	+	-	-	+	-	y_5
6	+	-	+	-	-	+	-	+	y_6
7	+	-	-	+	+	-	-	+	y_7
8	+	-	-	-	+	+	+	-	y_8

Calculating the effects for the full factorial design above would give the following:

Main effects

$$Effect\ of\ x_1 = \frac{(y_1 + y_2 + y_3 + y_4 - y_5 - y_6 - y_7 - y_8)}{4}$$

$$Effect\ of\ x_2 = \frac{(y_1 + y_2 - y_3 - y_4 + y_5 + y_6 - y_7 - y_8)}{4}$$

$$Effect\ of\ x_3 = \frac{(y_1 - y_2 + y_3 - y_4 + y_5 - y_6 + y_7 - y_8)}{4}$$

Two factor interactions

$$Effect\ of\ x_1x_2 = \frac{(y_1 + y_2 - y_3 - y_4 - y_5 - y_6 + y_7 + y_8)}{4}$$

$$Effect\ of\ x_1x_3 = \frac{(y_1 - y_2 + y_3 - y_4 - y_5 + y_6 - y_7 + y_8)}{4}$$

$$Effect\ of\ x_2x_3 = \frac{(y_1 - y_2 - y_3 + y_4 + y_5 - y_6 - y_7 + y_8)}{4}$$

Three factor interaction

$$Effect\ of\ x_1x_2x_3 = \frac{(y_1 - y_2 - y_3 + y_4 - y_5 + y_6 + y_7 - y_8)}{4}$$

Offset

$$Effect\ of\ Offset = \frac{(y_1 + y_2 + y_3 + y_4 + y_5 + y_6 + y_7 + y_8)}{4}$$

1.5.3 Fractional Factorial Designs

As stated before, full factorial designs are good for determining all of the main effects and all of the interaction effects but only when the number of factors is low. In reality, it is found that interactions of 3 or more factors are usually insignificant and can be discarded from the screening process. For this reason, is it is possible to use what is called fractional factorial design which uses a fraction of the number of experiments. The number of experiments in a fractional factorial design is described by Equation 1.6.

$$Number\ of\ experiments = levels^{k-m} \tag{1.6}$$

Where *m* is the degree of fractionation of the design, 1 for a half, 2 for a quarter etc.

The effect of a factor can be found using Equation 1.7.

$$Effect\ of\ x_i = \frac{\sum y_j\, x_{i,j}}{2^{k-m-1}} \tag{1.7}$$

And similarly, the coefficient of a factor or interaction can be found using Equation 1.8

$$b_i = \frac{\sum y_i\, x_{i,j}}{2^{k-m}} \tag{1.8}$$

The exact experiments which should be used in a fractional factorial design are not chosen at random. They must be chosen in a statistically designed manner, so as to minimise the

effects of confounding. Confounding is when two effects cannot be separated from each other due to an insufficient number of degrees of freedom in calculating the effects. For example, a 2^{3-1} half factorial using half of the design from Table 1.4 above could be described by Table 1.5 below. Figure 1.3 displays the factor combinations, levels and responses as a 3D diagram.

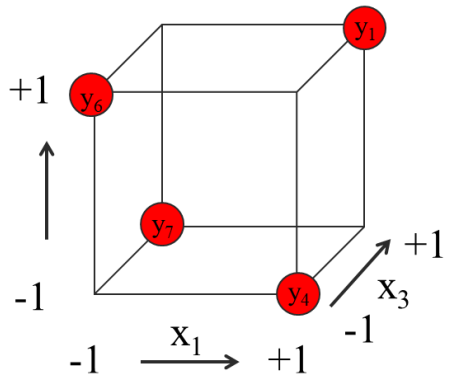

Figure 1.3: 3^{2-1} half factorial factor combination diagram

Table 1.5: 2^{3-1} half factorial design factor combinations and interactions levels

Experiment	Offset	x_1	x_2	x_3	x_1x_2	x_1x_3	x_2x_3	$x_1x_2x_3$	Response
1	+	+	+	+	+	+	+	+	y_1
4	+	+	-	-	-	-	+	+	y_4
6	+	-	+	-	-	+	-	+	y_6
7	+	-	-	+	+	-	-	+	y_7

Calculating the effects would give the following:

Main effects

$$Effect\ of\ x_1 = \frac{(y_1 + y_4 - y_6 - y_7)}{2}$$

$$Effect\ of\ x_2 = \frac{(y_1 - y_4 + y_6 - y_7)}{2}$$

$$Effect\ of\ x_3 = \frac{(y_1 - y_4 - y_6 + y_7)}{2}$$

Two factor interactions

$$Effect\ of\ x_1x_2 = \frac{(y_1 - y_4 - y_6 + y_7)}{2}$$

$$Effect\ of\ x_1x_3 = \frac{(y_1 - y_4 + y_6 - y_7)}{2}$$

$$Effect\ of\ x_2x_3 = \frac{(y_1 + y_4 - y_6 - y_7)}{2}$$

Three factor interaction

$$Effect\ of\ x_1x_2x_3 = \frac{(y_1 + y_4 + y_6 + y_7)}{2}$$

Offset

$$Effect\ of\ Offset = \frac{(y_1 + y_4 + y_6 + y_7)}{2}$$

We can clearly see that each of the effects on a factor or interaction has a corresponding effect with the same value. These factors are said to be confounded. Table 1.6 summarises the confounding in this design.

Table 1.6: 2^{3-1} half factorial confounded variables and the magnitude of the combined effect

Confounded Variables	Magnitude of effect
$x_1 + x_2x_3$	$\frac{(y_1 + y_4 - y_6 - y_7)}{2}$
$x_2 + x_1x_3$	$\frac{(y_1 - y_4 + y_6 - y_7)}{2}$
$x_3 + x_1x_2$	$\frac{(y_1 - y_4 - y_6 + y_7)}{2}$
Offset + $x_1x_2x_3$	$\frac{(y_1 + y_4 + y_6 + y_7)}{2}$

It should be noted that if the magnitudes of effects from Section 1.5.2 are summed for the confounded variable pairs in Table 1.6, it will be found to be equal to the confounded magnitude of effect. The model equation in Equation 1.2 has 8 unknown coefficients and so 8 experiments are required to determine all of the coefficients. With a half factorial design with only 4 experiments only 4 sets of confounded coefficients can be determined. The

equations are algebraically consistent, but there are not enough degrees of freedom in this fractional factorial example to determine the magnitude of the effect for every factor interaction.

The resolution of a fractional factorial design gives the extent to which the factors are confounded. The most common resolutions seen are:

1. Resolution III: main effects may be confounded with 2 factor interactions
2. Resolution IV: main effects may be confounded with 3 factor interactions, and 2 factor interactions may be confounded with other 2 factor interactions
3. Resolution V: assuming no 3 factor or higher interactions, main effects and 2 factor interactions can be estimated with no confounding.

Table 1.7 below describes the resolutions of all fractional factorial designs based on the number of factors, number of experiments and degree of fractionation.

In this work, any fractional factorial designs must be in resolution V or higher to allow for all main effects and 2 factor interactions to be estimated without confounding.

Table 1.7: Full and fractional factorial design resolutions for designs with up to 9 factors

		Number of Factors							
		2	3	4	5	6	7	8	9
Number of Experiments	4	2^2	2^{3-1}						
	8		2^3	2^{4-1}	2^{5-2}	2^{6-3}	2^{7-4}		
	16			2^4	2^{5-1}	2^{6-2}	2^{7-3}	2^{8-4}	2^{9-5}
	32				2^5	2^{6-1}	2^{7-2}	2^{8-3}	2^{9-4}
	64					2^6	2^{7-1}	2^{8-2}	2^{9-3}
	128						2^7	2^{8-1}	2^{9-2}
	256							2^8	2^{9-1}
	512								2^9

As stated above, the combinations chosen for a half factorial design must be chosen with care. In this work the National Institute for Standards and Technology (NIST) Engineering Statistics Handbook section on DoE was consulted to ensure any fractional factorial designs chosen were the optimal choice to minimise confounding (105).

1.5.4 Multivariate Analysis

While Equations 1.5 and 1.8 accurately calculate the coefficient values for our full and fractional factorial systems, the process can be quite time consuming and altering the step size for more complicated DoE systems can lead to complications in the calculation. For this reason, multivariate analysis using matrix algebra is used.

From the model equation for a 3^2 full factorial design, Equation 1.2, we can separate the coefficient from the factor levels in vector notation as shown in Equation 1.9.

$$y = (1 \quad x_1 \quad x_2 \quad x_3 \quad x_1x_2 \quad x_1x_3 \quad x_2x_3 \quad x_1x_2x_3) \begin{pmatrix} b_0 \\ b_1 \\ b_2 \\ b_3 \\ b_{12} \\ b_{13} \\ b_{23} \\ b_{123} \end{pmatrix} \tag{1.9}$$

Then, substituting in the full factorial combinations for each set of experimental conditions

$$\begin{matrix} y_1=(+ & + & + & + & + & + & + & +) \\ y_2=(+ & + & + & - & + & - & - & -) \\ y_3=(+ & + & - & + & - & + & - & -) \\ y_4=(+ & + & - & - & - & - & + & +) \\ y_5=(+ & - & + & + & - & - & + & -) \\ y_6=(+ & - & + & - & - & + & - & +) \\ y_7=(+ & - & - & + & + & - & - & +) \\ y_8=(+ & - & - & - & + & + & + & -) \end{matrix} \begin{pmatrix} b_0 \\ b_1 \\ b_2 \\ b_3 \\ b_{12} \\ b_{13} \\ b_{23} \\ b_{123} \end{pmatrix}$$

Which can then be rewritten in matrix notation as shown in Equation 1.10.

$$\begin{pmatrix} y_1 \\ y_2 \\ y_3 \\ y_4 \\ y_5 \\ y_6 \\ y_7 \\ y_8 \end{pmatrix} = \begin{pmatrix} + & + & + & + & + & + & + & + \\ + & + & + & - & + & - & - & - \\ + & + & - & + & - & + & - & - \\ + & + & - & - & - & - & + & + \\ + & - & + & + & - & - & + & - \\ + & - & + & - & - & + & - & + \\ + & - & - & + & + & - & - & + \\ + & - & - & - & + & + & + & - \end{pmatrix} \begin{pmatrix} b_0 \\ b_1 \\ b_2 \\ b_3 \\ b_{12} \\ b_{13} \\ b_{23} \\ b_{123} \end{pmatrix} \tag{1.10}$$

This is more generally written as Equation 1.11.

$$y = D.b \tag{1.11}$$

Where, D is the design matrix.

So, for known responses at each set of experimental condition, we can then solve for the coefficients of the model equation through matrix algebra using software such a MATLAB or Microsoft Excel.

For a Square Matrix *D*, the model coefficient matrix *b* can simply be found through Equation 1.12.

$$b = D^{-1}y \tag{1.12}$$

Where, D^{-1} is the inverse of matrix D.

For more complicated DoE systems, in which *D* is **not** a square matrix like optimisation models discussed later in Section 1.1.6, the model coefficient matrix *b* can be found by Equation 1.13.

$$b = D^{+}y \tag{1.13}$$

Where D^{+} is the pseudo- inverse of matrix *D*.

The pseudo-inverse can be found by:

$$D^{+} = (D^{T}D)^{-1}D^{T} \tag{1.14}$$

Where, D^{T} is the transpose of matrix *D*.

Note that the number of rows in *D* (i.e. The number of experiments ran) must be greater than or equal to the number of columns in *D* (i.e. The number of model coefficients) for proper calculation of the model coefficients matrix *b*.

1.5.5 Screening and Lenth's Analysis

The screening process is the act of determining the factors of significance to a process. Reducing the number of factors before optimisation allows for a vastly reduced number of experiments, reducing laboratory time and money spent on reagents. The standard method of determining factor significance involves running replicates of a data set, determining the variance of the data set and then using a method such at the root mean square formula to provide an estimation of fit. This however requires time consuming replications which can be avoided.

Lenth's analysis is a method for determining the factors of significance (106). It allows us to determine the pseudo standard error of factorial experiments without repetition of any experimental points. It is commonly used in many statistical software packages such as Minitab and Design-Expert. From this pseudo standard error, we calculate a critical value for the model coefficients calculated through multivariate analysis using a critical t-value for a given confidence interval and degrees of freedom. Any model coefficients with a magnitude lower than this critical value are assumed to be non-significant at this confidence interval. If a main effect is found to be non-significant it can be assumed that the interaction is also non-significant. A two-tailed critical t-value should be used for the analysis. The offset model coefficient should not be included in the analysis.

The method of Lenth's analysis is as follows:

1. Rank the magnitude of the coefficients from smallest to largest.
2. Calculate the median of the magnitude of the coefficients.
3. Calculate the pseudo standard error using Equation 1.15.

$$PSE = 1.5 \times Median \tag{1.15}$$

4. Exclude any values from the data-set which exceed $2.5 \times PSE_i$
5. Recalculate the median of the new data-set
6. Recalculate the pseudo standard error using Equation 1.15.
7. Calculate the degrees of freedom using Equation 1.16.

$$Degrees\ of\ Freedom = \frac{Number\ of\ coefficients}{3} \tag{1.16}$$

8. Calculate the critical t-value for the confidence interval chosen and the degrees of freedom using a 2-tail t-table. Note in this work a significance level of 0.05 or 95% confidence interval was used.

9. Calculate the critical value for the model using Equation 1.17.

$$Critical\ Value = t_{\alpha,\ DoF} \times PSE \tag{1.17}$$

The factors with coefficients with a magnitude greater than this critical value are said to be significant for this significance level and factor range investigated. They should be included in optimisation designs moving forward. Factors with coefficients less than this critical value should be set to a value to maximise key performance indicators for the process. For example, if residence time was deemed to be insignificant to the process, time should be minimised to allow for maximum production rate saving time and money.

1.5.6 Optimisation Designs

Two main types of optimisation design exist: Box-Behnken Designs and Central composite designs. In this work Central composite designs were chosen due to their simpler design and ease of design and calculation by hand, their ability to handle high numbers of factors and their better applicability at the extreme edges of the design space in comparison to Box-Behnken designs.

1.5.6.1 Central Composite Designs

The process of optimisation is that of determining the optimal factor levels for a certain response variable. While screening designs assume a linear relationship between factors and responses, optimisation designs consider non-linearity that we expect in more complex systems. For this reason, greater than 2 levels are required for the calculation of quadratic terms in the model equation. While we could use a full factorial design with 3 levels, the number of experiments greatly increases with increasing factors so more creative designs are incorporated.

In this work the Central Composite Designs (CCD) were considered. Central composite designs are comprised of 3 different types of points:

1. Factorial points, similar to those described above in Section 1.5.2
2. Axial points, also known as the “star points”
3. Centre points, repeated centre points, the number depends on the number of factors

CCD designs are recommended for 2-6 factors. Beyond this, the number of experiments becomes very large, hence the reason screening is carried out. The designs discussed here

are from the NIST database and in the interest of brevity and conceptualisation in 3D space, 2 factor and 3 factor designs will be used as examples moving forward.

CCD designs have 3 subtypes which all have their own specific use cases:

1. Central Composite Circumscribed (CCC)
2. Central Composite Inscribed (CCI)
3. Central composite Face-Centred (CCF)

The model equation for CCD models with 2 factors is shown in Equation 1.18, while the model equation for 3 factors is shown in Equation 1.19.

$$\boldsymbol{y = b_0 + b_1 x_1 + b_2 x_2 + b_{11} x_1^2 + b_{22} x_2^2 + b_1 x_1 x_2} \quad \textbf{(1.18)}$$

$$\boldsymbol{y = b_0 + b_1 x_1 + b_2 x_2 + b_3 x_3 + b_{11} x_1^2 + b_{22} x_2^2 + b_{33} x_3^2 + b_{12} x_1 x_2 + b_{13} x_1 x_3 + b_{23} x_2 x_3} \quad \textbf{(1.19)}$$

Each consists of the offset term, main effects, quadratic effects and two factor interactions.

1.5.6.2 Central Composite Circumscribed Designs

CCC designs give the best estimation of the whole design space and consist of 5 factor levels for each factor: $-\alpha_{CCC}$, -1, 0, 1 and α_{CCC}. They consist of a square in 2D or cube in 3D of factorial points on the permutations of 1 and -1, axial points extending from each edge in 2D and face in 3D at a distance of α from the centre point and a repeated centre point- 4 repetitions for 2D and 5 repetitions for 3D. α for CCC designs can be calculated from Equation 1.20.

$$\boldsymbol{\alpha_{CCC} = 2^{\left(\frac{factors}{4}\right)}} \quad \textbf{(1.20)}$$

As the name implies, the design is a square or cube with a side length of 2 (centre point to face size of size) circumscribed by a circle or sphere of axial points.

The factor combination table for a CCC with 2 factors is shown in Table 1.8 and for 3 factors in Table 1.9. A schematic representation of a 2 factor and 3 factor design are shown in Figure 1.4 and Figure 1.5. Note that the 2-factor schematic could also be treated as an orthogonal view of any one of the faces of the 3-factor schematic.

Table 1.8: 2 factor CCC factor combination table

Experiment	Point type	x_1	x_2
1	Factorial	-1	-1
2	Factorial	-1	1
3	Factorial	1	-1
4	Factorial	1	1
5	Axial	-1.414	0
6	Axial	1.414	0
7	Axial	0	-1.414
8	Axial	0	1.414
9	Centre	0	0
10	Centre	0	0
11	Centre	0	0
12	Centre	0	0
13	Centre	0	0

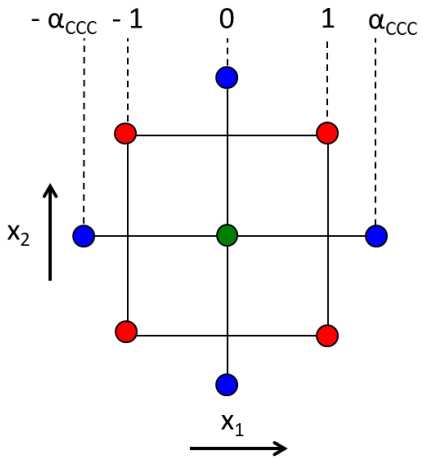

Figure 1.4: 2 factor CCC schematic

Table 1.9: 3 factor CCC factor combination table

Experiment	Point type	x_1	x_2	x_3
1	Factorial	1	1	1
2	Factorial	1	1	-1
3	Factorial	1	-1	1
4	Factorial	1	-1	-1
5	Factorial	-1	1	1
6	Factorial	-1	1	-1
7	Factorial	-1	-1	1
8	Factorial	-1	-1	-1
9	Axial	1.682	0	0
10	Axial	-1.682	0	0
11	Axial	0	1.682	0
12	Axial	0	-1.682	0
13	Axial	0	0	1.682
14	Axial	0	0	-1.682
15	Centre	0	0	0
16	Centre	0	0	0
17	Centre	0	0	0
18	Centre	0	0	0
19	Centre	0	0	0
20	Centre	0	0	0

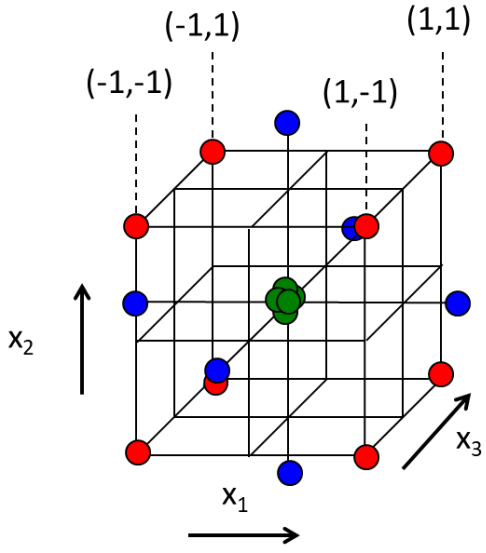

Figure 1.5: 3 factor CCC schematic

CCC designs as stated above give the best estimations for the design space. However, due to the axial points extending beyond the factorial design space, errors can occur from the factor ranges chosen. For example, if a full or fractional factorial screening design is being

retrofitted into the optimisation design where residence time was chosen as a factor with a range of 0.5 hours to 2.5 hours, corresponding to -1 and +1 in the design matrix. If $\boldsymbol{\alpha_{CCC}}$ is calculated for a three-factor system, a value of 1.682 would be equivalent to an upper limit of 3.182 hours but a lower limit at -1.682 of -0.182 hours, which is an impossible experimental condition. These errors can arise in a variety of factors, some may be deemed to be outside of a safe operating condition such as high temperature or pressure, some may be out with physical or operational feasibility such as long run times outside of site or laboratory opening hours, or numerical errors such as the example described above. The other CCD designs have ways of combating these range issues but come at penalties which will be described in the following sections.

1.5.6.3 Central Composite Inscribed Designs

The Central Composite Inscribed (CCI) designs differ from CCC designs described above by the entire design being enclosed within the -1 to +1 range while maintain 5 factor levels: -1, $-\alpha_{CCI}$, 0, α_{CCI} and 1. α_{CCI} can be calculated using Equation 1.21 below.

$$\boldsymbol{\alpha_{CCI}} = \frac{\mathbf{1}}{\mathbf{2}^{\left(\frac{\boldsymbol{factors}}{\mathbf{4}}\right)}} \qquad (\mathbf{1.21})$$

As the name suggests, the design is a circle in 2D or sphere in 3D with a square or cube inscribed within respectively. The designs consist of a square in 2D or cube in 3D of factorial points on the permutations of α_{CCI} and -α_{CCI}, axial points extending from each edge in 2D and face in 3D at a distance of 1 from the centre point and a repeated centre point- 4 repetitions for 2D and 5 repetitions for 3D.

The factor combination table for a CCI with 2 factors is shown in Table 1.10 and for 3 factors in Table 1.11. A schematic representation of a 2 factor and 3 factor design are shown in Figure 1.6 and Figure 1.7. Note that the 2-factor schematic could also be treated as an orthogonal view of any one of the faces of the 3-factor schematic.

Table 1.10: 2 factor CCI factor combination table

Experiment	Point type	x_1	x_2
1	Factorial	-0.707	-0.707
2	Factorial	-0.707	0.707
3	Factorial	0.707	-0.707
4	Factorial	0.707	0.707
5	Axial	-1	0
6	Axial	1	0
7	Axial	0	-1
8	Axial	0	1
9	Centre	0	0
10	Centre	0	0
11	Centre	0	0
12	Centre	0	0
13	Centre	0	0

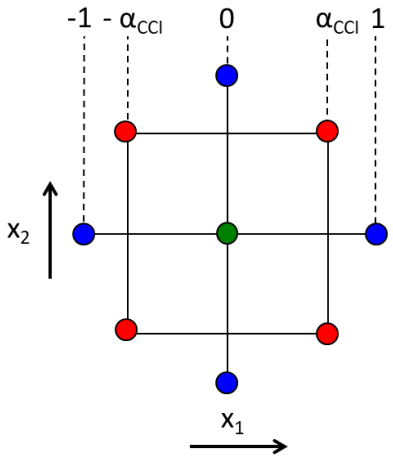

Figure 1.6: 2 factor CCI schematic

Table 1.11: 3 factor CCI factor combination table

Experiment	Point type	x_1	x_2	x_3
1	Factorial	0.595	0.595	0.595
2	Factorial	0.595	0.595	-0.595
3	Factorial	0.595	-0.595	0.595
4	Factorial	0.595	-0.595	-0.595
5	Factorial	-0.595	0.595	0.595
6	Factorial	-0.595	0.595	-0.595
7	Factorial	-0.595	-0.595	0.595
8	Factorial	-0.595	-0.595	-0.595
9	Axial	1	0	0
10	Axial	-1	0	0
11	Axial	0	1	0
12	Axial	0	-1	0
13	Axial	0	0	1
14	Axial	0	0	-1
15	Centre	0	0	0
16	Centre	0	0	0
17	Centre	0	0	0
18	Centre	0	0	0
19	Centre	0	0	0
20	Centre	0	0	0

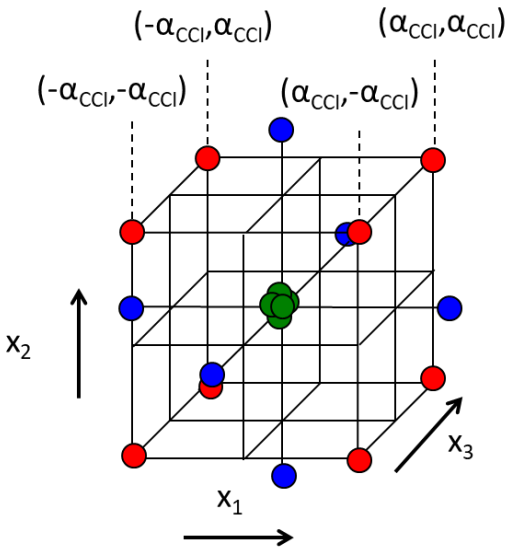

Figure 1.7: 3 factor CCI schematic

CCI offers the advantage of being entirely encapsulated within the -1 and +1 limits, ensuring no factor range issues as described in the CCC section above. It also has the advantage of 5 factor levels and so estimates main and quadratic effects well. However, it does have issues

with the estimation of values in the corner regions outside of the design space which may make it undesirable for designs where the optimal conditions are expected at the very extremes of the factor ranges.

1.5.6.4 Central Composite Face-Centred Designs

The Central Composite Face-Centred Design differs from both the CCC and CCF design as it only has 3 factor levels instead of 5. The entire design is enclosed with the -1 to +1 range with factor levels of -1, 0 and 1. The design is named after the face centred cubic crystal structure seen in nature, which the 3D design mimics. The designs consist of a square in 2D or cube in 3D of factorial points on the permutations of 1 and -1, axial points sitting on each edge in 2D and face in 3D at a distance of 1 from the centre point and a repeated centre point, 4 repetitions for 2D and 5 repetitions for 3D.

The factor combination table for a CCF with 2 factors is shown in Table 1.12 and for 3 factors in Table 1.13. A schematic representation of a 2 factor and 3 factor design are shown in Figure 1.8 and Figure 1.9. Note that the 2-factor schematic could also be treated as an orthogonal view of any one of the faces of the 3-factor schematic.

Table 1.12: 2 factor CCF factor combination table

Experiment	Point type	x_1	x_2
1	Factorial	-1	-1
2	Factorial	-1	1
3	Factorial	1	-1
4	Factorial	1	1
5	Axial	-1	0
6	Axial	1	0
7	Axial	0	-1
8	Axial	0	1
9	Centre	0	0
10	Centre	0	0
11	Centre	0	0
12	Centre	0	0
13	Centre	0	0

The CCF design is fully encapsulated within the -1 to 1 range and so no factor level issues can arise like with CCC design. The CCF design also has excellent estimation of the corners with comparison to CCI, allowing for good estimation of the response variable in the

extremes of the factor levels. However, due to only having 3 factor levels, the CCF design gives poor estimation of the quadratic effects in the model equation.

Table 1.13: 3 factor CCF factor combination table

Experiment	Point type	x_1	x_2	x_3
1	Factorial	1	1	1
2	Factorial	1	1	-1
3	Factorial	1	-1	1
4	Factorial	1	-1	-1
5	Factorial	-1	1	1
6	Factorial	-1	1	-1
7	Factorial	-1	-1	1
8	Factorial	-1	-1	-1
9	Axial	1	0	0
10	Axial	-1	0	0
11	Axial	0	1	0
12	Axial	0	-1	0
13	Axial	0	0	1
14	Axial	0	0	-1
15	Centre	0	0	0
16	Centre	0	0	0
17	Centre	0	0	0
18	Centre	0	0	0
19	Centre	0	0	0
20	Centre	0	0	0

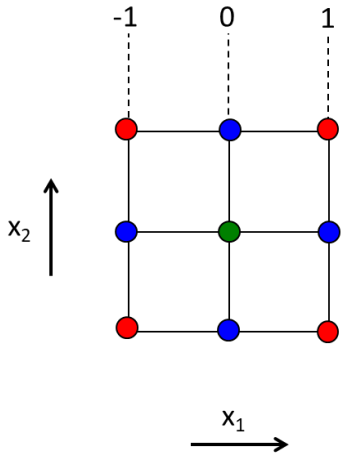

Figure 1.8: 2 factor CCF schematic

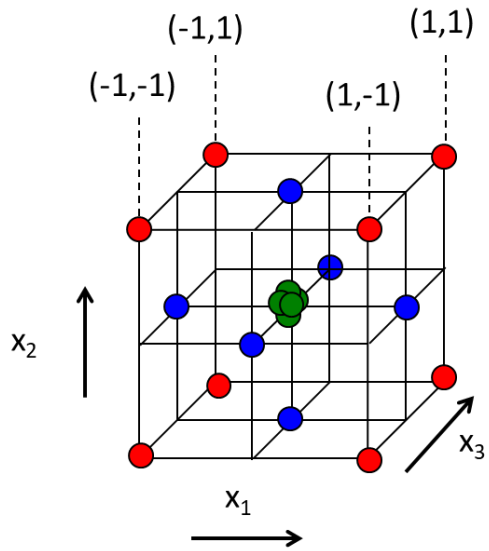

Figure 1.9: 3 factor CCF schematic

1.5.6.5 Central Composite Design Summary

As shown above, each of the CCD have their strengths and weaknesses and for this reason prior understanding and knowledge of the system being investigated through DoE is imperative to choosing the correct optimisation design. The pros and cons of the CCD design systems are summarised in Table 1.14 below.

Table 1.14: Advantages and shortcomings of each CCD design

Design	Potential factor range issues	Estimation of design space?	Estimation of quadratic effects
CCD	**Factor ranges must be checked for safety, operational and mathematical issues prior to proceeding**	**Good estimation of whole design space**	**Good estimation due to 5 factor levels**
CCI	**No problems with factor ranges**	**Poor estimation of extremes of factor levels**	**Good estimation due to 5 factor levels**
CCF	**No problems with factor ranges**	**Good estimation of whole design space**	**Poor due to only 3 factor levels**

In this work all DoE planning and calculation was carried out by hand on Microsoft Excel utilising matrix multiplication functions. This was to allow complete control of the design process at every stage and to show that DoE is not reliant on proprietary software for effective implementation.

1.5.7 Design of Experiments Development

1.5.7.1 Choice of Factors

For the synthesis of the biochars from brewer's spent grain, factor selection was initially approached in two ways. The first was from an extensive literature review of the synthesis parameters currently investigated for biochar production in a tube furnace. The planning step was investigation of the experimental set-up at the University of Strathclyde research labs. The equipment available, safety concerns and practical limitations were major contributors to the factors chosen for investigation in this study.

The ten factors identified as possibilities for investigation are as follows

1. **Tube Furnace Set-Point Temperature:** The maximum temperature at which the tube furnace will be held at during the synthesis procedure.
2. **Tube Furnace Residence Time at Set-Point**: The time the tube furnace will be held at the set-point temperature.
3. **Tube Furnace Temperature Ramping Rate:** The rate at which the tube furnace will be heated at to reach the set-point temperature.
4. **Inert Gas Flowrate:** The flowrate at which the inert gas is fed into the tube furnace. The inert atmosphere is to ensure no combustion takes place in the furnace, only pyrolysis. The inert gas will be used during the ramping and cooling phases of the synthesis process
5. **Activating Gas Flowrate:** The flowrate at which the activating gas is fed into the tube furnace. The activating gas is introduced during the isothermal step once the set-point temperature has been met for the duration of the residence time. The activating gas helps to promote the porous nature of the biochar and contributes to the surface chemistry of the material.
6. **Activating Gas Species:** Steam and carbon dioxide where both noted in the literature as activating gases for the production of biochar from lignocellulosic biomass.
7. **Chemical Activating Species:** Many chemical activators were noted in the literature including potassium hydroxide, phosphoric acid, sodium hydroxide and zinc chloride. The stage at which the chemical activators are introduced is also an important factor to consider, either prior or post pyrolysis. These also help to

develop the biochar porous matrix and contribute to the surface chemical environment of the produced biochar.

8. **Biomass Moisture Content:** Biochar can be produced as an as-received biomass or undergo drying prior to pyrolysis.
9. **Biomass Particle Size:** Biomass can be pelletised, powdered, sieved or ground to a uniform size prior to processing.
10. **Crucible Mass Loading:** The mass of biomass loaded into the tube furnace for pyrolysis.

The first 5 factors listed: Tube furnace set point temperature, referred to in the future as "hold temperature"; tube furnace residence time, referred to from now on as "hold time"; tube furnace temperature ramping rate, referred to from now on as "ramp rate"; inert gas flowrate and activating gas flowrate, were all chosen as design factors due to their ease of control and prevalence in the literature. The 5 unchosen from the list above were designated as constant factors, for the reasons detailed below.

Activating Gas Species: Carbon dioxide gas was chosen as the only activating gas to be investigated in this work due to the safety concerns. The risk of super-heated steam and condensation build up around the non-insulated Carbolite tube furnace used in this work was deemed an unresolvable hazard and so was eliminated from the process.

Chemical Activating Species: All chemical activation was initially eliminated from the process for both process safety reasons and to better align the synthesis of these biochars with the green chemistry and engineering principles as discussed in Section 1.4.5.

Biomass Moisture Content: Due to the biological nature of the lignocellulosic biomass used in this work and concerns around sample degradation due to fungal and bacteria growth, the biomass was frozen shortly after procurement. This unfortunately led to local sample variation, with ice aggregating at the base of the freezer containers, which would have led to sample heterogeneity between samples as well from the as-received basis. For this reason, all biochar was dried according to ASTM E871-82 as described in Section 4.2.1 to ensure, as much as reasonably practicable, that the biomass material was homogenised prior to pyrolysis. This had the added bonus of allowing the biomass material to be shelf stable for longer, allow for reduced use of the laboratory ovens and allow for greater speed of synthesis of the biochar materials.

Particle Size: This was chosen to be constant due to the pre-milled nature of the BSG as received from Tennent Caledonian brewers. Due to the milling process of the malted barley prior to the mashing process, the spent grain received was already fine milled and a homogenous particle size. In the interest of scale-up and reducing pre-processing, the particle size was taken as received and unmodified prior to drying and then pyrolysis.

Crucible Mass Loading: Due to the narrow bore of the tube furnace requiring a small crucible with a small volume alongside pre-screening experiments showing low yields for even low temperature pyrolysis, the mass loading was chosen to be the maximum volume of the crucible to maximise the mass of biochar produced for further characterisation. This was approximately 1.6g of dried brewer's spent grain which was used for every run carried out in this work.

1.5.7.2 Design Factor Range Selection

For the 5 design factors selected, the range of variables chosen were chosen to maximise the design space while ensuring safe and feasible ranges for the experimental equipment and local laboratory rules and regulations.

A local laboratory rule limited the allowable experimental conditions due to safety concerns. Cylinders of gases could not be run overnight due to the potential risk of a release while the laboratory was unmanned by competent laboratory user or technical staff. This is due to the risk to non-technical or untrained staff at the university who may have access out with normal laboratory opening times being exposed to asphyxiant gases. This therefore limited the furnace operation times from 9am till 5pm including sample preparation, purging, ramping, isothermal step and cooling. This had the knock-on effect which was noted as a quirk of the experimental set-up due to gas contraction during cooling. If there was no flow through the bubbler airlock system, which ensures a non-oxidising atmosphere was maintained within the pyrolysis tube of the tube-furnace, the contracting gas within the tube will cause water to be sucked into the tube. This would compromise the samples for accurate yield testing and potentially change the surface chemistry of the biochar samples through reaction with steam. For this reason, the bubbler stem had to be removed from the water reservoir prior to lab closure and gas cylinder shut-off. However, oxygen could not be introduced to the pyrolysis chamber while the furnace was at an elevated temperature as auto-ignition could occur not only ruining the biochar samples but causing a safety risk to operators and technical staff. For this reason, the

temperature of 450 °C (the minimum ignition temperature of carbon black of 500 °C with an extra safety allowance of 50 °C) was taken as the temperature at which oxygen could be safely allowed to enter the pyrolysis chamber (107).

Hold temperature range limits were determined through pre-screening runs on the experimental set-up. At temperatures below 500 °C, the biochar still had a brown colour, not the expected black of a biochar material and was determined completely non-porous through BET surface area analysis. At temperatures above 900 °C the biochar yield was extremely low; the materials had a very ashy grey appearance indicating almost all of the carbonaceous material had been volatilised in the pyrolysis process. These materials were also found to have very low surface areas. For this reason, 500-900 °C was set as the operating range for the hold temperature for the screening DoE.

The ramp rate lower limit was set as 5 °C min^{-1} to avoid unnecessarily long ramping times. The upper limit of 20 °C min^{-1} was chosen due to the tendency for the temperature to overshoot its set-point at ramping rates above this. As a safety feature on the tube furnace, a high alarm set at 25 °C above the set-point for the isothermal step, is included in programming which forces a shut-down of the heating regime if reached. The value of 20 °C min^{-1} limited overshoot to a maximum of a few degrees, ensuring this high alarm was never tripped during the course of this work.

The hold time upper limit was stipulated by the laboratory opening hours and cooling requirements as discussed above. It was determined through experimentation with the experimental apparatus that cooling from 900 °C to 450 °C would take approximately 2 hours and 20 minutes. This, alongside the maximum ramping time (20 °C to 900 °C at a rate of 5 °C min^{-1}) would take approximately 3 hours. For a normal 8 hour working day, this allows for a maximum hold time of 2 hours and 40 minutes. Allowing 10 minutes for sample preparation, the upper limit was taken as 2.5 hours. The lower limit was taken as 30 minutes (0.5 hours) to ensure sufficient time in the reactor and sufficient pyrolysis to occur but also to allow for a round range of 2 hours.

Both of the gas flowrates were limited by the available rotameters in the laboratory. Both had ranges from 60-600 mL min^{-1} which were chosen as the upper and lower bounds. The lower limit was required to be the first increment on the rotameter tube of 60 mL min^{-1} and not 0 or no flow, as no flow would lead to pyrolytic gases accumulating in the pyrolysis chamber. These would condense upon cooling, spoiling the biochar product.

1.5.7.3 Choice of Screening Response Variables

Three key performance indicators for the synthesis process of biochar from brewer's spent grain were selected. These were chosen based on the green chemistry principles as discussed before and to maximise the adsorbent performance and number of use cases for the adsorbents synthesised. The three response variables chosen for the screening portion of this work were:

- Yield
- Surface Area
- Point of Zero Charge

Yield was chosen as a response variable due to its importance in determining the efficiency of the synthesis process. This efficiency not only encapsulates cost effectiveness in upcycling the biomass to value added products but atom economy and effective use of the biomass material. While pyrolytic compounds can also be seen as value added products, their synthesis is not included in this work- only the yield of the biochar adsorbents is of interest.

Surface area was chosen as a response variable as a proxy to determine the usefulness of the synthesised materials as an adsorbent. Higher surface area materials have more sites for pollutant adsorptive molecules to adhere to and so high surface area materials are preferable in this work.

Point of zero charge, which will be better defined later in Section 4.5.1, was chosen as a response variable in this work as a proxy for tailorability of the biochar material surface chemistry. Point of zero charge is a reliable metric for determining if a pollutant is suitable for adsorption onto the surface of an adsorbent material. A wide range of points of zero charge are favourable as it allows for tuned synthesis depending on the pollutant requiring adsorption. If a factor or factors are capable of creating this change on the biochar materials it should be included in any optimisation process carried out in the future.

1.5.7.4 Screening Design

A 2 level, 5 factor full factorial design (2^5) consisting of 32 unique experimental runs was initially proposed for the screening section of this project. However, after consultation with Table 1.7 it was deemed possible to use a half factorial design, halve the number of

experiments required to 16 and still maintain a resolution V design if 3 factor or greater effects are assumed to be negligible.

This design would have a model equation as shown in Eq. 1.22.

$$y = b_0 + b_1x_1 + b_2x_2 + b_3x_3 + b_4x_4 + b_5x_5 + b_{12}x_1x_2 + b_{13}x_1x_3 + b_{14}x_1x_4 + b_{15}x_1x_5 + b_{23}x_2x_3 + b_{24}x_2x_4 + b_{25}x_2x_5 + b_{34}x_3x_4 + b_{35}x_3x_5 + b_{45}x_4x_5 \quad (\mathbf{1.22})$$

The half factorial design is detailed in Table 1.15.

Table 1.15: 2^{5-1} half factorial screening design

Experiment	Hold Temperature (°C)	x_1	Hold Time (Hours)	x_2	Ramp Rate (°C min^{-1})	x_3	Inert Gas Flowrate (mL min^{-1})	x_4	Activating Gas Flowrate (mL min^{-1})	x_5
1	500	-1	0.5	-1	5	-1	60	-1	600	1
2	900	1	0.5	-1	5	-1	60	-1	100	-1
3	500	-1	2.5	1	5	-1	60	-1	100	-1
4	900	1	2.5	1	5	-1	60	-1	600	1
5	500	-1	0.5	-1	20	1	60	-1	100	-1
6	900	1	0.5	-1	20	1	60	-1	600	1
7	500	-1	2.5	1	20	1	60	-1	600	1
8	900	1	2.5	1	20	1	60	-1	100	-1
9	500	-1	0.5	-1	5	-1	600	1	100	-1
10	900	1	0.5	-1	5	-1	600	1	600	1
11	500	-1	2.5	1	5	-1	600	1	600	1
12	900	1	2.5	1	5	-1	600	1	100	-1
13	500	-1	0.5	-1	20	1	600	1	600	1
14	900	1	0.5	-1	20	1	600	1	100	-1
15	500	-1	2.5	1	20	1	600	1	100	-1
16	900	1	2.5	1	20	1	600	1	600	1

The coded factor levels and factor combinations which will be used to form the D matrix for the multivariate analysis can be seen in Table 1.16.

Using yield, surface area and point of zero charge as response variables, the model coefficients of these factors and 2 factor interactions will be determined through multivariate analysis and ultimately their significance to each of the response variables will be determined through Lenth's analysis.

Table 1.16: 2^{5-1} half factorial design factor levels

Exp.	Offset	x_1	x_2	x_3	x_4	x_5	x_1x_2	x_1x_3	x_1x_4	x_1x_5	x_2x_3	x_2x_4	x_2x_5	x_3x_4	x_3x_4	x_4x_5
1	1	-1	-1	-1	-1	1	1	1	1	-1	1	1	-1	1	-1	-1
2	1	1	-1	-1	-1	-1	-1	-1	-1	-1	1	1	1	1	1	1
3	1	-1	1	-1	-1	-1	-1	1	1	1	-1	-1	-1	1	1	1
4	1	1	1	-1	-1	1	1	-1	-1	1	-1	-1	1	1	-1	-1
5	1	-1	-1	1	-1	-1	1	-1	1	1	-1	1	1	-1	-1	1
6	1	1	-1	1	-1	1	-1	1	-1	1	-1	1	-1	-1	1	-1
7	1	-1	1	1	-1	1	-1	-1	1	-1	1	-1	1	-1	1	-1
8	1	1	1	1	-1	-1	1	1	-1	-1	1	-1	-1	-1	-1	1
9	1	-1	-1	-1	1	-1	1	1	-1	1	1	-1	1	-1	1	-1
10	1	1	-1	-1	1	1	-1	-1	1	1	1	-1	-1	-1	-1	1
11	1	-1	1	-1	1	1	-1	1	-1	-1	-1	1	1	-1	-1	1
12	1	1	1	-1	1	-1	1	-1	1	-1	-1	1	-1	-1	1	-1
13	1	-1	-1	1	1	1	1	-1	-1	-1	-1	-1	-1	1	1	1
14	1	1	-1	1	1	-1	-1	1	1	-1	-1	-1	1	1	-1	-1
15	1	-1	1	1	1	-1	-1	-1	-1	1	1	1	-1	1	-1	-1
16	1	1	1	1	1	1	1	1	1	1	1	1	1	1	1	1

1.5.7.5 Optimisation DoE Development

The optimisation design will depend highly on the results of the screening experiments carried out in Chapter 5. It will depend on the number of significant factors, understanding of the design space and consideration of the factor ranges. This will be discussed further in Section 6.1.

1.6 References

1. Gleick PH. Water in crisis: New York: Oxford University Press; 1993.
2. DESA U. The Sustainable Development Goals Report: Special edition. UN, New York, USA. 2023.
3. Leonard AJ. War in Kyrgyzstan and Tajikistan: Freshwater Scarcity and the Path to Peace. 2025.
4. Matthews R, Vivoda V. 'Water Wars': strategic implications of the grand Ethiopian Renaissance Dam. Conflict, Security & Development. 2023;23(4):333-66.
5. Al-Shamaa M. Ethiopia's plan to fill reservoir opposed by Egypt at UN. ARAB NEWS [Internet]. 2022 [cited 2025 20/5]. Available from: https://www.arabnews.com/node/2132831/middle-east.
6. UNESCO. The United Nations world water development report 2024: Water for prosperity and peace: UN; 2024.
7. Connor R, Economic UN, Asia SCfW, Economic, Asia SCf, Pacific t, et al. The united nations world water development report 2017. wastewater: the untapped resource. 2017.

8. Helwig K, Cooper A, Pagaling E, Henderson F, Avery L, Roberts J, et al. Emerging Contaminants: Informing Scotland's strategic monitoring and policy approaches on substances of increasing concern. 2024.
9. Vieira L, Soares A, Freitas R. Caffeine as a contaminant of concern: a review on concentrations and impacts in marine coastal systems. Chemosphere. 2022;286:131675.
10. Raza'i TS, Amrifo V, Pardi H, Putra IP, Febrianto T, Ilhamdy AF. Accumulation of essential (copper, iron, zinc) and non-essential (lead, cadmium) heavy metals in Caulerpa racemosa, sea water, and marine sediments of Bintan Island, Indonesia. F1000Research. 2022;10:699.
11. Islam T, Repon MR, Islam T, Sarwar Z, Rahman MM. Impact of textile dyes on health and ecosystem: a review of structure, causes, and potential solutions. Environmental Science and Pollution Research. 2023;30(4):9207-42.
12. Richardson SD. Disinfection by-products and other emerging contaminants in drinking water. TrAC Trends in Analytical Chemistry. 2003;22(10):666-84.
13. Aus der Beek T, Weber FA, Bergmann A, Hickmann S, Ebert I, Hein A, et al. Pharmaceuticals in the environment—Global occurrences and perspectives. Environmental toxicology and chemistry. 2016;35(4):823-35.
14. Tovar-Sánchez A, Sánchez-Quiles D, Basterretxea G, Benedé JL, Chisvert A, Salvador A, et al. Sunscreen products as emerging pollutants to coastal waters. PLoS One. 2013;8(6):e65451.
15. Jagini S, Konda S, Bhagawan D, Himabindu V. Emerging contaminant (triclosan) identification and its treatment: a review. SN Applied Sciences. 2019;1:1-15.
16. Alberti S, Sotiropoulou M, Fernández E, Solomou N, Ferretti M, Psillakis E. UV-254 degradation of nicotine in natural waters and leachates produced from cigarette butts and heat-not-burn tobacco products. Environmental Research. 2021;194:110695.
17. Adeel M, Song X, Wang Y, Francis D, Yang Y. Environmental impact of estrogens on human, animal and plant life: A critical review. Environment international. 2017;99:107-19.
18. Dueñas-Moreno J, Vázquez-Tapia I, Mora A, Cervantes-Avilés P, Mahlknecht J, Capparelli MV, et al. Occurrence, ecological and health risk assessment of phthalates in a polluted urban river used for agricultural land irrigation in central Mexico. Environmental Research. 2024;240:117454.
19. Vale F, Sousa CA, Sousa H, Santos L, Simões M. Parabens as emerging contaminants: Environmental persistence, current practices and treatment processes. Journal of Cleaner Production. 2022;347:131244.
20. Yang J, Zhao Y, Li M, Du M, Li X, Li Y. A review of a class of emerging contaminants: the classification, distribution, intensity of consumption, synthesis routes, environmental effects and expectation of pollution abatement to organophosphate flame retardants (OPFRs). International journal of molecular sciences. 2019;20(12):2874.
21. Lippold A, Harju M, Aars J, Blévin P, Bytingsvik J, Gabrielsen GW, et al. Occurrence of emerging brominated flame retardants and organophosphate esters in marine wildlife from the Norwegian Arctic. Environmental Pollution. 2022;315:120395.
22. Stoiber T, Evans S, Naidenko OV. Disposal of products and materials containing per- and polyfluoroalkyl substances (PFAS): A cyclical problem. Chemosphere. 2020;260:127659.
23. Ford AT, Ginley F. Insights into PFAS contaminants before and after sewage discharges into a marine protected harbour. Chemosphere. 2024;366:143526.
24. Tang KHD. Per-and polyfluoroalkyl substances (PFAS) in wastewater streams: occurrence and current treatment. Academia Engineering. 2023;1(1).
25. Sanzana S, Fenti A, Iovino P, Panico A. A review of PFAS remediation: Separation and degradation technologies for water and wastewater treatment. Journal of Water Process Engineering. 2025;74:107793.

26. Authority EFS. Pesticides [Available from: https://www.efsa.europa.eu/en/topics/topic/pesticides.
27. Praveena SM, Cheema MS, Guo H-R. Non-nutritive artificial sweeteners as an emerging contaminant in environment: A global review and risks perspectives. Ecotoxicology and environmental safety. 2019;170:699-707.
28. Yu Z, Xu X, Guo L, Jin R, Lu Y. Uptake and transport of micro/nanoplastics in terrestrial plants: Detection, mechanisms, and influencing factors. Science of the Total Environment. 2024;907:168155.
29. Liu W, Liao H, Wei M, Junaid M, Chen G, Wang J. Biological uptake, distribution and toxicity of micro (nano) plastics in the aquatic biota: a special emphasis on size-dependent impacts. TrAC Trends in Analytical Chemistry. 2024;170:117477.
30. Li Y, Tao L, Wang Q, Wang F, Li G, Song M. Potential health impact of microplastics: a review of environmental distribution, human exposure, and toxic effects. Environment & Health. 2023;1(4):249-57.
31. Singh G, Thakur N, Kumar R. Nanoparticles in drinking water: Assessing health risks and regulatory challenges. Science of The Total Environment. 2024:174940.
32. Carballa M, Omil F, Lema JM, Llompart Ma, García-Jares C, Rodríguez I, et al. Behavior of pharmaceuticals, cosmetics and hormones in a sewage treatment plant. Water research. 2004;38(12):2918-26.
33. Ray S, Gusain R, Kumar N. Water purification using various technologies and their advantages and disadvantages. Carbon nanomaterial-based adsorbents for water purification. 2020:37-66.
34. Varjani SJ, Chaithanya Sudha M. Treatment technologies for emerging organic contaminants removal from wastewater. Water remediation. 2018:91-115.
35. Lee A, Elam JW, Darling SB. Membrane materials for water purification: design, development, and application. Environmental Science: Water Research & Technology. 2016;2(1):17-42.
36. AlSawaftah N, Abuwatfa W, Darwish N, Husseini G. A comprehensive review on membrane fouling: Mathematical modelling, prediction, diagnosis, and mitigation. Water 2021, 13, 1327.
37. Malaeb L, Ayoub GM. Reverse osmosis technology for water treatment: State of the art review. Desalination. 2011;267(1):1-8.
38. Mohammed HA, Sachit DE, Al-Furaiji M. Applications and challenges of the reverse osmosis membrane process: a review. Journal of Engineering and Sustainable Development. 2023;27(5):630-46.
39. Judd SJ. Membrane technology costs and me. Water research. 2017;122:1-9.
40. Çeçen F, Aktaş Ö. Water and wastewater treatment: Historical perspective of activated carbon adsorption and its integration with biological processes. Activated carbon for water and wastewater treatment: integration of adsorption and biological treatment. 2011;1.
41. Jonnalagadda S, Nadupalli S. Chlorine dioxide for bleaching, industrial applications and water treatment. Indian Chemical Engineer. 2014;56(2):123-36.
42. EPA U. Wastewater Technology Fact Sheet: Chlorine Disinfection. 1999.
43. Verma AK, Dash RR, Bhunia P. A review on chemical coagulation/flocculation technologies for removal of colour from textile wastewaters. Journal of environmental management. 2012;93(1):154-68.
44. Duan J, Gregory J. Coagulation by hydrolysing metal salts. Advances in colloid and interface science. 2003;100:475-502.
45. Lee CS, Robinson J, Chong MF. A review on application of flocculants in wastewater treatment. Process safety and environmental protection. 2014;92(6):489-508.

46. Ali A, Sadia M, Azeem M, Ahmad MZ, Umar M, Abbas ZU. Ion Exchange Resins and their Applications in Water Treatment and Pollutants Removal from Environment: A Review: Ion Exchange Resins and their Applications. Futuristic Biotechnology. 2023:12-9.
47. Bożęcka A, Orlof-Naturalna M, Sanak-Rydlewska S. Removal of lead, cadmium and copper ions from aqueous solutions by using ion exchange resin C 160. Gospodarka Surowcami Mineralnymi. 2016;32(4):129-39.
48. Rengaraj S, Yeon K-H, Moon S-H. Removal of chromium from water and wastewater by ion exchange resins. Journal of hazardous materials. 2001;87(1-3):273-87.
49. Lehman SG, Badruzzaman M, Adham S, Roberts DJ, Clifford DA. Perchlorate and nitrate treatment by ion exchange integrated with biological brine treatment. Water research. 2008;42(4-5):969-76.
50. Levchuk I, Màrquez JJR, Sillanpää M. Removal of natural organic matter (NOM) from water by ion exchange–a review. Chemosphere. 2018;192:90-104.
51. Miklos DB, Remy C, Jekel M, Linden KG, Drewes JE, Hübner U. Evaluation of advanced oxidation processes for water and wastewater treatment–A critical review. Water research. 2018;139:118-31.
52. Dong S, Feng J, Fan M, Pi Y, Hu L, Han X, et al. Recent developments in heterogeneous photocatalytic water treatment using visible light-responsive photocatalysts: a review. Rsc Advances. 2015;5(19):14610-30.
53. Fenton HJH. LXXIII.—Oxidation of tartaric acid in presence of iron. Journal of the Chemical Society, Transactions. 1894;65:899-910.
54. Khamparia S, Jaspal DK. Adsorption in combination with ozonation for the treatment of textile waste water: a critical review. Frontiers of Environmental Science & Engineering. 2017;11:1-18.
55. Adityosulindro S, Barthe L, González-Labrada K, Haza UJJ, Delmas H, Julcour C. Sonolysis and sono-Fenton oxidation for removal of ibuprofen in (waste) water. Ultrasonics sonochemistry. 2017;39:889-96.
56. Villegas LGC, Mashhadi N, Chen M, Mukherjee D, Taylor KE, Biswas N. A short review of techniques for phenol removal from wastewater. Current Pollution Reports. 2016;2:157-67.
57. Zou LY, Li Y, Hung Y-T. Wet air oxidation for waste treatment: Springer; 2007.
58. Gusain R, Kumar N, Ray SS. Recent advances in carbon nanomaterial-based adsorbents for water purification. Coordination Chemistry Reviews. 2020;405:213111.
59. Sathya R, Arasu MV, Al-Dhabi NA, Vijayaraghavan P, Ilavenil S, Rejiniemon T. Towards sustainable wastewater treatment by biological methods–A challenges and advantages of recent technologies. Urban Climate. 2023;47:101378.
60. Talaiekhozani A. A review on different aerobic and anaerobic treatment methods in dairy industry wastewater. Goli A, Shamiri A, Khosroyar S, Talaiekhozani A, Sanaye R, Azizi K A review on different aerobic and anaerobic treatment methods in dairy industry wastewater Journal of Environmental Treatment Techniques. 2019;7(1):113-41.
61. Garcia-Segura S, Ocon JD, Chong MN. Electrochemical oxidation remediation of real wastewater effluents—A review. Process Safety and Environmental Protection. 2018;113:48-67.
62. Moreno-Casillas HA, Cocke DL, Gomes JA, Morkovsky P, Parga J, Peterson E. Electrocoagulation mechanism for COD removal. Separation and purification Technology. 2007;56(2):204-11.
63. Chen X, Chen G. Electroflotation. Electrochemistry for the Environment: Springer; 2009. p. 263-77.

64. Chang J-H, Ellis AV, Yan C-T, Tung C-H. The electrochemical phenomena and kinetics of EDTA–copper wastewater reclamation by electrodeposition and ultrasound. Separation and Purification Technology. 2009;68(2):216-21.
65. Zhu Y, Fan W, Zhou T, Li X. Removal of chelated heavy metals from aqueous solution: A review of current methods and mechanisms. Science of the Total Environment. 2019;678:253-66.
66. Singh N, Goldsmith BR. Role of electrocatalysis in the remediation of water pollutants. Acs Catalysis. 2020;10(5):3365-71.
67. Martínez-Huitle CA, Andrade LS. Electrocatalysis in wastewater treatment: recent mechanism advances. Quimica Nova. 2011;34:850-8.
68. Zhang S, Fu J, Xing G, Zhu W, Ben T. Porous Materials for Atmospheric Water Harvesting. ChemistryOpen. 2023;12(5):e202300046.
69. Anastas PT, Zimmerman JB. Peer reviewed: design through the 12 principles of green engineering. ACS Publications; 2003.
70. Jackowski M, Niedźwiecki Ł, Jagiełło K, Uchańska O, Trusek A. Brewer's Spent Grains—Valuable Beer Industry By-Product. Biomolecules. 2020;10(12).
71. Mussatto SI, Dragone G, Roberto IC. Brewers' spent grain: generation, characteristics and potential applications. Journal of Cereal Science. 2006;43(1):1-14.
72. Arnison R, Carrick R. Sector Study on Beer, Whisky and Fish. 2015.
73. Weegels PL, Courtin CM, Arrachid A, Silvestri M. Abstracts: Technology Track: Posters. Consumer Driven Cereal Innovation: AACC International Press; 2008. p. 177-86.
74. Vanreppelen K, Vanderheyden S, Kuppens T, Schreurs S, Yperman J, Carleer R. Activated carbon from pyrolysis of brewer's spent grain: Production and adsorption properties. Waste Management & Research. 2014;32(7):634-45.
75. Cacace C, Cocozza C, Traversa A, Coda R, Rizzello CG, Pontonio E, et al. Potential of native and bioprocessed brewers' spent grains as organic soil amendments. Frontiers in Sustainable Food Systems. 2022;6:1010890.
76. Yoo J-H, Luyima D, Lee J-H, Park S-Y, Yang J-W, An J-Y, et al. Effects of brewer's spent grain biochar on the growth and quality of leaf lettuce (Lactuca sativa L. var. crispa.). Applied biological chemistry. 2021;64:1-10.
77. Paz A, Outeiriño D, Guerra NP, Domínguez JM. Enzymatic hydrolysis of brewer's spent grain to obtain fermentable sugars. Bioresource technology. 2019;275:402-9.
78. Meneses NG, Martins S, Teixeira JA, Mussatto SI. Influence of extraction solvents on the recovery of antioxidant phenolic compounds from brewer's spent grains. Separation and purification technology. 2013;108:152-8.
79. Liguori R, Soccol CR, Vandenberghe LPdS, Woiciechowski AL, Faraco V. Second generation ethanol production from brewers' spent grain. Energies. 2015;8(4):2575-86.
80. Pejin J, Radosavljević M, Kocić-Tanackov S, Djukić-Vuković A, Mojović L. Lactic acid fermentation of brewer's spent grain hydrolysate by Lactobacillus rhamnosus with yeast extract addition and pH control. Journal of the Institute of Brewing. 2017;123(1):98-104.
81. Czubaszek A, Wojciechowicz-Budzisz A, Spychaj R, Kawa-Rygielska J. Baking properties of flour and nutritional value of rye bread with brewer's spent grain. LWT. 2021;150:111955.
82. Shih YT, Wang W, Hasenbeck A, Stone D, Zhao Y. Investigation of physicochemical, nutritional, and sensory qualities of muffins incorporated with dried brewer's spent grain flours as a source of dietary fiber and protein. Journal of Food Science. 2020;85(11):3943-53.
83. Petrović JS, Pajin BS, Kocić TSD, Pejin JD, Fišteš AZ, Bojanić NĐ, et al. Quality properties of cookies supplemented with fresh brewer's spent grain. Food and Feed research. 2017;44(1):57-63.

84. He Y, Dietrich AM, Jin Q, Lin T, Yu D, Huang H. Cellulose adsorbent produced from the processing waste of brewer's spent grain for efficient removal of Mn and Pb from contaminated water. Food and Bioproducts Processing. 2022;135:227-37.
85. Stjepanović M, Velić N, Lončarić A, Gašo-Sokač D, Bušić V, Habuda-Stanić M. Adsorptive removal of nitrate from wastewater using modified lignocellulosic waste material. Journal of molecular liquids. 2019;285:535-44.
86. Wu J, Zhang Z, Xu J, Lu X, Wang C, Xu H, et al. Brewer's grains with different pretreatments used as bio-adsorbents for the removal of Congo red dye from aqueous solution. BioResources. 2020;15(3):6928-40.
87. Jagiełło K, Hińcz W, Kaczorowska W, Jackowski M, Bartman M, Kaczmarczyk J. Properties of activated carbon obtained from brewers spent grains. Biomass Conversion and Biorefinery. 2024;14(5):6475-93.
88. Vanderheyden S, Van Ammel R, Sobiech-Matura K, Vanreppelen K, Schreurs S, Schroeyers W, et al. Adsorption of cesium on different types of activated carbon. Journal of Radioanalytical and Nuclear Chemistry. 2016;310:301-10.
89. de Araújo TP, Quesada HB, Dos Santos DF, da Silva Fonseca BC, Barbieri JZ, Bergamasco R, et al. Acetaminophen removal by calcium alginate/activated hydrochar composite beads: Batch and fixed-bed studies. International Journal of Biological Macromolecules. 2022;203:553-62.
90. Xi X, Yan J, Quan G, Cui L. Removal of the pesticide pymetrozine from aqueous solution by biochar produced from brewer's spent grain at different pyrolytic temperatures. BioResources. 2014;9(4):7696-709.
91. Su Y, Böhm W, Wenzel M, Paasch S, Acker M, Doert T, et al. Mild hydrothermally treated brewer's spent grain for efficient removal of uranyl and rare earth metal ions. RSC advances. 2020;10(73):45116-29.
92. Olajire A, Abidemi J, Lateef A, Benson N. Adsorptive desulphurization of model oil by Ag nanoparticles-modified activated carbon prepared from brewer's spent grains. Journal of environmental chemical engineering. 2017;5(1):147-59.
93. Castro'º LEN, Mançano RR, Battocchio DAJ. Adsorption of food dye using activated carbon from brewers' spent grains. Acta Scientiarum Technology. 2023;45:e60443.
94. Su Y, Wenzel M, Paasch S, Seifert M, Böhm W, Doert T, et al. Recycling of brewer's spent grain as a biosorbent by nitro-oxidation for uranyl ion removal from wastewater. ACS omega. 2021;6(30):19364-77.
95. Lee HW, Jeon HG, Kim K-W. Removal of cobalt and strontium by adsorption using Brewer's spent grain formed by pyrolysis. Environmental Geochemistry and Health. 2023;45(10):7131-44.
96. Mussatto SI, Fernandes M, Rocha GJ, Órfão JJ, Teixeira JA, Roberto IC. Production, characterization and application of activated carbon from brewer's spent grain lignin. Bioresource technology. 2010;101(7):2450-7.
97. de Oliveira Fontoura CR, Dutra LV, Guezgüan SM, Nascimento MA, de Oliveira AF, Lopes RP. Optimization of one-pot H3PO4-activated hydrochar synthesis by Doehlert design: Characterization and application. Journal of Analytical and Applied Pyrolysis. 2022;168:105775.
98. Kukić DV, Vasić VM, Panić SN, Radosavljević MS, Šćiban MB, Prodanović JM, et al. Adsorption kinetics of Cr (VI) ions onto biochar from brewer's spent grain. Acta Periodica Technologica. 2019(50):134-42.
99. Nadolny B, Heineck RG, Bazani HAG, Hemmer JV, Biavatti ML, Radetski CM, et al. Use of brewing industry waste to produce carbon-based adsorbents: paracetamol adsorption study. Journal of Environmental Science and Health, Part A. 2020;55(8):947-56.

100. De Araújo TP, Quesada HB, Bergamasco R, Vareschini DT, De Barros MASD. Activated hydrochar produced from brewer's spent grain and its application in the removal of acetaminophen. Bioresource technology. 2020;310:123399.
101. Geremias R, Pelissari C, Libardi N, Carpiné D, Ribani RH. Chromium adsorption studies using brewer's spent grain biochar: kinetics, isotherm and thermodynamics. Ciência Rural. 2023;53:e20210914.
102. Bachmann SAL, Nunes KGP, Calvete T, Féris LA. Low-cost adsorbents prepared from brewer's spent grain for pollutants removal. Emergent Materials. 2023;6(2):741-53.
103. Anastas P, Eghbali N. Green chemistry: principles and practice. Chemical Society Reviews. 2010;39(1):301-12.
104. Schaubeder JB, Guizani C, Selinger J, Mautner A, Hummel M, Spirk S. Design of experiments as a tool to guide the preparation of tailor-made activated carbons. Scientific Reports. 2023;13(1):3977.
105. Heckert NA, Filliben JJ, Croarkin CM, Hembree B, Guthrie WF, Tobias P, et al. Handbook 151: Nist/sematech e-handbook of statistical methods. 2002.
106. Lenth RV. L enth's Method for the Analysis of Unreplicated Experiments. Wiley StatsRef: Statistics Reference Online. 2014.
107. Safety Data Sheet Carbon BLack [Internet]. 2021. Available from: https://www.birlacarbon.com/wp-content/uploads/hse/AUS-GHS-RCB-ENGLISH.pdf.

2 Aims and Objectives

As discussed previously, the advancement and innovation in water treatment processes are imperative to increase the efficiency and costs associated with protecting both people and the environment from unwanted contamination. Emerging contaminants are a new classification of pollutant chemicals increasing in prevalence within water streams all over the world. Biochar adsorbent technologies have been identified as a cost effective and feasible solution to the removal of some emerging contaminants from water streams. Brewer's spent grain has been identified as a potential precursor material for the synthesis of biochars due to its high volume, low cost and potential for development into a circular economic system. An optimisation study has been proposed due to previous gaps in the literature, in which green engineering and chemistry principles will guide all levels of decision making.

The overall aim of this work is to produce a low-cost and effective adsorbent biochar that can operate as an alternative to already existing adsorbent technologies for water remediation applications.

This work will utilise design of experiments on brewer's spent grain, which has only had rudimentary optimisation work carried out using multivariate methods previously. The work will carry out a screening design of experiments, an important but often ignored step in the optimisation process. Both the screening and optimisation designs will utilise multiple response variables, this will allow for the consideration of multiple key performance indicators of adsorbent performance and tailorability. Throughout the work, the green chemistry principles and circular economic reasoning will be used to guide every decision in the optimisation process, to ensure a sustainable and effective optimal material for liquid phase adsorption applications is synthesised.

The objectives that will be undertaken to meet this aim are:

- Develop a synthesis pathway for upcycling brewer's spent grain waste into a value-added biochar product for use as an adsorbent in removing target species from water.
- Determine the synthesis parameters which are of statistical significance to the response variables: yield, surface area and point of zero charge through a screening DoE.

- Determine the optimal synthesis parameters for the best adsorption properties through an optimisation DoE.
- Minimise environmental impact through green chemistry principles throughout every aspect of the project while maintaining maximum utility as an adsorbent technology.
- Fully characterise the optimal adsorbent to understand composition, surface chemical properties, textual properties, adsorption behaviour, adsorption thermodynamics and mechanism of pollutant removal.
- Identify other use cases for the materials synthesised.
- Identify gaps in the knowledge found throughout this work and propose future research avenues.

3 Adsorption

3.1 Fundamentals of Adsorption

3.1.1 Introduction

Adsorption is a phenomenon that occurs at interfaces or boundaries between two phases. It is characterised by an increase in concentration of the adsorbate species in very thin layers at the surface of the adsorbent material. These layers of adsorbed material can be as thin as one molecule thick, known as a monolayer, or as multiple layers stacked on top of each other, known as multilayer adsorption. Adsorption is localised to adsorption sites on the surface of a material, only one molecule can be adsorbed at one site. If all the sites on a material are energetically the same and have the same enthalpy of adsorption, the material is said to have a homogenous surface. If the sites are chemically different or have varying enthalpies, depending on the behaviours of the neighbouring sites or the fraction of the sites occupied, the surface can be said to be heterogenous.

The molecules prior to adsorption while still existing in the bulk are referred to as adsorptive molecules. Once adsorption has occurred the molecules are referred to as adsorbate molecules. The adsorbent is the surface on which the adsorbate has attached to. Desorption is the reverse of adsorption, where the adsorbate molecule detaches from the adsorbent and returns to the bulk. These concepts are illustrated in Figure 3.10.

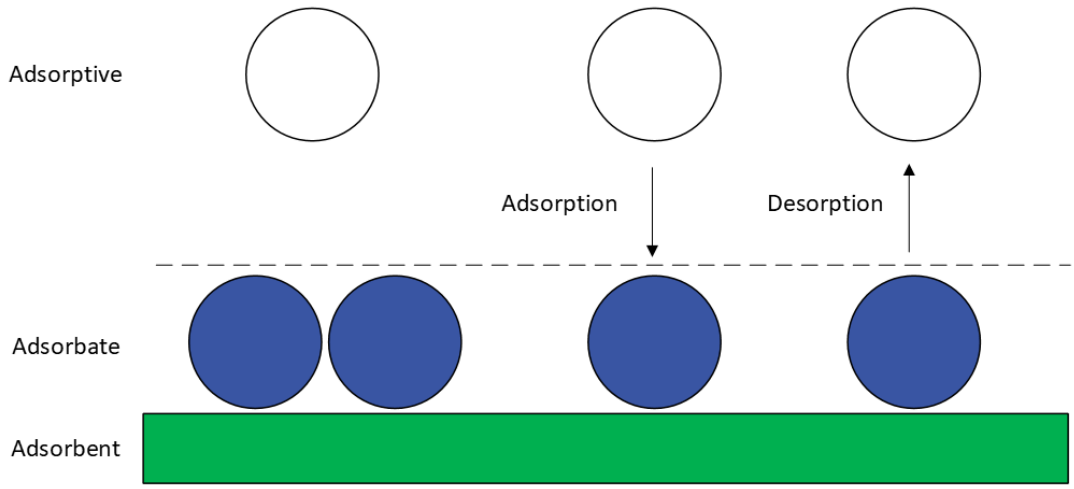

Figure 3.10: Labelled schematic of adsorption and desorption processes

Adsorption is a process which takes place in both liquid and gaseous phases and occurs as

one of two types: Physisorption or Chemisorption. Physisorption, also known as van der Waals adsorption, is caused by non-bonding intermolecular forces, such as electrostatic interactions, and van der Waals interactions between the adsorbent and adsorbate molecules (108). In physisorption, no chemical bonds are formed and the adsorbent and adsorbate both retain their chemical structures in the bulk. Physisorption is a dynamic equilibrium process where molecules are constantly adhering to and separating from the surface of the material. At equilibrium, the rate of adsorption and desorption are equal, and the amount of adsorbed material remains constant. In some cases, where there are strong adsorbate-adsorbate interactions, multilayers of physisorbed molecules can adsorb on top of the initial monolayer of adsorbate on the adsorbent surface. Due to the chemical integrity of the species involved in physisorptive interactions, the adsorbate molecules can be easily removed from the surface, by any of several processes, such as elevating the temperature, with the surface subsequently regenerated for reuse. Physisorption interactions are relatively weak, with a magnitude of generally agreed to be approximately 20-40 kJ mol^{-1} (108).

Chemisorption is an adsorption process where formal chemical bonds are made between the adsorbate and adsorbent surface. Due to this fact, chemisorption can only form a monolayer on the surface of a material, with chemisorbed multilayers not possible, although physisorption can still occur onto a chemisorbed monolayer. Bonds formed during chemisorption may be more stable in configuration than the internal bonds of the adsorbate prior to adsorption. This can lead to dissociation of the adsorbate, which may then be desorbed as a chemically different species, however, it should be noted that desorption in this case is also more energetically demanding than for physisorption. An example of this is oxygen adsorbing onto a carbon surface, where it bonds to the surface via dissociation into oxygen atoms, and desorbing as carbon monoxide (109). All chemisorbed layers begin formation as a physisorbed molecule, which then undergoes chemisorption and creates formal bonds with the adsorbent. Chemisorbed bond enthalpies are much stronger than those observed for physisorption, with formal chemical bonds being involved, and their magnitudes are generally agreed to be >80 $kJmol^{-1}$ (108).

3.1.2 Adsorption Mechanism

As physisorption involves intermolecular forces, and must be achieved preceding chemisorption, careful consideration and understanding of the intermolecular forces

experienced during adsorption processes should be investigated. Many types of intermolecular interactions can take place including but not limited to: charge- charge, charge dipole, dipole-dipole, charge-induced dipole, dipole-induced dipole, hydrogen bond, cation-π, π-π, van der Waals London forces and Van der Waals repulsion forces.

Depending on the chemical nature of the adsorbent and adsorbate, any number of these interactions may take place, in tandem with each other, to give the unique adsorbate-adsorbent behaviours present in any adsorption system. The system will tend to the interactions that leave the system in the lowest energy state possible i.e. the most spontaneous interaction and greatest payoff between release of heat and increase in disorder. For example, given the option between van der Waals forces and forming a hydrogen bond, the system will tend to form a hydrogen bond between the adsorbate and adsorbent as more energy is released.

The conditions at which adsorption takes place can also cause variation in the interactions that occur. Raising or lowering the pH of a liquid phase system is one such way to greatly alter the interactions taking place between the adsorbate and adsorbent (110). For example, proton addition to unsaturated carbonyl groups on the surface of an adsorbent will reduce the n-π interactions between the lone pairs and the adsorbate and replace them with hydrogen bonding interactions from the new, highly electronegative, hydroxyl functional group present on the surface. The chemistry of the adsorptive molecule may also change with varying pH (111). For example, creating formal charges and other new avenues for adsorption, like the adsorbent example above. Investigation of how hydrogen ion concentration affects the adsorption capacity of a material, along with knowledge of the adsorbate and adsorbent chemistry can be used to build a picture of the intermolecular interactions governing the adsorption mechanism.

3.2 Adsorption Equilibria

3.2.1 Introduction

Isotherms are one of the 3 ways of quantifying adsorption processes:

1. ***Isotherms:*** At constant temperature, driving force (pressure or concentration) is varied while uptake of adsorbate (or surface coverage) is measured;
2. ***Isobars:*** At constant driving force (pressure or concentration), temperature is varied and the uptake of adsorbate (or surface coverage) measured;

3. ***Isosteres:*** At constant surface coverage (uptake or mass adsorbed), temperature is varied and the response in driving force (pressure or concentration) is measured.

Isobars and isosteres are difficult to measure experimentally, so isotherms are the most commonly reported and, consequently, most studies report adsorption data in the form of isotherms. As a consequence of this, isotherms have become important in the classification of adsorbents, they can be used to determine the maximum capacity of the adsorbate and to evaluate equilibrium constants, thereby determining the suitability of an adsorbent-adsorbate pair.

By performing isotherms at various temperatures, we can determine the exothermic or endothermic nature of the adsorption process. Information from this, such as the mechanism of adsorption, can be elucidated. A trend of increased uptake at an elevated temperature would imply an endothermic enthalpy of adsorption and, subsequently, a chemisorption system, while a decrease in adsorption at elevated temperature would imply an exothermic system, which can involve either physisorption or chemisorption (112). Further rationalisation and discussion of adsorption thermodynamics will be covered in Section 3.3

By creating isosteres, i.e. determining the equilibrium concentration at constant coverage for different temperatures and using the van't Hoff equation, the isosteric heats of adsorption can also be found at various surface coverages (113). Discerning if and how the enthalpy of adsorption varies with surface coverage can help with the interpretation of the adsorption mechanism.

By fitting various isotherm models, such as Langmuir (114), Brunauer-Emmett-Teller (BET) (115), Freundlich (116) and Temkin (117), to experimentally obtained adsorption data, various parameters can be determined which describe the behaviour of those specific isotherms. The Langmuir and BET isotherm models are based on derivations from first principles, while the Freundlich and Temkin isotherm models are based on empirical data (118); however, all these models are based on inherent assumptions. The isotherm that fits the experimental data most appropriately can lend evidence that the data meets these assumptions better than other models. This can give an idea of the surface character of the adsorbent, and the adsorbent-adsorbate interactions occurring, such as the homogeneity or heterogeneity of the surface, the relationship between the enthalpy of adsorption and the surface coverage, and the existence of single or multilayer adsorption on the surface.

3.2.2 Langmuir Adsorption Theory

Langmuir adsorption theory was devised by the chemist Irving Langmuir who used the kinetic theory of gases to describe the behaviour of adsorption onto homogenous surfaces (114). The theory was first presented in 1916.

The key assumptions in Langmuir's isotherm theory are:

1. The surface of an adsorbent is a two-dimensional array of energetically homogenous sites;
2. Only one molecule can adsorb onto any one site, and saturation of adsorption occurs at monolayer coverage;
3. There are no interactions between adsorbed molecules.

This gives us the following variables:

$N_m =$ The total number of surface sites available for adsorption.

$N =$ The number of sites occupied by adsorbent molecules under specific conditions.

And, therefore:

$$\theta = \frac{N}{N_m} \tag{3.1}$$

Where $\theta =$ The fraction of occupied sites.

For a specific adsorbent at a fixed temperature, N_m is constant but N varies with the concentration or pressure of the adsorbate molecules in the system.

The rate of adsorption is dependent on the likelihood of a successful collision between an adsorbate molecule and an empty site. As collision rate is directly proportional to the concentration or pressure of the adsorbate in the system, then:

$$Rate\ of\ adsorption \propto P.(1-\theta)$$

$$Rate\ of\ adsorption = k_{ads}.P.(1-\theta) \tag{3.2}$$

While the desorption rate is dependent on the number of sites occupied by adsorbate molecules:

$$Rate\ of\ desorption \propto \theta.$$

$$Rate\ of\ desorption = k_{des}.\theta \tag{3.3}$$

Where:

P = System pressure at equilibrium, in bar (can be interchanged with concentration or any other measure of chemical activity, note that this will change the units of the other variables in the derivation).

k_{ads} = Rate constant of adsorption in bar^{-1}.

k_{des} = Rate constant of desorption which is dimensionless.

At equilibrium, the rate of adsorption and the rate of desorption are equal, so:

$$k_{ads}.P.(1-\theta) = k_{des}.\theta \tag{3.4}$$

By stating:

$$K_L = \frac{k_{ads}}{k_{des}} \tag{3.5}$$

Where K_L = Langmuir equilibrium constant in bar^{-1}.

Equation 3.4 can be simplified to:

$$\theta = \frac{K_L.P}{1 + K_L.P} \tag{3.6}$$

And by substituting in:

$$\theta = \frac{n}{n_m} \tag{3.7}$$

Where:

n = Moles of adsorbate adsorbed onto the surface at pressure P in mol g^{-1}.

n_m = Monolayer capacity of the adsorbent in mol g^{-1}.

We arrive at the final form of the Langmuir isotherm equation as:

$$n = \frac{n_m.K_L.P}{1 + K_L.P} \tag{3.8}$$

Note that n_m and n can be swapped for any measurable unit that quantifies adsorption on the surface, e.g. q_m and q for the mass of adsorbate, or v_m and v for volume of adsorbate, etc.

The Langmuir isotherm equation shown in Equation 3.8 can be linearised to the form shown in Equation 3.9:

$$\frac{P}{n} = \frac{1}{K_L.n_m} + \frac{P}{n_m} \tag{3.9}$$

If experimental data fits the Langmuir isotherm, it can indicate that the assumptions suit the system being investigated well. It can suggest that only monolayer coverage is present in the system, as well as the surface sites being homogenous and adsorption on these sites being independent of each other. This homogeneity can be validated through thermodynamic studies, such as those discussed later in Section 3.3.

3.2.3 Brunauer-Emmett-Teller Adsorption Theory

BET theory is an extension of Langmuir adsorption theory. It was developed, in 1938, after researchers observed that Langmuir theory breaks down at high pressures/concentrations (115). This is due to the assumption, within the derivation of Langmuir theory, that only monolayer coverage occurs. BET, by contrast, allows for multilayer coverage, increasing the validity of results obtained at high pressures/concentrations.

The key assumptions of BET theory are:

1. The adsorbent consists of an array of adsorption sites equal in energy; this energy is ΔH_A.
2. Adsorption in the first layer occurs only on these surface sites.
3. Adsorbed molecules do not interact with neighbouring molecules.
4. Multilayer formation can occur.
5. Adsorption energy in the second and higher layers is equal to the heat of liquefaction, ΔH_L.
6. Adsorption and desorption occur only on/from exposed sites.

The BET equation is shown in Equation 3.10:

$$\frac{P}{n\left(P^0 - P\right)} = \frac{1}{n_m} + \left[\frac{(c-1)}{n_m c}.\frac{P}{P^0}\right] \tag{3.10}$$

Where:

P^0 = Saturation vapour pressure of the adsorptive gas

P = Equilibrium pressure of the adsorptive

n = Adsorbate uptake at pressure P

n_m = Adsorbate monolayer coverage

c = Dimensionless BET constant related to adsorption energy.

The BET adsorption isotherm, and its applications, are discussed further in Section 3.5

3.2.4 Freundlich Adsorption Theory

The Freundlich Adsorption isotherm model is an empirical relationship proposed by Herbert Freundlich in 1909, prior to the theoretically derived models described above; the model was, by contrast, developed from empirical observations.

The Freundlich isotherm is based on the following assumptions:

1. The adsorbent consists of an array of energetically heterogenous sites.
2. Adsorption in the first layer is localised to these sites.
3. Adsorbed molecules can interact with neighbouring molecules.
4. Multilayer formation can occur.
5. Enthalpy of adsorption varies logarithmically with increasing surface coverage
6. Adsorption and desorption occur only on/from exposed sites.

The isotherm has, subsequently, been derived non-empirically from the van't Hoff isochore equation, by assuming an exponential relationship between the enthalpy of adsorption and surface coverage (119), this will be discussed further in Section 3.3.2. Irrespective of the derivation pathway, the Freundlich isotherm assumes a heterogenous surface, caused by one or more of three instances:

1. As adsorption takes place, adsorbed molecules interact with each other and alter the enthalpy of neighbouring sites;
2. There exists more than one unique, chemically different site for adsorption with varying adsorption enthalpies and entropies. In this case, adsorption occurs at the sites most favourable for adsorption, then the less favourable sites at higher pressures or concentrations;

3. A variety of potential adsorbate- adsorbent interactions occur. While a lowest energy state is most probable to occur in the system, local minima also exist and adsorption interactions may take place in these configurations.

The Freundlich equation for gaseous systems takes the form in Equation 3.11 below:

$$q = K_F P^{\frac{1}{n_F}} \tag{3.11}$$

Where:

$q =$ Uptake of adsorbate per mass of adsorbent, in mg g^{-1}

$P =$ Pressure of the system at equilibrium, in bar

$K_F =$ Freundlich characteristic constant, in mg g^{-1} $bar^{-1/n}$

$n_F =$ Heterogeneity parameter, a dimensionless constant, which gives a measure of the distribution of energy sites on the adsorbent, or the adsorption affinity between the adsorbent and adsorbate (120).

In the case of adsorbent surface heterogeneity:

- <1 suggests relatively heterogenous surface;
- >1 Suggests a relatively homogenous surface.

In the case of adsorption affinity:

- <1 suggests poor affinity between the adsorbent and the adsorbate molecule and may be physisorptive in nature;
- 1-2 suggests moderate affinity between the adsorbent and the adsorbate;
- 2-10 represents a strong affinity in the system and may be chemisorptive in nature.

In liquid systems, the Freundlich isotherm takes the form shown in Equation 3.12:

$$q = K_F C_e^{\frac{1}{n_F}} \tag{3.12}$$

Where:

$C_e =$ Concentration of the system at equilibrium, in mg L^{-1}

$K_F =$ Freundlich characteristic constant, in $mg^{(n-1)/n} L^{1/n} g^{-1}$

The Freundlich isotherm can be linearised to the equation shown in Equation 3.13, for gas phase systems:

$$\log(q) = \log(K_F) + \frac{1}{n_F}\log(P) \tag{3.13}$$

Or, for liquid phase systems, we arrive at Equation 3.14:

$$\log(q) = \log(K_F) + \frac{1}{n_F}\log(C_e) \tag{3.14}$$

The Freundlich isotherm model breaks down at high pressures, and concentrations, as it never reaches a theoretical maximum. It also does not obey Henry's law at low pressures, and concentrations (i.e. a linear response at low chemical activity).

If the Freundlich isotherm fits a system well, it may well indicate a system with heterogeneous surface character, where the enthalpy of adsorption varies exponentially with surface coverage. Multilayer coverage is also possible for these systems.

3.2.5 Temkin Adsorption Theory

Temkin adsorption theory is another empirical relationship developed as a response to the limitations of the Langmuir isotherm, proposed by Mihail Temkin in the 1930's. The Temkin isotherm model assumes the following:

1. The adsorbent consists of an array of energetically heterogenous sites.
2. Adsorption in the first layer is localised to these sites.
3. Adsorbed molecules can interact with neighbouring molecules.
4. Multilayer formation can occur.
5. Enthalpy of adsorption varies linearly with increasing surface coverage
6. Adsorption and desorption occur only on/from exposed sites.

The Temkin isotherm can also be validated thermodynamically using the van't Hoff isochore equation, by showing that the enthalpy of adsorption varies linearly with surface coverage. The Temkin isotherm assumes that indirect adsorbate-adsorbate interactions are the cause of the heterogenous behaviour of the surface. It is noted, experimentally, that the heat of adsorption tends to decrease with increasing surface coverage.

The Temkin isotherm model takes the form in Equation 3.15 below:

$$\mathrm{q} = n_T \ln(K_T P) \tag{3.15}$$

Where:

q = Uptake of adsorbate per unit mass of adsorbent, in mg g^{-1}

P = Pressure of the system at equilibrium, in bar

K_T = Temkin equilibrium binding constant, in bar^{-1}

n_T = Constant, with units mg g^{-1}, which is defined as, $n_T = \frac{RT}{b_t}$

Where:

R = Universal gas constant, 8.3145 J mol^{-1} K^{-1}

T = Temperature in K

b_T = Temkin constant, which is related to the heat of adsorption in J g mg^{-1} mol^{-1}

In liquid systems, the Temkin isotherm equation takes the form of Equation 3.16 below:

$$\mathrm{q} = n_T \ln(K_T C_e) \tag{3.16}$$

Where:

C_e = Concentration of the adsorbate at equilibrium, in mg L^{-1}

K_T = Temkin equilibrium binding constant, in L mg^{-1}

The Temkin isotherm model can be linearised to the form in Equation 3.17, for gas phase systems, below:

$$\mathrm{q} = n_T \ln K_T + n_T \ln P \tag{3.17}$$

Alternatively, for liquid phase systems, we obtain Equation 3.18:

$$\mathrm{q} = n_T \ln K_T + n_T \ln C_e \tag{3.18}$$

If the Temkin isotherm gives a good fit to experimental data, it may suggest a system with heterogenous character caused by interactions between particles in the adsorbate phase. This heterogeneity will linearly reduce the enthalpy of adsorption of the interactions, as surface coverage increases due to the assumption that adsorbate-adsorbate interactions

can occur, and highest energy sites fill first. Multilayer coverage may also be present in the system.

3.3 Adsorption Thermodynamics

3.3.1 Introduction

For adsorption to take place spontaneously, the Gibbs free energy of a system must be negative (112). Gibbs free energy is a function of the enthalpy, temperature and entropy of a system, and the relationship between these is shown in Equation 3.19 below:

$$\Delta G = \Delta H - T.\Delta S \tag{3.19}$$

Where:

$\Delta G =$ Change in Gibbs free energy of the system, in J mol^{-1}

$\Delta H =$ Enthalpy change in the system, in J mol^{-1}

$\Delta S =$ Entropy change in the system, in J mol^{-1} K^{-1}

$T =$ Temperature of the system, in K

In physisorption, a liquid or gaseous bulk phase contains adsorptive molecules, which are then immobilised on an adsorbent surface, reducing the degrees of freedom and, therefore, reducing the entropy of the system. This means that $\Delta S < 0$ (negentropic) for all physisorptive processes. In order for these processes to proceed spontaneously, i.e. $\Delta G < 0$, the enthalpy of a physisorptive process must always be negative, and therefore exothermic (112). These systems follow Le Chatelier's principle, where the equilibrium will move towards the desorbed state, as temperature increases (Gibbs free energy increases) and the amount adsorbed at an equilibrium concentration or pressure will increase at lower temperatures. There is also a critical temperature where, if the temperature is elevated above that value, the Gibbs free energy of the system will become positive, driving equilibrium towards the unadsorbed state due to the entropic term becoming larger than the enthalpic term.

In chemisorptive systems the relationship between the enthalpy and entropy of the system is much more intricate. As chemical reactions- bond cleaving and synthesis- are highly dependent on the reactants involved and products created, the total enthalpy change of the system is highly specific to the adsorbents and adsorptives involved. Using the logic

outlined above, if the enthalpy change in the system is positive, in order for the process to be spontaneous, the entropy of the system must always be positive (entropic) (112). An example of this is dissociative adsorption, where the adsorbed molecule dissociates into fragments of the original adsorbed species, which then bond to the adsorbent through chemisorptive bonds. This increases the number of degrees of freedom of the system, in turn, increasing the entropy of the system. These systems favour higher temperatures, obeying Le Chatelier's principle by decreasing the Gibbs free energy of the system, driving equilibrium towards the adsorbed phase.

Exothermic chemisorbed systems may either be entropically positive or entropically negative. Entropically negative exothermic chemisorbed systems behave exactly like physisorbed systems. Exothermic and entropically positive systems are spontaneous, at any temperature, but more spontaneous at higher temperature. This is counter intuitive to Le Chatelier's principle.

Physisorption enthalpies, as stated above, are always exothermic, but also have weaker magnitudes than those of chemisorption systems, at ~20-40 $kJmol^{-1}$ for the initial monolayer coverage. Subsequent multilayers have enthalpy magnitudes analogous to heats of liquefaction. Chemisorption heats of adsorption have magnitudes of ~80 $kJmol^{-1}$ or greater (121).

The magnitude and the sign of the enthalpy are both imperative to determining the type of adsorption occurring in the system.

3.3.2 Van't Hoff Isochore

The van't Hoff isochore equation is a relationship used in adsorption studies to determine the relationship between surface coverage and the enthalpy of adsorption (122). Many isotherm models make implicit assumptions between the surface coverage and the enthalpy of adsorption. Langmuir assumes a constant enthalpy, regardless of surface coverage, while Freundlich assumes an exponential change, and Temkin assumes a linear change with increasing surface coverage. An isochore, as stated above, is a method of measuring the change in adsorption parameters, where surface coverage is kept constant and the temperature is varied, allowing the change in equilibrium pressure or concentration of the adsorptive to be measured. Here, we use a series of isotherms, drawing a horizontal line at a given uptake on the y-axis and determining where this line

intercepts the isotherms, which are carried out at various temperatures. The corresponding equilibrium concentrations or pressures of the intersections at which these horizontal isochore lines intersect with the isotherms are noted. An example of this is shown in Figure 3.11 below:

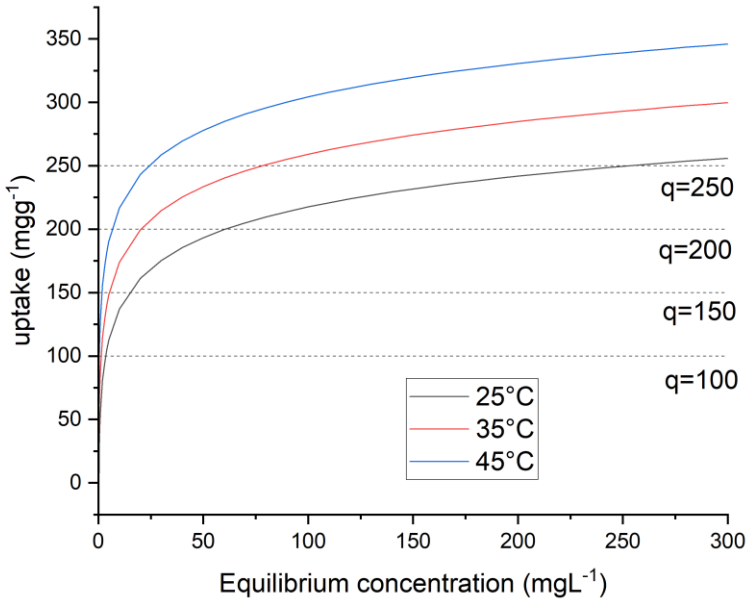

Figure 3.11: Van't Hoff isochore example plot

The natural logarithm of these pressures or concentrations are then plotted against the inverse of the temperature, at which the isotherm was carried out, to produce a straight-line plot. The gradient of this line is related to the enthalpy of adsorption, at the chosen surface coverage for the isochore, as shown in the Equation 3.20 below:

$$\left(\frac{\partial lnP}{\partial\left(\frac{1}{T}\right)}\right)_{\theta} = \frac{\Delta_{ad}H^{\circ}}{R} \tag{3.20}$$

Where,

$\Delta_{ad}H^{\circ}$ = The isosteric enthalpy of adsorption in J mol^{-1}

This isochore process is repeated for multiple constant surface coverages to obtain the trend in enthalpy of adsorption with surface coverage.

3.3.3 Gibbs Free Energy

In order to use the isotherm equilibrium constant in the determination of Gibbs free energy, the isotherm equilibrium constant must be unitless to have any physical meaning. A correction is required, which is different for each isotherm, due to varying units and adsorption mechanisms (119). The standard equilibrium constant is related to the standard Gibbs free energy in Equation 3.21:

$$\Delta G^{\theta} = -RTlnK^{\theta} \tag{3.21}$$

Where:

K^{θ} = Standard equilibrium constant

ΔG^{θ} = Change in standard Gibbs free energy

In general, for adsorption processes:

$$m\,Sites \quad + \quad n\,Adsorptive \quad \leftrightarrow \quad p\,(Site - Adsorbate) \quad + \quad q\,Product$$

Where m, n, p and q are the stoichiometric coefficients of the four terms above, respectively.

The equilibrium constant of this reaction is:

$$K = \frac{{q_e}^p {C_b}^q}{{C_e}^n (q_m - q_e)^m} \tag{3.22}$$

Where:

q_e = Number of adsorption sites occupied at equilibrium

q_m = Total number of sites for adsorption

C_e = Equilibrium adsorptive concentration

C_b = Equilibrium product in solution concentration

K = Equilibrium constant of the adsorption interaction

Generally, this K still has dimensions and cannot be used in Equation 3.21 so must be corrected to the standard equilibrium constant K^{θ}:

$$K^{\theta} = \frac{\left(\frac{q_e}{q^{\theta}}\right)^{p}\left(\frac{C_b}{C^{\theta}}\right)^{q}}{\left(\frac{C_e}{C^{\theta}}\right)^{n}\left(\frac{q_m - q_e}{q^{\theta}}\right)^{m}} \tag{3.23}$$

Or by substituting in Eq. 3.22:

$$K^{\theta} = K\left(C^{\theta}\right)^{n-q}\left(q^{\theta}\right)^{m-p} \tag{3.24}$$

Where:

C^{θ} = Standard state of solution

q^{θ} = Standard state of solid

IUPAC (International Union of Pure and Applied Chemistry) recommends using $C^{\theta} =$ 1 mol L^{-1} and $q^{\theta} = 1$ mol kg^{-1}. This means any thermodynamic properties calculated using the equilibrium constants are relative to the adsorption of 1 mole of adsorbate from a liquid phase of concentration 1 mol L^{-1} on to a solid phase with 1 mol kg^{-1} concentration (119). As knowledge of the exact stoichiometry, and mechanism, of adsorption are not always known, assumptions are made depending on the isotherm model used to determine the K constant used for derivation.

Langmuir:

In the Langmuir model, the Langmuir isotherm constant can be rearranged from Equation 3.8 to give Equation 3.25:

$$K_L = \frac{q_e}{(q_m - q_e)C_e} \tag{3.25}$$

We make it dimensionless by multiplying the denominator by $\frac{q^{\theta}}{q^{\theta}}$ and by $\frac{C^{\theta}}{C^{\theta}}$ and rearranging to give Equation 3.26:

$${K_L}^{\theta} = \frac{\frac{q_e}{q^{\theta}}}{\left(\frac{q_m - q_e}{q^{\theta}}\right)\frac{C_e}{C^{\theta}}} = K_L.C^{\theta} \tag{3.26}$$

More generally, in Langmuirian adsorption, assuming localised adsorption and only monolayer coverage, m, n and p from Equation 3.22 will be equal. This gives an equilibrium constant K as shown the Equation 3.27:

$$K = \left[\frac{q_e}{(q_m - q_e)C_e}\right]^n {C_b}^q \tag{3.27}$$

Substituting in Equation 3.25 gives Equation 3.28

$$K = {K_L}^n {C_b}^q \tag{3.28}$$

And, therefore:

$${K_L}^\theta = {K_L}^n {C_b}^q \left(C^\theta\right)^{n-q} \tag{3.29}$$

The standard Gibbs free energy for the system can be found from the equation 3.30:

$$\Delta G^\theta = -RTln(K_L . C^\theta) \tag{3.30}$$

Temkin:

The Temkin isotherm model is thought to follow the same regime as the Langmuir isotherm model, so:

$${K_T}^\theta = K_T . C^\theta \tag{3.31}$$

As the enthalpy of adsorption decreases with increasing surface coverage, the Gibbs free energy calculated is the maximum free energy of the system:

$${\Delta G_{max}}^\theta = -RTln(K_T . C^\theta) \tag{3.32}$$

Freundlich:

If we assume that the number of adsorption sites is much greater than the number of molecules adsorbed onto the surface, i.e. $q_m \gg q_e$, Equation 3.23 becomes Equation 3.33:

$$K = \frac{{q_e}^p {C_b}^q}{{C_e}^n {q_m}^m} \tag{3.33}$$

The Freundlich isotherm shown in Equation 3.12 can be derived from Equation 3.33, which can be rearranged to:

$$q_e = (K {C_e}^n {q_m}^m {C_b}^{-q})^{\frac{1}{p}} \tag{3.34}$$

By taking the logarithm of both sides, and rearranging, we get:

$$\log q_e = \frac{1}{p}\log(K {q_m}^m {C_b}^{-q}) + \frac{n}{p}\log C_e \tag{3.35}$$

If we assume that $K_F = (K{q_m}^m {C_b}^{-q})^{\frac{1}{p}}$, and the Freundlich heterogeneity parameter, $n_F = \frac{p}{n}$, Equation 3.35 above becomes the linearised form of the Freundlich Equation 3.14. This shows a kinetic derivation of the Freundlich model, which was discovered empirically.

We can rearrange $K_F = (K{q_m}^m {C_b}^{-q})^{\frac{1}{p}}$ to get Equation 3.36:

$$K = {K_F}^P {C_b}^q {q_m}^{-m} \tag{3.36}$$

Therefore:

$${K_F}^\theta = {K_F}^P {C_b}^q {q_m}^{-m} \left(C^\theta\right)^{n-q} \left(q^\theta\right)^{m-p} \tag{3.37}$$

Due to the unknown nature of the exact mechanisms of adsorption in this work, the complex nature of the Freundlich adsorption mechanism did not allow for its use in determination of the Gibbs free energy of the systems.

Once the appropriate equilibrium constant has been determined, the relationship below can be derived from the Gibbs free energy definition in Equation 3.19, and the Gibbs equilibrium relationship in Equation 3.21, to find the relationship below:

$$lnK^\theta = \frac{\Delta S^\theta}{R} - \frac{\Delta H^\theta}{RT} \tag{3.38}$$

Where:

ΔH^θ = Change in standard enthalpy of adsorption

ΔS^θ = Change in standard entropy of adsorption

By determining isotherms at varying temperatures and plotting the natural logarithm of their corrected equilibrium constants vs the inverse of the temperature they were carried out at, a straight line can be obtained.

The gradient and the y-intercept of this line can be found, and changes in entropy and enthalpy determined using Equation 3.39 and Equation 3.40 below:

$$Gradient = \frac{-\Delta H^\theta}{R} \tag{3.39}$$

$$y - intercept = \frac{\Delta S^\theta}{R} \tag{3.40}$$

3.3.4 Scatchard Analysis

Scatchard plot analysis is used to determine the homogeneity or heterogeneity of a surface (123). The Scatchard equation is shown in Equation 3.41 below:

$$\frac{q_e}{C_e} = q_s K_b - q_e K_b \tag{3.41}$$

Where:

q_e = Uptake of the adsorbate on the adsorbent at equilibrium in, mg g^{-1}

C_e = Equilibrium concentration of the adsorptive in mg L^{-1}

q_s = Theoretical maximum uptake on the adsorption site in mg g^{-1}

K_b = Equilibrium constant of adsorption on to the adsorption site in L mg^{-1}

By plotting $\frac{q_e}{C_e}$ vs q_e, a Scatchard plot can be acquired. q_m and K_b can be determined using Equation 3.42 and Equation 3.43 below:

$$slope = -K_b \tag{3.42}$$

$$y - intercept = q_s K_b \tag{3.43}$$

q_s is a measure of the capacity of the adsorption site, while K_b is a measure of the affinity of the adsorbate to the adsorption site.

For a completely homogenous surface, a linear Scatchard plot is expected. This provides evidence that the surface follows a Langmuirian regime. However, if a plot with multiple linear sections is achieved, the surface can be said to be heterogenous, with multiple binding sites available for adsorption. The relative affinity and capacity of these binding sites can be calculated by carrying out linear regression on each linear section. These individual sections can be discerned as high affinity or low affinity sites, based on their relative K_b values. The chemical nature of the binding sites can be discerned via cross-reference with techniques such as XPS and FTIR, as well as using information from SEM-EDS and thermodynamic studies.

3.4 Adsorption Kinetics

3.4.1 Introduction

Kinetic modelling is vital to the determination of the optimal characteristics of synthesised adsorbents. By analysing kinetic data obtained experimentally, it is possible to determine, not only the speed of adsorption but also, the maximum uptake that can be achieved by a sorbent, both of which must be maximised to have an efficient material for separation processes. In this work, kinetic data was fitted to the pseudo first order kinetic model, proposed by Lagergren (124), the pseudo second order kinetic model, proposed by Ho (125), the Elovich model proposed by Zeldowitsch (126), and the intraparticle diffusion model (127).

3.4.2 Pseudo First Order Model

The pseudo first order (PFO) kinetic model assumes that the rate of adsorption is directly proportional to the driving force of adsorption: the difference between the concentration of adsorbate on the surface at equilibrium and amount of adsorbate adsorbed at time t (128).

The PFO model equation can be seen in Equation 3.44:

$$\frac{dq_t}{dt} = k_1(q_e - q_t) \tag{3.44}$$

Where:

q_t = Uptake at time t in mg g^{-1}

q_e = Uptake at equilibrium in mg g^{-1}

k_1 = Pseudo-first order rate constant in s^{-1}

t = Time in s

Integrating Equation 3.44, with boundary conditions $q_t = 0$ at t = 0, and $q_t = q_t$ at t = t, gives:

$$Ln(q_{e-}q_t) = Lnq_e - k_1 t \tag{3.45}$$

Or:

$$q_t = q_e\left(1 - e^{-k_1 t}\right) \tag{3.46}$$

If a plot of q_t vs t is made, then a curve with a steep increase in q_t as t increases, reaching a plateau at an equilibrium value, is expected.

3.4.3 Pseudo Second Order Model

The pseudo second order (PSO) kinetic model assumes that the adsorption rate is dependent on the adsorption capacity of the sorbent, not the concentration of the adsorptive in solution (128).

The PSO model equation can be seen in Equation 3.47:

$$\frac{dq_t}{dt} = k_2(q_e - q_t)^2 \tag{3.47}$$

Where:

q_t = Uptake at time t in mg g^{-1}

q_e = Uptake at equilibrium in mg g^{-1}

k_2 = Pseudo-second order rate constant in g mg^{-1} s^{-1}

Integrating Equation 3.47, with boundary conditions $q_t = 0$ at t = 0, and $q_t = q_t$ at t = t,

$$\frac{t}{q_t} = \frac{1}{{q_e}^2 k_2} + \frac{t}{q_e} \tag{3.47}$$

Or, non-linearly:

$$q_t = \frac{{q_e}^2 k_2 t}{1 + q_e k_2 t} \tag{3.48}$$

A plot of q_t vs t should produce a curve with a steep increase in q_t as t increases, reaching a plateau at an equilibrium value.

3.4.4 Physical Meaning of Pseudo First and Second Order Models

It has been noted, experimentally, that the PFO model fits data sets more accurately where there are very high initial adsorptive concentrations, or when there are fewer active sites available for adsorption. The PSO model fits data sets better at low concentrations, or when there is a relatively high proportion of active sites compared to adsorptive molecules (8). These high and low concentration considerations also align with the observation that many systems seem to fit the PFO model better at low adsorption times, when the adsorptive

concentration is high, and fit the PSO model better at longer adsorption times, when the adsorptive concentration is lower.

In some cases, due to the low number of active sites or high adsorptive concentration, it is suggested that systems where the PFO model fits the data well are controlled by internal or external diffusion of adsorptive molecules to and from the active sites present. Due to the high number of sites present, or low concentration of adsorptive molecules, it is suggested that the rate limiting step in systems where the PSO model fits the data well, is the adsorption of adsorptive molecules on to the active sites (129).

It has also been suggested that the PFO model indicates that the adsorbate-adsorbent interactions are of a physisorptive nature, meaning that only intermolecular forces are involved; while the PSO model is related to chemisorption, where formal chemical bonds are formed between the adsorbent and the adsorptive species (130). However, these are now points of contention and further investigation must be carried out to confirm the mechanism of adsorption through thermodynamic studies (131).

3.4.5 Elovich Model

The Elovich equation was outlined by Zeldowitsch (126) in 1934 to describe the kinetic behaviour of carbon monoxide onto a manganese dioxide adsorbent. This was later found to fit well the kinetic data for the chemisorption of gases onto solids, and also for adsorption of liquid pollutants in aqueous systems (129). It is thought that the Elovich model broadly describes chemisorption systems, and that the chemisorption process is the rate limiting step (129). It assumes that the rate of an adsorption process decreases exponentially as surface coverage increases. The Elovich model is shown below:

$$\frac{dq_t}{dt} = a_E e^{-b_E q_t} \tag{3.49}$$

Integrating, between $q_t = 0$ at $t = 0$ and $q_t = q_t$ at $t = t$, gives:

$$q_t = \frac{\ln(b_E a_E)}{b_E} + \frac{\ln(t)}{b_E} \tag{3.50}$$

Where:

$a_E =$ Elovich desorption constant

$b_E =$ Elovich initial adsorption rate

3.4.6 Intra-Particle Diffusion Model

The intra-particle diffusion model can be seen in Equation 3.51:

$$q_t = k_{int}\sqrt{t} + C_{int} \tag{3.51}$$

Where:

k_{int} = Intraparticle diffusion rate constant, in mg g^{-1} $s^{-0.5}$

C_{int} = Boundary layer thickness constant, in mg g^{-1}

If the plot of q_t vs $\sqrt{t}$ gives a straight line passing through the origin, the intraparticle diffusion of the adsorbate is the sole rate limiting step. However, for many systems multiple linear sections can be identified, each indicating different diffusion systems corresponding to diffusion through films to the outer surface of the adsorbent, diffusion through the pores of the adsorbent, and/or adsorption/desorption processes at the surface. Each of these linear sections can be fitted to lines obtained in the aforementioned plot, and the rate constants and boundary thickness constants found to determine the number of, and relative speeds of, the respective diffusion processes (132).

3 different types of plots following the intraparticle diffusion model have been identified by Wu et al (133):

1. q_t vs $t^{0.5}$ shows one linear section which is a straight line passing through the origin. This indicates rapid initial adsorption where the diffusion is controlled by the diffusion across the boundary layer to the outer surface of the adsorbent.
2. q_t vs $t^{0.5}$ shows multiple (2 or 3) linear regions. The first is that described in regime 1 above, an initial steep linear section passing through the origin indicating the adsorption onto the outer surface of the adsorbent particle. The second is a less steep linear section with a smaller k value, indicating a slower rate of adsorption which has intraparticle diffusion as the rate limiting step. The third is s linear section where the line gradient decreases again, indicating a final equilibrium step where adsorption rate slows even further.
3. q_t vs $t^{0.5}$ shows a single linear section but does not pass through the origin, and has a positive intercept on the uptake axis. This linear section represents section 2 from regime 2 above, indicating the rate limiting step for the adsorption is the intra-particle diffusion. This also indicates that the initial rapid adsorption step indicative

of diffusion onto the surface of the adsorbent particles happens within a short period of time prior to the data points collected.

3.5 Porous Materials & Quantification of Porosity

3.5.1 Introduction

As outlined before, adsorption is a surface phenomenon occurring at the interface between two phases. The adsorption capacity of a material is directly proportional to its surface area; hence, a high surface area is an advantageous trait for a material used in adsorption applications.

Porous adsorbents are a family of materials that exhibit relatively high surface areas and adsorption capabilities, while retaining minimal density and volume of the material. This allows for adsorption systems to be reduced in weight and volume, while increasing their adsorption capacities and number of surface sites upon which adsorption can take place.

Porous materials can have a wide variety of sizes of internal pores, as set out in the IUPAC classification (134), which are summarised in Table 3.17 below.

Table 3.17: Pore size classification (134)

Classification	Size (nm)
Macropores	>50
Mesopores	2 - 50
Micropores	<2

Micropores are subdivided into three further classifications as shown in Table 3.18 below.

Table 3.18: Micropore size classification (134)

Classification	Size (nm)
Supermicropores	1.4 - 2
Micropores	0.7 - 1.4
Ultramicropores	<0.7

Knowledge of the pore size distribution of an adsorbent material is imperative to its application in an adsorption system, due to pore sieving effects that may be observed for adsorption of larger molecules, and to allow for correct transport of target adsorptive species to adsorption sites.

Pores in a material can be described as open, closed, transport or blind, and by the shape of their opening. A closed pore is a pore inaccessible to an external fluid, while an open pore has access to the external surface of the porous solid. A blind pore is one that finishes in a dead end and does not open onto another part of the external surface of the porous solid. A transport pore is one that opens at two or more different places on the external surface of the solid. Pore shapes can be described as cylindrical, ink-bottle-shaped, funnel-shaped or slit-shaped. Surface roughness can be described as porosity, if the roughness is deeper than it is wide. Figure 3.12 and Table 3.19 give examples of the different classifications of pore types, as outlined by Rouquerol and Avnir in 1994 (135).

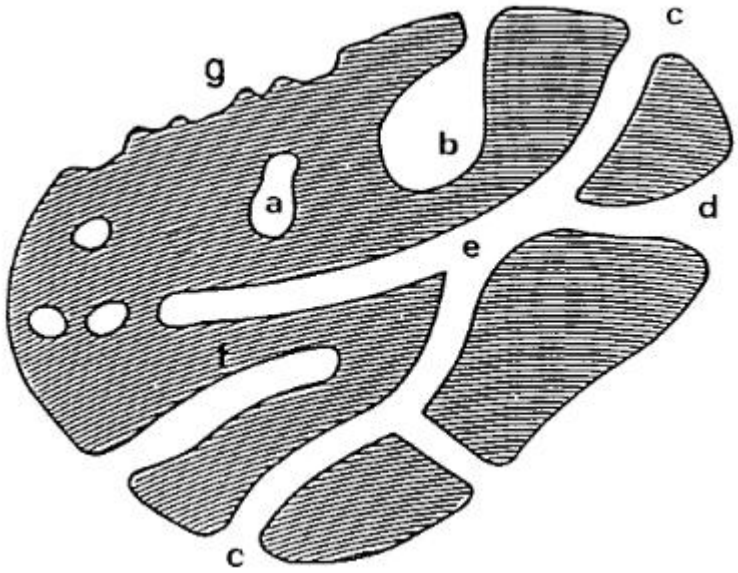

Figure 3.12: Schematic cross-section of a porous solid (135)

Table 3.19: Characteristics of pores in Figure 3.12

Pore	**Description**
a	Closed pore
b	Open, blind inkbottle shaped pore
c	Open cylindrical pore
d	Open funnel shaped pore
e	Open, cylindrical transport pore
f	Open, blind, cylindrical shaped pore
g	Surface roughness

3.5.2 Surface Area Analysis

Gas adsorption and desorption isotherms can be used in a variety of methods to determine the textural properties of a porous material. One such method is the application of Brunauer Emmett and Teller (BET) adsorption theory to determine the surface area of a porous material.

In this study nitrogen was utilised as the adsorptive probe molecule at its normal boiling point of 77.4 K utilising liquid nitrogen as the cryogen.

In applying the BET equation, as discussed in Section 3.2.3, a plot of $\frac{P}{n(P^0-P)}$ vs $\frac{P}{P^0}$ is produced. Using linear regression, n_m and c can be determined using Equation 3.52 and Equation 3.53.

$$c = \frac{slope}{intercept} + 1 \tag{3.52}$$

$$n_m = \frac{1}{(slope + intercept)} \tag{3.53}$$

Using n_m the BET surface area of an adsorbent can be found using Equation 3.54:

$$S = n_m \cdot N_A \cdot A_m \tag{3.54}$$

Where:

S = Surface area of the adsorbent in $m^2\ g^{-1}$

n_m= Adsorbate monolayer coverage in $mol\ g^{-1}$

N_A = Avogadro's constant, 6.02×10^{23} molecules mol^{-1}

A_m = Cross-sectional area of one adsorbate molecule in m^2 $molecule^{-1}$

In the case of nitrogen gas A_m = 1.62 $x10^{-19}$ m^2 $molecule^{-1}$ (136).

3.5.3 Enthalpy of Adsorption

Assuming that the second and subsequent layers of adsorption have a heat of adsorption equal to the heat of liquefaction, then the dimensionless BET constant can be used to determine the enthalpy of adsorption of the monolayer onto the surface of the adsorbent. It is found using Equation 3.55:

$$c = e^{\left[\frac{|\Delta H_A| - |\Delta H_L|}{RT}\right]} \tag{3.55}$$

Where:

$c =$ Dimensionless BET constant

$|\Delta H_A| =$ Modulus of the enthalpy of adsorption of the adsorbent in J mol^{-1}

$|\Delta H_L| =$ Modulus of the heat of liquefaction of the adsorbate in J mol^{-1}

$R =$ Universal gas constant, 8.3145 J mol^{-1} K^{-1}

$T =$ Temperature of adsorption vessel in K

3.6.4 Microporous Correction for Brunauer-Emmett-Teller Analysis

Traditionally, in the linear regression step of BET surface area analysis, a relative pressure range $\left(\frac{P}{P^0}\right)$ of 0.05-0.3 is used for analysis. However, in the case of microporous adsorbents, this often gives rise to regressions with low R^2 values due to a lack of fit in this range, indicating that the BET equation, in its traditional form, is unsuitable to interpret the surface areas of such materials. Another commonly found error is that regressions in this range give negative BET dimensionless constants, which are impossible and have no meaning physically. It is, therefore, necessary to carry out a Rouquerol correction on adsorption data where the adsorbent is suspected of containing micropores within is network (134). The Rouquerol function is shown in Equation 3.56:

$$f(x) = n\left[1 - \frac{P}{P^0}\right] \tag{3.56}$$

Points applicable for use in calculating the surface area of an adsorbent are those in which the rate of change of the Rouquerol function is continually increasing. A plot of $n\left[1 - \frac{P}{P^0}\right]$ vs $\frac{P}{P^0}$ is obtained and only the points where the gradient is positive are used in the linear regression. An example Rouquerol plot with the upper cut-off limit is shown in Figure 3.13 below.

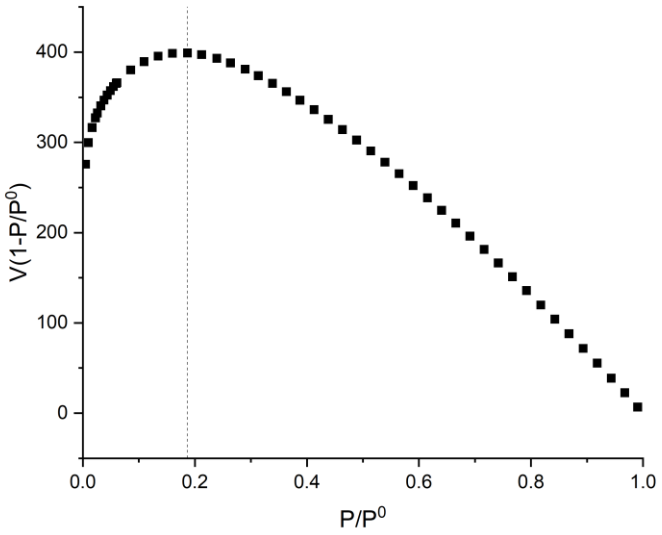

Figure 3.13: Example Rouquerol plot

3.5.5 Mesopore Size Distribution

The built in ASAP2020 software calculates pore sizes from Barrett-Joyner-Halenda (BJH) analysis (137). This analysis is only applicable for pores in the mesopore and small macropore range, i.e. 2-50 nm. The system does this by using a modified form of the Kelvin equation to calculate film thicknesses inside the pores. This is, in turn, used to calculate an average pore size. The incremental decrease in volume adsorbed is then calculated for each decrease in relative pressure. These incremental decreases are used to calculate a cumulative pore volume for each relative pressure. This cumulative volume is then differentiated with respect to pore width and the data plotted. Any peaks in this differential cumulative volume indicate a rapid emptying of pores at the relevant relative pressure and, therefore, indicate an associated average pore width and the existence of pores of that width within the material being analysed. In this work, a Faas correction (138) was applied, and the thickness equation used was that for carbon black.

3.5.6 Micropore Analysis

To further analyse the microporous structures within the material, the Dubinin-Radushkevich (DR) model was applied (139). The DR equation is shown in Equation 3.57:

$$\log(n) = log \cdot n_0 - D_{DR} \cdot log^2\left(\frac{P^0}{P}\right) \qquad (3.57)$$

Where:

n = Number of moles of adsorbate at a given pressure in mol g^{-1}

n_0 = Total moles of adsorbate adsorbed onto the surface of micropores in mol g^{-1}

D_{DR} = DR constant in log(mol g^{-1})

P^0 = Saturation vapour pressure of the adsorptive gas

P = Equilibrium pressure of the adsorptive

D_{DR} is related to the strength of interactions between the adsorbent and adsorbate and can, therefore, be used to determine the pore size distribution of the adsorbent.

In applying the DR equation, a plot of $\log(n)$ vs $log^2\left(\frac{P^0}{P}\right)$ is produced. Linear regression can be carried out and n_0, and D_{DR}, calculated through Equation 3.58 and Equation 3.59.

$$n_0 = 10^{Intercept} \tag{3.58}$$

$$D_{DR} = -Gradient \tag{3.59}$$

The micropore area can then be calculated using Equation 3.54.

A perfectly linear DR relationship implies that the micropore size distribution is a Gaussian distribution centred around 1 nm. Low pressures (high $\frac{p^0}{p}$) are where adsorption occurs in small micropores (ultramicropores), and high pressure (low $\frac{p^0}{p}$) is where adsorption occurs in large micropores (supermicropores). Deviations from this ideality can occur, values for $\log(n)$ lower than the expected straight line imply reduced adsorption in the pores in that pressure region. Conversely, deviations higher than the expected ideal line imply increased adsorption in the pores at that pressure (140).

The percentage of pore volume attributed to micropores can be found using Equation 3.60:

$$Micropore\ volume\ \% = \frac{n_0}{MQA} * 100 \tag{3.60}$$

Where:

$Micropore\ volume\ \%$ = Percentage of pore volume attributed to micropores

n_0 = Total moles of adsorbate adsorbed onto the surface of micropores in mol g^{-1}

MQA = Maximum quantity adsorbed of adsorptive at $\frac{P}{P^0}$ close to 1 in mol g^{-1}

3.5.7 Isotherm and Hysteresis Classification

The shape of the adsorption isotherm allows elucidation of key information relating to the textural properties of the tested material (134). Physisorption isotherms may show characteristics of one or more of the eight isotherm classifications shown in Figure 3.14.

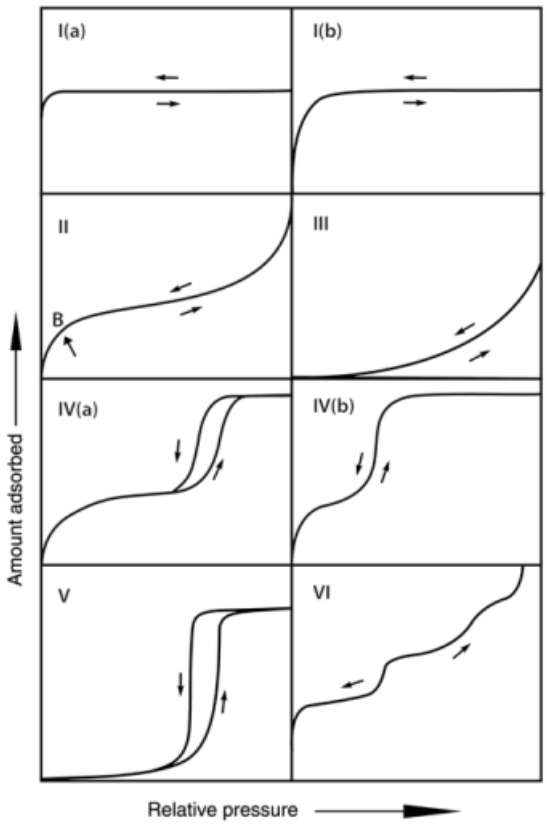

Figure 3.14: Physisorption isotherm classifications (134)

A summary of how these isotherm classifications inform the sorbents characteristics is shown in Table 3.20:

By studying the shape of the hysteresis loop of the isotherm, information can be gained as to the nature of the porous structures present within the material. The six main types of hysteresis loops found are shown in Figure 3.15.

Table 3.20: Isotherm classifications and sorbent characteristics (134)

Isotherm type	Sorbent characteristics
I(a)	Microporous with narrow micropores <~1 nm
I(b)	Microporous over a broader range, possibly small mesopore <~2.5 nm
II	Nonporous/macroporous sorbent
III	Weak adsorbent/adsorbate interactions
IV(a)	Capillary condensation in mesopores above a critical width
IV(b)	Mesopores with no capillary condensation, mesopores below a critical width
V	Weak adsorbent/adsorbate interactions but increased uptake during multilayer formation due to strong adsorbate/adsorbate interactions
VI	Layer by layer adsorption on highly uniform nonporous surface

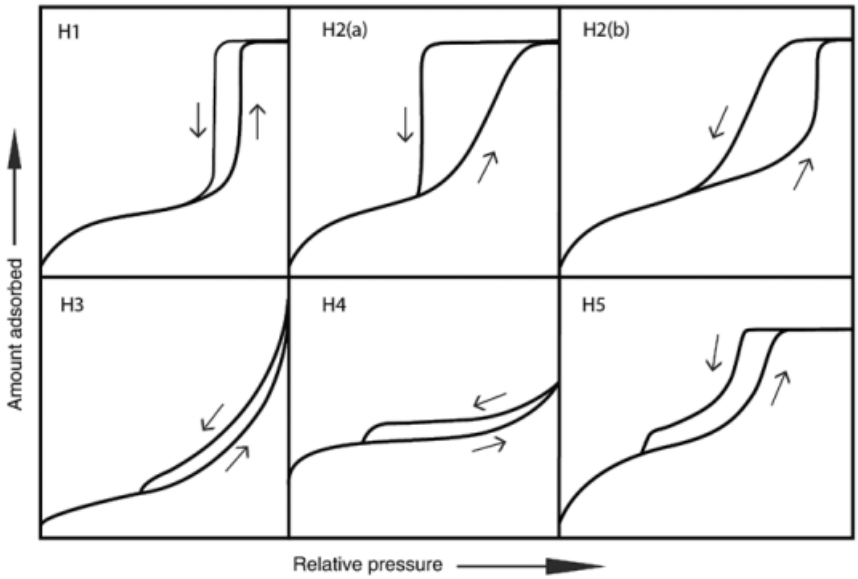

Figure 3.15: Hysteresis loop classification (134)

A summary of the behaviours leading to these hysteresis loops can be seen in Table 3.21.

Table 3.21: Summary of hysteresis type and pore characteristics (134)

Hysteresis type	Pore characteristics
H1	Ink-bottle pores
H2(a)	Pore-blocking in narrow range of mesopores or cavitation induced evaporation
H2(b)	Pore blocking across a large range of mesopores
H3	Non-rigid aggregates of plate-like particles or milling of macropores
H4	Filling of micropores
H5	Partially blocked mesopores

3.6 References

1. Pourhakkak P, Taghizadeh A, Taghizadeh M, Ghaedi M, Haghdoust S. Fundamentals of adsorption technology. Interface science and technology. 33: Elsevier; 2021. p. 1-70.
2. Wiśniewski M, Moszczyńska J, Liu X. Room-Temperature Oxygen Dissociative Chemisorption on Carbon Surface–Experimental Evidence. Langmuir. 2023;40(1):193-200.
3. Haghseresht F, Nouri S, Lu GM. Effects of carbon surface chemistry and solution pH on the adsorption of binary aromatic solutes. Carbon. 2003;41(5):881-92.
4. Lee G, Ahmed I, Lee HJ, Jhung SH. Adsorptive removal of organic pollutants with a specific functional group from water by using metal–organic frameworks (MOFs) or MOF-derived carbons: A review. Separation and Purification Technology. 2024:127602.
5. Paso KG. Constructing thermodynamic models of toxic metal biosorption. Microbial biodegradation and bioremediation: Elsevier; 2022. p. 109-43.
6. Zhao X, Xiao B, Fletcher A, Thomas K. Hydrogen adsorption on functionalized nanoporous activated carbons. The Journal of Physical Chemistry B. 2005;109(18):8880-8.
7. Langmuir I. The constitution and fundamental properties of solids and liquids. Part I. Solids. Journal of the American chemical society. 1916;38(11):2221-95.
8. Brunauer S, Emmett PH, Teller E. Adsorption of gases in multimolecular layers. Journal of the American chemical society. 1938;60(2):309-19.
9. Freundlich H. Kapillarchemie: eine Darstellung der Chemie der Kolloide und verwandter Gebiete: akademische Verlagsgesellschaft; 1922.
10. Temkin M. Kinetics of ammonia synthesis on promoted iron catalysts. Acta physiochim URSS. 1940;12:327-56.
11. Daniels R. Adsorption—Theory, Modelling, and Analysis, József Tóth (Ed.), Marcel Dekker, New York (2002), p. 878, pp $188.50; ISBN 0-8247-0747-8. Elsevier; 2005.
12. Chen T, Da T, Ma Y. Reasonable calculation of the thermodynamic parameters from adsorption equilibrium constant. Journal of Molecular Liquids. 2021;322:114980.
13. Madaeni S, Salehi E. Adsorption of cations on nanofiltration membrane: Separation mechanism, isotherm confirmation and thermodynamic analysis. Chemical Engineering Journal. 2009;150(1):114-21.
14. Thakur A, Assad H, Kaya S, Kumar A. Plant extracts as environmentally sustainable corrosion inhibitors II. Eco-Friendly Corrosion Inhibitors: Elsevier; 2022. p. 283-310.
15. Rowley H, Innes W, editors. Application of the Van't Hoff Equation to Adsorption Equilibria. Proceedings of the Iowa Academy of Science; 1940.
16. Ayar A, Gezici O, Küçükosmanoğlu M. Adsorptive removal of Methylene blue and Methyl orange from aqueous media by carboxylated diaminoethane sporopollenin: On the usability of an aminocarboxilic acid functionality-bearing solid-stationary phase in column techniques. Journal of hazardous materials. 2007;146(1-2):186-93.

17. Lagergren S. Zur theorie der sogenannten adsorption geloster stoffe. 1898.
18. Revellame ED, Fortela DL, Sharp W, Hernandez R, Zappi ME. Adsorption kinetic modeling using pseudo-first order and pseudo-second order rate laws: A review. Cleaner Engineering and Technology. 2020;1:100032.
19. Low M. Kinetics of chemisorption of gases on solids. Chemical Reviews. 1960;60(3):267-312.
20. Alkan M, Demirbaş Ö, Doğan M. Adsorption kinetics and thermodynamics of an anionic dye onto sepiolite. Microporous and mesoporous materials. 2007;101(3):388-96.
21. Sahoo TR, Prelot B. Chapter 7 - Adsorption processes for the removal of contaminants from wastewater: the perspective role of nanomaterials and nanotechnology. In: Bonelli B, Freyria FS, Rossetti I, Sethi R, editors. Nanomaterials for the Detection and Removal of Wastewater Pollutants: Elsevier; 2020. p. 161-222.
22. Wang J, Guo X. Adsorption kinetic models: Physical meanings, applications, and solving methods. Journal of Hazardous Materials. 2020;390:122156.
23. Sha'arani SAW, Khudri MAMRS, Othman AR, Halmi MIE, Yasid NA, Shukor MYA. Kinetic Analysis of the Adsorption of the Brominated Flame Retardant 4-bromodiphenyl Ether onto Biochar-immobilized Sphingomonas sp. Bioremediation Science and Technology Research. 2019.
24. Vareda JP. On validity, physical meaning, mechanism insights and regression of adsorption kinetic models. Journal of Molecular Liquids. 2023;376:121416.
25. Qiu H, Lv L, Pan B-c, Zhang Q-j, Zhang W-m, Zhang Q-x. Critical review in adsorption kinetic models. Journal of Zhejiang University-Science A. 2009;10(5):716-24.
26. Wu F-C, Tseng R-L, Juang R-S. Initial behavior of intraparticle diffusion model used in the description of adsorption kinetics. Chemical engineering journal. 2009;153(1-3):1-8.
27. Thommes M, Kaneko K, Neimark A, Olivier J, Rodriguez-Reinoso F, Rouquerol J, et al. Physisorption of gases, with special reference to the evaluation of surface area and pore size distribution (IUPAC Technical Report). Pure and Applied Chemistry. 2015;87.
28. Rouquerol J, Avnir D, Fairbridge CW, Everett DH, Haynes J, Pernicone N, et al. Recommendations for the characterization of porous solids (Technical Report). Pure and applied chemistry. 1994;66(8):1739-58.
29. Mikhail RS, Brunauer S. Surface area measurements by nitrogen and argon adsorption. Journal of Colloid and Interface Science. 1975;52(3):572-7.
30. Barrett EP, Joyner LG, Halenda PP. The determination of pore volume and area distributions in porous substances. I. Computations from nitrogen isotherms. Journal of the American Chemical society. 1951;73(1):373-80.
31. Micromeritics. ASAP 2020 Accelerated Surface Area and Porosimetry System Operator's Manual2011.
32. Dubinin M, Radushkevich L. Equation of the characteristic curve of acti vated charcoal: Proe. A cad Sei USSR, Phys Chem Sec. 1974:55,331-3.
33. Marsh H. Adsorption methods to study microporosity in coals and carbons—a critique. Carbon. 1987;25(1):49-58.

4 Experimental Techniques

4.1 Materials

The brewer's spent grain (BSG) samples were acquired from Tennent Caledonian Breweries UK's Wellpark brewery site. The parent sample that was used for all syntheses was recovered from a mash completed that day to avoid contamination, ensure no post processing of the grains had taken place and reduce potential degradation of the biological material. Other chemicals used within this study were:

- Carbon dioxide, nitrogen and oxygen gases acquired from BOC UK.
- Sodium nitrate, used in the point of zero charge and adsorption experiments, extra pure grade acquired from Thermo Scientific UK.
- Nitric acid stock solution purchased from Thermo Scientific UK at ACS reagent grade.
- Sodium hydroxide, analytical reagent grade, purchased from Fisher Scientific UK.
- pH 4.01 (910104) and pH 10.01 (910110) Orion Application buffer solutions purchased from Thermo Scientific UK.
- Methyl orange dye powder, 85% dye content, purchased from Sigma-Aldrich UK. The balance consists of sodium chloride, residual water and stabilising agents.
- Hydrochloric acid, ACS reagent- 37% solution in water, purchased from Thermo Scientific UK.

4.2 Biochar synthesis

4.2.1 Drying of Brewer's Spent Grain

4.2.1.1 Introduction

As received, the brewer's spent grain contains a large amount of water, retained from the mashing process. This must be removed to homogenise the feedstock prior to pyrolysis, to increase the ambient shelf life of the spent grains by reducing removing optimal conditions for mould growth, and to determine the water content of the feedstock. Prior to drying, the as received brewer's spent grain is stored at -18 °C in a LEC laboratory freezer. The brewer's spent grain is dried in accordance with an abridged method from the American Society for Testing Materials (ASTM) E871-82 Standard Test Method for Moisture Analysis of Particulate Wood Fuels (141).

4.2.1.2 Method

Approximately 30 g of the wet brewer's spent grain was placed on a glass dish and placed into a Memmert UFE400 vacuum oven set at 103 °C. The sample was allowed to dry for 6 h before being removed and placed into a desiccator and allowed to cool to room temperature. Once cooled, the samples were removed from the desiccator, weighed, and returned to the vacuum oven. After 2 h, the samples were removed, cooled in the desiccator, and weighed again. This process was repeated until the weight difference in two consecutive measurements varied by no more than 0.2%. This was repeated in triplicate to determine the water content of the brewer's spent grain as received.

4.2.2 Pyrolysis of Brewer's Spent Grain

4.2.2.1 Introduction

The pyrolysis of the brewer's spent grain was carried out using a Lenton Thermal Designs LTF 12/38/500 tube furnace. An alumina crucible was used to hold the spent grains, while an alumina tube with 25 mm bore housed the pyrolysis chamber. Nitrogen and carbon dioxide gas with their respective rotameters were connected via tubing to a bung at one side of the alumina tube. The other side of the bung was connected to a bubbler to maintain an inert atmosphere in the event of gas failure, but also to rapidly cool the exhaust gases and remove any volatile material from the gas stream on its way to the ventilation system. The entire apparatus was housed within a fume cupboard. The apparatus set-up is shown in Figure 4.16.

Figure 4.16: Tube furnace and bubbler set-up

The operation of the tube furnace consists of three distinct phases: ramping, holding, and cooling. In the ramping phase, the temperature is elevated at a constant rate to a predetermined setpoint temperature under a constant flow of nitrogen. During the holding

phase, the setpoint temperature is maintained for a predetermined time under a constant flow of carbon dioxide gas. Finally, during the cooling phase, the furnace apparatus is allowed to cool under a flow of nitrogen gas until 450 °C, the gas flow stopped, and the bubbler stem removed. The apparatus was then allowed to cool to ambient temperatures overnight. The five process variables: hold temperature, hold time, ramp rate, nitrogen gas flowrate and carbon dioxide gas flowrate are all determined by the experimental design matrix in use.

Due to local lab policy, cylinders could not be left open overnight, an operator must be present or appropriate interlocking control measures in place. This is due to the risks associated with an uncontrolled release of an asphyxiant gas. It was observed that if the gas flow was stopped and the bubbler stem left submerged, due to gas contraction in the tube, water would be drawn up into the tube and spoil the samples. This meant that samples needed to be cool enough by the end of the lab operating hours to allow gases to be turned off, hence, the autoignition temperature of carbon black (450°C) was taken as the safe temperature at which the samples could be exposed to an oxygenated environment without safety concerns, which allowed for an increased range of values to be used for the ramp rate and hold time, increasing the usefulness of the design of experiments.

4.2.2.2 Method

Approximately 1.6 g of dried brewer's spent grain was weighed out and inserted into the alumina crucible. The crucible was then inserted into the centre of the alumina tube. The bungs were attached, and the nitrogen gas flow was allowed to purge the system for 20 min. After this, the furnace was turned on and the ramping phase commenced. Once the setpoint temperature had been reached, the gas flow was switched from nitrogen to carbon dioxide. Once the isothermal hold phase had completed, the heating element in the furnace was turned off and the gas flow manually switched back to nitrogen. Once the temperature had cooled to 450 °C, the gas flow was halted, and the bubbler stem removed. The following morning, once the full furnace apparatus had been allowed to cool to ambient temperature, the crucible was removed and weighed to determine the biochar yield.

4.2.3 Post Synthesis Acid Activation

4.2.3.1 Introduction

Some biochar samples were washed post-pyrolysis with hydrochloric acid to increase their efficacy in liquid phase adsorption studies. Washing biochar removes ash from the pore matrix, which may block pores and reduce the adsorption capacity. Ash content of less than 10% is mandated for activated carbons and biochars by the Indonesian national standards authority (SNI No. 06-3730-1995) (142). In some cases, washing may also modify the surface chemistry of the material, depending on the washing solvent used. This may or may not be desirable depending on the application for the biochar.

In this work, the biochar was washed with dilute hydrochloric acid; this was not only to increase the ash removal rate but also to protonate the surface of the biochar. This would potentially decrease the point of zero charge and make the surface more favourable for the adsorption of anionic pollutants.

4.2.3.2 Method

After pyrolysis, the biochar was weighed and added to a conical flask containing 100 mL of 0.1 M hydrochloric acid and agitated for 1 h at room temperature. The sample was then strained through a sieve and the residue added to a beaker containing 500 mL of boiling deionised water, on a VWR VMS-C4 hotplate. This was mixed manually, and via convection currents, for 10 min. Meanwhile, the filtrate was passed through a Büchner funnel with qualitative-grade QL100 filter paper to preserve any particulate which may had passed through the sieve. The boiling water and biochar mixture was then passed through a sieve and the residue added to 500 mL of room temperature deionised water, and the filtrate again passed through a Büchner funnel with qualitative grade QL100 filter paper. The last step was repeated a further four times to ensure any excess acid had been washed from the biochar. The residue and Büchner funnel contents were collected and dried at 103 °C in a Memmert UFE400 vacuum oven for 24 h. The dried char is then collected and weighed to determine the washing yield.

4.3 Sample Composition and Morphology

4.3.1 Thermogravimetric Analysis

4.3.1.1 Introduction

Thermogravimetric analysis (TGA) can be used to determine the content of a carbonaceous material, which falls in to four categories: moisture, volatiles, fixed carbon, and ash. This proximate analysis data can be used to determine the macromolecular makeup of the biochars and elucidate the changes the synthesis processes make to the biomass precursor material.

4.3.1.2 Method

The samples were analysed using a NETZSCH STA 449 F4 Jupiter simultaneous thermogravimetric analyser, shown in Figure 4.17.

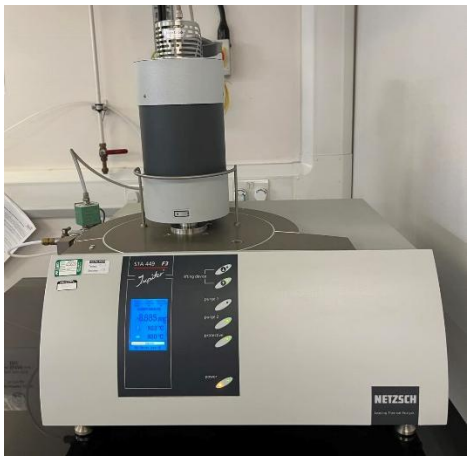

Figure 4.17: NETZSCH STA 449 F4 Jupiter STA apparatus

The procedure was carried out using a gas flow of 50 mL min^{-1} in the chamber with a 60 mL min^{-1} protective flow of Nitrogen gas in the anulus. Alumina crucibles were used due to the high temperatures of the analysis with the reference crucible remaining empty for all runs. The analysis consisted of three phases: ramping under an inert nitrogen atmosphere to 900 °C at a rate of 7.5 °C min^{-1}, a 10 min isothermal step under nitrogen at 900 °C and a 10 min isothermal step in an atmosphere of 20% oxygen and 80% nitrogen. The instrument was then cooled to 800°C before the gas flows were halted and the instrument allowed to cool to ambient temperature.

The moisture content can be found by determining the mass at the plateau occurring around 100 °C. The volatile matter is the mass lost during the ramping and higher

isothermal step under inert atmosphere, minus the moisture content. The fixed carbon is the mass lost during the isothermal step where oxygen is introduced. The ash content of a sample is the residual mass remaining after the step within which oxygen is introduced to the system. An example TGA mass loss curve can be seen in Figure 4.18.

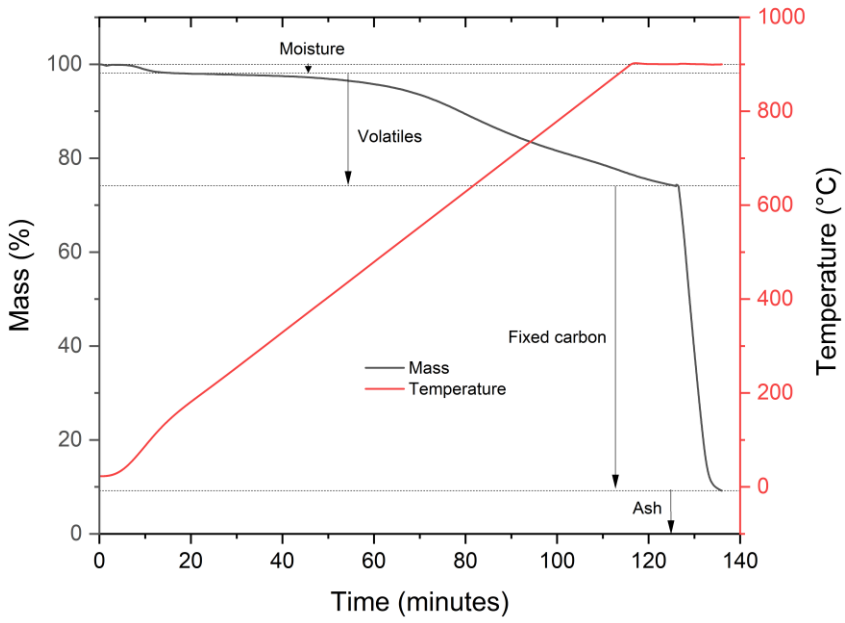

Figure 4.18: Example TGA mass loss curve

By plotting the first derivative of percentage mass with respect to time vs time, the minimum turning points can be found, and the times at which the rate of change of mass with respect to time is at its maximum can be determined. These minimum turning points are associated with the points of inflection of the mass loss curve, the temperatures of the points of inflection can be found using the temperature vs time graph. By finding these burn-off temperatures and checking the pyrolysis temperatures of certain compounds expected within the material we can determine the macromolecular make-up of the sample. An example derivative mass loss curve can be seen in Figure 4.19.

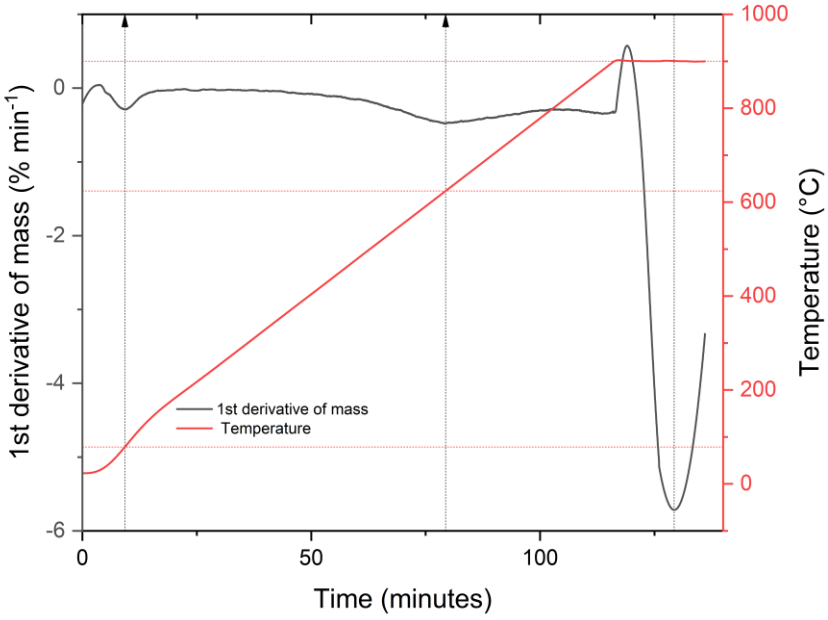

Figure 4.19: Example 1st derivative of mass loss curve

4.3.2 Carbon, Hydrogen and Nitrogen Elemental Analysis

4.3.2.1 Introduction

Carbon, hydrogen and nitrogen (CHN) elemental analysis is a method used to determine the percentage of hydrogen, nitrogen, carbon, and residue in a material through combustion. It can be used alongside other techniques to determine the chemical makeup of a material. A high carbon content is imperative to biochar function, but knowledge of hydrogen and nitrogen proportions can tell us about surface chemistry and functionalisation of the material. Low hydrogen content could imply the existence of graphene rings or high oxygen functionality. If nitrogen is present, it can imply amine groups or the existence of proteins in the feedstock. High residue percentages can imply presence of metals and heavier non-metals in the precursor material. Cross validation with other techniques is essential to determine the material composition.

CHN analysis determines the carbon, nitrogen, and hydrogen content of a material by fully oxidising the material, removing unwanted analytes, separating the resultant water, carbon dioxide and nitrogen gas mixture, and measuring the gas mixture masses. The residual mass of all non-carbon, hydrogen and nitrogen elements is then determined by difference.

4.3.2.2 Method

The experimental procedure for this was carried out by the technical staff in the department of Civil and Environmental Engineering at the University of Strathclyde on a ThermoScientific FlashSmart Elemental analyser shown in Figure 4.20 on the CHN analysis setting. In this setting, Helium was chosen as the carrier gas and approximately 0.5-3.5 mg of sample was used per run. Each sample was run in duplicate.

Figure 4.20: ThermoScientific FlashSmart Elemental Analyser apparatus

Material samples were weighed and encased in tin metal pans which were crimped to ensure no sample loss. The chamber was evacuated and purged with the carrier gas. The samples were dropped into oxidation chamber at 950 °C by an auto sampler controlled by the apparatus. When the crucible reaches the hottest part of the reactor, a pulse of pure oxygen was injected into the chamber. Oxidation of tin is highly exothermic so the temperature spikes rapidly to approximately 1800 °C, completely combusting the material. The resulting gaseous mixture of water, carbon dioxide, nitrous oxides, sulphurous oxides, nitrogen, unreacted oxygen, and halogenated compounds then entered the reduction chamber containing a coil of copper wire where the nitrous oxides are reduced to dinitrogen gas and sulphurous oxides are reduced to sulphur dioxide. Elemental oxygen is completely retained within the reduction chamber. The gas mixture is passed through a bed of cobaltic oxide catalyst to remove any sulphur dioxide and halogenated compounds. The gas mixture of carbon dioxide, water and nitrogen then enters a gas chromatography column where the gases are separated prior to analysis in the thermal conductivity detector which reports the percentages of carbon, hydrogen, and nitrogen on an atomic basis. The software then converts this into a mass % basis.

4.3.3 Scanning Electron Microscopy and Energy Dispersive Spectroscopy

4.3.3.1 Introduction

Scanning electron microscopy (SEM) is a technique employing the use of an electron beam, focused, and scanned across a sample to render an image of the sample surface to massive magnifications, simply not possible with a conventional optical microscope.

The sample chamber is evacuated to an ultra-high vacuum. The electron beam is generated at the thermionic cathode and accelerated down towards the sample through the hole in the positively charged anode. An electromagnetic lens focuses the beam to a point while another electromagnetic deflection field generating component is used to move the beam. The sample chamber contains two detectors, a secondary electron detector (SED) covered with a positively charged grating to attract the secondary electrons, and an energy dispersive X-ray detector (EDX).

In image generation, the deflection field is used to point the beam to the top left part of the image collection area, it targets the beam to this area for a short time, bombarding the area with primary electrons from the beam. These primary electrons collide with the electrons in the sample, knocking some of them out producing secondary electrons which are then attracted to the SED. The SED counts the number of electrons being detected and registers this as a dot with varying brightness, depending on the number of electrons counted. The deflection field then pans to the right and repeats this process until slowly building up an image shown on the display. Areas where lots of secondary electrons are detected show us brighter spots and where fewer secondary electrons are generated show up as darker spots.

While in operation for the energy dispersive X-ray spectroscopy (EDS) mode, the detector is changed to the EDX detector. X-rays are produced as electrons from higher energy levels drop down to fill the holes left by the secondary electrons being ejected from the atoms. These X-rays are characteristic of energy level transitions in specific elements, so not only the intensity of each X-ray but the energies are monitored as well. In a similar operating procedure to the image generation, using the X-ray detector an intensity vs energy spectrum for each pixel can be obtained. This can be translated by the software into relative intensities of each element using curve fitting software and knowledge of the energy transitions of each element at every pixel. This data can then be shown as an image showing a heat map of different elements on the surface of the material. An overall

elemental makeup of the surface scanned can also be obtained. It should be noted that these elemental make-ups calculated are only for the surface of the material because of the inability of the electrons to penetrate deep into the sample.

4.3.3.2 Method

The SEM and EDS measurements were carried out on a JEOL JSM-IT100 InTouchScope Tungsten low-vacuum SEM in the Department of Physics at the University of Strathclyde. The SEM EDS setup is shown in Figure 4.21 below:

Figure 4.21: JEOL JSM-IT100 InTouch Scope apparatus

Due to the suspected high proportion of graphitic carbon in the biochar samples measured, the samples were deemed to be conductive and not required to be coated in gold to carry out the measurements.

Nitrile gloves were used on all apparatus that would go into the specimen chamber to ensure no contamination from oils from skin in the chamber. The oils easily volatilise and gather at the detectors, skewing results and requiring expensive and time intensive cleaning procedures.

Due to the powdery nature of the samples and the high vacuum environment of the analysis chamber, the samples had to be immobilised to ensure accurate measurement and to avoid any damage to the detectors. This was achieved though the used of adhesive carbon tape mounted on aluminium stubs. The samples were milled, in a mortar and pestle, and stamped with the adhesive carbon tape to immobilise a thin layer of powder. The stubs were then blown with compressed air to remove powder not firmly secured to the adhesive. While it is possible the adsorbent characteristics of the material may be affected by the particle size of the samples, this milling procedure was only carried out for this measurement due to the experimental constraint. All other measurements in this work were carried out on as produced material.

The stubs loaded with sample were loaded onto the sample stage, placed into the specimen chamber and the chamber evacuated. The sample stage can be seen in Figure 4.22 below:

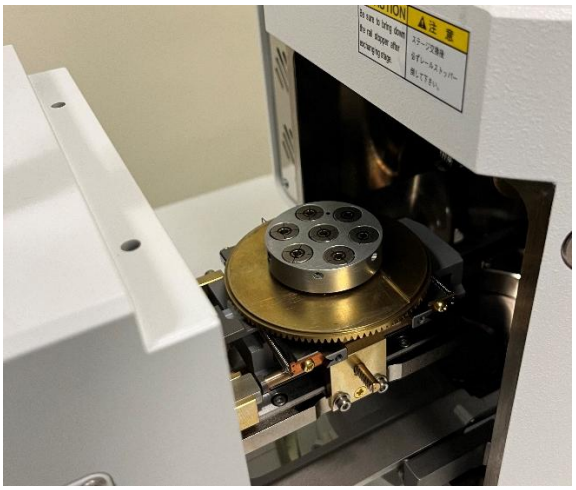

Figure 4.22: JEOL JSM-IT100 sample stage

The working distance was set to 10 mm, the accelerating voltage set to 20 kV. The probe current variable has arbitrary units and varies from 0-99. The larger the probe current, the more electrons are fired from the thermionic cathode per second, as electrons repel each other this leads to a larger probe diameter and larger spot size. Larger spot sizes lead to lower resolution images but smoother image quality. Higher probe currents are sometimes desirable when detecting X-rays to increase the signal received. For SEM image acquisition a probe current of 50 a.u. was selected to obtain a balance between image quality and resolution. For EDS spectral analysis and elemental mapping, a probe current of 80 a.u. was selected, as this method requires higher energy input to improve the X-ray signal quality.

For analysis, sites of interest were located, and the lenses focused to provide a sharp image. Magnifications in the range of 100- 1000x were employed in this work. Both SEM images through SED detection and EDS spectra through EDX detection are carried out at all sites of interest. Topographical and morphological data analyses were carried out on the SEM images while quantitative elemental analysis and elemental heat mapping were carried out on the EDS data.

4.4 Nitrogen Adsorption Characterisation

4.4.1 Method

Nitrogen adsorption isotherms were obtained using a Micromeritics ASAP 2420 Surface Area and Porosity Analyser, shown in Figure 4.23. In this work, nitrogen gas was used as the adsorptive and adsorption measured at 77.4 K.

Figure 4.23: Micromeritics ASAP 2420 apparatus used in this study

The BET analysis tubes were first removed from the drying oven and allowed to cool to room temperature before being weighed and the mass recorded. The target surface area in the tube was approximately 50 m^2g^{-1}, allowing calculation of approximate sample mass, based on the expected specific surface area of the material. The mass of sorbent was added to the tube and the exact mass recorded. The sample tube was then attached to a degas port on the Micromeritics assembly, and a heating jacket clipped in place around the bulb. The system was then set to degas the sample, at 250 °C for 4 h under vacuum, to remove

any adsorbed moisture or volatile material from the surface prior to analysis. A high temperature was chosen because of the high thermal stability of the samples and to ensure maximum degassing prior to analysis due to the highly microporous nature of these samples, as indicated by initial experiments. The sample tube was then removed from the degas section and the weight recorded. The analysis ports were cooled using liquid nitrogen at its normal boiling point; the liquid nitrogen level in the analysis port was topped up prior to each analysis run. The sample tube was then fitted with an insulating jacket, with a filler rod inserted to reduce the dead volume within the tube, before inserting the tube into an analysis port. A 49-point adsorption profile from 0.005-1 relative pressure, and a 30-point desorption profile from 0.1-1 relative pressure, was devised and used to measure the sorption isotherms. Extra analysis points in the low-pressure zone were required, due to the highly microporous nature of the samples. The analysis was run at 77.4 K with an equilibration time of 20 s. Once completed, the sample was recovered, as nitrogen adsorption is a non-destructive analysis technique, and the tube and filler rod washed and returned to the drying cabinet.

4.5 Surface Characterisation

4.5.1 Point of Zero Charge

4.5.1.1 Introduction

In this work, the point of zero charge (PZC) was determined using a salt addition method, performed using sodium nitrate, with an ionic strength of 0.1, as the medium. A point of zero charge experiment shows the pH at which a material exhibits no electrical charge. At pH values above that of the point of zero charge, the surface of the material will exhibit a net negative charge, making the material suitable for adsorption of cations. At pH values below the point of zero charge, the surface of a material will exhibit a net positive charge, making the material suitable for adsorption of anionic species.

This behaviour can be explained through le Chatelier's principle. At the point of zero charge, the hydrogen ion concentration of the surface of the material is at equilibrium with the solution it is in. If the pH the solution is above or below the PZC, the material will attempt to correct this perturbation. If the pH of the solution is above the PZC, hydrogen ions will dissociate from the material to attempt to lower the PZC, this results in a negative surface charge with the lone pairs left behind after hydrogen dissociation. If the pH of the solution is below the PZC, the material will adsorb hydrogen ions to reduce the hydrogen

ion concentration and attempt to increase the pH of the solution. The hydrogen ions will associate at sites where hydrogen ions can be accepted such as lone pairs of electrons, and result in a positive charge on the surface.

A low PZC can therefore indicate a greater proportion of weak acid functional groups such as phenol of hydroxyl groups, while a high PZC can indicate a greater proportion of functional groups containing lone pairs or delocalised electrons such as amines, carbonyl or aromatic rings.

4.5.1.2 Method

A Vernier pH sensor with Vernier Go-Link USB interface was used, with LabQuest data logging software, to measure solution pH. Before use, the sensor was calibrated by a 2-point calibration method using pH 4.01 and pH 10.01 buffer solutions.

A bulk solution of 0.1 M $NaNO_3$ was prepared and split into five separate sealed containers of 500 mL. Each container then had the pH probe inserted and the solution titrated to a new pH using 0.1 M HNO_3 and 0.1 M NaOH, to achieve end pH values of 3, 5, 7, 9 and 11 ± 0.1. 10 mL samples of each of these solutions were then pipetted into 15 mL centrifuge tube and the pH checked. If required, they were titrated again with 0.01 M HNO_3 or 0.01 M NaOH to within the ±0.1 limit of the desired value. The initial pH was then recorded and denoted as pH_i. 25 mg of the sample to be tested was then added to the centrifuge tube and the mixture was agitated for 24 h at room temperature before the final pH was once again measured and denoted as pH_f. A plot of ΔpH ($pH_f - pH_i$) vs pH_i was obtained, and where the plot crosses the x-axis (i.e., $\Delta pH = 0$) is noted as the point of zero charge.

4.5.2 Fourier Transform Infrared Spectroscopy

4.5.2.1 Introduction

Fourier Transform Infrared Spectroscopy (FTIR) is an analysis technique used to determine the functional groups present on the surface of a material. Materials absorb infrared light at specific wavelengths depending on the species present. The wavelengths of light are proportional to energies required for specific molecular vibrations in the sample, which come in two main types: stretching vibrations, those that change the bond length, and bending vibrations, those that change the bond angle. These categories are further broken down into sub-types, all giving slightly different peaks which are highly important for identifying species.

Stretching vibration sub-types are:

- **Symmetric:** Where bonds of the same type stretch in phase with each other.
- **Asymmetric:** Where bonds of the same type stretch out of phase with each other.

Bending vibration sub-types are:

- **Scissoring:** An in-plane bend, where the two atoms approach each other then move away from each other in line with the plane.
- **Rocking:** An in-plane bend, where the two atoms move in line with the plane in the same direction.
- **Wagging:** An out of plane bend, where the two atoms move to one side of the plane then move up and down through the plane.
- **Twisting:** An out of plane bend where one atom moves above the plane, and one moves below the plane.

The six types of molecular vibration are demonstrated graphically in Figure 4.24

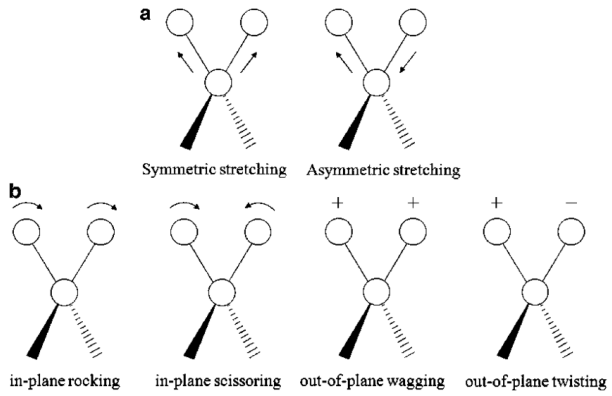

Figure 4.24: Molecular vibrations schematic (143)

In this work, absorption of mid-IR spectrum (400-4000 cm^{-1}) was carried out and analysed. The mid-IR spectrum can be further split into four regions in analysis:

- single bond region (2500-4000 cm^{-1})
- triple bond region (2000-2500 cm^{-1})
- double bond region (1500-2000 cm^{-1})

- fingerprint region (600-1500 cm^{-1})

A database of wavenumbers associated with various species stretches and bends are referred to during analysis. Each peak falls within the range for multiple different species, so cross validation, and prior knowledge of the sample, must be used to determine the true functional groups present. This task becomes increasingly difficult with the addition of multiple peaks. Any species with more than five absorption bands can be described as a complex molecule.

4.5.2.2 Method

In this work, a Perkin Elmer Spectrum 100 Fourier Transform infrared Spectrometer was employed, as shown in Figure 4.25.

Figure 4.25: Perkin Elmer Spectrum 100 apparatus

Firstly, two sodium chloride disks were washed with deionised water and dried thoroughly. The sample was ground in a mortar and pestle and sprinkled into the centre of one of the salt cells. The second salt cell was placed on to and carefully used to spread the sample across the centre of the salt disk. The salt disks were clamped in the brass vice to hold it in place. A sample ready for analysis is shown in Figure 4.26.

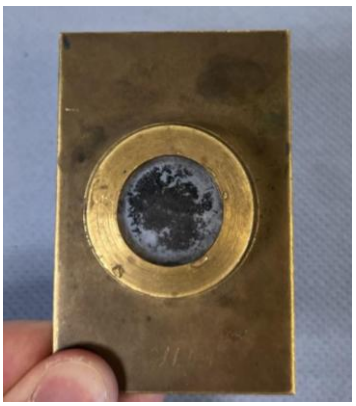

Figure 4.26: Sample prepared for FTIR analysis

A background spectrum was first collected and automatically subtracted from the analysis signal. The brass clamp was placed in the analysis chamber between the source and detector. The analysis was run in triplicate. A baseline correction and curve smoothing were carried out in Origin prior to analysis.

4.5.3 Attenuated Total Reflectance Fourier Transform Infrared Spectroscopy

4.5.3.1 Introduction

Attenuated Total Reflectance Fourier transform infrared spectroscopy (ATR FTIR) is a subclass of FTIR. Where FTIR in Section 4.5.2 above describes an experimental setup and procedure where the light source and detector are on opposite sides of the sample, where the light is transmitted through the sample. By contrast, the ATR FTIR setup allows for direct measurement of a non-transparent solid sample, utilising internal reflection within the crystal-sample arrangement, without the need to reduce the concentration of the sample through making KBr disks or by spreading a small layer on NaCl cells. This removes the need for destructive and time-consuming sample preparation of FTIR samples.

In ATR FTIR, the infrared light (IR) passes through the ATR crystal made of a material with a high refractive index such as zinc selenide, diamond, or germanium. The light passes through the crystal and is totally internally reflected at the crystal-sample interface. Part of the IR light, known as the evanescent wave, passes through the sample and can be absorbed, the rest of the light is reflected into the ATR crystal and onto the detector. The depth that the evanescent wave penetrates the sample material is dependent on the wavelength of light, the angle of incidence and the refractive indices of the ATR crystal and the sample material. This relationship is shown in Equation 4.1:

$$d_p = \frac{\lambda}{2\,\pi\,n_c\sqrt{sin^2\,\varphi - \frac{n_s}{n_c}}} \tag{4.1}$$

Where:

d_p= Penetration depth of the evanescent wave, in metres

λ = Wavelength of the infrared light, in metres

φ = Angle of incidence of the light at the crystal- sample interface, in radians

n_c = Refractive index of the ATR crystal

n_s = Refractive index of the sample

We can see from the relationship, that for the penetration depth to be real at acute angles of incidence (1-90°) that are required for total internal reflection, $n_s < n_c$. We can also see there is a critical angle for a sample and ATR crystal pair; at angles below this critical angle there will be no penetration by the evanescent wave. The smaller the ratio of the refractive indices, the larger the range of incident angles that can be used for analysis. Most ATR FTIR have a fixed incident angle so this must be above the critical value for a given crystal sample pair.

Highly absorbing samples, such as black materials like biochar, are notoriously difficult to carry out on transmission FTIR on due to their high opacity. Carbon black also has a very high refractive index which further increases around absorption bands, sometimes preventing the internal reflection of the light altogether. Known as anomalous dispersion effects, this manifests as severe distortions in the spectra such as absorbance below the baseline recorded. This can be mitigated by selecting an ATR crystal with a refractive index much higher than that of the sample. This has the knock-on effect of decreasing the penetration depth of the evanescent wave, reducing the signal intensity and increasing the signal to noise ratio. The low penetration depth makes higher refractive index ATR crystals better for surface studies, pertinent to this research.

In this work, a germanium (Ge) ATR crystal was employed due to the high refractive index of the biochar samples tested, to minimise the anomalous dispersion effects. The lower penetration depth suits the samples well as only the surface functional groups are of importance in adsorbent materials. The data is only being used qualitatively to determine

the groups present and their relative proportions, so the signal to noise trade-off is deemed to be a fair sacrifice.

The Ge ATR crystal runs on an external reflectance mode, meaning the angle of incidence is 45°. Assuming the biochar samples have a similar refractive index of carbon black at approximately 1.84 (144) and assuming the germanium crystal has a refractive index of 4.0 (145) at a wavelength of 10 microns, this gives a critical angle of approximately 43° or greater. The 45° angle of operation allows for measurement while also giving close to the greatest depth on penetration and therefore greatest signal to noise ratio.

4.5.3.2 Method

This work was carried out on an Agilent 4300 handheld FTIR Spectrometer with Germanium ATR crystal attachment shown in Figure 4.27.

The equipment was set-up in benchtop configuration with pressure tower in place. The ATR crystal surface and pressure tower tip were cleaned with acetone prior to use and in between each sample. A background spectrum was taken prior to analysis, this background spectrum was automatically subtracted from any measurements taken by the Agilent software.

A small spatula full of the analyte sample was placed on the ATR crystal and pressed onto the crystal by tightening the pressure tower. The measurement was run in triplicate to determine an average spectrum for each sample.

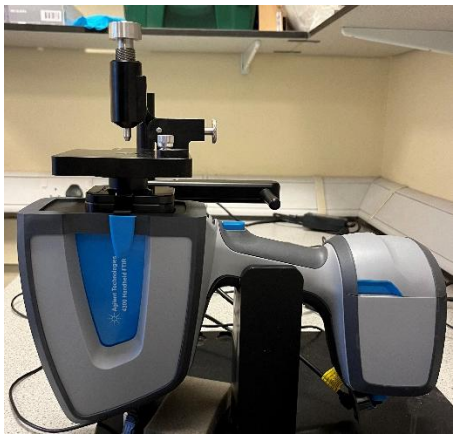

Figure 4.27: Agilent 4300 handheld FTIR Spectrometer apparatus

4.5.4 X-Ray Photoelectron Spectroscopy

4.5.4.1 Introduction

X-ray photoelectron spectroscopy (XPS) is a technique which can be used to not only determine the elemental composition on the surface of a material but also the local chemical environment of those elements. The relative proportion of functional groups and their local environment can be determined through analysis of the spectra. The operating principle of XPS is rooted in knowledge of the photoelectric effect and quantum mechanics. X-ray photoelectrons of a known frequency are irradiated on a sample, excitation of core shell electrons then occurs which are subsequently emitted from the sample. These emitted electrons are then observed by a detector and their kinetic energy recorded.

In an ideal case, the binding energy characteristic of the excitation and emission of the electron for the target atom can be found from Equation 4.2:

$$E_{Photon} = E_{Binding} + E_{Kinetic} \tag{4.2}$$

Where:

E_{Photon} = Energy of the incident X-ray photoelectron, in eV

$E_{Binding}$ = Binding energy of the electron to the target atom, in eV

$E_{Kinetic}$ = Kinetic energy of the electron after ejection from the atom, in eV

This can be expanded to:

$$E_{Binding} = hv - E_{Kinetic} \tag{4.3}$$

Where:

h = Planck's constant, 6.63×10^{34} J.s

v = Frequency of the X-ray in s^{-1}

In real world cases, a work function ϕ must be included to consider energy lost by the emitted electron passing through the solid state of the detector. Other losses or gains due

to electric force fields resulting in acceleration or deceleration of the electron may also occur. Because of this work function, it is imperative a calibration of the equipment is undertaken. Equation 4.3 is expanded to Equation 4.4:

$$E_{Recorded\ Binding} = hv - (E_{Kinetic} - \Phi) \quad (4.4)$$

Where:

$E_{Recorded\ Binding}$ = Binding energy measured experimentally, in eV

4.5.4.2 Method

The experimental procedure for the XPS analysis was carried out by staff at the National EPSRC (Engineering and Physical Sciences Research Council) XPS Users' Service (NEXUS) in the nanoLAB at the University of Newcastle on a Thermo Scientific K-Alpha X-ray Photoelectron Spectrometer System. The relevant experimental information is shown in Table 4.22.

Table 4.22: XPS experimental information

Scan	Step size (eV)	Number of scans	Dwell time (ms)	Pass energy (eV)
Survey	0.4	20	10	150
C1s	0.1	10	100	40
O1s	0.1	10	100	40
N1s	0.1	20	200	40

Each XPS sample must be corrected to correct for the work function and any other non-ideal factors. The leftmost peak on the C1S peak is identified as the C=C/C-H functional group. This peak should occur at 284.8eV and all the spectra for this measurement must be translated to the left or right on the x-axis to correct for variations in this peak.

Each sample is irradiated with X-rays of a specific energy for the designated dwell time before the X-ray energy is changed by the step size and repeated until the entire sweep has taken place. The entire spectrum is then repeated for the number of sweeps designated. The measured kinetic energies of the electrons and the known energy of the X-rays are then used to calculate the binding energies. The electrons counted per second by the detector are then plotted against binding energy for further analyses.

The spectra file was then loaded into the Fityk software and the 'Remove Shirley background' function used to remove the background signal from the sample. The

corrective translation in the x-axis is then implemented and the peak of interest highlighted. The Voight curve fitting function is then iterated multiple times to determine the constituent gaussian peaks of the target curve. The binding energies at the centre of the constituent curves are then cross referenced against the NIST database and the elements and chemical environment discerned. The area under the curve of each peak was noted for use in evaluation of the relative atomic fractions of each functional group present on the surface. Equation 4.5 can be used to find the atomic fraction of each of the identified functional groups.

$$Atomic\ fraction = \frac{\frac{I_i}{F_{Sensitivity,i}}}{\sum_J \frac{I_j}{F_{Sensitivity,j}}} \tag{4.5}$$

Where,

$I =$ The background subtracted peak area of a photoelectron

$F_{Sensitivity} =$The sensitivity factor of the element of the photoelectron peak

$i =$ The photoelectron peak being investigated

$j =$ All photoelectron peaks identified in the analysis

The sensitivity factors for carbon, nitrogen and oxygen used in this study are 1, 1.8 and 2.93 respectively.

4.6 Concentration Measurement

4.6.1 UV-Vis Spectroscopy

4.6.1.1 Introduction

Ultraviolet-Visible (UV-Vis) spectroscopy is underpinned by the concept of transitions of electrons from their highest occupied electron orbital (HOMO) to their lowest unoccupied electron orbital (LUMO). These transitions have an associated energy required for the electron to be moved from a lower energy state to a higher, excited state. This energy can be provided by light, which is absorbed by the molecule, provided it has the energy necessary to make the transition. According to the Planck-Einstein relation, energy is directly proportional to the frequency of light as shown in Equation 4.6.

$$E = h.v \tag{4.6}$$

Where:

E = Energy of the wave in J

h = Planck's constant, 6.63×10^{34} J.s

v = Frequency of light in s^{-1}

Energy is also inversely proportional to the wavelength of light, as shown in Equation 4.7.

$$E = \frac{h.c}{\lambda} \tag{4.7}$$

Where:

c = Speed of light in m s^{-1}

λ = Wavelength of light in m

So, the higher the frequency, or the lower the wavelength, of light, the greater the energy.

In single-bonded, or non-conjugated double-bonded molecules, σ to σ^* or π to π^* transitions require large amounts of energy; such energies have wavelengths much too small to be accurately measured by most UV-Vis spectrometers. UV-Vis becomes a useful tool for analysis with highly conjugated molecules, as the energy gap in their π to π^* transitions become narrower. These lower energies are associated with larger wavelengths, which are in the analysis range for UV-Vis spectrometers λ > 200 nm. In molecules with large degrees of conjugation, the HOMO-LUMO transition energy gap becomes so small that it can be achieved with absorbance of visible light at much larger wavelengths. Molecules or parts of molecules that absorb light strongly are known as chromophores. Multiple chromophores can exist within a molecule, each absorbing different wavelengths of light and giving rise to different peaks on a UV-Vis spectrum. Conjugated systems with lone pairs of electrons can undergo ground state to anti-pi (n to π^*) transitions, giving a secondary peak at longer wavelengths. The absorbance at these peaks is often lower than that of the π to π^* transitions.

4.6.1.2 Beer-Lambert

The Beer-Lambert law states that light passing through a solution will be absorbed, and that this absorbance is directly proportional to the concentration of the detected material in the solution, as well as directly proportional to the path length of the light through the sample. The Beer-Lambert relationship is shown in Equation 4.8.

$$A = \varepsilon . l . C \tag{4.8}$$

Where:

$A =$ Absorbance of the light through the solution

$\varepsilon =$ Absorptivity in mg $L^{-1}cm^{-1}$

$l =$ Path length of the light through the sample in cm

$C =$ Concentration of the solution in mg L^{-1}

In a calibration experiment, a linear relationship can be obtained by plotting absorbance vs known concentrations of a target analyte in solution. From this, the absorptivity can be found and used to find the concentration of any solution, if the absorbance is known.

4.6.1.3 Method- General

The measurements were performed using a Varian CARY 500 UV-Vis-NIR spectrophotometer, as shown in Figure 4.28.

Figure 4.28: Varian Cary 500 UV-Vis-NIR apparatus

A wavelength range of 200-800 nm was chosen with measurements being taken at 1 nm intervals. A Hellma Analytics high precision quartz cell with 1 cm path length was used, shown in Figure 4.29.

Figure 4.29: Hellma QS High Precision Cell

A baseline measurement was recorded for 100% transmittance. The beam path was then covered, and a 0% baseline taken. This file was saved and imported into the measurement software to be automatically set as the limits for subsequent measurements. The cuvette was first rinsed multiple times with deionised water before draining, and rinsing with acetone, before being allowed to dry completely. A small amount of the analyte solution was pipetted into the cuvette, rinsing the cuvette, and the contents discarded. The cuvette was then filled with analyte solution and the cuvette cap fitted. The cuvette was inserted into the analysis slot, ensuring the markings on the cuvette were facing towards the source of the light. The light shields were closed, and the measurement started. Each measurement was run in triplicate. The analysis files were exported and analysed in Microsoft Excel. The mean absorbance of the repeated measurements was found for each wavelength and the average absorbance plotted against wavelength. The plot was inspected for noise due to low intensities of light (high absorbance) and the sensitivity of the detector. If large amounts of noise were present, the measurement was re-run with a higher dilution factor, this is discussed in more detail in Section 4.7.1.1. The wavelength the absorbance peak is expected at for the analyte species was found in the literature and the local maximum around this wavelength taken. This absorbance value was used in Equation 4.8 to calculate the concentration of the target species.

4.6.1.4 Method- Calibration

For the calibration experiment, 20 mL solutions of 5-65 mg L^{-1} in steps of 5 mg L^{-1} were prepared from a stock solution of 100 mg L^{-1}. This is done following the calibration standard plan shown in Table 4.23.

Table 4.23: Calibration solution method

Final concentration	Volume of 100 mg L^{-1} stock solution (mL)	Volume of deionised water (mL)
65	13	7
60	12	8
55	11	9
50	10	10
45	9	11
40	8	12
35	7	13
30	6	14
25	5	15
20	4	16
15	3	17
10	2	18
5	1	19

One more sample with a concentration of 1 mg L^{-1} was prepared using 2 mL of the 10 mgL^{-1} solution prepared previously and 18 mL of deionised water. Each of these samples was run according to the method described in Section 4.6.1.3 and their absorbance values noted. Any plots with signal noise were disregarded. The largest concentration with no noise was noted as the C_{Max} for the analyte, the maximum measurable concentration. A plot of absorbance vs concentration was taken, with the line fixed to pass through the origin, as zero concentration of analyte should produce zero absorption. The gradient was used in Equation 4.8 to find the absorption coefficient, ε.

4.7 Liquid Phase Adsorption Experiments

4.7.1 Adsorption Kinetics

4.7.1.1 Full Kinetic Modelling Method

Adsorption times of 10, 20, 30, 40, 50, 60, 90, 120, 240 and 1440 minutes were chosen for the kinetic studies. Many points at low contact times were used to obtain a good fit of the initial steep rise in adsorption, while longer times were included to ensure an accurate determination of the maximum uptake as the adsorption process comes to equilibrium. 30 mL of 100 mg L^{-1} adsorptive solution was pipetted into each of ten conical flasks, which were subsequently covered with Parafilm™ and marked with one of the times listed above. 10 mg of the adsorbent was weighed, and the precise mass recorded, before being added to the conical flask and placed on the orbital shaker.

Once the prescribed time had elapsed, the contents of the flask were transferred into a centrifuge tube, which was then centrifuged, using a Sigma 2-16 small batch centrifuge with swinging bucket rotor installed, for 30 s. 4 mL of the solution was pipetted into a beaker and diluted with a volume of deionised water, the exact volume of which was dependent on the dilution factor.

The dilution factor can be found using Equation 4.9:

$$Dilution\ factor = \frac{C_0}{C_{Max}} \tag{4.9}$$

Where:

$C_0 =$ Initial concentration of the adsorptive solution in mg L^{-1}

$C_{Max} =$ Maximum measurable concentration for the analyte in mg L^{-1}

The dilution factor was rounded up to the nearest whole even number.

The required volume of deionised water can be found using Equation 4.10:

$$V_{Water} = (Dilution\ factor - 1).V_i \tag{4.10}$$

Where:

$V_{Water} =$ Volume of water required for the dilution in mL

$V_i =$ Initial volume of solution pipetted into the beaker in mL

The beaker was swirled to ensure homogeneity within the sample. Concentration measurement of the diluted sample was then carried out using the method described in Section 4.6.1.3.

The concentration of the adsorptive solution at time t can be found by multiplying the concentration of the diluted sample by the dilution factor. This method was employed to ensure that the measured concentration was never above C_{Max}. It also allowed for the use of the same pipette at the same volume setting to avoid introducing error from using multiple differently calibrated pipettes. Simply adding the dilution factor minus 1 amounts of the same volume of the initial analyte gives a sample with a measurable concentration less than C_{Max}.

Once concentration data for the suite of solutions were determined, providing data for each time interval, the corresponding adsorbent uptakes could be calculated using Equation 4.11:

$$q_t = \frac{(C_0 - C_t).V}{m_A} \tag{4.11}$$

Where:

C_0 = Initial concentration of the adsorptive solution in mg L^{-1}

C_t = Concentration in the solution at time t in mg L^{-1}

V = Volume of adsorptive solution in the adsorption vessel in L

m_A = Mass of adsorbent added to the adsorption vessel in g

q_t = Uptake in mg g^{-1} at time t

A plot of uptake vs adsorption time was obtained, and the kinetic models fit to the data (146).

4.7.1.2 Design of Experiments Kinetic Modelling Introduction

To reduce experimental times, save reagents and to minimise the amount of adsorptive solution going to waste disposal, a reduced number of data points were taken to determine the adsorption capabilities of the adsorbents synthesised. While full kinetic modelling would be preferable to determine the kinetic parameters and maximum uptake value, running ten samples at varying contact times for every point on a design of experiments followed by full modelling and analysis becomes a monumental task. It was decided that two points will be taken for each synthesised sample of the design of experiments. One point at a short time of 1 h to model and find the optimal synthesis conditions of an adsorbent with the best efficacy at short contact times and therefore the best adsorbent with the best kinetics. The other sample, done at a long contact time of 1 week will allow for the determination of the optimal synthesis parameters for the adsorbent with the highest uptake at equilibrium. The uptakes at these times will be used as response variables in an optimisation design of experiments to determine the optimal conditions to maximise the response variable. It is important to note that these synthesis conditions optimal to these two outcomes may be different. For example, increased capacity may come at the expense of surface characteristics which are favourable to the fast adsorption of pollutants.

4.7.1.2 Design of Experiments Kinetic Modelling Method

A bulk solution of 100 mg L^{-1} adsorptive was prepared. For each adsorbent, two conical flasks containing the solution were prepared, at volumes of 10-30mL depending on the experiment. 10 mg of the adsorbent was weighed, its exact weight recorded and added to the flask which was agitated on the orbital shaker at room temperature. One flask was agitated for 1 h before being removed and the bulk adsorbent concentration measured using the method described in Section 4.6.1.3 and 4.7.1.1. The other flask was agitated for 24 h or 7 days depending on the experiments, before being removed and its bulk adsorbent concentration measured.

4.7.2 Liquid Phase Adsorption Isotherms

4.7.2.1 Method

Initial adsorptive concentrations of 25, 50, 75, 100, 150, 200, 250, 300, 400 and 500 mgL^{-1} were chosen for the isothermal studies. This range of concentrations was used to allow for a range of unsaturated adsorbents with varying coverage and saturated adsorbents in equilibrium with varying concentrations of solution to be obtained to allow for extensive investigation of the materials. 500 mgL^{-1} was chosen as the upper limit due to the solubility limit the pollutant studied in this work. Temperatures of 25 °C, 35 °C and 45 °C were chosen as the isothermal target temperatures.

30 mL of each of the solutions was pipetted into one of ten 50 mL conical flasks, which were then covered with parafilm and labelled. 10 mg of the adsorbent was weighed, its exact mass recorded and added to the conical flask. The flasks were agitated on the orbital shaker with the incubator set to the isothermal temperature for the run.

The flasks were allowed to thermally equilibrate and achieve adsorption equilibrium over a period of 24 h. After the 24 h had elapsed, the process for measuring the concentration via UV-Vis spectroscopy described in Section 4.6.1.3 was then followed. The equilibrium adsorbent uptakes were then calculated using Equation 4.12:

$$q_e = \frac{(C_0 - C_e).V}{m_A} \tag{4.12}$$

Where:

C_0 = Initial concentration of the adsorptive solution in mg L^{-1}

C_e = Concentration in the solution at equilibrium in mg L^{-1}

V = Volume of adsorptive solution in the adsorption vessel in L

m_A = Mass of adsorbent added to the adsorption vessel in g

q_e = Uptake in mg g^{-1} at equilibrium

A plot of uptake vs equilibrium adsorptive concentration was obtained, and the isotherm models outlined in Section 3.2 fitted to the data using non-linear curve fitting.

This was repeated for each of the isothermal temperatures.

4.7.3 pH Controlled Adsorption

4.7.3.1 Method

The effect of solution pH on the adsorption uptake was investigated. Sample solutions were prepared at 100 mg L^{-1} with a solution volume of 30 mL. The solution pH was subsequently altered to pH 3, 5, 7, 9 and 11 using 0.1M Sodium hydroxide and 0.1M Hydrochloric acid.

30 mL of each solution was added to five 50 mL conical flasks. 10 mg of the adsorbent was added to each conical flask and sealed with parafilm. The conical flask was then added to the orbital shaker and allowed to equilibrate at room temperature for 24 h. After the 24 h has elapsed, the process for measuring the concentration via UV-Vis spectroscopy described in Section 4.6.3.1 was then followed. The equilibrium uptakes were found using Equation 4.12.

4.7.4 Liquid Phase Desorption

4.7.4.1 Method

Two conical flasks containing 30 mL of 500 mg L^{-1} adsorptive solution were prepared. 10 mg of adsorbent was weighed and added, and the flask agitated for 24 h at room temperature and allowed to achieve equilibrium. After 24 h, one vial was selected, and the liquid adsorptive solution decanted. The solid adsorbent was added to a watch glass and any liquid remaining, due to the hydrophilicity of the adsorbent, was siphoned off with the corner of a paper towel. The watch glass was labelled as ‘unwashed char’ and placed into the drying oven at 103 °C for 24 h to dry.

The second vial had the adsorptive solution removed and the majority of the solid adsorbent retained. The solid adsorbent is then mixed with 30 mL of deionised water. The solution is allowed to settle and the approximately 20 mL of the solution removed to waste.

The remaining 10 mL with the adsorbent sediment is added to a centrifuge tube and centrifuged for 30 s. The remaining solution is removed to waste, and the adsorbent recovered and added to 500 mL of deionised water. This adsorbent-water mixture is then agitated for 10 min to allow the adsorbate to form a new equilibrium with the bulk liquid. This was repeated a minimum of ten times and until after 10 min the bulk solution runs clear indicating no desorption into the bulk. The solid is finally recovered as described above and placed onto a watch glass. The watch glass was labelled as 'washed char' and placed into the drying oven for 24 h.

The unwashed, washed and an unadsorbed 'clean' sample of the biochars were then analysed through ATR FTIR.

4.8 References

1. Materials ASfT. Standard Test Method for Moisture Analysis of Particulate Wood Fuels. Procedure 1996.
2. Pandia S, Hutagalung A, Siahaan A. Utilization of Cocoa Peel as Biosorbent for Oil and Color Removal in Palm Oil Mill Effluent (POME). IOP Conference Series: Materials Science and Engineering. 2018;300:012066.
3. Ojeda J, Dittrich M. Fourier Transform Infrared Spectroscopy for Molecular Analysis of Microbial Cells. Methods in molecular biology (Clifton, NJ). 2012;881:187-211.
4. Medalia A, Richards L. Tinting strength of carbon black. Journal of Colloid and Interface Science. 1972;40(2):233-52.
5. Spectral Systems L. Ge ATR Optical Elements 2024 [Available from: https://www.spectral-systems.com/products/ge-atr-optical-elements/.
6. Kumar KV, Sivanesan S. Selection of optimum sorption kinetics: Comparison of linear and non-linear method. Journal of Hazardous Materials. 2006;134(1):277-9.

5. Screening of Biochar Synthesis Parameters

5.1 Sample Composition and Pyrolysis

5.1.1 Yield and Proximate Analysis

Experiments to create all 16 samples of the design of experiments screening were carried out in duplicate and the resulting yields were calculated, with associated errors, and the results are summarised in Table 5.24. Also included are the proximate analysis data obtained for these 16 samples, as well as the 'as received' (AR), and dried, BSG.

Table 5.24: Yield and proximate analysis data

Sample	*Yield[1] (% dry basis)*	*Moisture (%)*	*Volatiles (%)*	*Fixed carbon (%)*	*Ash (%)*
S1	29.4 ± 0.3	3.7	21.3	59.8	15.2
S2	20.9 ± 0.0	4.2	14.7	63.8	17.8
S3	27.3 ± 0.5	1.9	24.0	64.9	9.2
S4	6.7 ± 0.0	1.5	7.8	45.5	45.2
S5	28.0 ± 0.9	1.6	21.2	68.0	9.2
S6	18.6 ± 0.6	2.6	8.3	72.7	16.4
S7	27.5 ± 0.4	1.9	8.5	66.6	12.8
S8	8.9 ± 0.0	1.2	18	52.9	37.4
S9	28.8 ± 0.0	1.3	8.8	68.3	12.4
S10	18.9 ± 0.5	4.5	8.8	70.0	16.7
S11	27.3 ± 0.5	1.8	21.1	65.5	11.6
S12	9.0 ± 0.1	2.0	9.2	52.4	36.4
S13	27.5 ± 0.5	2.7	19.6	64.7	13.0
S14	19.2 ± 0.1	3.6	7.0	71.8	17.6
S15	28.1 ± 0.0	1.6	19.6	66.9	11.9
S16	6.1 ± 0.1	1.2	8.1	36.5	54.2
BSG (AR)	-	71.9	22.0	5.2	0.9
BSG (Dried)	-	2.1	76.7	18.1	3.1

Proximate analyses for BSG reported within the scientific literature show good agreement with the results obtained in this work. Water content of BSG was reported in the range 71%- 83%, on an 'as received' basis (147-150), agreeing well with the 71.9% moisture content of the BSG used in this study as received. The proximate analysis data for BSG on a dry basis was also in good agreement with literature, where ash values in the range 3.5-

[1] Samples were synthesized in duplicate for the purpose of error calculation. The individual data sets can be seen in Appendix A. The standard error equation is detailed in Appendix D

5.0%, fixed carbon in the range 16.2-19.0% and volatile matter values of 77-79% have been reported (147-152). The ash content was noted to be high across all samples, being over or close to the 10% limit imposed by the Indonesian standards authority, possibly indicating blocked pores.(142, 153) This may indicate that the biochars made in this study require post-synthesis modification to remove excess ash to improve their performance as adsorbent materials.

A graph of the relative component make-up per 100 g of each sample is shown in Figure 5.30.

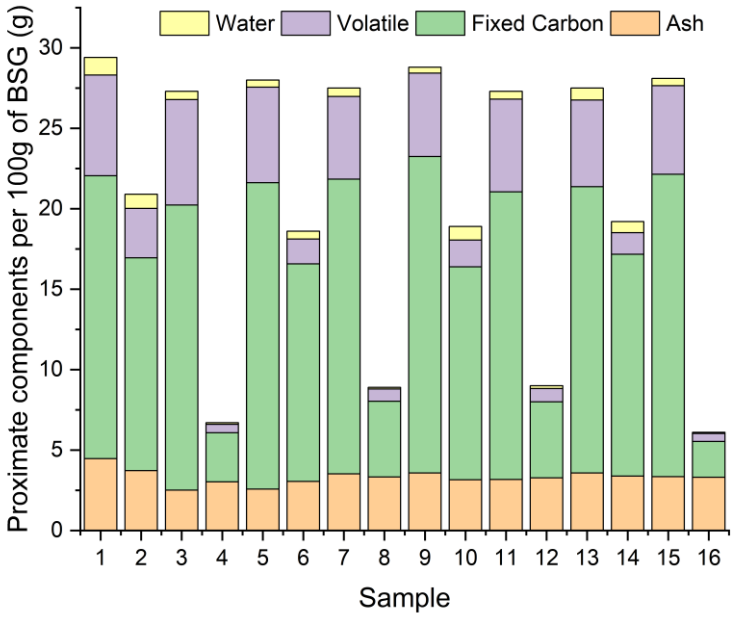

Figure 5.30: Proximate components of biochars samples per 100 g of BSG

These results show that the samples can be grouped into three distinct categories:

- ***a.*** Samples with both high fixed carbon and volatile fractions - odd numbered samples
- ***b.*** Samples with a high fixed carbon and a low but non-negligible volatile fraction - samples 2, 6, 10 and 14.
- ***c.*** Samples with almost no volatile fraction and a very fixed carbon fraction almost equal to that of the ash content - samples 4, 8, 12, 16.

These groups correspond to permutations of temperature and hold time, from the screening design of experiments, used to synthesize them. Category ***a*** are all synthesized at

low temperatures at both long and short hold times, while category ***b*** are those synthesized at high temperatures and short hold times, whereas category ***c*** are those synthesized at high temperatures and long hold times.

A first-order differential analysis of the TGA curves was performed. The temperatures at which the weight loss mechanisms occurred are listed in Table 5.25.

Table 5.25: Thermogravimetric analysis weight loss temperatures for screening biochar samples and BSG

Sample	*Weight loss 1 Temperature (°C)*	*Weight loss 2 Temperature (°C)*	*Weight loss 3 Temperature (°C)*	*Weight loss 4 Temperature (°C)*	*Weight loss 5 Temperature (°C)*
S1	89	598	900	-	-
S2	62	890	900	-	-
S3	79	624	900	-	-
S4	82	893	900	-	-
S5	82	615	900	-	-
S6	88	889	900	-	-
S7	83	625	900	-	-
S8	77	892	900	-	-
S9	82	616	900	-	-
S10	77	880	900	-	-
S11	84	619	900	-	-
S12	88	890	900	-	-
S13	75	611	900	-	-
S14	88	884	900	-	-
S15	77	633	900	-	-
S16	92	893	900	-	-
BSG (Dried)	86	286	347	394	900

Weight loss 1 is attributed to the desorption of water from the surface of the samples. The varying temperatures at which this mechanism occurs are due to the different affinities of the water for the surface of the sample. The second weight losses are grouped into two sets: odd samples have a weight loss range of 598-633 °C, while the even samples have a weight loss range of 880-893 °C. This group corresponds to the synthesis temperature of the two groups, showing that, in the samples synthesized at lower temperatures there still exists volatile material within the structures, which is evolved at these lower temperatures. The samples synthesized at higher temperatures have already experienced sufficiently high thermal regimes to remove this more volatile material during synthesis. For all biochar samples, the third, and final, weight loss corresponds to the introduction of oxygen to the

pre-heated system and is attributed to the oxidation of the fixed carbon within the samples.

In the BSG (Dried) sample there were five weight loss sections noted within the thermograph. The first and last were associated with the desorption of moisture and oxidation steps, as also observed for the biochar samples tested. It is believed that the three remaining weight loss sections are representative of the three macromolecules constituting the bulk of the BSG: hemicellulose, cellulose, and lignin. Hemicellulose is the most volatile of the macromolecules, with a reported pyrolysis temperature range of 220-315 °C, then cellulose with a range of 315-400 °C, and finally lignin with a range of 180-900 °C (154). It is thought that all cellulose and hemicellulose will have been pyrolyzed in the biochar samples synthesized in this work, as the synthesis temperatures are well above that of the thermal ranges for cellulose and hemicellulose pyrolysis. The temperatures noted for the volatile weight loss in Table 5.25 only lie within the range of lignin pyrolysis. It is, therefore, assumed that the lack of porosity in the odd numbered samples (discussed later in Section 5.2) is not due to incomplete pyrolysis of the cellulose and hemicellulose, but is ascribed to the lack of pyrolysis of the more volatile lignin biopolymer sections during biochar synthesis.

5.1.2 CHN Elemental Analysis

CHN analysis was carried out in duplicate on each of the biochar samples produced according to the design of experiments plan and on dried BSG precursor. A table of the carbon, hydrogen, nitrogen and 'other elements' content is summarised in Table 5.26 below.

Table 5.26: CHN elemental analysis of screening biochar samples[2]

Sample	*Carbon (mass %)*	*Hydrogen (mass %)*	*Nitrogen (mass %)*	*Other (mass %)*
S1	66.9 ± 0.5	2.8 ± 0.1	5.9 ± 0.0	24.5 ± 0.3
S2	65.6 ± 0.3	1.2 ± 0.1	3.3 ± 0.1	29.9 ± 0.5
S3	68.5 ± 0.1	2.4 ± 0.0	5.3 ± 0.0	23.8 ± 0.1
S4	50.0 ± 0.1	0.3 ± 0.1	2.0 ± 0.0	47.7 ± 0.0
S5	67.7 ± 1.0	2.6 ± 0.2	5.7 ± 0.2	24.0 ± 1.3
S6	61.4 ± 1.8	1.0 ± 0.3	3.3 ± 0.2	34.3 ± 2.3
S7	68.4 ± 0.2	2.4 ± 0.0	5.9 ± 0.1	23.3 ± 0.3
S8	55.9 ± 0.5	0.2 ± 0.1	2.1 ± 0.2	41.8 ± 0.8
S9	68.7 ± 0.8	2.9 ± 0.1	5.6 ± 0.3	22.9 ± 1.2
S10	63.2 ± 0.2	1.0 ± 0.1	3.4 ± 0.1	32.4 ± 0.3
S11	67.8 ± 0.1	2.6 ± 0.1	5.3 ± 0.2	24.2 ± 0.4
S12	57.0 ± 0.4	0.2 ± 0.0	2.1 ± 0.0	40.7 ± 0.4
S13	67.0 ±0.4	2.7 ± 0.0	5.5 ± 0.0	24.9 ± 0.4
S14	63.1 ± 0.0	1.1 ± 0.2	3.0 ± 0.0	32.8 ± 0.1
S15	66.5 ± 0.5	2.3 ± 0.0	5.5 ± 0.0	25.7 ± 0.5
S16	41.7 ± 0.2	0.3 ± 0.0	4.3 ± 0.4	53.7 ± 0.6
BSG (Dried)	47.5 ± 1.6	6.6 ± 0.3	3.7 ± 0.8	42.2 ± 2.7

A graph of the relative elemental make-up per 100 g of BSG in each sample is shown in Figure 5.31.

[2] Errors calculated in from duplicate measurement, standard error formula is detailed in Appendix D.

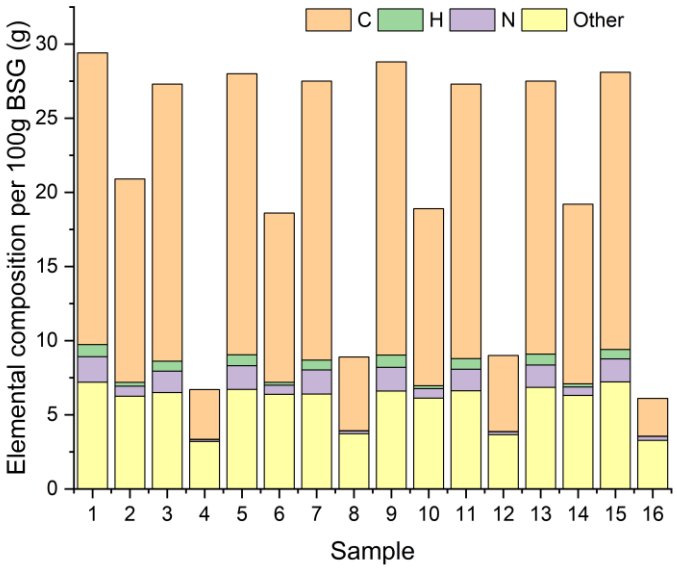

Figure 5.31: CHN elemental components of biochars samples per 100 g of BSG

The results above in Table 5.26 and Figure 5.31 corroborate the pattern shown by the proximate analysis results shown in Table 5.24 and Figure 5.30: the samples can again be categorised into 3 groups, exactly matching those presented within the proximate analyses results.

By taking a 100 g BSG precursor as a basis: Group ***a*** samples contain 18.4-19.8 g carbon, 0.6-0.8 g hydrogen, 1.4-1.7 g nitrogen and 6.4-7.2 g other elements; group ***b*** samples contain 11.4-13.7 g carbon, 0.2-0.3 g hydrogen and 0.6-0.7 g nitrogen and 6.1-6.4 g other elements; and group ***c*** samples are 2.5-5.1 g carbon, 0 g of hydrogen, 0.1-0.3 g nitrogen and 3.2-3.7 g other elements. There is a sharp drop off in the mass of hydrogen making up the materials from group ***a*** and ***b*** to group ***c***. This matches the drop off in volatile content in the proximate analysis and could be further evidence to show that the group ***c*** samples produced at high temperatures and high hold times contain almost no cellulose and hemicellulose derived material in the porous matrix and are made almost entirely of lignin derived material.

All of the samples show a decrease in nitrogen content from the 5.9 g of nitrogen per 100 g of BSG, showing that some or all of the protein content of the precursor material is pyrolyzed during the synthesis process, and removed. The nitrogen content of the biochars may be due to readsorption of nitrogen containing materials back onto the surface, or by

insertion of nitrogen atoms into the structures of the materials. One of the main elements in the 'other' category is likely to be oxygen, given the macromolecular biopolymer makeup of the precursor BSG.

A large difference between the percentage ash from the proximate analysis and percentage other elements in the elemental analysis can give a hint to the oxygen content present in the biopolymers (volatile and fixed carbon fractions) of the materials. The ash percentage and other element percentage of the group ***c*** samples show good agreement, being less than 5% different, while the group ***a*** and ***b*** samples differ by 9-18%. This lends evidence to the fact that group ***c*** samples may have a lower oxygen functionality than the other samples from groups ***a*** and ***b***.

5.1.3 Yield Screening Design of Experiments

Using the yield data as a response variable within the screening process allowed a screening model equation to be obtained through multivariate analysis as part of the design of experiments. The screening model equation is shown in Equation 5.1.

$$\begin{aligned} y = 20.8 - 7.2x_1 - 3.2x_2 - 0.3x_3 - 0.2x_4 - 0.5x_5 - 2.7x_1x_2 - 0.1x_1x_3 - 0.1x_1x_4 - 0.5x_1x_5 \\ +0.3x_2x_3 + 0.2x_2x_4 - 0.2x_2x_5 - 0.1x_3x_4 - 0.2x_4x_5 \end{aligned} \quad (5.1)$$

The coefficients of the equation were used in a Lenth's analysis of the data to determine which factors are of statistical significance to the yield. Using a 95% confidence interval, the critical magnitude of the coefficient for statistical significance was found to be 0.6, meaning that only the coefficients of temperature, hold time, and their interaction, are deemed to be of statistical significance. This is shown graphically on the Pareto plot in Figure 5.32.

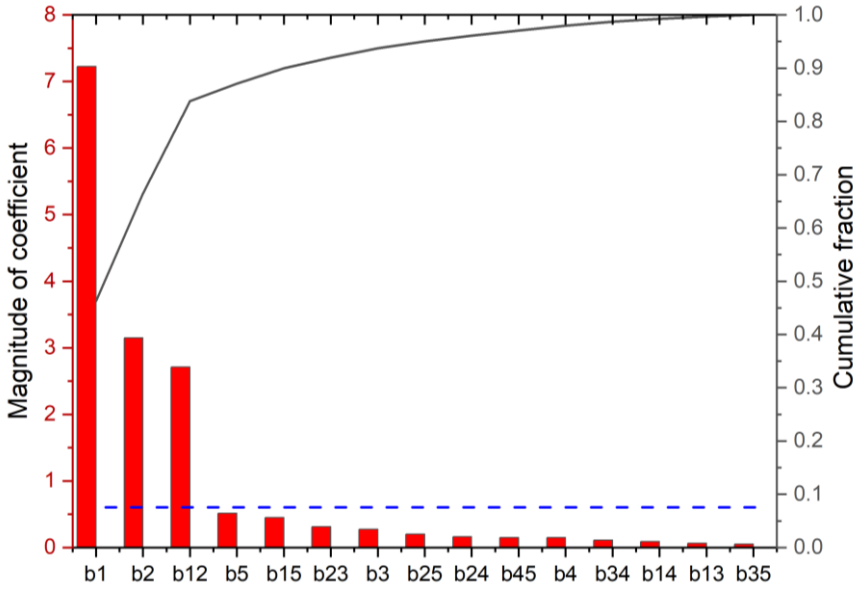

Figure 5.32: Pareto plot for yield data

This corroborates the findings from the TGA and CHN data, showing that hold time and hold temperature are of vital importance to the final composition of the biochars synthesised in this study, and must be considered in any onward optimization design of experiments matrix.

5.2 Nitrogen Adsorption

5.2.1 BET and Isotherm Analysis

Due to low uptakes of nitrogen at 77.4 K and resulting low BET surface areas, it was deemed that the odd samples (those synthesized at 500 °C) were essentially non-porous. This is in line with the fact that the isotherms obtained could be classified as Type II, which is indicative of non-porous materials. In tandem with the thermogravimetric analysis data, this led to the conclusion that a temperature of 500 °C was insufficient to pyrolyse the less volatile material in the material and unlock the porous structures contained therein. These isotherms can be seen in Figure 5.33 and Figure 5.34. The duplicate sample isotherms can be seen in Appendix A.

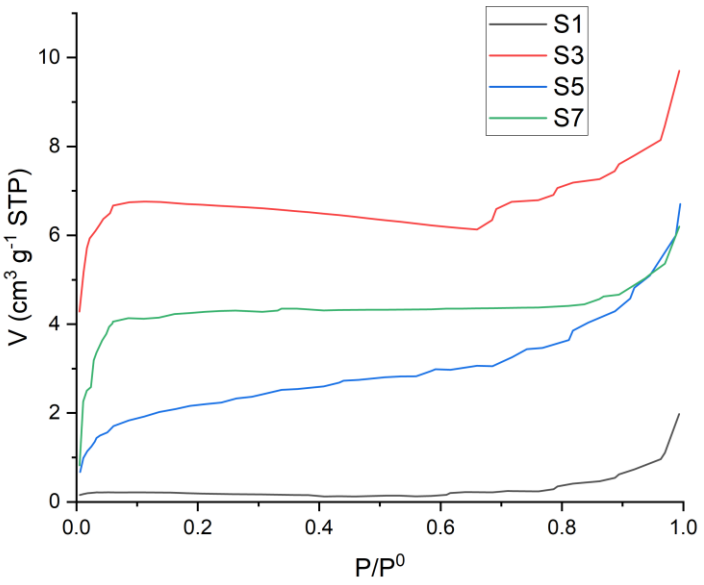

Figure 5.33: Nitrogen adsorption isotherms for biochar produced at 500 °C S1, S3, S5 & S7

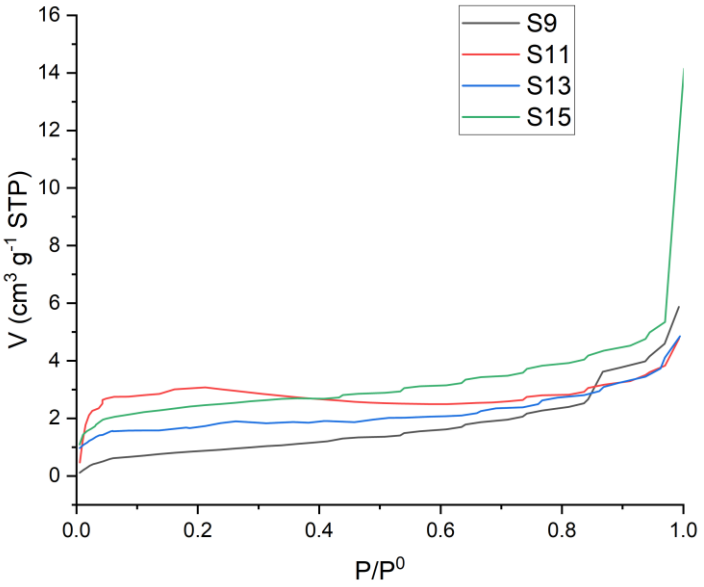

Figure 5.34: Nitrogen adsorption isotherms for biochar produced at 500 °C S9, S11, S13 & S15

Isotherms produced at 900 °C predominantly show IUPAC Brunauer-Deming-Deming-Teller (BDDT) classification Type I(b) isotherms, characterized by their high uptake at low P/P^0,

concave shape facing the P/P^0 axis and plateau, indicating monolayer coverage. Type I(b) isotherms are indicative of materials with large micropores and narrow mesopores (134). They also show Type H4 hysteresis, indicative of the emptying of micropores(155). These isotherms can be seen in Figure 5.35 and Figure 5.36.

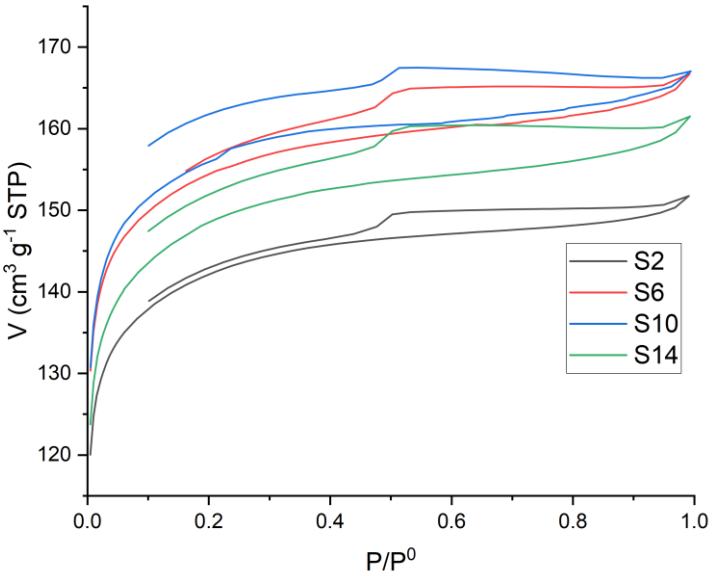

Figure 5.35: Nitrogen adsorption isotherms for biochar produced at 900°C and 0.5 hours

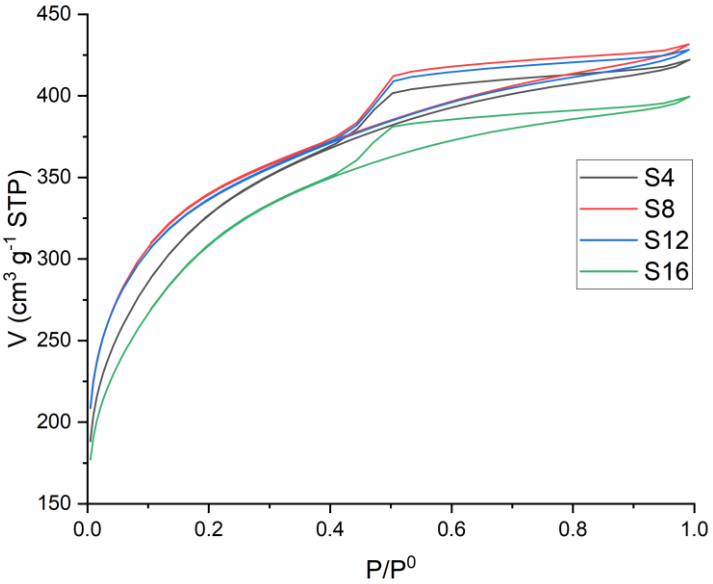

Figure 5.36: Nitrogen adsorption isotherms for biochar produced at 900°C and 2.5 hours

Due to the evidence of microporosity within these biochars, a Rouquerol microporous correction was carried to find the appropriate data range for application of the BET equation to the data obtained for these samples, allowing calculation of a surface area appropriate to the microporous character (156).

A summary of the monolayer capacity, BET constant, surface area, enthalpy of adsorption, IUPAC isotherm classification and hysteresis type for each sample are summarized in Table 5.27.

Table 5.27: BET parameters calculated from nitrogen adsorption isotherms on biochar samples[3]

Sample	*Monolayer capacity (cm^3g^{-1})*	*BET constant*	*BET Surface area (m^2g^{-1})*	*Enthalpy of adsorption($kJmol^{-1}$)*	*IUPAC isotherm classification*	*Hysteresis Type*
S1	3 ± 2	223 ± 88	14 ± 9	8.9 ±0.3	II	-
S2	128 ± 0	2566 ± 20	560 ± 0	10.6 ± 0.0	I(b)	H4
S3	4 ± 2	273 ± 54	15 ± 9	9.1 ± 0.1	II	-
S4	269 ± 0	193 ± 7	1170 ± 1	8.9 ± 0.0	I(b)	H4
S5	1 ± 0	106 ± 14	6 ± 1	8.5 ±0.1	II	-
S6	141 ± 1	2412 ± 17	614 ± 4	10.5 ± 0.0	I(b)	H4
S7	7 ± 2	74 ± 18	33 ± 7	8.3 ±0.2	II	-
S8	283 ± 0	280 ± 7	1234 ± 1	9.2 ± 0.0	I(b)	H4
S9	3 ± 2	45 ± 4	15 ± 8	8.0 ± 0.1	II	-
S10	138 ± 2	2133 ± 19	600 ± 11	10.5 ± 0.0	I(b)	H4
S11	9 ± 3	129 ± 63	37 ± 15	8.5 ± 0.4	II	-
S12	283 ± 2	286 ± 9	1233 ± 7	9.2 ± 0.0	I(b)	H4
S13	6 ± 3	150 ± 12	25 ± 13	8.8 ± 0.1	II	-
S14	133 ± 0	2435 ± 96	579 ± 1	10.6 ± 0.0	I(b)	H4
S15	8 ± 4	168 ± 3	37 ± 20	8.9 ± 0.0	II	-
S16	256 ± 3	173 ± 8	1116 ±12	8.9 ± 0.0	I(b)	H4

In comparison to other activated carbons made from BSG using only physical activation with CO_2, all biochars synthesized at 900 °C, within this study, outperformed those reported in the literature, in terms of surface area, with the highest reported value being 338 m^2g^{-1} (157). Caution is required in a direct comparison, as the quoted value was not obtained through application of a microporous correction to the data, instead the authors calculated their value using a P/P^0 range of 0.05-0.30 for the linearised form, likely leading to a considerable underestimate. Without Rouqerol correction, some of the samples in this

[3] Errors calculated from duplicates, the individual datasets can be seen in Appendix A. The standard error formula can be seen in Appendix D.

work have their surface area underestimated by as much as 130 m^2g^{-1}. While a significant change, it is still unlikely that if corrected the values for surface area in the literature obtained would be of the same magnitude as the samples created in this work. It is therefore possible to state that many of the samples produced in this work outperform those reported in the literature on a surface area basis.

It should be noted that the desorption curve hysteresis in Figure 5.35 for the high temperature and low hold time biochars S2, S6, S10 and S14 do not fully close. This is deemed to be anomalous and thought to be a result of the long equilibration times associated with desorption in highly microporous materials. As a consequence the desorption arm data may not represent the true equilibrium for these samples and some inaccuracies may occur in results derived from this data.

The surface area was used as a response variable in a multivariate analysis, allowing a screening model to be obtained, as shown in Equation 5.2.

$$y = 455.5 + 432.8x_1 + 153.9x_2 - 0.3x_4 - 4.4x_5 + 146.1x_1x_2 - 2.5x_1x_3 - 6.0x_1x_4 \\ -8.9x_1x_5 - 4.4x_2x_3 - 3.4x_2x_4 - 16.0x_2x_5 - 16.0x_3x_4 - 4.1x_3x_5 - 6.4x_4x_5 \quad (5.2)$$

The coefficients were used in a Lenth's analysis to calculate the parameters of significance to the surface area.

Using a 95% confidence interval, the critical value for the magnitude of the coefficients was found to be 16.9, meaning that once again hold temperature, hold time, and their interactions, are the only parameters of statistical significance to the surface area. This is shown graphically in the Pareto plot in Figure 5.37.

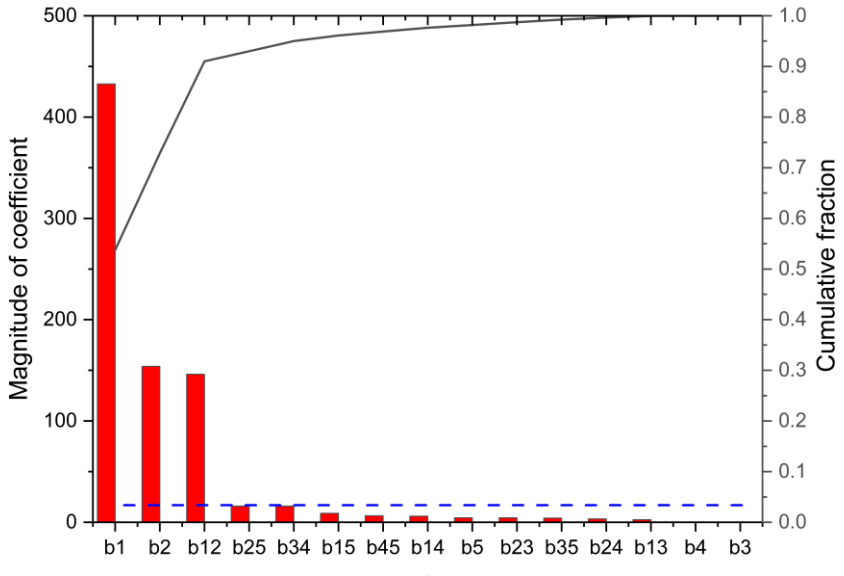

Figure 5.37: Pareto plot for surface area data

5.2.2 Pore Size Characterisation

5.2.2.1 Mesopores

Using the Micromeritics ASAP 2420 software, cumulative pore volumes and their derivatives were found using the BJH method for pore size distribution in the mesopore range. As the BJH method uses desorption isotherm data, only the even numbered samples were analysed using this method. The plot of the pore size distributions can be seen in Figure 5.38.

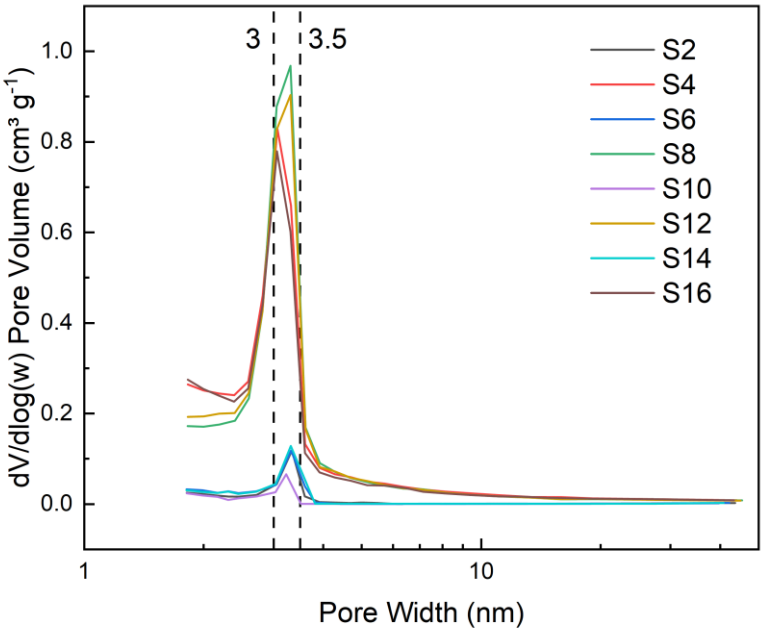

Figure 5.38: BJH plot for porous biochars

The BJH plots all show a good agreement in the pore size distribution, with all samples showing a main peak in pore size at approximately 3 nm.

5.2.2.2 Micropores

The Dubinin-Radushkevich equation was used to further characterize the microporous character of the biochar samples produced within this study. As above, only the even numbered samples were analysed using this method due to the lack of accurate desorption isotherm data for the samples pyrolysed using the lower hold temperature. These plots can be seen in Figure 5.39 and Figure 5.40

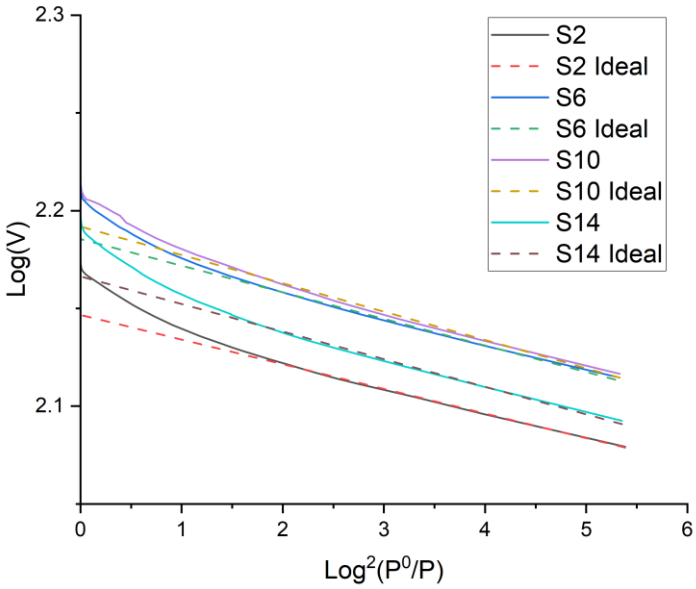

Figure 5.39: Dubinin-Radushkevich plots for porous biochar samples at 900°C and 0.5 hours

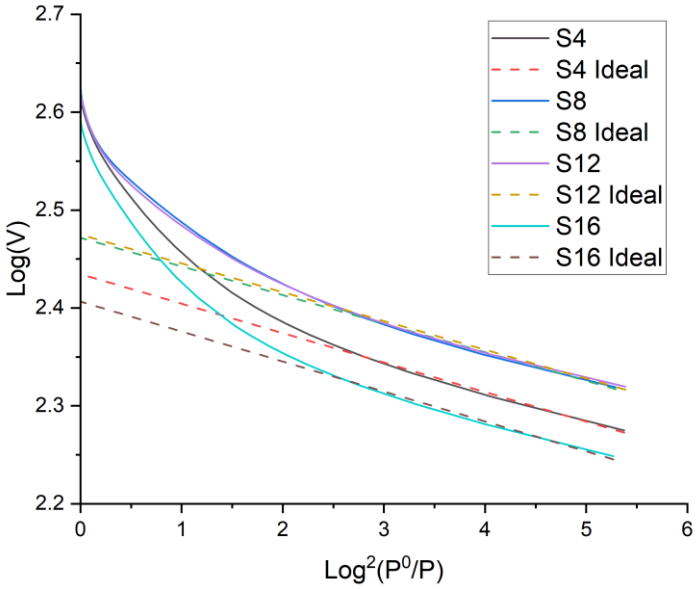

Figure 5.40: Dubinin-Radushkevich plots for porous biochar samples at 900°C and 2.5 hours

The data clearly shows an upwards deviation in the high-pressure region. This suggests that the samples have a larger number of supermicropores (greater than 1.4 nm) than would be expected from a Gaussian pore size distribution of the microporous volume.

The Dubinin-Radushkevich equation was used to calculate the micropore area and percentage of pore volume associated with the micropores. This data is summarized in Table 5.28.

Table 5.28: Dubinin-Radushkevich microporous analysis results for porous biochars[4]

Sample	*Micropore surface area (m^2g^{-1})*	*Percentage pore volume attributed to micropores (%)*
S2	611 ± 1	92.4 ± 0.1
S4	1185 ± 13	64.4 ± 0.7
S6	668 ± 1	91.9 ± 0.1
S8	1290 ± 15	68.6 ± 0.8
S10	677 ± 1	93.1 ± 0.2
S12	1300 ± 15	69.7 ± 0.8
S14	639 ± 1	90.8 ± 0.2
S16	1111 ± 12	63.8 ± 0.7

All the micropore surface areas calculated, and shown above, are either greater than or equal to the total surface areas calculated in Table 5.27. This cannot be correct, as it has been demonstrated that mesoporous structures are present within the samples contributing to the surface area. This error could be due to the extreme levels of supermicroporosity contained within the samples, the significant skewing away from linearity makes it difficult to determine the linear region of the Dubinin Radushkevich plot and determine the intercept with the y-axis for calculation using the Dubinin-Radushkevich equation. As a result of this, the values reported in Table 5.28 for the micropore surface area and percentage pore volumes attributed to micropores may be inaccurate and care is required when using these values.

As discussed above, the desorption arm on the isotherms for samples S2, S6, S10 and S14 does not fully close. This means that the derived values like the micropore surface area and

[4] Errors calculated from regression error on Dubinin-Radushkevich fits

percentage pore volume attributed to micropores should be treated with caution for these samples.

5.2.2.3 Summary

Other reports of biochar produced from BSG activated with CO_2 state the average pore size to be 1.4 nm (157), considering the samples here show the presence of supermicropores (1.4 nm-2 nm) and mesopores with sizes of 3 nm, this seems to give good agreement. It should be noted that Gonçalves et al reported an average pore size of 1.4nm, but also states this was calculated through the BJH method, which is traditionally only used to determine the size of mesopores and macropores greater than 2nm. Therefore, this assertion must be treated with caution. The pore volumes were reported in the literature sample as being 42.6% micropores, 54.2% mesopores and 3.3% macropores, indicating there is a mixture of microporosity and mesoporosity contained within the structure. The percentage pore volume from micropores for samples synthesised in this work range from 90.8-93.1%, for samples produced at short hold times, to 63.8-69.7%, for samples produced at long hold times. These values are much higher than those reported in the literature, but the values calculated here should be treated with caution due to the difficulties in the Dubinin Radushkevich quantitative analysis discussed above.

5.3 Surface Chemistry

5.3.1 Transmission Fourier Transform Infrared Spectroscopy

Analyses of the FTIR spectra obtained for the synthesised samples were performed using the peak identification function in Origin. The samples were categorized as complex molecules, due to the large number of absorbance bands found in the spectra obtained. There was good agreement on the locations of the peaks across all samples, as can be seen in Figure 5.41 and Figure 5.42.

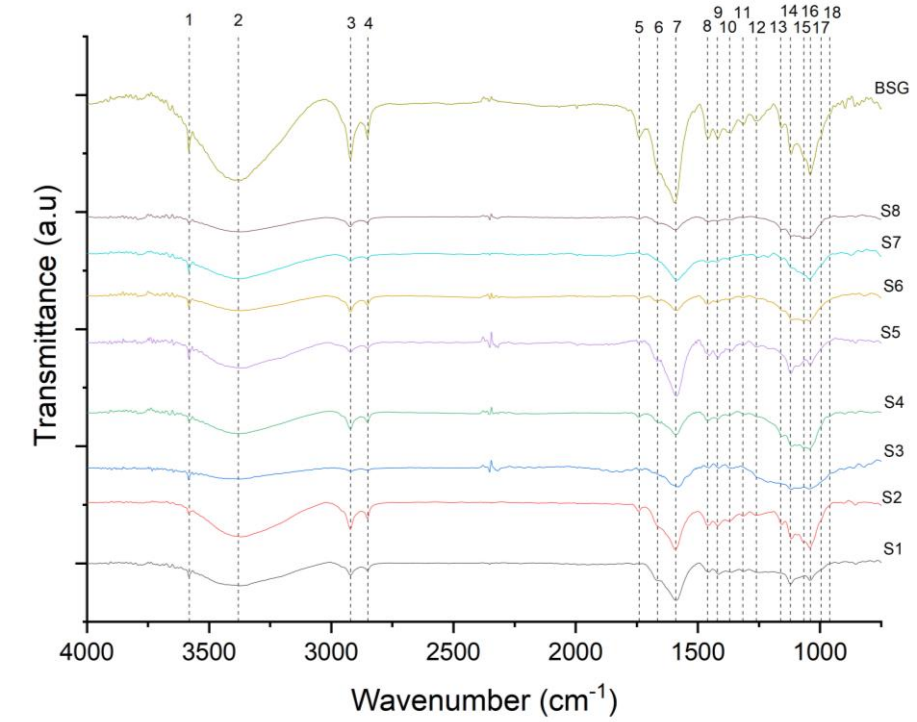

Figure 5.41: FTIR spectra S1-S8 and BSG

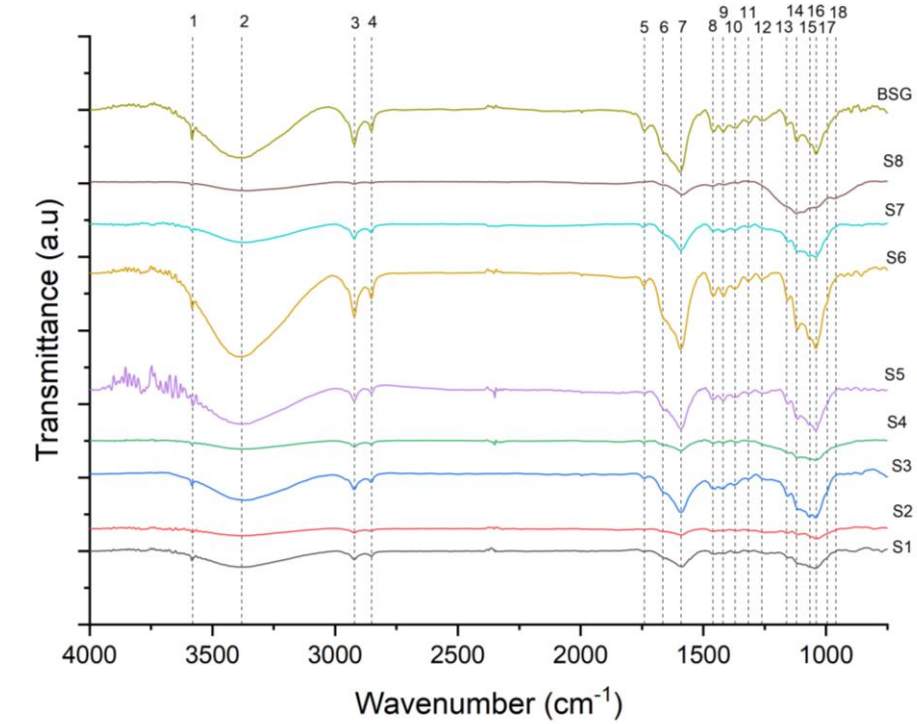

Figure 5.42: FTIR spectra S9-S16 and BSG

Each band identified was assigned to a specific functional group (158), and the peaks were cross referenced with each other, using knowledge of constituents of lignocellulosic biomass to estimate the functional groups present. A table of the absorbance bands and their potential functional group attributions is shown in Table 5.29 and Table 5.30.

Table 5.29: Absorbance bands and potential functional groups

Peak number	*Wavenumber (cm^{-1})*	*Potential functional group*				
1	3580	Tertiary alcohol/phenol OH stretch				
2	3380 (broad)	Hydroxyl group, H-bonded OH stretch				
3	2920	Methylene C-H asymmetric/symmetric stretch				
4	2850	Methylene C-H asymmetric/symmetric stretch	Methoxy methyl ether O-CH_3, CH stretch			
5	1740	Aromatic combination bands (aromatic rings)	Aldehyde	Ester	6-member lactone ring	
6	1665	Alkenyl C=C stretch	Aromatic combination bands (aromatic rings)	Amide		
7	1590	C=C-C aromatic ring stretch	Primary amine NH bend	Secondary amine >NH bend		
8	1460	Methyl C-H asymmetric/ symmetric bend	Methylene C-H bend	C=C-C aromatic ring stretch		
9	1420	Vinyl C-H in-plane bend	Phenol/tertiary alcohol OH bend			
10	1370	Methyl C-H asymmetric/ symmetric bend	Phenol/ tertiary alcohol OH bend	Gem-dimethyl or 'iso'- (doublet)		
11	1315	Primary/secondary/tertiary alcohol or phenol OH bend	Aromatic primary or secondary amine CN stretch			
12	1260	Skeletal C-C vibrations	Primary or secondary alcohol OH stretch	Aromatic ethers aryl-O stretch	Epoxy/ oxirane rings	Aromatic primary amine CN stretch

Table 5.30: Absorbance bands and potential functional groups (continued)

Peak number	*Wavenumber (cm^{-1})*	*Potential functional group*				
13	1160	Skeletal C-C vibrations	Aromatic C-H in-plane bend	Tertiary alcohol C-O stretch	Secondary or tertiary amine CN stretch	Cyanate -OCN stretch
14	1120	Skeletal C-C vibrations	Aromatic C-H in-plane bend	Secondary C-O stretch	Alkyl substituted ether C-O stretch	Cyclic ether
15	1065	Skeletal C-C vibrations	Aromatic C-H in-plane bend	Primary or Secondary C-O stretch	Alkyl substituted ether C-O stretch	Primary amine CN stretch
16	1040	Cyclohexane ring vibrations	Skeletal C-C vibrations	Aromatic C-H in-plane bend	Primary or Secondary alcohol C-O stretch	Primary amine CN stretch
17	995	Cyclohexane ring vibrations	Skeletal C-C vibration	Trans C-H out-of-plane	Aromatic C-H in plane bend	
18	960	Cyclohexane ring vibrations	Skeletal C-C vibrations	Trans C-H out-of-plane bend	Aromatic C-H in plane bend	

Evidence of aromatic rings, and tertiary OH/phenolic groups, was supported by knowledge of lignin (polyphenol) present within the structure. Evidence of amine groups was corroborated by the known presence of high protein contents in BSG (159). Strong evidence exists for OH groups from primary/secondary/tertiary alcohol groups or phenol, all of which are present in cellulose, hemicellulose, and lignin. Skeletal vibrations, and CH bending and stretching, give evidence of long carbon chains. Some evidence of other oxygen containing groups in the form of esters, aldehydes, ether, and epoxy groups can also be seen. The FTIR spectrum obtained for the BSG sample shows good agreement with those reported in the literature (160-162).

Most, if not all, of the peaks observed for BSG were also present in the biochar samples but at much-reduced intensities. Peak 1, at 3580 cm^{-1}, was unchanged, indicating the presence of tertiary/phenol OH groups, likely within lignin, which is still present after pyrolysis. Peak 2, at 3380 cm^{-1}, the broad hydrogen bond peak, is reduced for all samples, perhaps due to the removal of hemicellulose and cellulose whose monomers: glucose, xylose, arabinose, galactose, and mannose (163) all contain OH functional groups. This could also be an indication of the reduction of amine groups from the protein constituents within BSG, which are also responsible for hydrogen bonding. Peaks 3 and 4, at 2920cm^{-1}, and 2850 cm^{-1}, indicative of long chain aliphatic carbon chain C-H symmetric and asymmetric vibrations, are also greatly reduced, likely due to similar reasons outlined above for peak 2. Peaks 5, 6 and 7, at 1740 cm^{-1}, 1665 cm^{-1} and 1590 cm^{-1} respectively, associated with the aromatic ring structures, are also reduced in intensity due to the partial volatilisation of the lignin structures. Intensity reduction was observed for peaks 8-12, at 1460cm^{-1}, 1420cm^{-1}, 1370cm^{-1}, 1315 cm^{-1}, and 1260 cm^{-1} respectively, which are associated with the primary, secondary tertiary, or phenolic OH groups (for reasons similar to those described for Peak 2) as well as secondary amine and oxygen containing groups like ethers and epoxy groups, due to the removal of proteins and cross-linkages between the macromolecules, through pyrolysis. Peaks 13-18, at 1160 cm^{-1}, 1120 cm^{-1}, 1065 cm^{-1}, 1040 cm^{-1}, 995 cm^{-1} and 960 cm^{-1} respectively, are associated with skeletal C-C vibrations and cyclic ring vibrations, and exhibited a reduction in peak intensity due to removal of carbon chains from hemicellulose and cellulose, as well as partial loss of the lignin fraction.

Despite the reductions in peak intensity, the presence of the functional groups is still noted for the biochars, demonstrating a high degree of variety of surface binding sites for

pollutant adsorption. π-π interactions can occur between the carboxyl sites and aromatic ring structures. Amine and hydroxyl groups can act as centres for hydrogen bonding, which is very important for strong physisorption processes. However, as all of these functional groups were found on all of the materials, the transmission FTIR was not able to differentiate between the different samples present. This is a somewhat unexpected result, as there are multiple results showing the variations in, not only composition through FTIR and CHN, but also, behaviour in surface interactions through the nitrogen adsorption isotherms. As transmission FTIR is a measurement of the functional groups present in the bulk, not necessarily on the surface, ATR FTIR was carried out as a follow up to these measurements to try and determine the difference in surface character on the materials synthesised.

5.3.2 Attenuated Total Reflectance Fourier Transform Infrared Spectroscopy

To more accurately determine not only the functional groups within the material, but to determine the functional groups present on the surface of the material, ATR FTIR was carried out using a high refractive index germanium crystal. It was hoped that this would help resolve issues associated with the black colour, and likely highly absorbing nature, of the synthesised biochar samples.

The spectra obtained showed similarities with other samples within the groups **a**, **b** and **c** highlighted in Section 5.1.1. Peaks at approximately 3000-2800 cm^{-1} were ignored and thought to be due to contamination from the acetone solvent used to clean the ATR crystal between runs. The spectra of the group ***a*** samples, produced at low temperature, are shown in Figure 5.43 and Figure 5.44.

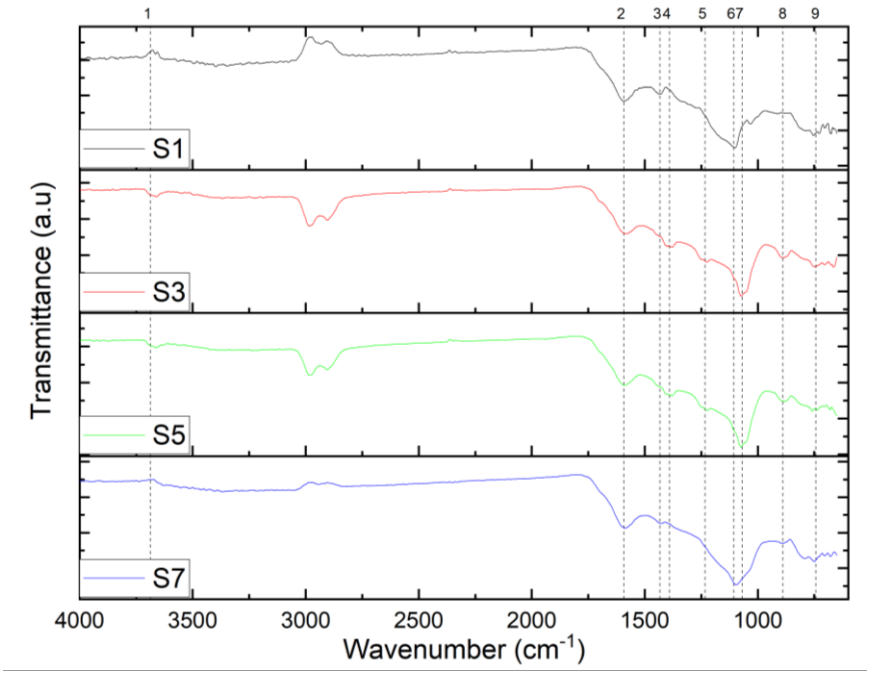

*Figure 5.43: Group **α** ATR FTIR spectra: S1, S3, S5 and S7*

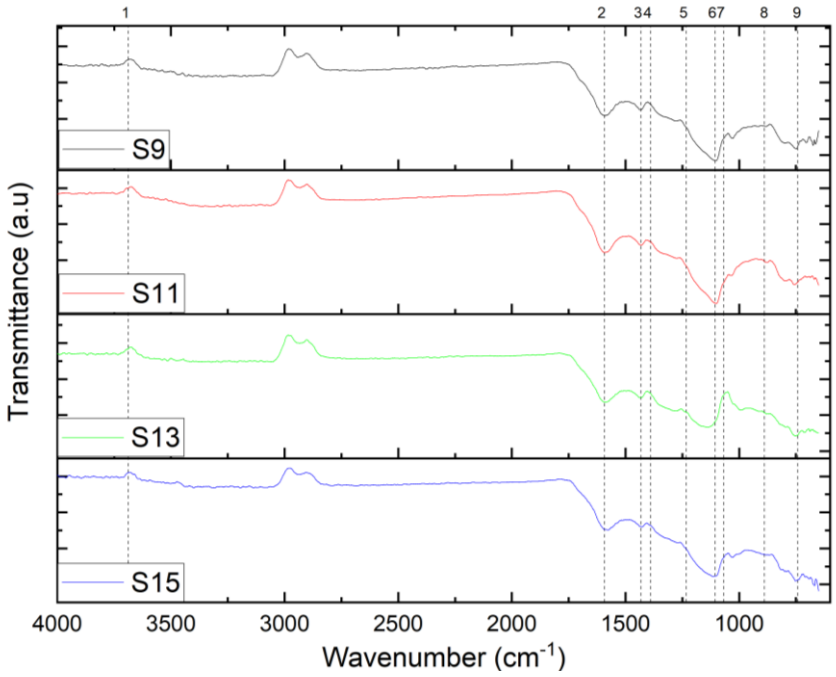

*Figure 5.44: Group **α** ATR FTIR spectra: S9, S11, S13 and S15*

Table 5.31 details the absorbance peaks found and potential functional groups to which they are ascribed.

*Table 5.31: Group **a** ATR FTIR peaks and potential functional groups*

Peak	Wavenumber (cm^{-1})	Potential functional group		
1	3670	Alcohol OH stretch		
2	1592	C=C-C Aromatic ring stretch	Primary amine, NH bend	
3	1432	Methyl C-H asym. /sym. Bend		
4	1390	Phenol or tertiary alcohol, OH bend		
5	1231	Aromatic C-H in-plane bend	Phenol, C-O stretch	Aromatic ethers, aryl -O stretch
6	1106	Aromatic C-H in-plane bend	Secondary alcohol, C-O stretch	Organic siloxane or silicone (Si-O-Si)
7	1069	Aromatic C-H in-plane bend		Organic siloxane or silicone (Si-O-Si)
8	888	Aromatic C-H out-of-plane bend		
9	743	Aromatic C-H out-of-plane bend		

Peaks 2, 3 and 5-9 could be interpreted as coming from the aromatic ring structures present in the material through C=C-C ring stretches or C-H bends. Peak 1 at 3670 cm^{-1}, Peak 4, at 1390 cm^{-1}, peak 5, at 1231 cm^{-1}, and peak 6, at 1106 cm^{-1}, indicate the presence of hydroxyl groups from O-H stretches or C-O stretches. These could be from phenol groups on the lignin derived material, or on the saccharide monomers from the cellulose derived material thought to be present in these samples. Peak 2, at 1592 cm^{-1}, could also be evidence of amine functional groups, from the protein derived material from the BSG precursor.

The spectra of the group ***b*** samples, produced at high temperature and short hold times, are shown in Figure 5.45.

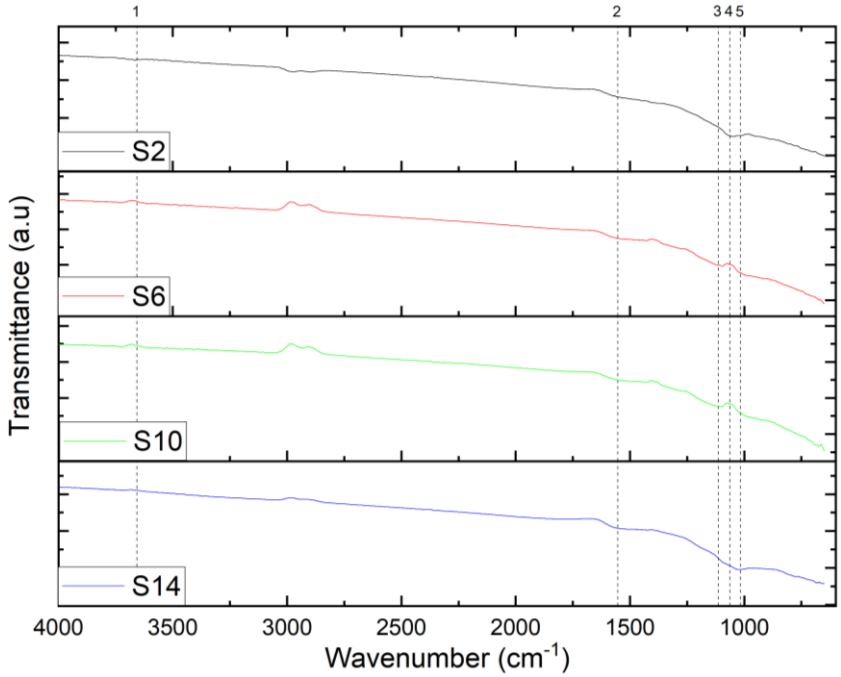

*Figure 5.45: Group **b** ATR FTIR spectra*

Table 5.32 details the absorbance peaks found and potential functional groups to which they are ascribed.

*Table 5.32: Group **b** ATR FTIR peaks and potential functional groups*

Peak	Wavenumber (cm^{-1})	Potential functional group			
1	3657	Alcohol OH stretch			
2	1553	Secondary amine, >N-H bend			
3	1114	Secondary alcohol, C-O stretch			
4	1063	Organic siloxane or silicone (Si-O-Si)	Aromatic C-H in-plane bend	Primary alcohol, C-O stretch	Primary amine, CN stretch
5	1015	Organic siloxane or silicone (Si-O-Si)	Aromatic C-H in-plane bend		Primary amine, CN stretch

Peaks 1, 3 and 4, at 3657 cm^{-1}, 1114 cm^{-1}, and 1063 cm^{-1} respectively, could indicate hydroxyl groups on the surface through O-H bend and C-O alcohol stretches. Peaks 4 and 5, at 1063 cm^{-1} and 1015 cm^{-1}, indicate potential aromatic ring structures. Peak 2, at 1553 cm^{-1}, indicates, which may be corroborated by peaks 4 and 5, the presence of amine stretches. Peaks 4 and 5 may also be indicative of silicon and oxygen complexes on the surface which will be discussed in more detail later.

The spectra of the group ***c*** samples, produced at high temperature and long hold times, are shown in Figure 5.46.

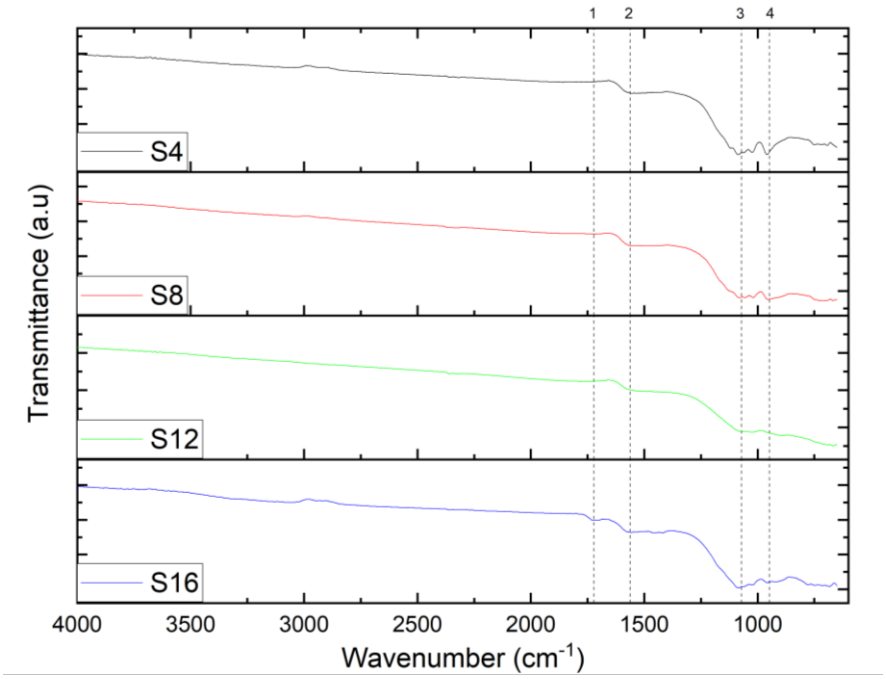

*Figure 5.46: Group **c** ATR FTIR spectra*

Table 5.33 details the absorbance peaks found and potential functional groups to which they are ascribed.

Peak 1, at 1721 cm^{-1}, indicates some form of carbonyl group, either ketone or carboxylic acid present on the surface. Peak 2, at 1562 cm^{-1}, indicates some secondary amine groups present, which could be aromatic in nature. Peak 3, at 1071cm^{-1}, indicates either a secondary or primary alcohol structure on the surface, or the same silicon and oxygen complexes noted in the other ATR FTIR Ge measurements. Peak 4, at 948 cm^{-1}, indicates some of the aromatic character through C-H bends expected within biochar samples.

*Table 5.33: Group **c** ATR FTIR peaks and potential functional groups*

Peak	Wavenumber (cm^{-1})	Potential functional group		
1	1721	Carboxylic acid	Ketone	
2	1562	Secondary amine, >N-H bend		
3	1071	Organic siloxane or silicone (Si-O-Si)	Primary alcohol, C-O stretch	Secondary alcohol, C-O stretch
4	948	Aromatic C-H in-plane bend		

The ATR FTIR Ge measurements successfully pointed towards differences in the surface character, aligning along the same groups noted in the sample composition and nitrogen adsorption isotherm investigations. However, the distortion of the peaks, caused by the nature of the ATR measurements and high absorbance of the samples, made it extremely difficult to fully characterise the samples and to be able to say with certainty which functional groups are present on the surface. Alternative advanced methods are required to determine the exact nature of the surface functional groups present and XPS was chosen for this purpose.

5.3.3 Point of Zero Charge

The point of zero charge (PZC) was determined for each of the 16 biochar samples created in the screening phase and the raw BSG. The results are shown in Table 5.34.

All samples exhibited a consistent PZC of around pH 7.5-8.5, slightly more basic than neutral. This would manifest as a net positive charge on the surface at pH=7 and below, the pH at which liquid phase adsorption experiments are performed, as this closely mimics the pH in wastewater streams. This indicates that the biochars produced will be more effective at removing anions at pH=7 and below and cations at basic pHs, due to the net charge on the surface varying with pH (158). This does not indicate that there are no negative charges on the surface, simply that there is a greater number of positive charges. The basic character, negative charges or proton acceptors of the biochars produced were deemed to originate from the delocalized electrons in the aromatic rings or from the lone pairs of electrons on nitrogen containing and carbonyl functional groups identified from the FTIR

measurements. The acidic character, positive charges or proton donors come from the alcohol and phenol groups acting as weak acids.

Table 5.34: Point of zero charge results

Sample	*PZC (pH)*	*Net charge at pH 7*
S1	7.3	Neutral
S2	8.1	**Positive**
S3	7.5	Neutral
S4	8.0	**Positive**
S5	8.0	**Positive**
S6	7.9	Neutral
S7	7.8	Neutral
S8	8.4	**Positive**
S9	7.4	Neutral
S10	8.2	**Positive**
S11	7.6	Neutral
S12	7.6	Neutral
S13	7.6	Neutral
S14	7.9	Neutral
S15	7.7	Neutral
S16	7.2	Neutral
BSG	4.8	**Negative**

The BSG sample tested showed a much lower PZC than all of the biochars tested at a value of 4.8. This is likely due to the higher proportion of hydroxyl groups from the cellulose and hemicellulose macromolecules present in the BSG sample which are removed during the pyrolysis synthesis of the biochars. At pH=7 this acidic PZC would manifest as a net negative charge, as the hydrogen ions dissociate from the hydroxyl groups in an attempt to lower the pH, following Le Chatilier's principle. This results in the oxygen atoms in the hydroxyl group having another lone pair of electrons and manifests as a negative charge.

The PZC values were compared with other values stated in the literature. Biochars made from BSG at 800-850 °C with 30–45-minute hold times, under steam activation, were reported to have PZCs of pH 10.6-10.7, notably much higher than the values found in this study (164). This is likely due to the noted differences in surface chemistry, occurring as a result of activation with steam rather than CO_2. Other biochars produced from the pyrolysis of walnut shell, pyrolysed at 900 °C for 1 h and chemically activated with potassium carbonate, gave much more acidic PZC at approximately pH=6.1 (165). The discrepancies here are likely due to the chemical activation step, and the reduced protein content in

walnut shell compared to BSG. As indicated above, the carbons produced in this study will likely be effective for adsorption of both anions and cations due to the amphoteric nature of the surface with a PZC close to neutral.

A screening model, obtained using the PZC as a response variable, is shown in Equation 5.3.

$$y = 7.8 + 0.2x_1 + 0.1x_3 - 0.1x_4 - 0.1x_5 - 0.1x_1x_2 - 0.1x_1x_3 - 0.1x_1x_4 \\ -0.1x_2x_4 - 0.1x_3x_4 - 0.1x_3x_5 + 0.1x_4x_5 \quad (5.3)$$

The model coefficients were used in a Lenth's analysis to determine the parameters of statistical significance. With a 95% confidence interval the critical value was found to be 0.29. This is shown graphically in the Pareto plot in Figure 5.47.

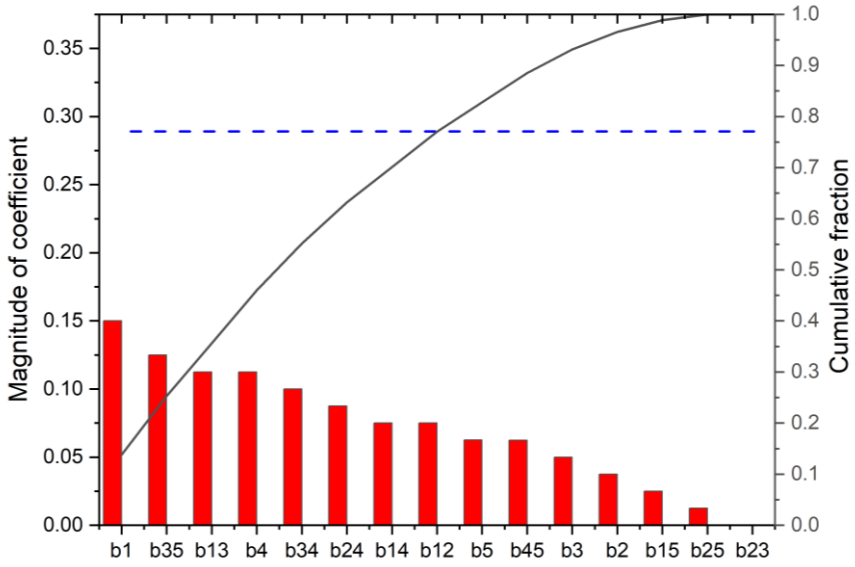

Figure 5.47: Point of zero charge Pareto plot

Since no synthesis parameter met the critical value, it was deemed that none were statistically significant to the value of PZC, which must be dependent on other factors, such as the biomass precursor. In future work, if it is desirable to control PZC, other experimental factors should be included as process variables.

5.4 Acid Washing

5.4.1 Introduction

It was deemed necessary to chemically treat the biochars synthesised in the screening design of experiments due to the lack of statistical significance of the synthesis variables tested on the point of zero charge. This indicated a lack of tailorability of the surface

character, a characteristic imperative to the functionalisation of biochar adsorbents for use in water treatment systems. The high ash content of the biochars was also of concern as, for every char, it was greater than the guideline limit introduced by the Indonesian Standards authority for biochar materials (142). Acid washing has been shown in the literature to be an effective way of both removing ash content (166) and altering the point of zero charge, through protonation of functional groups on the biochar surface (167).

Hold temperature and hold time were found to be statistically significant for the surface area and yield screening design of experiments. This statistical significance manifested as 3 groups first identified in Section 5.1: Group ***a*** synthesised at low temperatures and both long and short hold times; group ***b*** synthesised at high temperatures and short hold times; and group ***c*** synthesised at high temperatures and long hold times. By utilising these groups, time and resources could be saved by choosing 1 sample from each group at random to be washed and compared to their unwashed counterparts. These samples were chosen as S9, S14 and S16: one from each of groups ***a***, ***b*** and ***c*** respectively.

5.4.2 Sample Composition of Washed Samples

5.4.2.1 Yield and Proximate Analysis of Washed Samples

Acid washing of three samples representative of the three categories described in Section 5.1 was carried out. These samples were chosen at random from within the categories. Their yields, after washing, and data obtained from proximate analyses are shown in Table 5.35.

Table 5.35: Acid washed biochar yield and proximate analyses

Sample	*Percentage recovered from washing (%)*	*Yield (% dry BSG basis)*	*Moisture (%)*	*Volatiles (%)*	*Fixed carbon (%)*	*Ash (%)*
S9	-	28.8	1.3	8.8	68.3	12.4
S9W	98.3	28.3	2.9	20.0	67.6	9.5
S14	-	19.2	3.6	7.0	71.8	17.6
S14W	93.3	17.7	13.6	11.9	65.3	9.2
S16	-	6.1	1.2	8.1	36.5	54.2
S16W	63.2	3.9	7.8	20.1	52.4	19.7

A graph of the relative component make-up per 100 g of each of the washed samples, alongside their unwashed counterparts is shown in Figure 5.48.

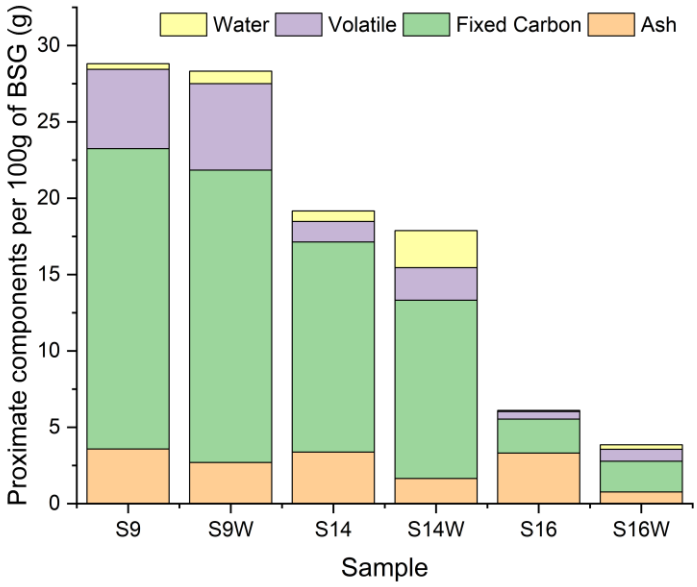

Figure 5.48: Comparison of washed and unwashed proximate analysis data

The acid washing shows removal of ash content from all of the samples, while volatile and fixed carbon components stay relatively constant. The water component of the post-washed samples has increased slightly, this may be due to the increased hydrophilicity of the biochar surfaces due to the washing process. While the ash fraction has been reduced during the washing process, all of the biochar samples have not been brought below the 10% ash content limit, as dictated by the Indonesian standards authority. This indicates their performance as liquid phase adsorbents may not be adequate and further modifications may be required.

5.4.2.2 Elemental Analysis of Washed Samples

CHN elemental analysis was carried out in duplicate for the washed samples. A summary of the results alongside their unwashed counterparts are shown in Table 5.36 below.

Table 5.36: CHN analysis of washed and unwashed biochar samples[5]

Sample	*Carbon (%)*	*Hydrogen (%)*	*Nitrogen (%)*	*Other (%)*
S9	68.7 ± 0.8	2.9 ± 0.1	5.6 ± 0.3	22.9 ± 1.2
S9W	69.5 ± 0.4	2.7 ± 0.0	5.3 ± 0.1	22.5 ± 0.3
S14	63.1 ± 0.0	1.1 ± 0.2	3.0 ± 0.0	32.8 ± 0.1
S14W	76.5 ± 0.1	0.4 ± 0.0	4.0 ± 0.1	19.1 ± 0.0
S16	41.7 ± 0.2	0.3 ± 0.0	4.3 ± 0.4	53.7 ± 0.6
S16W	66.2 ± 0.9	1.0 ± 0.3	4.1 ± 0.3	28.7 ± 1.4

A graph of the elemental make-up per 100 g of BSG in each sample is shown in Figure 5.49.

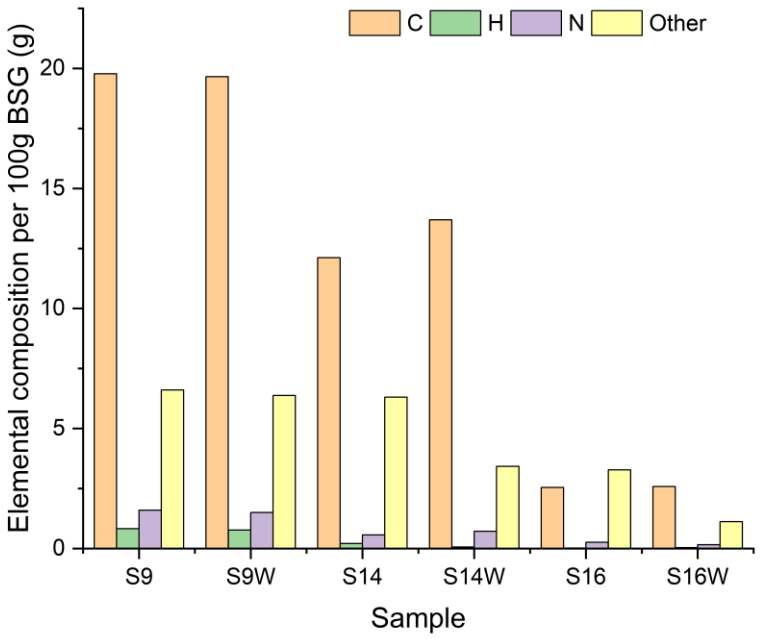

Figure 5.49: CHN elemental analysis of unwashed and washed biochar samples

The group ***a*** samples, S9 and S9W, show very little change in their elemental makeup after the washing process. This is likely due to the non-porous nature of both samples, discussed later in Section 5.4.3, and the inability of the acid washing medium to penetrate into the pores of the porous matrix and protonate the surface functional groups, and remove the ash content. The group ***b*** samples, S14 and S14W, show a large decrease of 45.8% in the other elements such as metal ions, oxygen and other heavier non-metals. This is likely due to the washing process being much more effective in being able to penetrate into the

[5] Errors calculated in from duplicate measurement, standard error formula is detailed in Appendix D

porous matrix of the material, and remove these non-organic materials much easier. The decrease in hydrogen is an unexpected result but could be due to the removal of oxygen containing metal and non-metal oxides, which act as sites for protonation. The mass of carbon seemingly increases, which has no reasonable basis in the chemistry of the system. This may be due to the inherent variability in the precursor material and small batch size of each synthesis. This reason could similarly explain the decrease in hydrogen content. The group ***c*** samples, S16 and S16W, show a relatively constant mass of nitrogen, carbon and hydrogen, but a very large decrease of 65.9% in the other elements similar to the group ***b*** samples. This increase in the proportion of the other elements is likely due to the even greater porous character in the group ***c*** samples compared to the group ***b*** samples allowing for even greater penetration of the washing solvent into the porous matrix to remove the non-organic material such as metal ions and other inorganic substances constituting the samples.

5.4.3 Nitrogen Adsorption Characterisation of Washed Samples

5.4.3.1 Surface Area and Isotherm Analysis

Nitrogen adsorption characterisation was carried out for the washed samples, the results are summarised in Table 5.37.

Table 5.37: Nitrogen adsorption characterisation of acid washed and unwashed biochar samples[6]

Sample	*Monolayer capacity (cm^3g^{-1})*	*BET constant*	*BET Surface area (m^2g^{-1})*	*Enthalpy of adsorption ($kJmol^{-1}$)*	*IUPAC isotherm classification*	*Hysteresis Type*
S9	3 ± 2	45 ± 4	15 ± 8	8.0 ± 0.1	II	-
S9W	1 ± 0	575 ± 99	4 ± 0	9.6 ± 0.1	II	-
S14	133 ± 0	2435 ± 96	579 ± 1	10.6 ± 0.0	I(b)	H4
S14W	143 ± 0	2308 ± 125	622 ± 1	10.5 ± 0.1	I(b)	H4
S16	256 ± 3	173 ± 8	1116 ±12	8.9 ± 0.0	I(b)	H4
S16W	408 ± 3	171 ± 17	1776 ± 12	8.9 ± 0.1	I(b)	H4

The BET surface areas, before and after washing, are shown for comparison in Figure 5.50 below.

[6] Errors calculated from propagation of error in BET isotherm fits, the error propagation equations are detailed in Appendix D

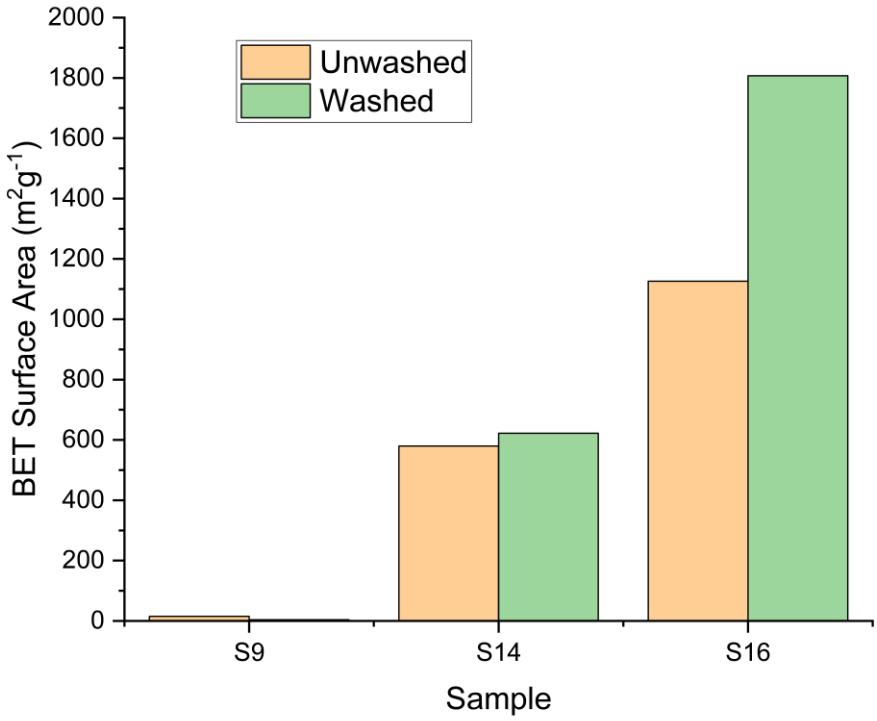

Figure 5.50: Comparison of surface area before and after acid washing

Sample S9 remained non-porous after washing, indicating that the removal of the ash has not affected its porous characteristics. In S14 and S16, both surface areas increased after washing, by 7.4% and 59.1%, respectively. This indicates that the removal of ash has opened blind pores in their network, opening up additional sites for adsorption.

5.4.3.2 Pore Size Characterisation

Mesopores

BJH analysis of the porous washed samples was carried out. The BJH plots can be seen below in Figure 5.51.

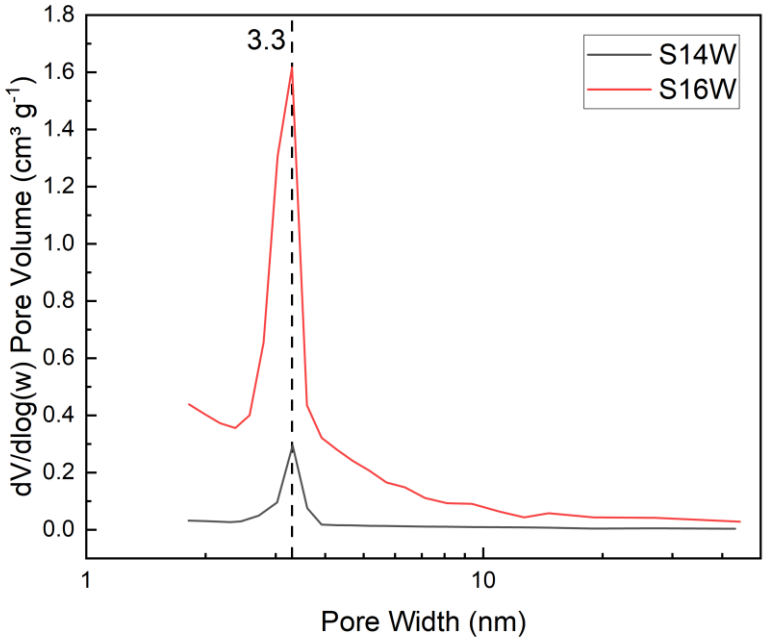

Figure 5.51: BJH plot for porous acid washed samples

These results are consistent with the BJH mesopore sizes found before washing at approximately 3nm, indicating the acid wash has not affected the size of the mesopores in the material.

Micropores

The Dubinin-Radushkevich equation was used to characterize the microporous character of the porous washed biochar samples. The plots can be seen in Figure 5.52.

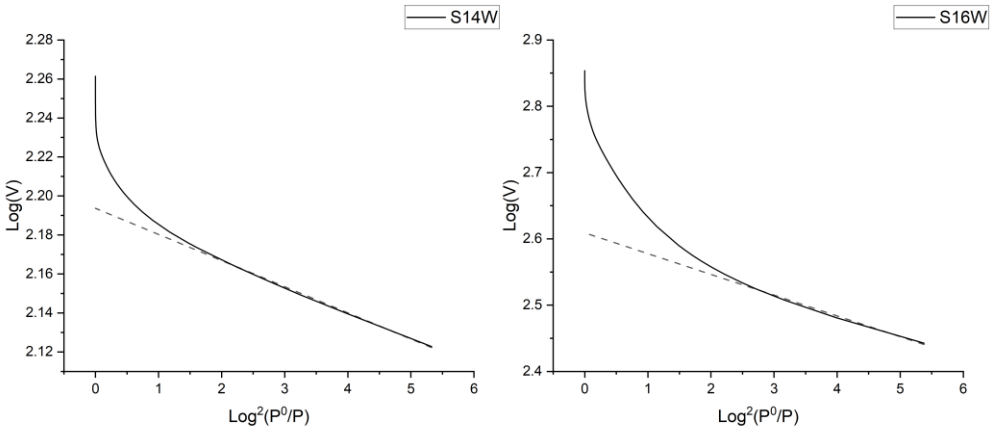

Figure 5.52: Dubinin-Radushkevich plots for washed porous biochar

The data maintains the upwards deviation in the high-pressure region shown in the pre-washed samples. This suggests that the samples retain their supermicroporous character, as before.

The Dubinin-Radushkevich equation was used to calculate the micropore area and percentage of pore volume associated with micropores. This data is summarized in Table 5.38.

Table 5.38: Dubinin-Radushkevich microporous characterisation results for porous acid washed samples[7]

Sample	*Micropore surface area* (m^2g^{-1})	*Percentage pore volume attributed to micropores* (%)
S14	639 ± 1	90.8 ± 0.2
S14W	680 ± 1	85.6 ± 0.1
S16	1111 ± 12	63.8 ± 0.7
S16W	1771 ± 19	56.9 ± 0.6

The micropore surface areas of the porous samples before and after washing are compared in Figure 5.53 below.

Both samples show an increase in microporous surface area, with the micropore surface area of S14 increasing by 6.4%, after washing, and that for S16 increasing by 59.4%, after washing. The percentage of pore volume attributed to micropores of the porous samples, before and after washing, are compared in Figure 5.54 below.

[7] Errors calculated from propagation of error in Dubinin- Radushkevich fits

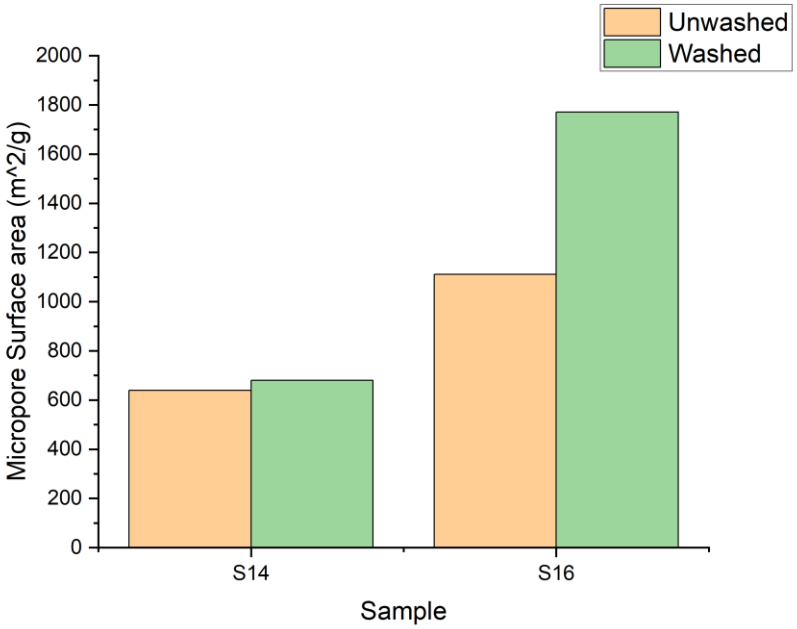

Figure 5.53: Comparison of micropore surface area before and after acid washing

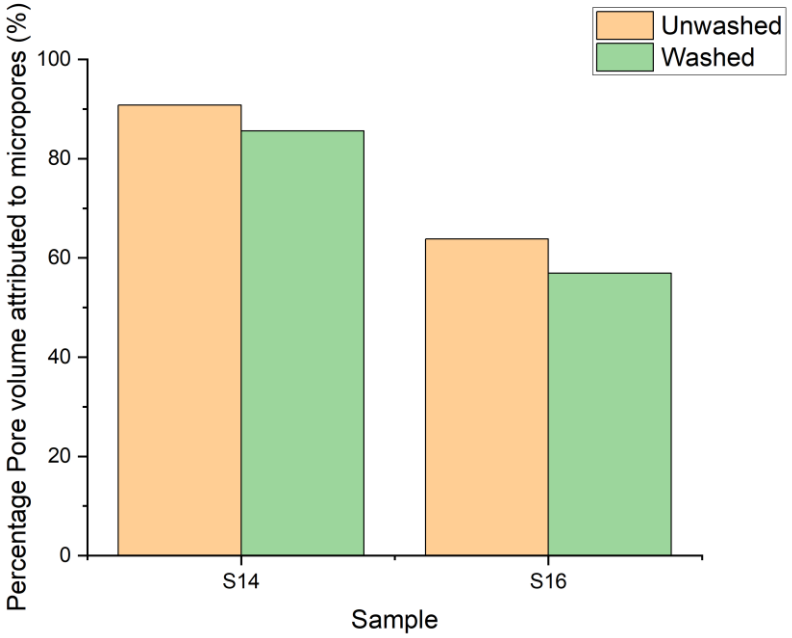

Figure 5.54: Comparison of percentage pore volume attributed to micropores before and after washing

Both samples shown a decrease in the percentage of the volume attributed to micropores, with S14 decreasing by 5.2% and S16 decreasing by 6.9%, after washing. These two facts indicate that the removal of ash and other materials has unblocked both closed micropores and mesopores within the porous structures of the materials.

5.4.4 Surface Characterisation of Washed Samples

5.4.4.1 Point of Zero Charge

The point of zero charge was determined following the same procedure as before for the new washed biochar samples. The results can be seen in Table 5.39.

Table 5.39: PZC of acid washed and unwashed biochar samples

Sample	*PZC (pH)*	*Net charge at pH 7*
S9	7.4	Neutral
S9W	6.5	Neutral
S14	7.9	Neutral
S14W	6.9	Neutral
S16	7.2	Neutral
S16W	5.5	**Negative**

A comparison of the samples before and after washing can be seen in Figure 5.55 below.

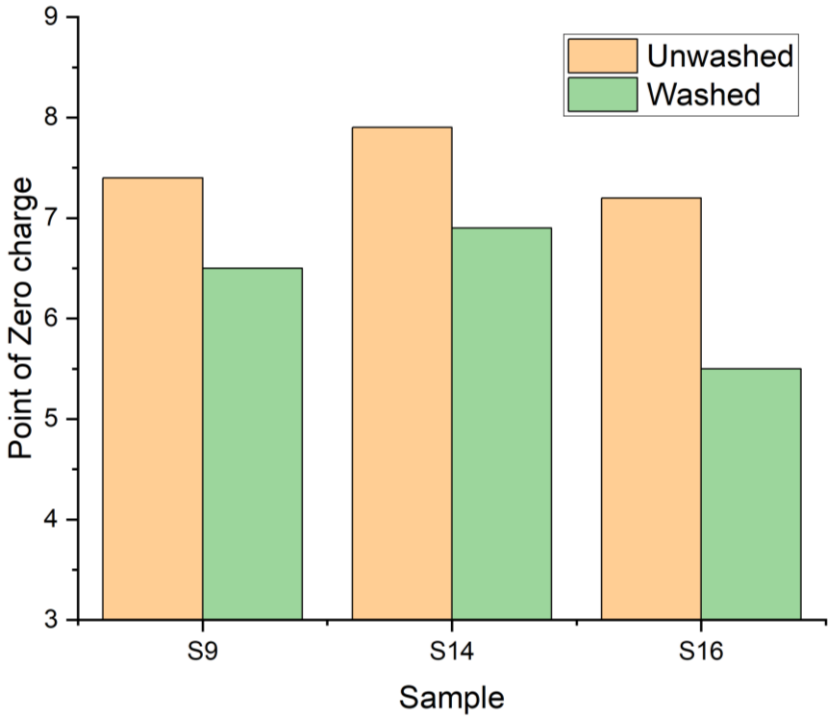

Figure 5.55: Point of zero charge for samples before and after acid washing

The acid wash treatment has been shown to significantly decrease the point of zero charge of each of the biochars tested through protonation of functional groups on the surface. The greatest washed PZC was for sample S14W, with a value of 6.9, but this was still a

significant decrease of 1.0. Next was S9W with a PZC of 6.5, this is thought to be due to its non-porous nature and the fact it still contains some hemicellulose and cellulose macromolecules, which both contain oxygen functional groups in the form of ethers and hydroxyl groups with lone pairs, which can become easily protonated by the acid. The lowest and most significantly altered PZC is that of S16W, the most porous of the three samples tested. The magnitude of this change is thought to be due to the highly porous structure, and large surface area, giving easy access for a vast number of functional groups to become protonated (168). Easier diffusion and transport of the acid solution into the pores of S16W may also have been a contributing factor to the PZC. This is due to the higher proportion of porosity being attributed to mesopores than S14W, as shown in Table 5.38.

The acid washing does show, however, that the surface chemistry can be significantly altered, but chemical activation is required to achieve this. For this reason, it was deemed necessary to use an acid wash in the optimisation design of experiments moving forwards.

5.4.4.2 FTIR Ge characterisation

The FTIR ATR spectra of the group ***α*** samples, S9 and S9W can be seen in Figure 5.56 below.

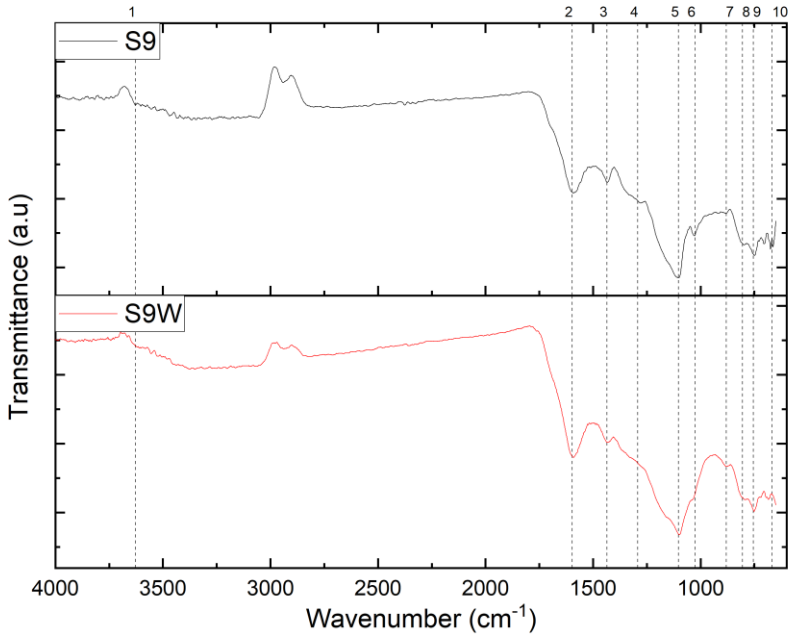

*Figure 5.56: Group **α** FTIR ATR Ge spectra*

The peaks found between 3050 cm^{-1} and 2800 cm^{-1} were discounted from the analysis, due to their presence above the baseline. These peaks were thought to be present due to contamination in the baseline due to the acetone used to clean the ATR crystal in between measurements. Table 5.40 details the absorbance peaks, the samples in which they were found, and the potential functional groups that they represent.

Peak 1, found at 2627 cm^{-1}, is attributed to a secondary alcohol or phenolic OH stretch. Peak 2, found at 1596 cm^{-1}, is attributed to either a secondary amine >N-H bend or in conjunction with peak 3, at 1435 cm^{-1}, attributed to C=C-C aromatic ring stretch. In the fingerprint zone, peaks 4, 5 and 10, found at 1292 cm^{-1}, 1103 cm^{-1} and 667 cm^{-1} respectively, indicate the possible presence of secondary OH alcohol groups, potentially from phenol functionalities. Peak 4 indicates the possible presence of either primary or secondary amines. Peaks 4-10 also could be attributed to the aromatic ring structures of the materials, either from the C-H in and out of plane bending vibrations or the C-C skeletal vibrations. Peaks 4, 6 and 10 were absent from the S9W spectra; this could be as a consequence of the removal of the material which was present and creating these peaks, during the washing process: such as nitrogen containing materials or adsorbed carbonaceous material adsorbed onto the surface of the material from the synthesis process.

*Table 5.40: Group **a** FTIR ATR Ge functional group identification*

Peak	Wavenumber (cm^{-1})	Present in S9	Present in S9W	Potential functional group			
1	3627	Yes	Yes	Nonbonded hydroxy group, OH stretch	Secondary alcohol OH stretch	phenol OH stretch	
2	1596	Yes	Yes	C=C-C aromatic ring stretch	Secondary amine, >N-H bend		
3	1435	Yes	Yes	C=C-C aromatic ring stretch			
4	1292	Yes	No	Primary or secondary, OH in-plane bend	Aromatic primary amine, CN stretch	Aromatic secondary amine, CN stretch	Skeletal C-C vibrations
5	1103	Yes	Yes	Secondary alcohol, C-O stretch	Aromatic C-H in-plane bend	Skeletal C-C vibrations	
6	1026	Yes	No	Aromatic C-H in-plane bend	Skeletal C-C vibrations		
7	881	Yes	Yes	Skeletal C-C vibrations			
8	805	Yes	Yes	Aromatic C-H out-of-plane bend	Skeletal C-C vibrations		
9	755	Yes	Yes	Aromatic C-H out-of-plane bend	Skeletal C-C vibrations		
10	667	Yes	No	Aromatic C-H out-of-plane bend	Alcohol, OH out-of-plane bend	Skeletal C-C vibrations	

The FTIR ATR spectra of the group ***b*** samples, S14 and S14W can be seen in Figure 5.57 below.

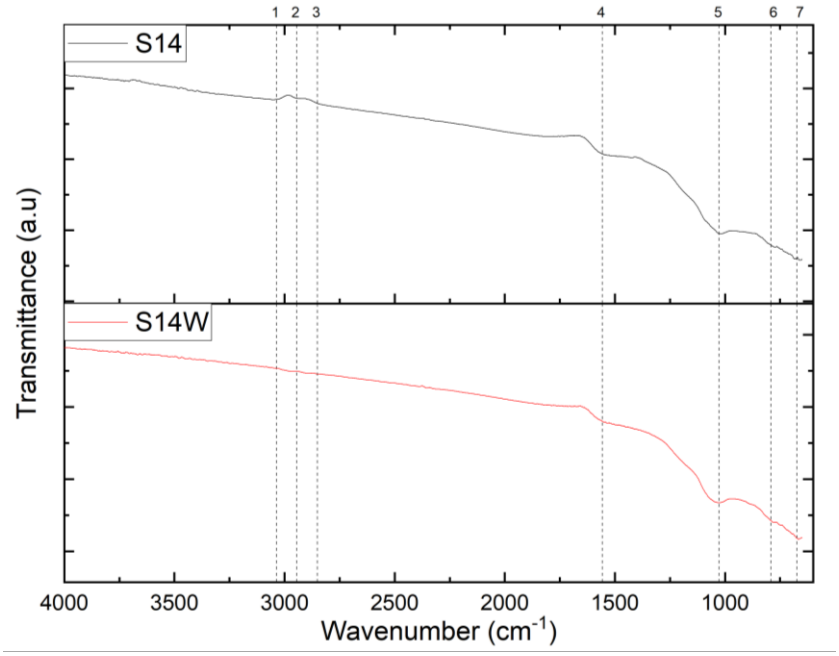

*Figure 5.57: Group **b** FTIR ATR Ge spectra*

The spectra obtained from these samples proved significantly difficult to identify peaks and analyse due to the small deviations from the baseline. This is thought to be an artefact of the ATR measurement technique and the refractive index of the samples tested material. These results should, therefore, be carefully validated with other techniques and conclusions drawn from it treated with caution. Table 5.41 details the absorbance peaks, the samples for which they were found, and the potential functional groups that they represent.

Due to the distortions arising from the similarities between the ATR crystal refractive index and the material, the peaks are significantly warped, and little information can be obtained from both of the spectra obtained. In the single bond zone, from peaks 1-3, at 3036, 2944 and 2851 cm^{-1}, there is evidence of methyl and methylene groups, which could be from the aromatic ring structures in the material. Peak 4, at 1557 cm^{-1}, indicates the presence of secondary amine groups in the material. In the fingerprint region, peaks 5-7, at 1026, 790 and 672 cm^{-1}, could corroborate the aromatic character of the material, representing C-H in and out of plane bends, or skeletal C-C vibrations. Alternatively, peaks 5 and 7 could be

evidence of alcohol groups. Peak 5 could also be representative of siloxane or silicone groups on the surface, which may be a constituent of the ash content of the material.

*Table 5.41: Group **b** FTIR ATR Ge functional group identification*

Peak	Wavenumber (cm^{-1})	Present in S14	Present in S14W	Potential functional group			
1	3036	Yes	Yes	Terminal (vinyl) C-H stretch	Medial, cis- or trans-C-H stretch		
2	2944	Yes	Yes	Methyl C-H asym./sym. Stretch			
3	2851	Yes	Yes	Methylene C-H asym./sym. Stretch			
4	1557	Yes	Yes	Secondary amine, >N-H bend			
5	1026	Yes	Yes	Skeletal C-C vibrations	Primary alcohol, C-O stretch	Organic siloxane or silicone (Si-O-Si)	Aromatic C-H in-plane bend
6	790	Yes	Yes	Skeletal C-C vibrations	Aromatic C-H out-of-plane bend		
7	672	Yes	Yes	Skeletal C-C vibrations	Alcohol, OH out-of-plane bend	Aromatic C-H out-of-plane bend	

The FTIR ATR spectra of the group **c** samples, S16 and S16W can be seen in Figure 5.58 below.

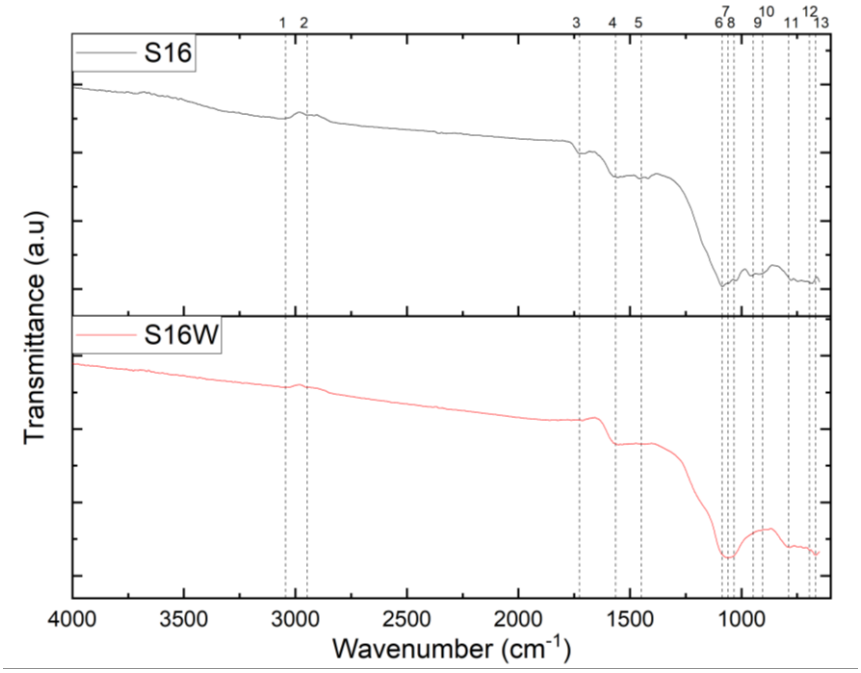

*Figure 5.58: Group **c** FTIR ATR Ge spectra*

Similar to the group **b** samples, there was difficulty in identifying peaks due to the suspected ATR refractive index issue. The results here should also be cross validated, and treated with scepticism at present. Table 5.42 details the absorbance peaks, the samples for which they were found, and the potential functional groups that they represent.

*Table 5.42: Group **c** FTIR ATR Ge functional group identification*

Peak	Wavenumber (cm^{-1})	Present in S16	Present in S16W	Potential functional group			
1	3044	Yes	Yes	Aromatic rings			
2	2947	Yes	Yes	Methyl C-H asym. /sym. Stretch			
3	1726	Yes	Yes	carbonyl, ketones aldehydes esters or carboxyl			
4	1563	Yes	Yes	Secondary amine >N-H bend			
5	1449	Yes	No	Methyl asym. /sym. bend	methylene C-H bend	C=C-C Aromatic ring stretch	
6	1087	Yes	No	Primary or secondary alcohol C-O stretch	Organic siloxane or silicone (Si-O-Si)	Skeletal C-C vibrations	
7	1059	No	Yes	Primary alcohol stretch	primary amine C-N stretch	Organic siloxane or silicone (Si-O-Si)	Skeletal C-C vibrations
8	1032	Yes	No	Organic siloxane or silicone (Si-O-Si)	Primary or secondary alcohol C-O stretch	Skeletal C-C vibrations	
9	947	Yes	No	Aromatic C-H in-plane bend	Skeletal C-C vibrations		
10	906	Yes	No	Aromatic C-H out-of-plane bend			
11	788	No	Yes	Aromatic C-H out-of-plane bend	Skeletal C-C vibrations		

12	695	Yes	No	Alcohol, OH out-of-plane bend	Aromatic C-H out-of-plane bend		
13	667	No	Yes	Alcohol, OH out-of-plane bend	Aromatic C-H out-of-plane bend		

Peaks 1 and 2, at wavenumber of 3044 and 2947 cm^{-1} respectively, give evidence of aromatic rings. Peak 3, at 1726 cm^{-1}, gives evidence to the presence of carbonyl, ketones, aldehyde, esters or carboxyl groups, containing a C=O stretch. Peak 4, at 1564 cm^{-1}, indicates the presence of secondary amine groups. For the unwashed sample (S16), peaks 5, 6, 8, 9, 10 and 12 give further evidence of aromatic ring structures through methyl group bends, and C-C or C=C stretches. Peaks 6, 8 and 12 could be evidence of primary or secondary alcohol stretches. Similar to the group ***b*** samples, there is also evidence of siloxane or silicone Si-O-Si groups present from peak 8, at 1032 cm^{-1}. For the washed sample (S16W), peaks 7, 11, 12 and 13 all corroborate the existence of aromatic ring structures, through C-H bends and skeletal vibrations. Peaks 7 and 13 show evidence of alcoholic OH groups present. Peak 7, at 1059 cm^{-1}, could also indicate the existence of amines, or the aforementioned siloxane or silicone Si-O-Si groups.

The FTIR ATR Ge data shows evidence for aromatic rings, and a variety of oxygen and nitrogen surface functional groups. The distinct functionality of these groups will be investigated through XPS measurements, presented in Section 5.4.4.3. There is also evidence of silicon and oxygen complexes on the surface, which will be investigated later through EDS studies.

5.4.4.3 X-ray Photoelectron Spectroscopy

As discussed earlier, more advanced characterisation methods were required to identify surface functional groups in this study. X-ray photoelectron spectroscopy (XPS) was identified as a good measurement to this end due to it's shallow penetration depth and the measurement technique compatibility with the black coloured organic samples.

The relative atomic concentrations of each functional group found of the surface of each of the prewash and post-wash materials, as well as raw BSG, are shown in Table 5.43. An example of the three XPS scans curves with deconvoluted peaks for sample S9W Point 1 and fitting data can be seen in Appendix F.

The raw BSG biomass showed global heterogeneity across the 3 points investigated. Points 1 and 2 showed good agreement with 43-48% C=C, 28-29% C-O and 0-1% C=O. These points indicate an area of cellulose or hemicellulose in the macromolecular matrix, with C-O being highly prevalent in the saccharide pyran rings found in those structures. Point 3 indicates a lignin structure within the materials, with both C=C and C-C bonds from aromatic rings. The N1s scan shows good agreement across all 3 points, with 3-4% pyrrolic rings and 2-3% from quaternary nitrogen functional groups. These pyrrolic nitrogen functional groups indicate a high proportion of 5 atom rings with a nitrogen in the structure, it can be seen later in the analysis of the biochar samples below that these structures completely disappear after pyrolysis. The O1s scans show a high proportion of OI oxygen functional groups, such as ketones or quinone groups, at relative concentrations of 12-16% on the BSG surface, as well as a significant proportion (0-6%) of OIII functional groups, such as carboxylic groups or physisorbed water.

Table 5.43: XPS atomic functional group percentages for washed and unwashed biochar samples

Binding energy (eV)		284.6	285.5	286.5	288	290.4	398.2	399.5	400.8	402.8	532.4	533.2	535.5
Functional Group		C=C	C-C	C-O	C=O	O-C=O	N6	N5	N-Q	N-X	O-I	O-II	O-III
Sample	Point	Relative atomic concentration (%)											
BSG	1	48	0	28	1	0	0	3	3	0	16	0	0
	2	43	0	29	0	0	0	4	2	0	15	0	6
	3	24	45	0	10	0	0	4	3	0	12	0	2
S9	1	48	0	20	0	0	4	0	12	3	9	4	0
	2	42	11	7	10	0	4	0	10	2	0	13	0
	3	47	0	23	0	0	3	0	13	0	4	11	0
S9W	1	33	27	0	13	0	5	0	11	3	3	7	0
	2	50	0	8	13	0	4	0	12	2	3	9	0
	3	33	23	15	0	0	4	0	13	0	3	9	0
S14	1	33	28	0	19	0	4	0	6	1	9	0	0
	2	33	28	0	17	0	3	0	6	3	8	2	0
	3	37	25	0	14	0	2	0	5	6	6	4	1
S14W	1	28	28	0	18	0	2	0	14	0	2	6	1
	2	30	28	0	16	0	3	0	10	4	1	8	0
	3	31	27	0	19	0	3	0	9	3	2	6	0
S16	1	19	20	0	19	0	4	0	18	0	20	0	0
	2	18	21	0	20	0	0	0	19	2	0	20	0
	3	18	20	0	19	0	4	0	18	0	21	0	0
S16W	1	26	26	0	21	0	2	0	8	2	2	12	2
	2	27	25	0	23	0	2	0	11	3	2	6	1
	3	28	22	0	18	0	2	0	11	3	3	13	1

The group ***a*** sample, produced at low hold time and low temperature (S9), shows large global heterogeneity across each point investigated on the surface. Points 1 and 3 show close agreement, with C=C and C-O dominating the carbon character and both ketone or quinone and esters or phenol groups on the surface. Point 2 shows a more heterogenous carbons character showing C=C, C-C, C-O and C=O but only ester or phenol groups in the O1s scan. The N1s scan is consistent across the 3 points, showing pyridinic N substituted graphitic rings, quaternary nitrogen and some pyridine-N-oxide groups in the cases of points 1 and 2. Points 1 and 3 are likely from cellulose or hemicellulose derived regions in the macromolecular structure of the material, known to be present from TGA derivative analysis of the low temperature, low hold time samples. This is due to the higher prevalence of C-O and C=C stretches present in the saccharide monomers containing pyran rings with unsaturated C=C bonds and C-O stretches, alongside C-O stretches from hydroxyl groups on the saccharide structures. After washing, S9W still shows global heterogeneity in its character, each of the 3 points having a different permutation of C=C, C-C, C-O and C=O. The nitrogen character is very consistent with the unwashed sample. The oxygen character shows more consistency between samples, and a greater value of OII groups than OI. This could be due to protonation of lone pairs of electrons on quinone or ketone groups into hydroxyl groups, like phenols, during to the acid washing process.

The group ***b*** samples, produced at low hold time but high temperature, show much greater global homogeneity across the 3 spots investigated. It shows 33-35% of surface functional groups from C=C, 25-28% from C-C and 14-19% from C=O in the C1s scan. This is more consistent with the C1s expected from a purely lignin derived material, with fewer pyran rings and almost all C=C and C-C from aromatic rings. The N1s scan shows good consistency with pyridine, quaternary and pyridine-N-oxide groups found. The oxygen structure is the most varied of the three scans done, due to the knowledge of the largely ringed structures it is thought OI groups will manifest as quinone, OII groups will manifest as phenol groups and OIII will present as carboxylic acid or water. Point 1 shows only quinone groups. Point 2 shows mostly quinone groups with some phenol. Point 3 shows almost equal numbers of quinone and phenol groups, and also some presence of carboxylic acid or water on the surface. After washing, the carbon character remains largely unchanged, showing good global homogeneity, and good agreement with the unwashed sample, with 28-31% C=C, 27-29% C-C and 16-19% C=O. The relative proportion of C=C has decreased slightly, this could be due to protonation of unsaturated polyphenol ring structures. The nitrogen character

shows good agreement in the pyridinic and pyridine-N-oxide groups but a vast increase in quaternary nitrogen. This increase in quaternary groups may be due to the addition of hydrogen ions onto the lone pair of electrons located on the nitrogen of the pyridinic groups to form quaternary groups through the washing with acidic solvent. The oxygen character shows much better global homogeneity, it shows a decrease in OI groups, like quinones, from 6-9% in the unwashed (S14) to 1-2% in the washed (S14W). To contrast this, the OII groups increased from 2-4% in the unwashed sample to 6-8% in the washed sample. There was still some evidence of carboxylic acid or water on the surface, in point 1 of S14. This shift from OI groups to OII groups is evidence of the protonation of unsaturated C=O in quinone groups to C-OH in phenol groups.

The group ***c*** sample, produced at high temperature and long hold times, shows good global homogeneity across all 3 points. It exhibited 18-19% C=C, 20-21% C-C and 19-20% C=O. This is a total relative decrease in carbon functional groups, coming from mostly the C=C and C-C function groups, as compared to the group ***b*** sample analysed above. This is an expected result and fits with what was discovered through TGA, that only the lignin fraction of the macromolecular matrix is being removed during the extra hold time. The N1s scan shows consistent quaternary nitrogen groups across all 3 samples. Samples 1 and 3 shows pyridinic nitrogen functional groups, while sample 2 shows pyridine-N-oxide groups: the oxidised form of the N6 pyridine group. This is a vast increase in quaternary nitrogen groups, as compared to the group ***b*** sample, perhaps due to greater N substitution in the polyphenol ring structures at the higher temperatures or from greater pyrolysis uncovering these surfaces from within the macromolecular matrix of the BSG. The O1s scan shows only one type of functional group at each point. Points 1 and 3, which also displayed the less oxidised form of the pyridinic nitrogen, indicated quinone groups in the O1s scan. Point 2, which displays greater amount of pyridine-N-oxide, showed phenolic groups on the surface. After washing, sample S16W shows a much higher proportion of functional groups attributed to carbon, more in line with S14W than with S16. It had 26-28% due to C=C, 22-26% due to C-C and 18-23% due to C=O. The nitrogen is much more globally homogenous across the 3 points than for the unwashed sample, 2% due to pyridinic groups, 7-9% due to quaternary and 2-3% due to pyridine-N-oxide. The total number of nitrogen groups, after the washing process, has decreased from an average of 22% to an average of 15%, across the 3 points. The relative share of the oxidised pyridine-N-oxide form is greater than that of the unwashed sample, while the pyridinic and quaternary share is lower than that of the

washed samples, perhaps indicating the quaternary groups are removed during the washing process. The O1s scan shows a greater variety of oxygen functional groups than that of the unwashed samples with OI, OII and OIII functional groups found at all 3 points in a generally homogenous manner. Quinone groups were found at relative concentration of 2%, phenol groups found at 6-13% and carboxylic acid and water found at 1-2%.

Generally, for the porous samples, the C1s scan shows global homogeneity, with C=C and C-C in an almost 1:1 ratio as would be expected from polyphenolic aromatic ring structures as those found in lignin derived materials. No C-O stretches are found in the porous samples, due to the complete removal of pyran rings attributed to cellulose and hemicellulose from the structures at high pyrolysis temperatures. S16 showed a lower proportion of aromatic carbon functional groups, as compared to the other porous samples. This, however, increased after washing, reaching similar levels to S14 and S14W, perhaps due to the high ash content of the sample.

The N1s scans in the porous samples showed a relative increase in concentrations of nitrogen functional groups after washing in the group ***b*** samples, but a relative decrease in nitrogen functional groups in the group ***c*** samples. The nitrogen functional groups could occur as a consequence of insertion of nitrogen atoms in the ring structures at the high temperatures of the ramping phase of the pyrolysis synthesis. Upon closer inspection, the pyridinic nitrogen and pyridine-N-oxide relative concentration remains relatively constant. It is only the quaternary nitrogen that varies across the 4 samples: increasing after washing for S14 but decreasing after washing for S16. In the case of the group ***b*** sample (S14W), this increase in surface nitrogen character compared to S14 after washing is due to hydrolysis of the sample during the washing process, exposing further the nitrogen groups in the porous matrix due to inherent protein content in the BSG. It is likely that the greater porosity of the group ***c*** sample (S16) follows this logic, with the greater hold time allowing for more of the porous matrix to be exposed to the surface, revealing more nitrogen containing functional groups. However, after washing, S16W loses much of this nitrogen character due to hydrolysis of the surface, and the nitrogen rich protein macromolecule derived content and nitrogen substituted surface polyphenol structures being lost in the filtrate of the wash process. Additional repeat measurements would be required to test this hypothesis.

The O1s scan in the porous samples showed that the group ***b*** sample had a relatively constant relative oxygen concentration before and after washing but the group ***c*** sample

had an overall decrease in the relative concentrations of oxygen functional groups on the surface after washing. But more interestingly, the general trend is for the oxygen functional groups to become protonated after washing due to the acid environment, with OI type oxygen groups decreasing and OII type oxygen functional groups increasing. This agrees with PZC experiments discussed in Section 5.4.4.1. After washing, the surface also became more hydrophilic, with indications of water being found on all washed samples in significant proportions. Hydrophilicity is imperative to biochar function in water remediation systems to enhance pore diffusion.

5.4.4.4 Scanning Electron Microscope Imaging

SEM images of samples from all three groups, before and after washing, were obtained. Two different, and distinct, morphologies were found for all the samples investigated and are shown below. The SEM SED images for the group ***α*** samples, S9 and S9W, are shown in Figure 5.59 and Figure 5.60, respectively.

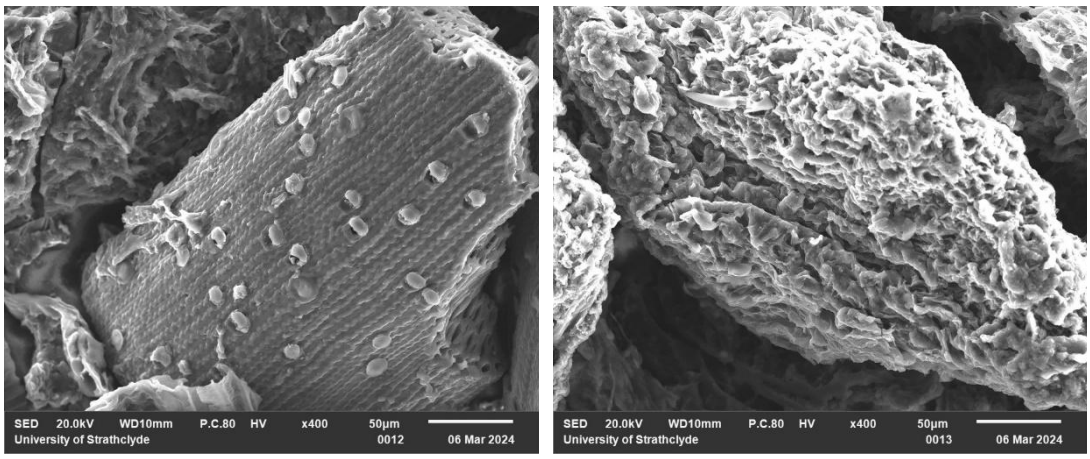

Figure 5.59: S9 SEM SED images, glassy beads (left) amorphous (right)

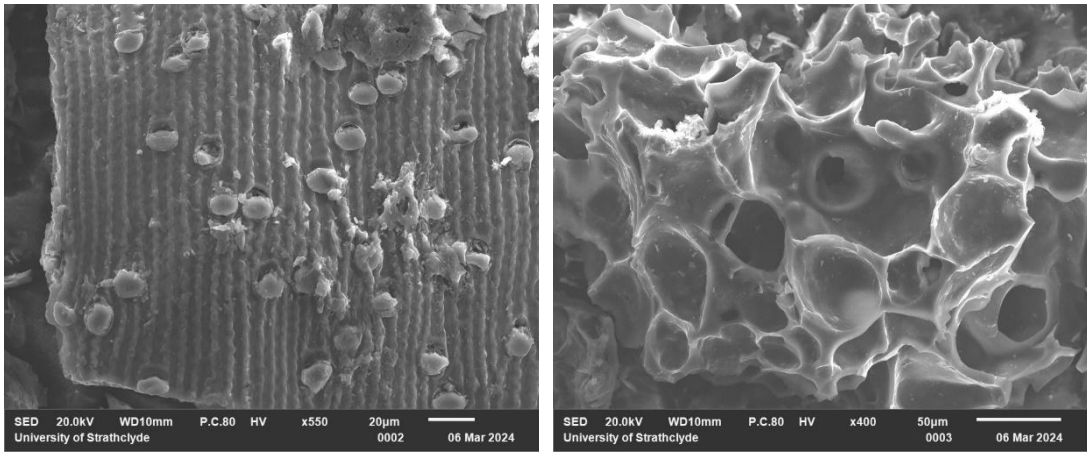

Figure 5.60: S9W SEM SED images, glassy beads (left), amorphous (right)

The amorphous images of both S9 and S9W show large channels penetrating into the bulk of the material. These channels are very large and indicate the gasification of material previously occupying these voids, which were created in the pyrolysis process. The glassy bead images on the left of Figure 5.59 and Figure 5.60 show the outer wall of a fibre of BSG with what looks like small glassy beads on the surface. The surface behind these beads also seems to be much more well-structured and regular than the amorphous regions previously observed.

The SEM images for the group ***b*** samples, S14 and S14W, are shown in Figure 5.61 and Figure 5.62, respectively.

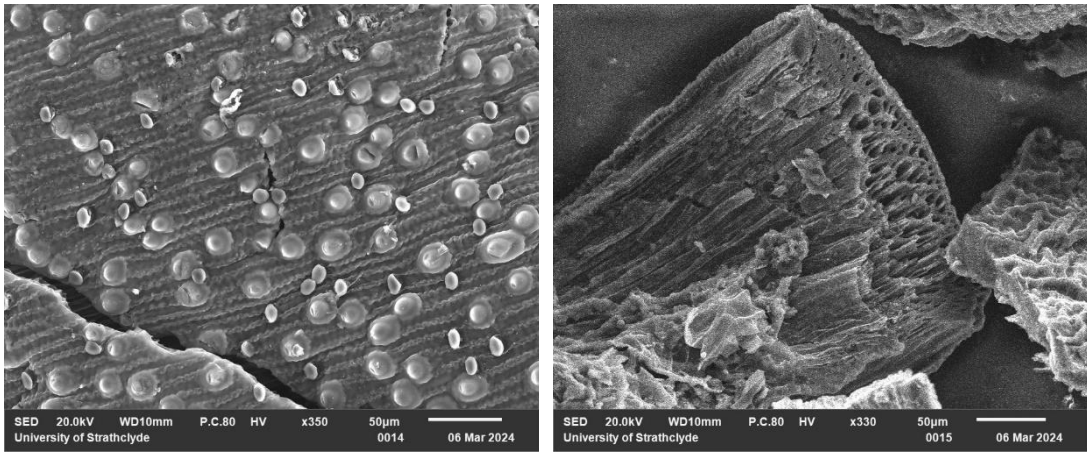

Figure 5.61: S14 SEM SED images, glassy beads (left), honeycomb structure (right)

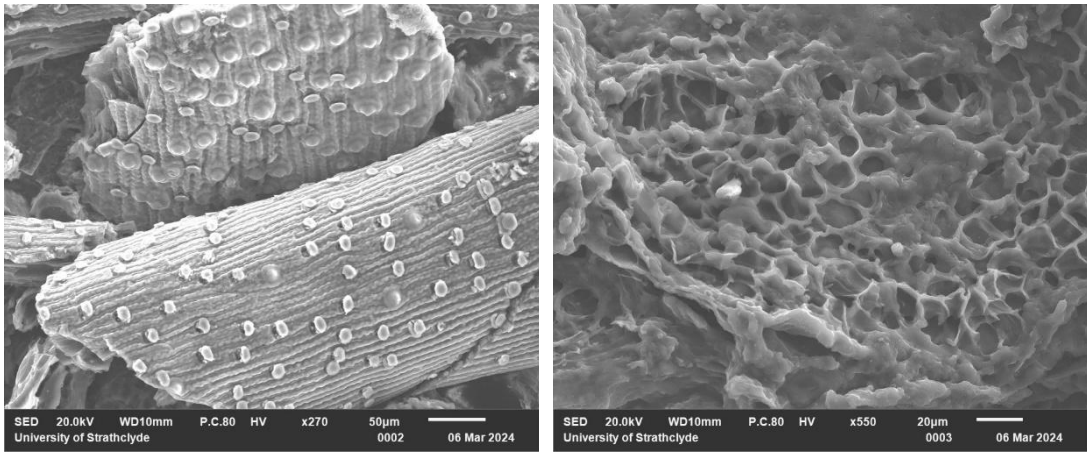

Figure 5.62: S14W SEM SED images, glassy beads (left), amorphous (right)

The above figures demonstrate the honeycomb structure of S14 and amorphous region of S14W, both showing regions with channels accessing deeper into the structures of the biochar materials. While these channels are many orders of magnitude larger than the

micro and mesopores found during the nitrogen adsorption experiments, these large channels are indicative of a hierarchical pore structure penetrating deep into the bulk of the materials. The glassy beads once again appear in both S14 and S14W, however, seem to be much denser in their concentration on the surfaces of the materials.

The SEM images for the group ***c*** samples, S16 and S16W, are shown in Figure 5.63 and Figure 5.64, respectively.

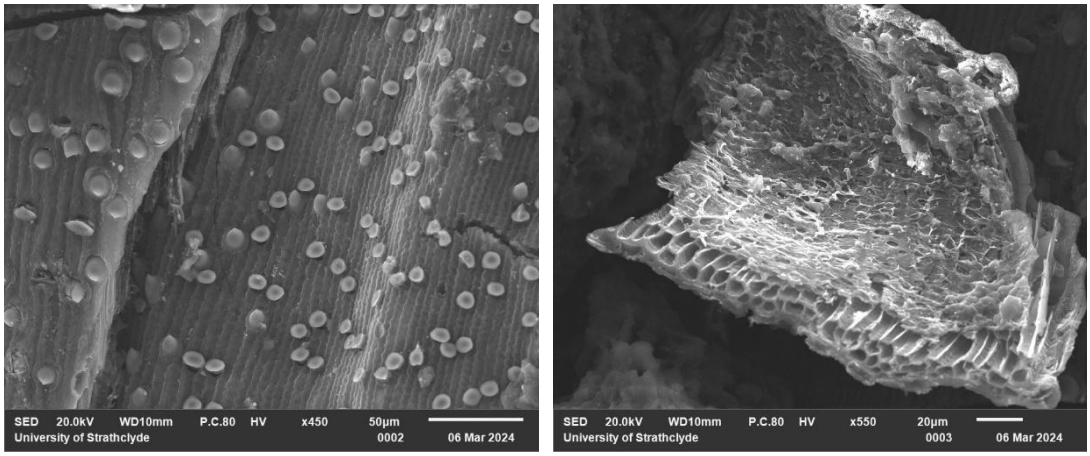

Figure 5.63: S16 SEM SED images, glassy beads (left) honeycomb structure (right)

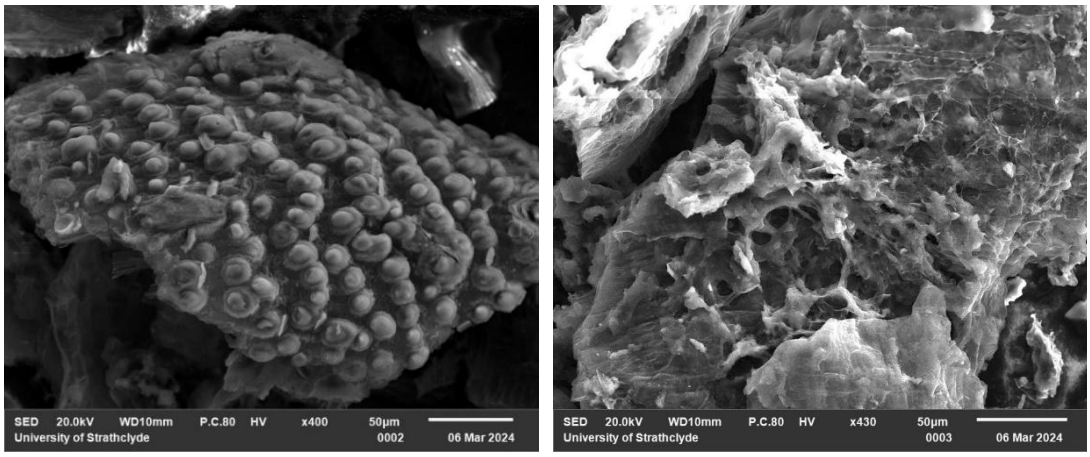

Figure 5.64: S16W SEM SED images, glassy beads (left), amorphous (right)

The S16 and S16W samples show very similar morphologies to those of the group ***b*** samples, the amorphous and honeycomb structures showing similar indicators of a hierarchical porous structure. The honeycomb structure seen in the S16 sample shows much more regular channel sizes than that of the honeycomb structure in S14. This may be due to the more easily pyrolyzed walls being completely removed during the additional pyrolysis time, making the macroporous structure much more uniform in nature. The glassy

beads, once again, are present in both S16 and S16W, this time in their densest iteration yet, with the entire surface of the particle in the S16W image covered in glassy beads. The nature of these glassy beads was investigated through EDS mapping and analysis, in Section 5.4.4.5 and later in Section 7.3.6.

It appears that the concentration of glassy beads increases as pyrolysis nears completion (longer hold time, higher temperature). The porous carbons in groups ***b*** and ***c*** both show macroporous character, some with amorphous regions and some with highly ordered honeycomb-like structures.

5.4.4.5 Energy Dispersive Spectroscopy

Energy dispersive spectroscopy was employed to determine the mass percentage of the elements present on the surface of the materials. Both of the different site types observed in the SEM imaging were investigated. The mass percentage surface compositions of the group ***a*** samples, S9 and S9W, as determined by EDS, are shown in Table 5.44

*Table 5.44: Mass % EDS results for Group **a** samples*

Element	S9 glassy beads (%mass)	S9 amorphous (%mass)	S9W glassy beads (%mass)	S9W amorphous (%mass)
C	72.23	72.12	71.40	77.28
O	19.94	21.25	21.76	19.59
Mg	0.45	0.93	0.22	0.47
Si	5.11	0.45	5.94	0.12
P	1.44	3.43	0.31	1.35
S	-	-	-	0.08
Cl	-	-	0.10	0.07
K	-	0.17	0.08	0.21
Ca	0.82	1.64	0.18	0.82
Ash[8]	7.82	6.62	6.83	3.12
Non-Si ash[9]	2.71	6.17	0.89	3.00

The major difference between the glassy bead sites and the amorphous sites are the elements comprising the ash fraction. In the images where glassy beads were noted, the 3rd most prevalent element was silicon, while in the amorphous regions the 3rd most prevalent element was phosphorus. The ash fraction of the glassy bead regions is predominantly silicon, while the ash content of the amorphous regions is principally other elements, such

[8] Ash is defined as all elements that are not carbon or oxygen
[9] Non-Si Ash is defined as all elements that are not carbon, oxygen or silicon

as magnesium, phosphorus and calcium. During washing, the ash content of the materials decreases, with the majority of this decrease coming from loss of non-silicon ash elements. The EDS maps were investigated to determine the nature of the distribution of the elements on the surface of the samples. The EDS maps for the group ***a*** samples are shown in Figure 5.65, Figure 5.66, Figure 5.67 and Figure 5.68.

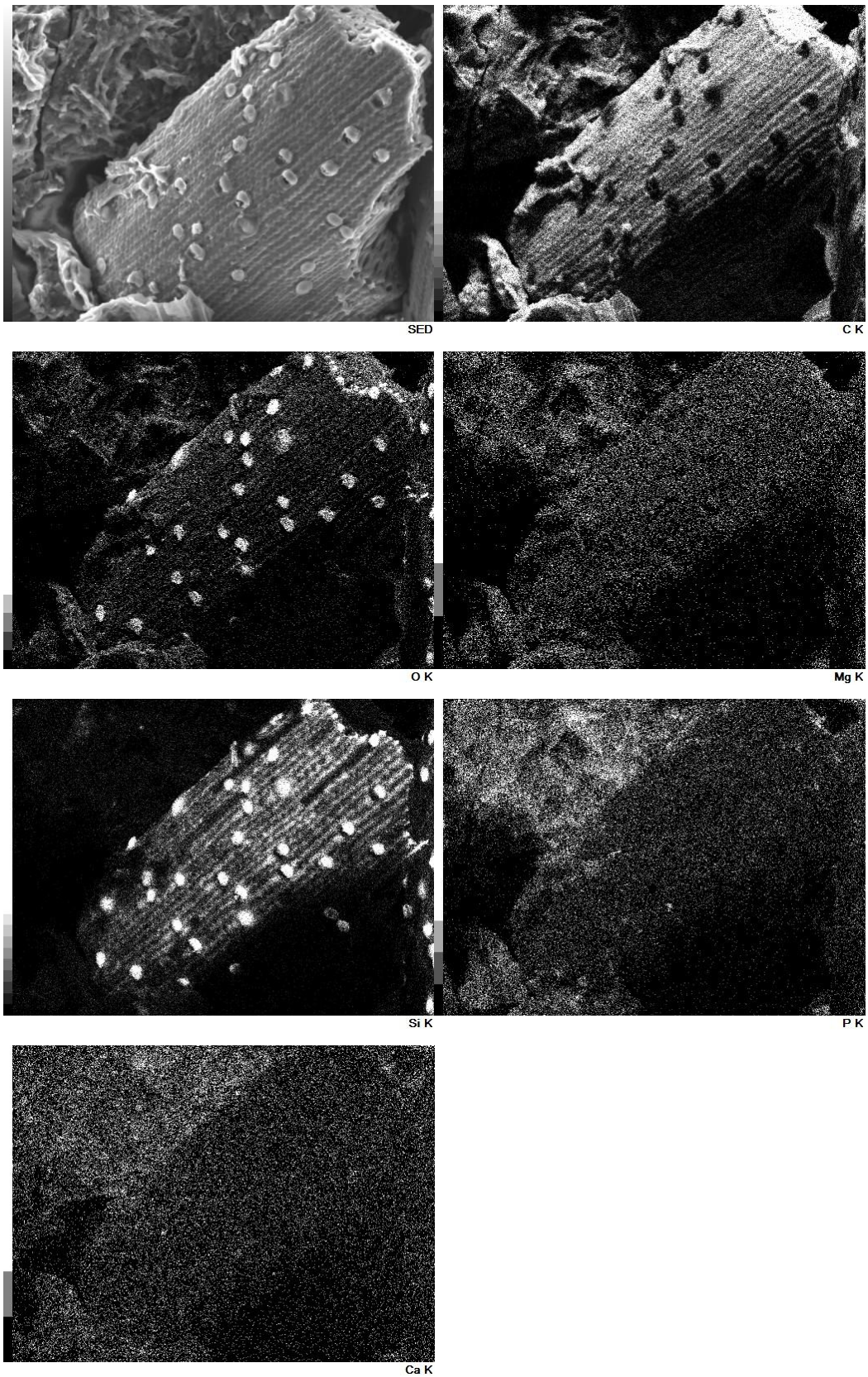

Figure 5.65: EDS elemental mapping of S9 glassy beads

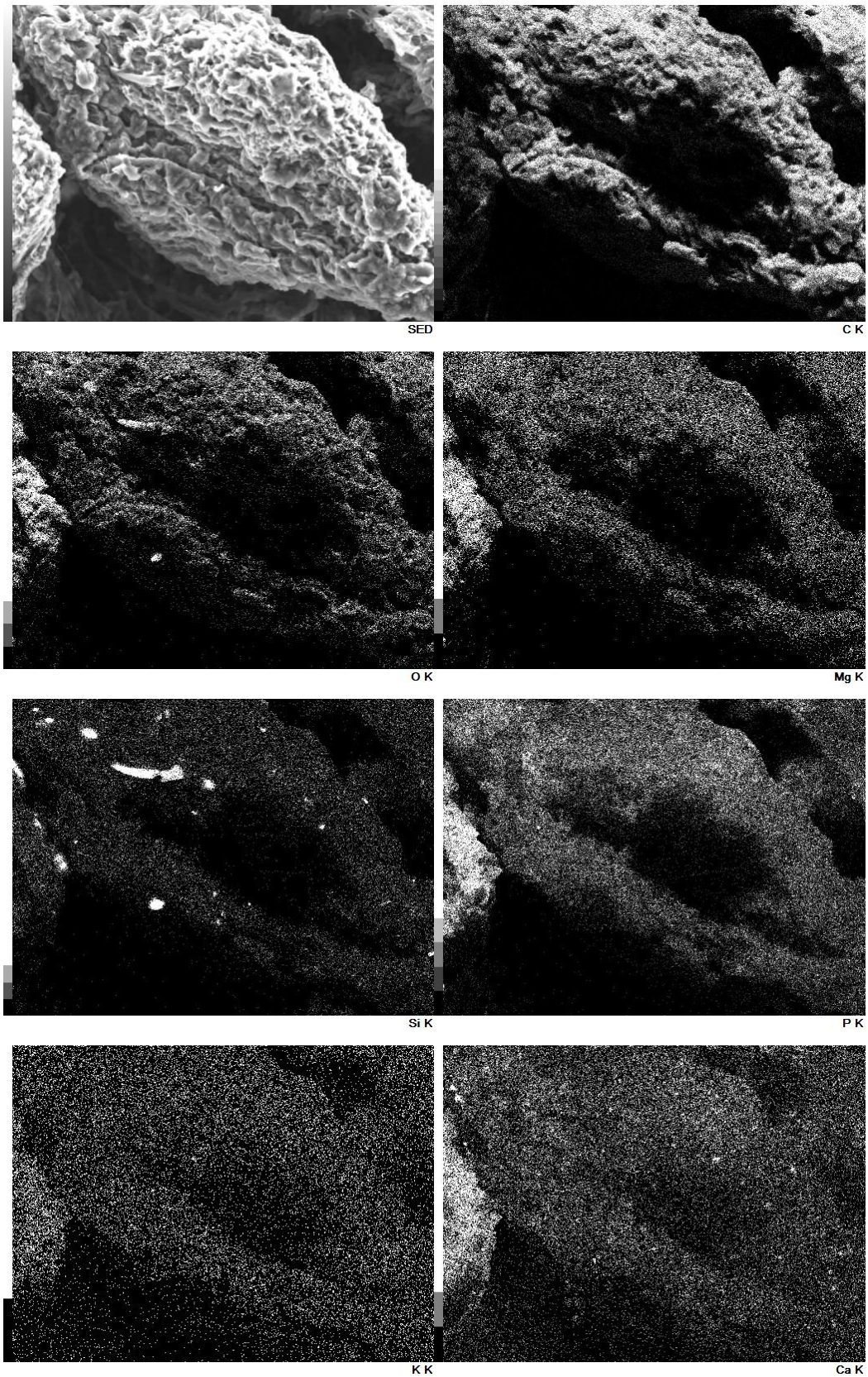

Figure 5.66: EDS elemental mapping of S9 amorphous

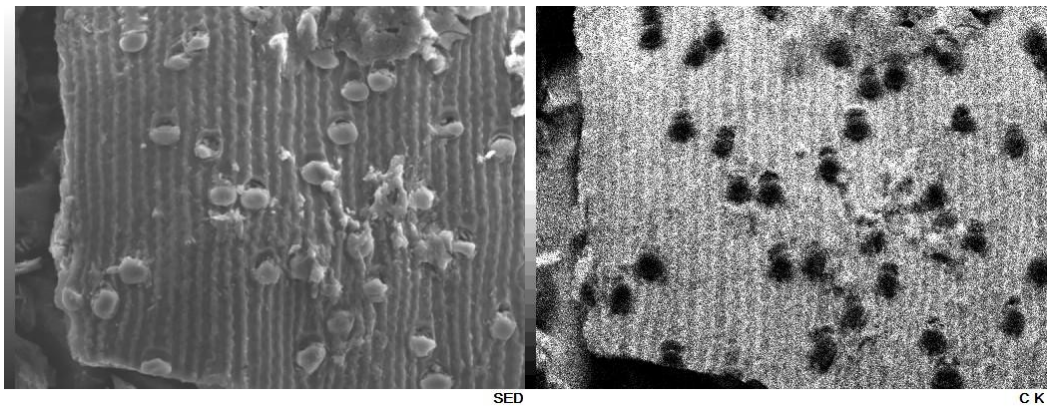
SED
C K

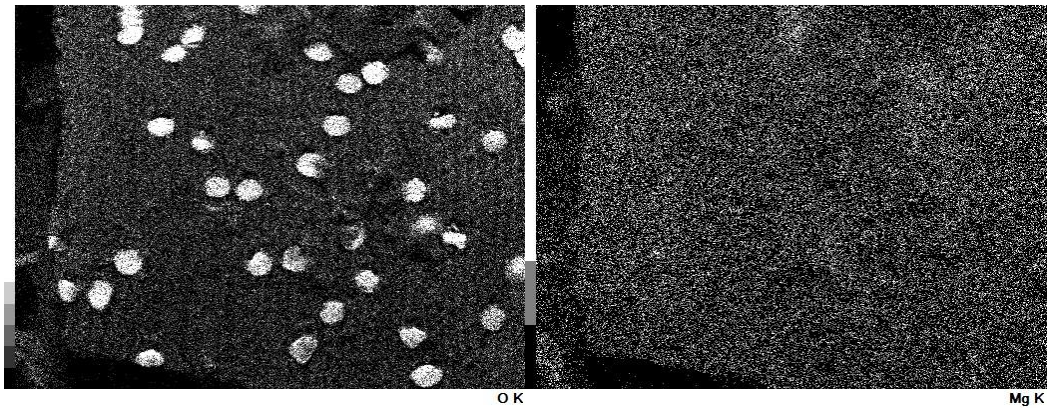
O K
Mg K

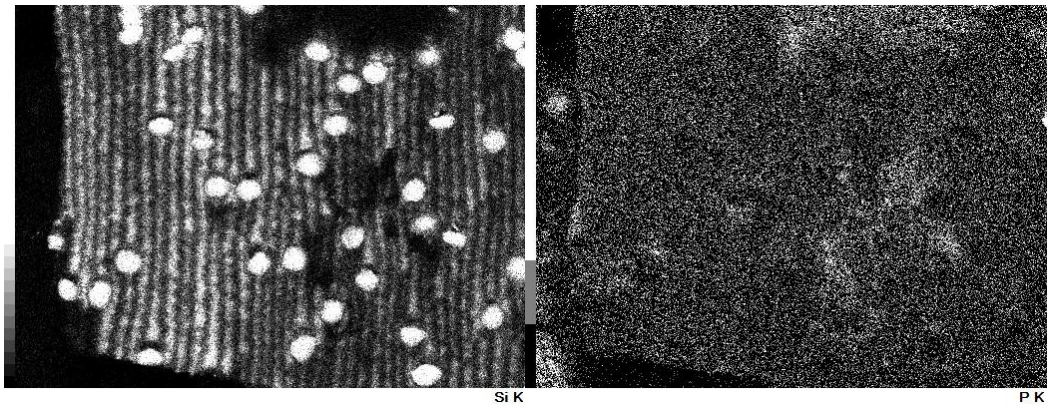
Si K
P K

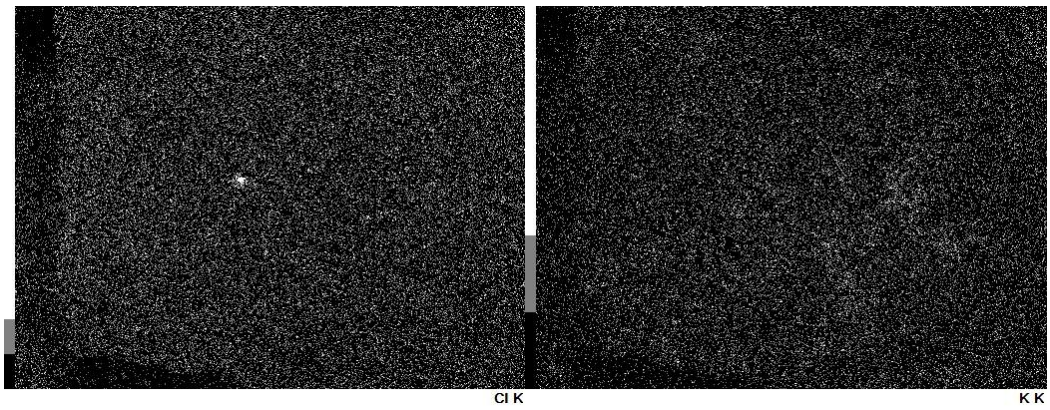
Cl K
K K

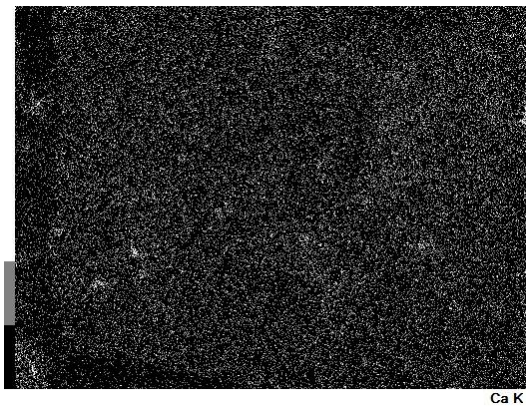

Figure 5.67: EDS elemental mapping of S9W glassy beads

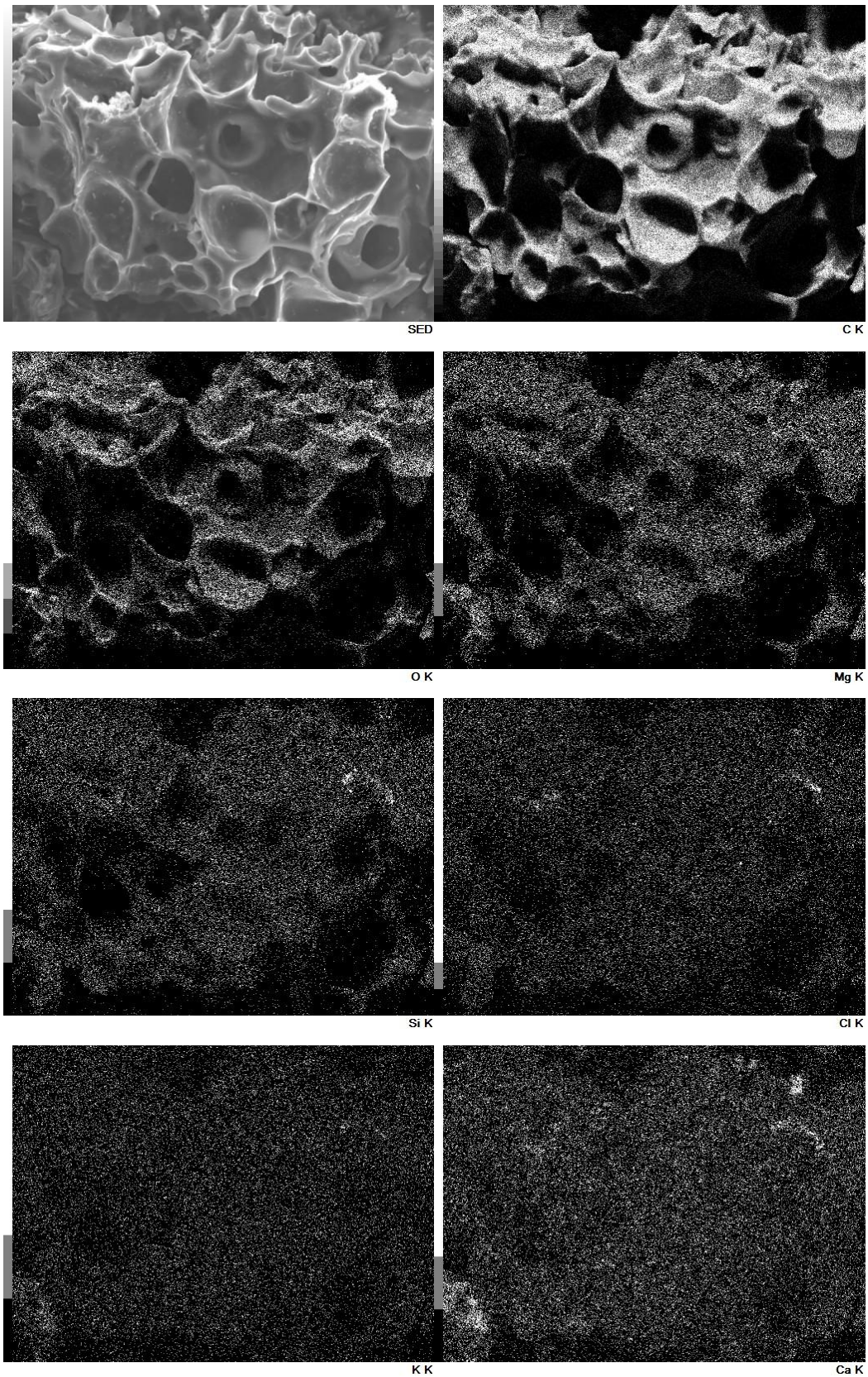

Figure 5.68: EDS elemental mapping of S9W amorphous

The glassy beads EDS maps of both the S9 and S9W show high concentrations of silicon and oxygen at the sites of the glassy beads. The glassy beads are therefore thought to be silicon oxide complexes on the surface of the biochar materials. These maps also show that the long, straight, zip-like structures, running axially along the fibres, seen in the images with the glassy beads, are primarily made up of silicon and carbon.

The amorphous maps show the majority of the material is carbon and oxygen, more typical of the composition expected from a biochar material. The S9 amorphous maps also show localised hotspots of silicon and oxygen, indicating that the silicon oxides present at the glassy beads sites are present within the amorphous bodies as well.

For all samples, it can be seen that the non-silicon ash material is relatively homogeneously distributed throughout the material and does not concentrate at any distinguishable features of the morphology of the material. This, in conjunction with the EDS data shown in Table 5.44, shows that the washing process leads to a decrease in the amount of this non-silicon ash content, which suggests that the acid washing process results in removal of the internal non-organic fraction of the biochar material, but does not affect the silicon oxides present as the glassy beads.

The mass percentage surface compositions of the group ***b*** samples, S14 and S14W, as determined by EDS, are shown in Table 5.45.

*Table 5.45: Mass % EDS results for Group **b** samples*

Element	S14 glassy beads (%mass)	S14 honeycomb structure (%mass)	S14W glassy beads (%mass)	S14W amorphous (%mass)
C	52.37	73.52	55.37	84.24
O	32.47	20.90	30.78	12.88
Mg	0.20	0.81	0.17	0.15
Si	14.05	1.25	12.46	0.33
P	0.55	2.15	0.52	1.43
S	-	0.13	-	0.07
Cl	-	-	0.18	0.21
K	0.09	0.14	-	-
Ca	0.29	1.10	0.26	0.49
Fe	-	-	-	0.10
Cu	-	-	0.26	0.11
Ash	15.18	5.58	13.85	2.89
Non-Si ash	1.13	4.33	1.39	2.56

The honeycomb structure and amorphous regions both show much larger percentages of carbon compared to the glassy bead regions on S14 and S14W. The oxygen content of the glassy beads regions is larger, this could be linked to the higher silicon content found at the glassy beads regions and, like in the group ***a*** EDS maps analysed above, the silicon existing as silicon oxides. Also similar to the S9 and S9W samples analysed above, the glassy beads have silicon as their 3rd most prevalent element, while the honeycomb and amorphous regions on S14 and S14W have phosphorus as their 3rd most prevalent element after carbon and oxygen. After washing, once again the ash content of the biochars decreases, with the majority of this decrease coming from the non-silicon ash elements.

The EDS maps for the group ***b*** samples are shown in Figure 5.69, Figure 5.70, Figure 5.71 and Figure 5.72.

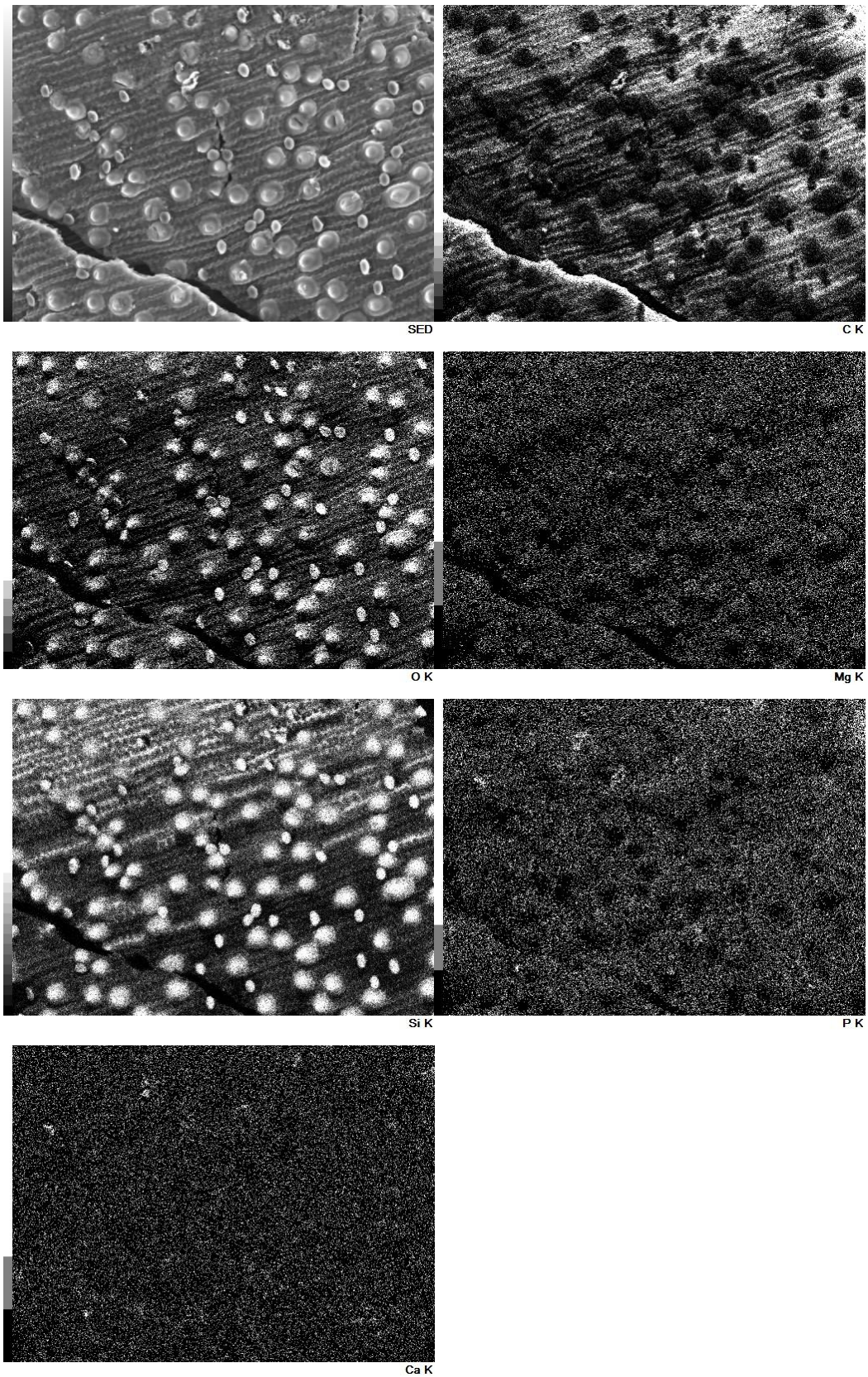

Figure 5.69: EDS elemental mapping of S14 glassy beads

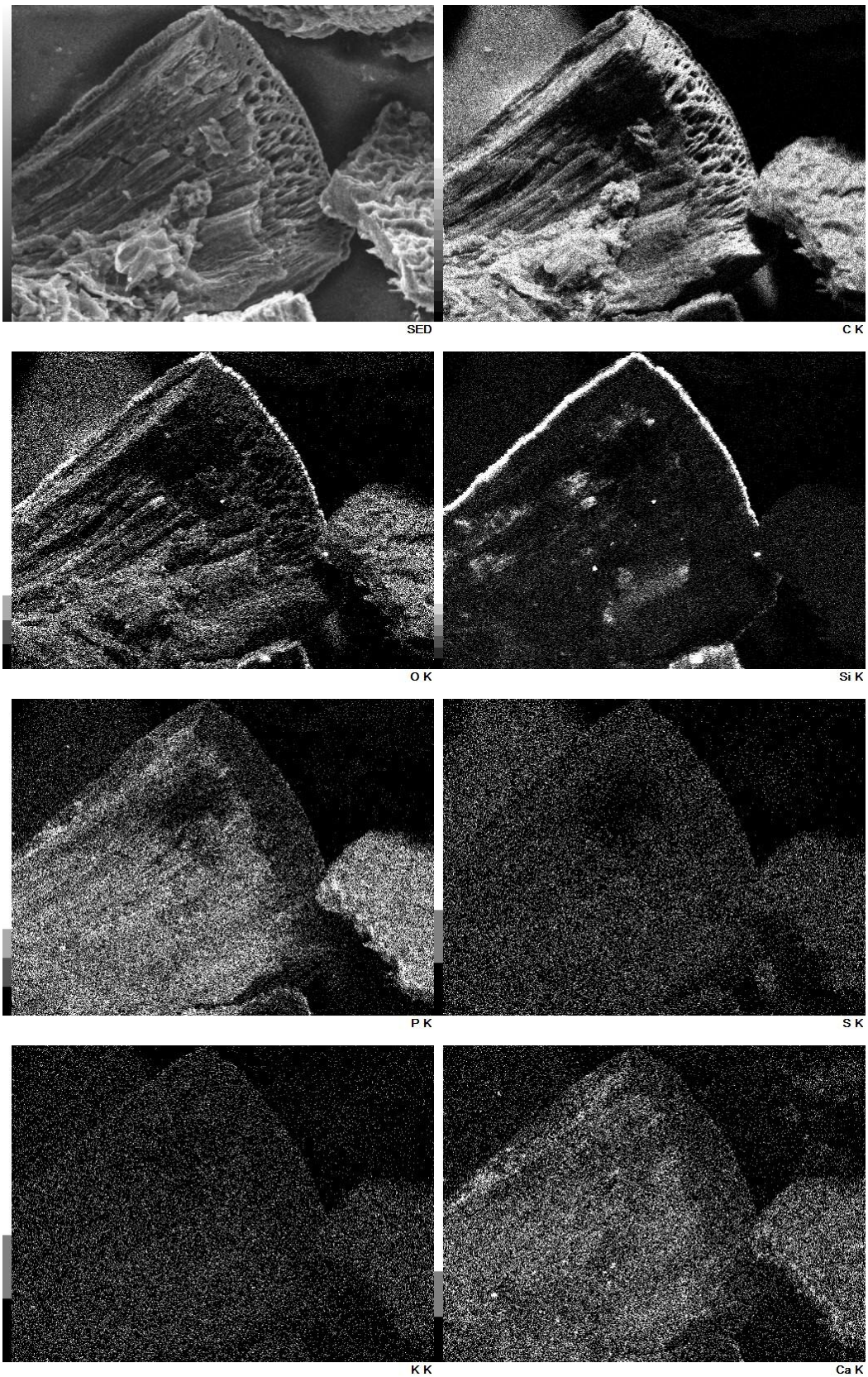

Figure 5.70: EDS elemental mapping of S14 honeycomb structure

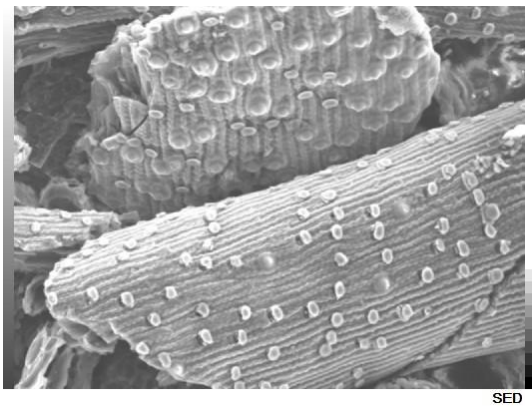

SED

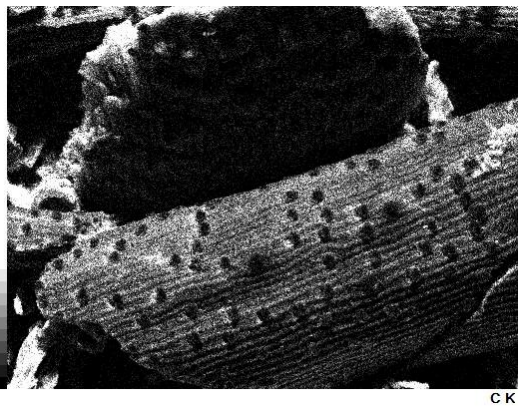

C K

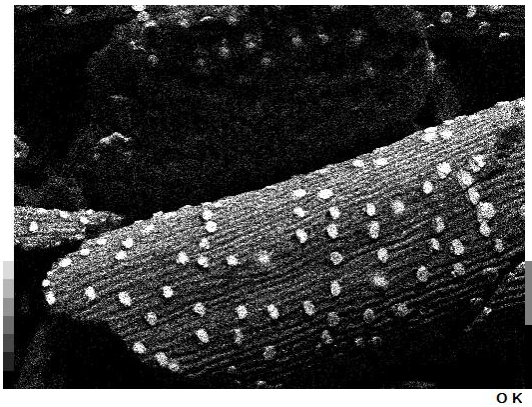

O K

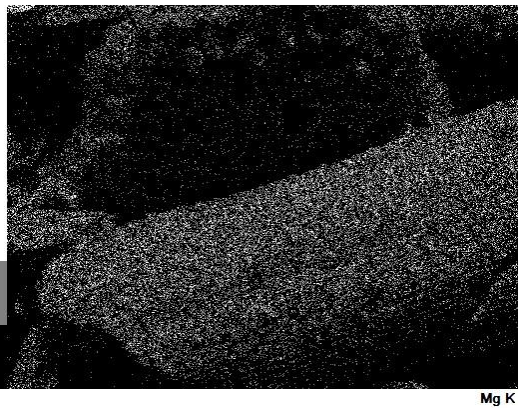

Mg K

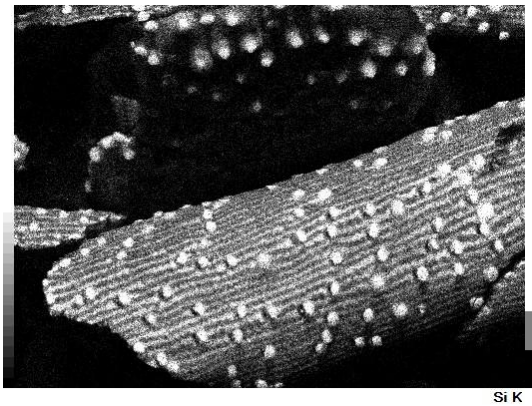

Si K

P K

S K

Cl K

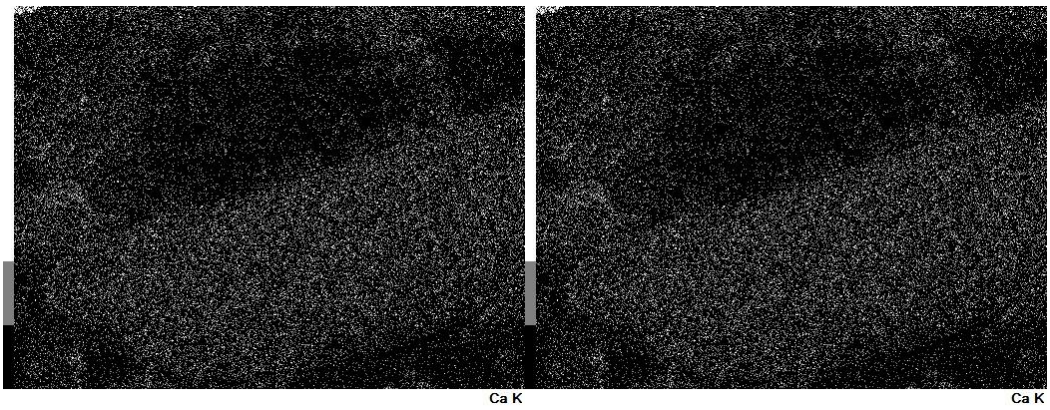

Figure 5.71: EDS elemental mapping of S14W glassy beads

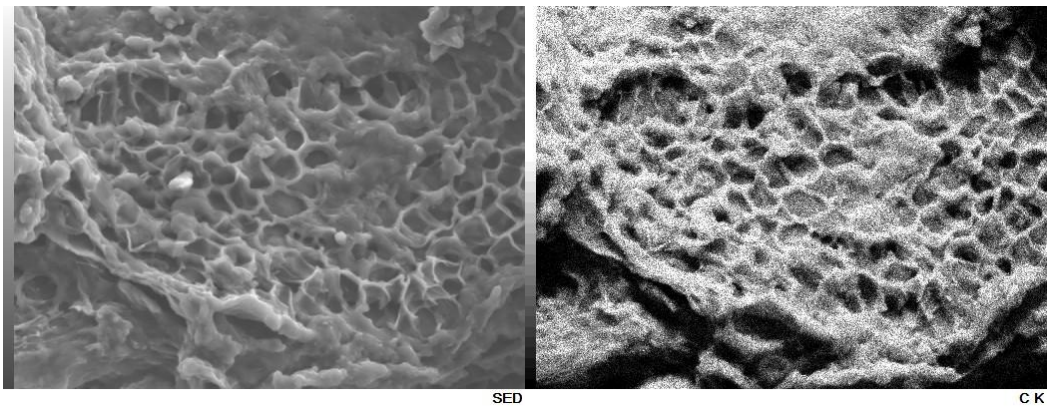
SED
C K

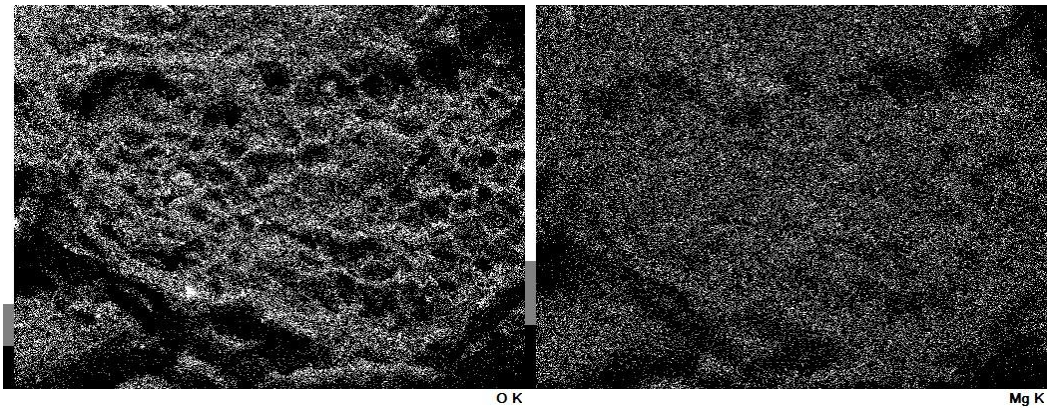
O K
Mg K

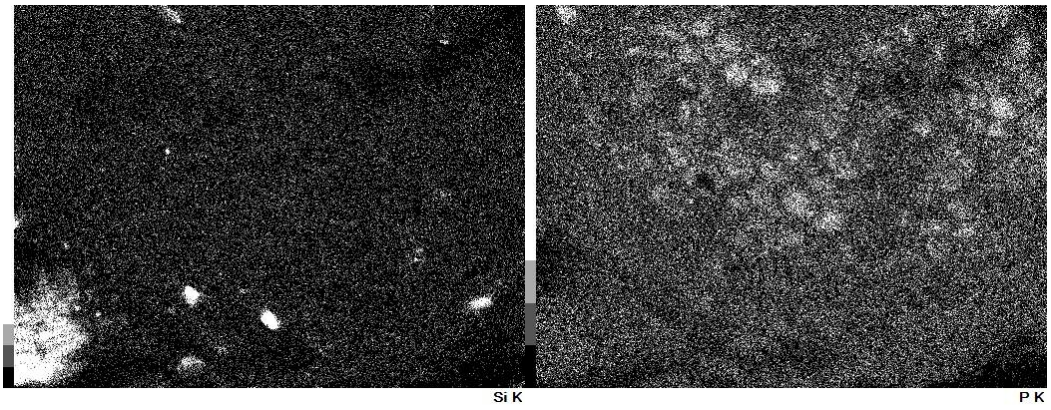
Si K
P K

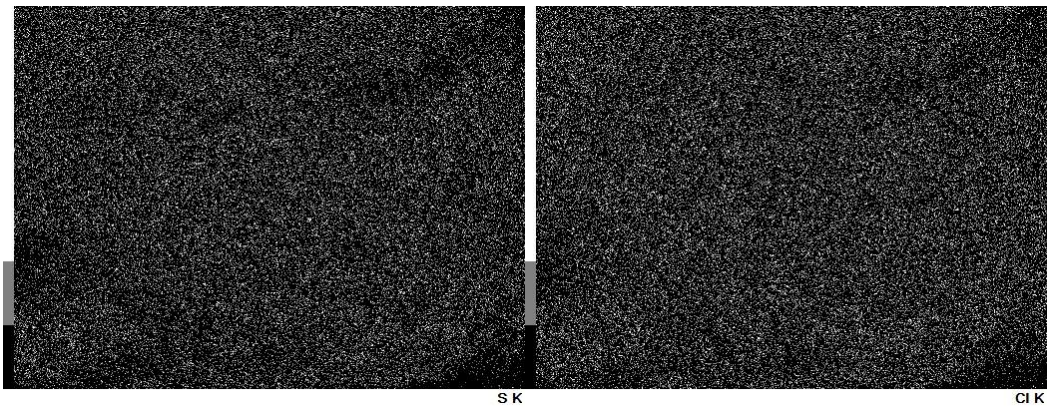
S K
Cl K

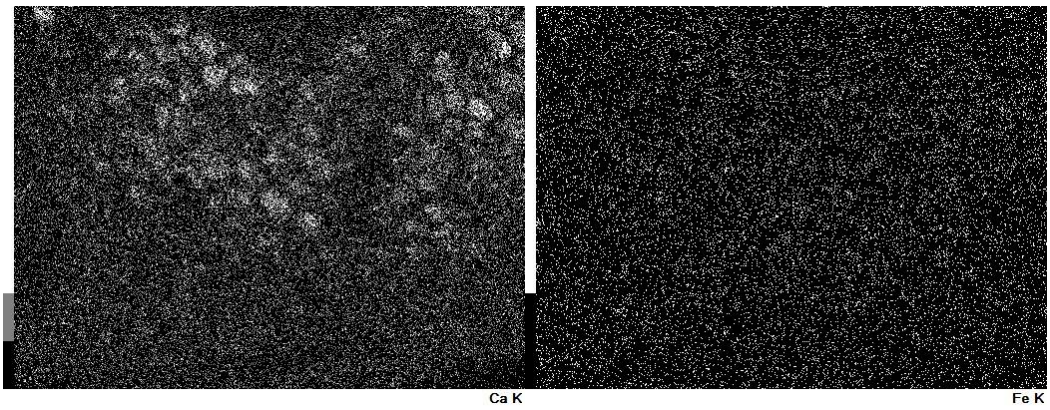

Figure 5.72: EDS elemental mapping for S4W amorphous

The EDS maps above show clearly once again that the regions where glassy beads are seen there is an increased concentration of silicon and oxygen, leading to the conclusion that the glassy beads are silicon oxide compounds. In the S14 honeycomb structure it can also be seen that there is a thin layer of silicon and oxygen material surrounding the honeycomb structure, showing that the silicon oxide material is inherent to the fibre composition of the BSG and is not added during the synthesis process. This layer of silicon dioxide surrounding the honeycomb structure may be the precursor state of silicon dioxide in the material before it is pyrolyzed and coalesces into the glassy beads seen in other regions of the biochar materials.

The non-silicon ash is once again distributed homogenously through all the biochar materials. This fact, alongside the reduction in this non-silicon ash fraction during washing, and higher surface area after washing, points to the conclusion that the removal of the non-silicon ash fraction is what opens up the blind pores within the matrix of the biochar material, increasing sites for adsorption.

The mass percentage surface compositions of the group ***c*** samples, S16 and S16W, as determined by EDS, are shown in Table 5.46.

Here, once again, the glassy beads sites show silicon as the third most prevalent element, while compositional analysis of the honeycomb and amorphous regions demonstrate that phosphorus is the third most common element, after oxygen and carbon.

*Table 5.46: Mass % EDS results for Group **c** samples*

Element	S16 glassy beads (%mass)	S16 honeycomb structure (%mass)	S16W glassy beads (%mass)	S16W amorphous (%mass)
C	60.29	60.61	52.55	79.27
O	25.97	27.13	34.91	16.89
Mg	1.19	1.49	-	-
Si	6.68	3.71	11.03	1.20
P	3.74	4.54	0.89	1.73
S	0.14	-	0.18	0.19
K	0.37	0.32	-	-
Ca	1.63	2.02	-	-
Fe	-	0.17	0.19	0.34
Cu	-	-	0.23	0.37
Ash	13.75	12.25	12.52	3.83
Non-Si ash	7.07	8.54	1.49	2.63

In the washed samples, the non-silicon ash content in both samples is very low. As stated before, washing removes the majority of the non-silicon ash, but this seems to be enhanced in these samples, as compared to the others, due to their greater pore volume and surface area. Seemingly, the more open the structure, the easier the washing solution can penetrate the material and remove the non-silicon ash material blocking the blind pores.

The EDS maps for the group ***c*** samples are shown in Figure 5.73, Figure 5.74, Figure 5.75 and Figure 5.76.

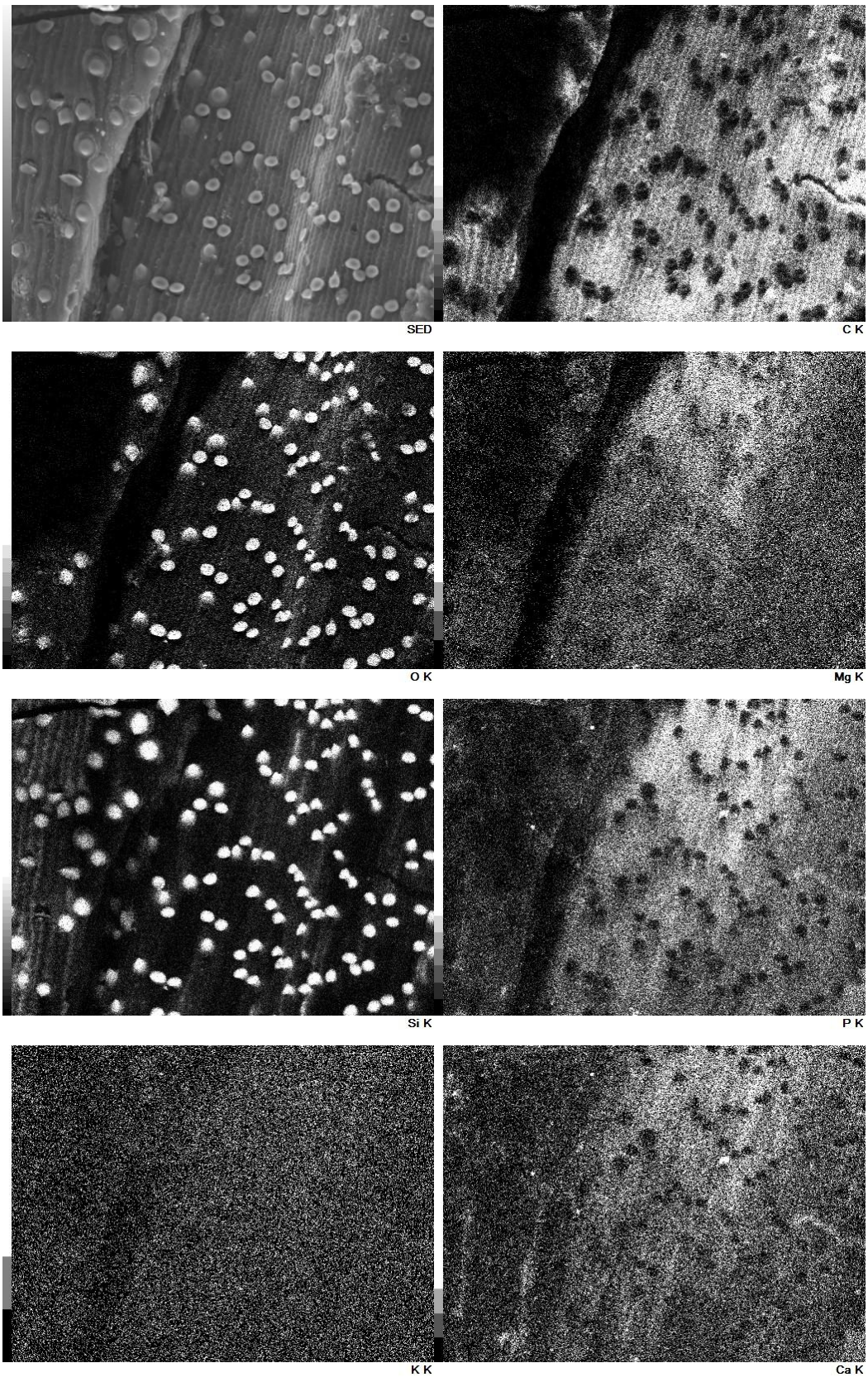

Figure 5.73: EDS elemental mapping of S16 glassy beads

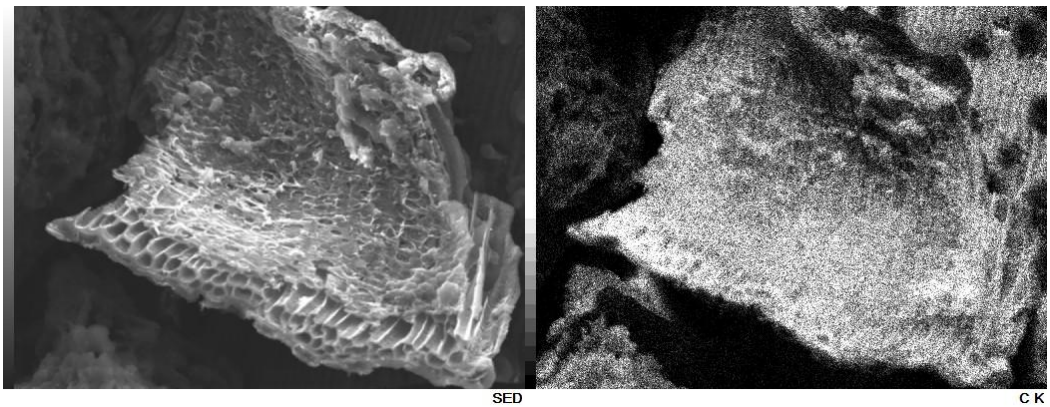
SED
C K

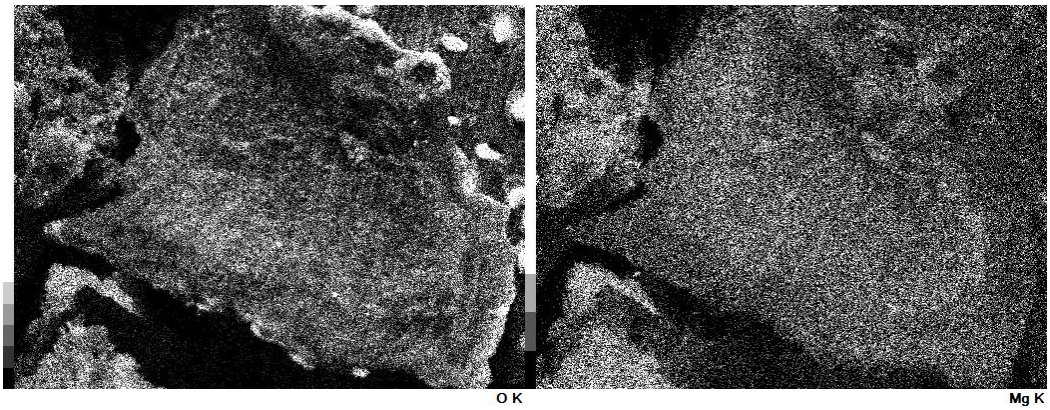
O K
Mg K

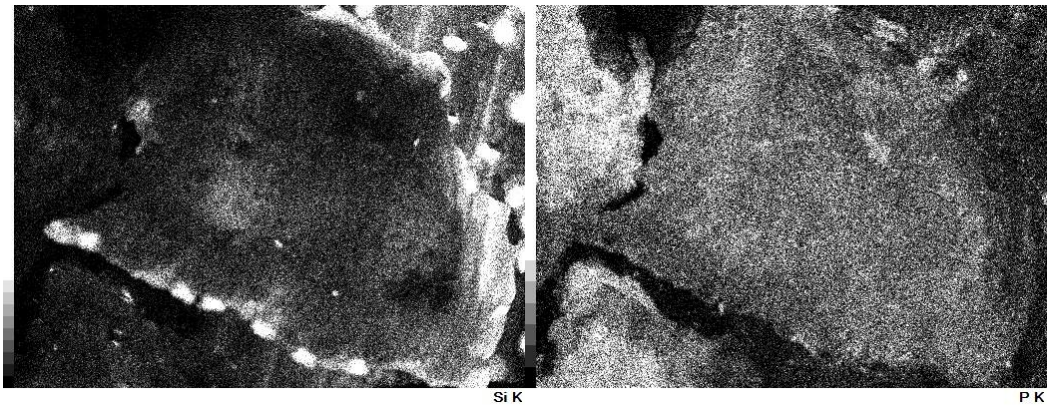
Si K
P K

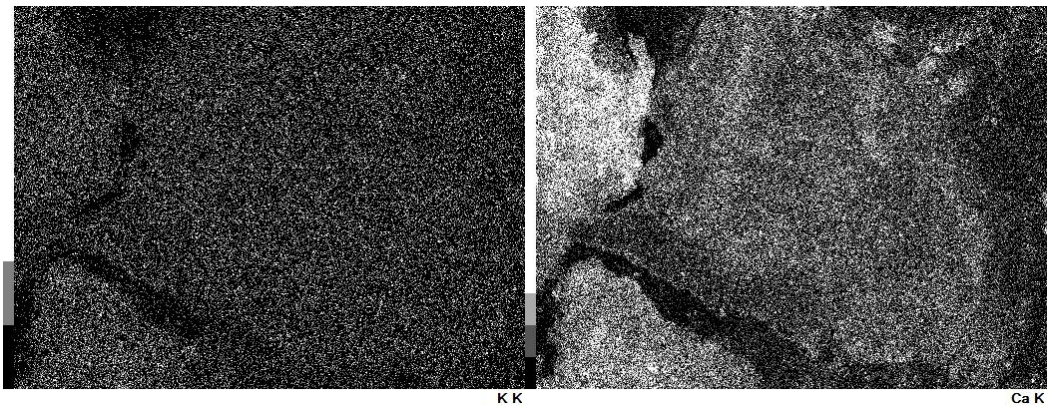
K K
Ca K

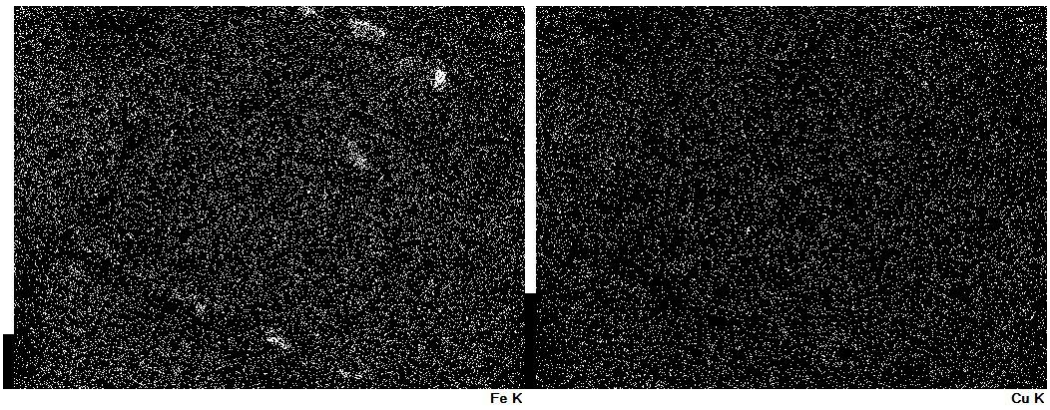

Figure 5.74: EDS elemental mapping of S16 honeycomb structure

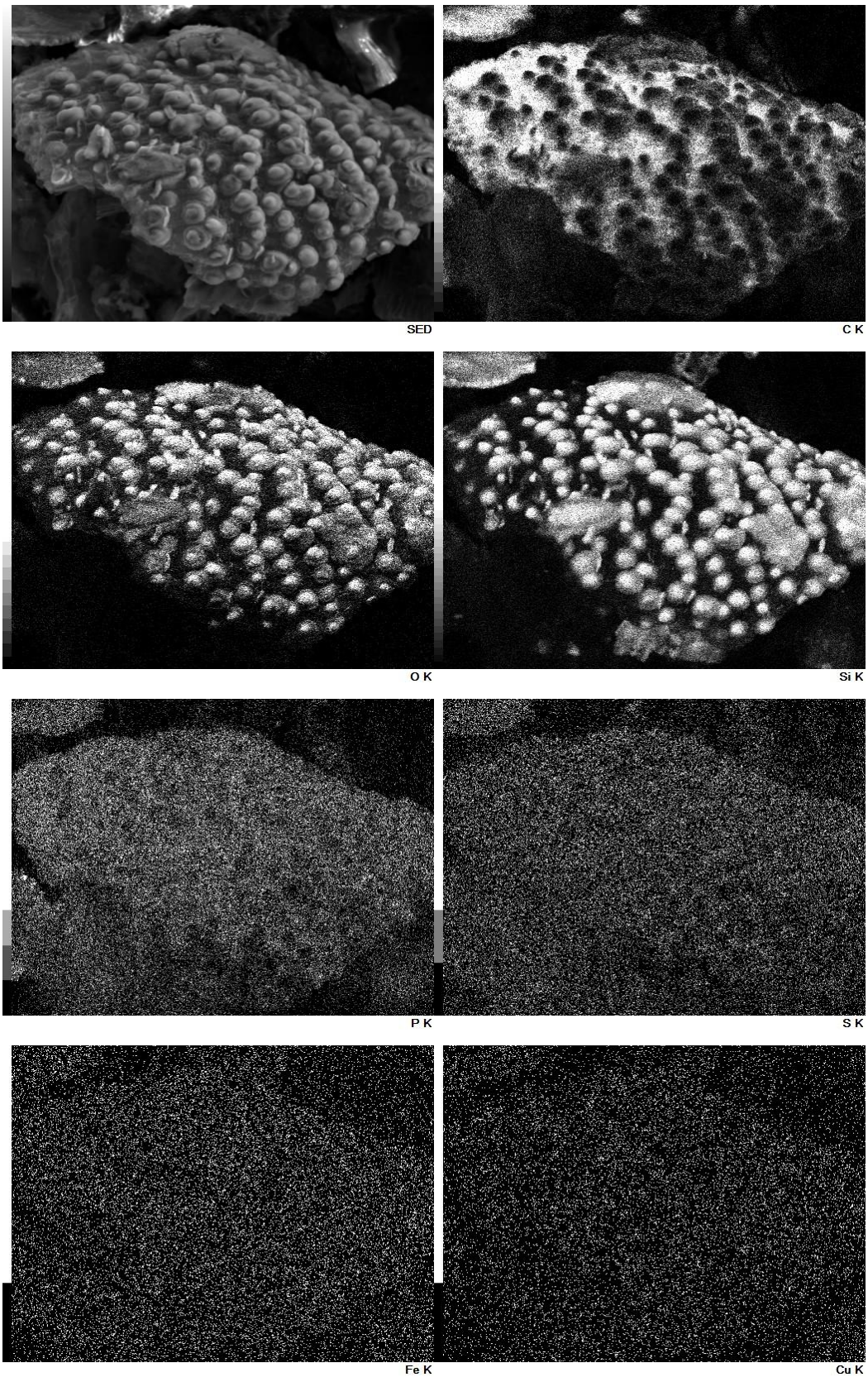

Figure 5.75: EDS elemental mapping of S16W glassy beads

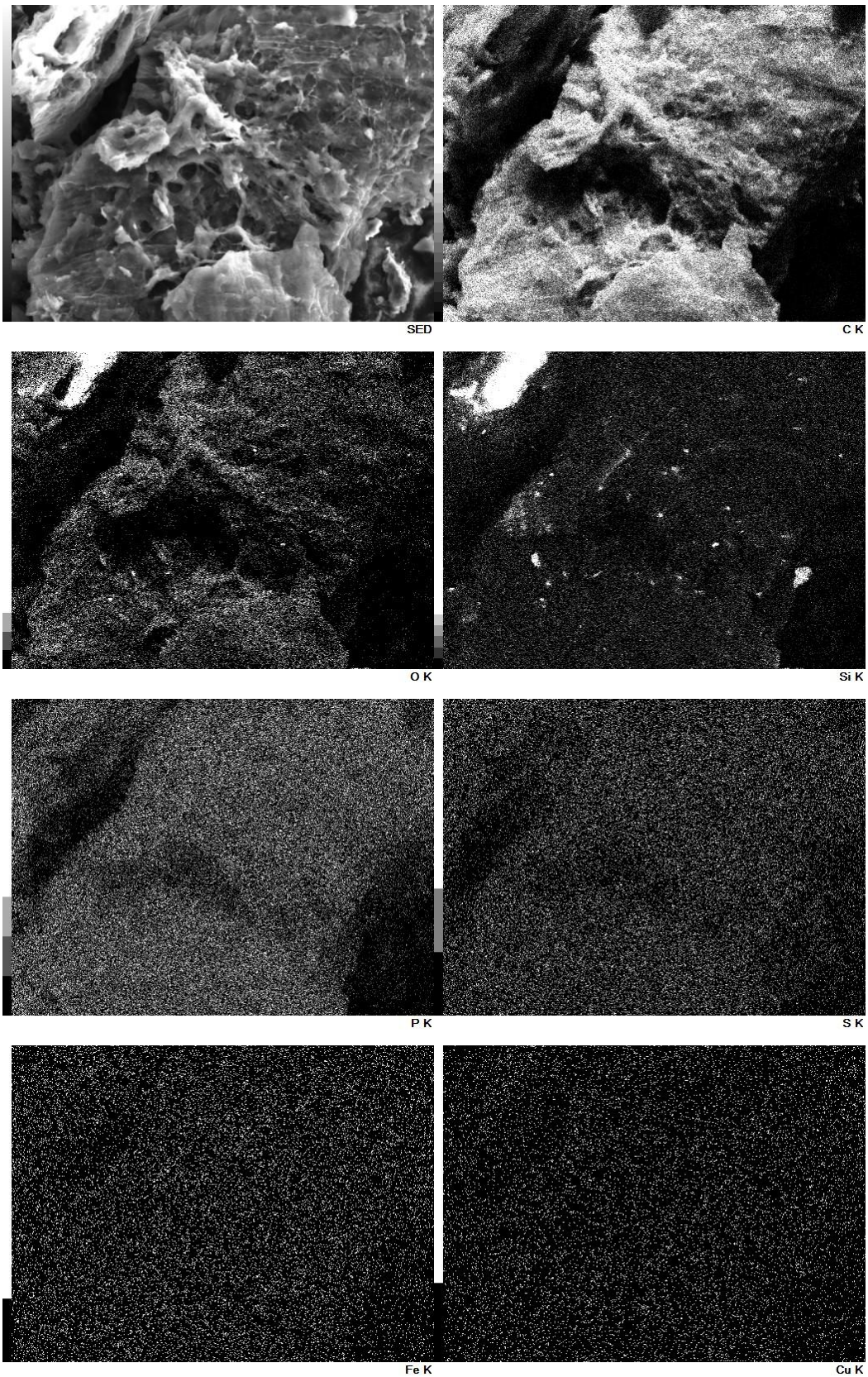

Figure 5.76: EDS elemental mapping of S16W amorphous

Once again, EDS mapping shows high concentrations of silicon and oxygen on the sites of the glassy beads, demonstrating the prevalence of these silicon oxide beads on the surface of each material made, irrespective of temperature. The S16 honeycomb structure, once again, shows the thin layer of silicon oxide material surrounding the fibre containing the porous, honeycomb-like channels, similar to the S14 honeycomb structure material.

The high silicon content, after washing of the glassy bead sites, and the prevalence of these on the surface, as seen from the elemental mapping, lends further evidence to the fact that the acid washing does not remove the silicon oxide materials from the surface of the biochars but only the non-silicon ash fraction.

The presence of these silicon oxide surface groups validates the peaks observed in the fingerprint region of the Ge-ATR FTIR measurements, at approximately 1020-1095 cm^{-1}, indicating silicon-oxy compounds (158).

It should be noted that the EDS mapping did not detect any nitrogen in this analysis, while we know from CHN elemental analysis, and from XPS analysis, that there is a not insignificant amount of nitrogen present in the biochars tested. This could be explained by the difficulty of EDS detectors in detecting nitrogen due to its low atomic number, the low concentration of nitrogen in the material or masking from the large signals received from both oxygen and carbon. Due to the general unreliability in EDS measurements which can have large errors, this data should be used strictly qualitatively. Furthermore, as XPS has a very shallow penetration depth of approximately 10nm, and EDS has a much larger penetration depth of about 10µm, the high levels of nitrogen detected in the XPS analysis could be due to only the carbons in the organic rings on the outer surface of the material being replaced with nitrogen atoms. This may be limited by slow diffusion of the nitrogen gas into the pores of the material and result in low nitrogen levels deeper in the biochar matrix. In this case, the nitrogen would be a small fraction of the composition analysed by EDS, but relatively large for XPS. Additionally, as an averaged bulk measurement, the nitrogen detected by the CHN elemental analysis may provide a combined result of surface and bulk compositions, including the fraction deeper within the biochar matrix, which may not be detectable by the relatively shallow EDS surface measurement.

5.5 Batch Adsorption Tests

5.5.1 Target Species

From the investigation of the surface characteristics of the washed biochar materials methyl orange (MO) dye was identified as an appropriate adsorptive species to test the capabilities of the synthesised materials. The acidic PZCs of the porous biochars, indicating a greater number of positively charged surface functional groups on the surface of the materials, would provide sites for electrostatic interaction with the negative charge of the anionic dye molecules located at the sulphone functional group on the methyl orange. The large variety of oxygen and nitrogen containing functional groups identified through FTIR and XPS, and the inorganic silicon containing functionalities identified through FTIR and EDS, may also provide many sites for interaction with the other moieties of the MO molecules such as the tertiary amine, aromatic rings or azo group.

Many azo dyes like methyl orange are considered recalcitrant pollutants, which are difficult to break down by traditional waste water treatment systems means. Many azo dyes are resistant to aerobic biological degradation(169), and those that do degrade form toxic by-products such as aromatic amines, which require further processing (170). Methyl orange is utilised in the textile and leatherworking industries, utilised as a chemical indicator in laboratory and (ironically) waste water treatment plants due to its pH dependant colour change. Unlike many azo dyes, methyl orange is not banned under UK or EU law despite its mutagenic and carcinogenic properties (171).

While MO is not considered an emerging contaminant, it provides several attractive properties from a material testing standpoint. Methyl orange has been widely tested as an adsorptive for many adsorbents used in liquid phase separations, and so has a plethora of studies to benchmark our synthesised materials against. The interactions methyl orange undertakes are well understood; with this understanding, an adsorption mechanism and accurate picture of the adsorption sites on our material can be evaluated with certainty. Methyl orange is a complex adsorptive with many different functional groups present in its structure. This makes it appropriate as a proxy for many target species requiring remediation from water systems. By understanding the adsorption behaviour between the tested biochar materials and methyl orange, we hope to identify potential target species for real world application of the synthesised materials.

Methyl orange, as the name suggests, has an orange colour and therefore a chromophore peak in the visible range of light. This makes it easy to measure through colorimetric spectroscopy measurement in the visible range, a simple and reliable method of measuring concentration of substances in solution. This will allow for cheap, quick and accurate measurement of the concentrations and determine uptakes after adsorption onto the surface of the tested materials.

From the hierarchy of controls, elimination or substitution of a hazard is always preferable to mitigating or controlling a hazard (172). For this reason, using a proxy adsorptive species like MO is preferable to using a real emerging contaminant which may present not only a hazard to lab users and university staff, but also a remediation problem if accidental uncontrolled release to water, soil or air occurs.

There is also a significant gap in the literature for BSG biochar materials with regards to methyl orange, with no previous studies being reported as utilising BSG derivative biochars as an adsorbent for its removal. It was, therefore, selected as the target species for determining the efficacy of the biochars, made in this study, as adsorbents.

5.5.2 Methyl Orange Calibration

Calibration curve experiments were performed to determine the molar absorptivity and applicable range for the determination of unknown methyl orange concentrations. The molar absorptivity was determined to be 0.0885 ± 3.6 $\times^{-4}$ L mg^{-1} cm^{-1} for a range of 0-45mg L^{-1}. The calibration curves can be seen in Appendix B and the error propagation equations can be seen in appendix D.

5.5.3 Methyl Orange Batch Adsorption Tests

Moving on from the characterisation experiments, the ability of the biochars to act as effective adsorbents for water treatment applications was also investigated. Batch adsorption experiments of 10 mL of 100 mg L^{-1} methyl orange dye were carried out for the sample from the three groups, before and after washing were carried out. The experiments were run for contact times of 1 h and 24 h for every sample. The results are summarised in Table 5.47 below.

Table 5.47: Adsorption uptakes after 1 and 24 h for washed and unwashed samples[10]

Sample	Uptake after 1 h (mg g^{-1})	Uptake after 24 h (mg g^{-1})
S9	3 ± 1	0 ± 1
S9W	0 ± 1	0 ± 1
S14	0 ± 1	40 ± 1
S14W	7 ± 1	11 ± 1
S16	136 ± 1	231 ± 0
S16W	122 ± 1	231 ± 0

These results are shown graphically in Figure 5.77.

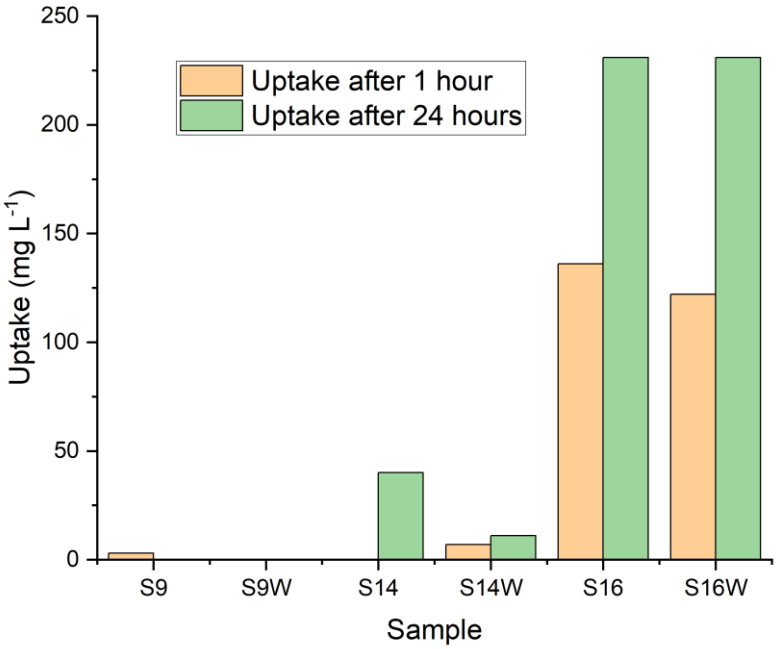

Figure 5.77: Adsorption uptake of methyl orange dye after 1 and 24 h, for washed and unwashed biochar samples

For the group ***a*** samples, S9 and S9W, little or no adsorption was found to have occurred regardless of contact time with the adsorptive dye solution, or washing state. This is expected, due to the non-porous nature and small surface areas reported from nitrogen adsorption characterisation.

[10] Errors calculated from propagation of error in Beer-Lambert law fit, the error propagation equations are detailed in Appendix D

For the group ***b*** samples, S14 and S14W, an expected increase in adsorption over time occurs in the case of both samples, from 0 to 40 mg L^{-1}, for the unwashed sample, and from 7 mg L^{-1} to 11 mg L^{-1}, for the washed sample. We also see a decrease in the maximum uptake, at the presumed equilibrium in this experiment, after washing, but an increase in the uptake at low times implying faster kinetics of adsorption. The decrease in capacity is an unexpected result, due to the increase in surface area after acid washing. This increase in surface area may however not translate to more adsorption sites if the adsorptive dye molecules are too large to access the pores. The improved kinetics may be due to the protonation of the lone pair of electrons on functional groups such as carbonyl and amine, increasing the number of favourable electrostatic interactions occurring between the adsorbent and the negative charge on the dye adsorptive molecules. This surface chemical shift is seen in the XPS data in Section 5.4.4.3 above through the shift from OI quinone groups to OII phenolic groups. In the case of group ***b*** samples, there seems to be a trade-off between a larger maximum capacity of the adsorbent when unwashed and faster kinetics when washed.

The group ***c*** samples, S16 and S16W, exhibited the highest adsorption uptakes of all of the samples tested, an expected result, due to their extremely high surface areas, in comparison to the other groups. The equilibrium uptake at 24 h, for both S16 and S16W, was 231 mg L^{-1}, outperforming many other adsorbents in the literature such as biochars from hazelnut shell, cellulose, glucose (173), pomelo peel (174), chicken manure (175) and activated carbons from coconut shell (176) and aloe vera (177). Contrary to the result from the group ***b*** samples, washing did not seem to increase the capacity of the sample, even though the surface area increased with washing, according to nitrogen adsorption analysis. The increase in surface area was attributed mostly to micropore availability in S16W – resulting in an increase in surface area of 681 m^2g^{-1} (from 1125 m^2g^{-1} in S16 to 1807 m^2g^{-1} in S16W) while the micropore surface area increased by 659 m^2g^{-1} (from 1111 m^2g^{-1} in S16 to 1770 m^2g^{-1} in S16W). These micropores may be too narrow for the large dye molecules to enter and adsorb onto the walls of the pores, meaning that the increase in surface area does not translate to an increase in adsorption capacity. This indicates that in this instance, surface area cannot be taken as a directly proxy for liquid phase adsorbent capacity. Extensive liquid phase adsorbent testing must be included as a optimisation response variable to ensure a true optimum carbon is chosen. The 1 h experiments show a decrease in dye uptake during washing from 136 mg L^{-1} for S16 to 122 mg L^{-1} for S16W. This is also

counter to the group ***b*** samples, and may be attributed to the decrease in the number of protonated nitrogen surface functional groups found after washing as shown from XPS data in Section 5.4.4.3. These positively charge functional groups would be attracted to the negative charge on the methyl orange dye molecules. Further investigation into intermolecular interactions between the biochar surface functional groups and methyl orange functionalities is carried out in Chapter 7.

While the decrease in uptake after washing for the 1-hour residence time samples for the group **c** samples is a concern, the surface tailorability, increase in surface area and adherence to the ash content consent limits as outlined by the Indonesian Standards authority that can be achieved from washing are seen as necessary. Washing therefore will be carried out on all samples in the optimisation design of experiments in the next chapter, with hold time and hold temperature as the synthesis parameters under investigation. Yield, surface area, methyl orange uptake after 1 h and methyl orange uptake after 7 days will be used as response variables.

It should be noted that the above analysis is based on single batch adsorption experiments without repetitions and conclusions should be treated with caution. These were carried out as a proof of concept to confirm adsorption of the methyl orange dye on the synthesised materials. Moving forward, the optimisation design of experiments will be carried out with duplicated centre points to account for batch to batch variation.

5.6 Screening Conclusions

The low activation temperatures investigated have resulted in a non-porous material, unsuitable for adsorbent applications. The high temperature material is highly porous with a mixture of mesoporosity and microporosity. The synthesis parameters hold temperature and hold time were found to be the only factors of significance to the yield and BET surface area and so should be used in optimisation studies moving forward.

PZC and surface charge cannot be adequately tailored by just pyrolysis alone and so an acid washing step must be introduced to alter the biochars produced. Washing also helps to reduce the ash content of the materials, allowing for better compliance with international carbonaceous adsorbent standards.

The materials are largely made up of lignin macromolecule derived carbon. Both transmission and Germanium ATR FTIR are incapable of adequately characterising the

surface of the material. For this reason more advanced surface characterisation methods, like XPS, SEM and EDS are required to understand the materials.

XPS has identified many chemical moieties for adsorption interactions to take place including oxygen and nitrogen containing functional groups and aromatic carbon. While SEM and EDS have shown a hierarchical pore structure alongside inorganic silica surface groups which warrant further investigation.

The materials synthesised show good adsorption capacities with methyl orange dye, which has been identified as a good surrogate molecule to investigate the adsorption interactions occurring for use in real world applications with various organic emerging contaminants. It has also been noted that surface area and methyl orange adsorption capacity are not directly correlated and so moving forward, methyl orange adsorption capacity should be used as a response variable in optimisation design of experiments at both short and long hold times to differentiate between maximum capacity and kinetic performance.

5.7 References

1. Mathias TRdS, Alexandre VMF, Cammarota MC, de Mello PPM, Sérvulo EFC. Characterization and determination of brewer's solid wastes composition. Journal of the Institute of Brewing. 2015;121(3):400-4.
2. Buffington J. The Economic Potential of Brewer's Spent Grain (BSG) as a Biomass Feedstock. Advances in Chemical Engineering and Science. 2014;04:308-18.
3. Coronado Ortega M, Montero G, Montes DG, valdez salas B, Ayala Bautista J, Garcia C, et al. Physicochemical Characterization and SEM-EDX Analysis of Brewer's Spent Grain from the Craft Brewery Industry. Sustainability. 2020;12.
4. Machado RM, Rodrigues RAD, Henriques CMC, Gameiro MLF, Ismael MRC, Reis MTA, et al. Dewatering of brewer's spent grain using an integrated membrane filter press with vacuum drying capabilities. Separation Science and Technology. 2016;51(4):692-700.
5. Becidan M, Skreiberg Ø, Hustad JE. Products distribution and gas release in pyrolysis of thermally thick biomass residues samples. Journal of Analytical and Applied Pyrolysis. 2007;78(1):207-13.
6. Xiros C, Christakopoulos P. Biotechnological Potential of Brewers Spent Grain and its Recent Applications. Waste and Biomass Valorization. 2012;3(2):213-32.
7. Pandia S, Hutagalung A, Siahaan A. Utilization of Cocoa Peel as Biosorbent for Oil and Color Removal in Palm Oil Mill Effluent (POME). IOP Conference Series: Materials Science and Engineering. 2018;300:012066.
8. Efiyanti L, Darmawan S, Saputra N, Wibisono H, Hendra D, Pari G. Quality evaluation of coconut shell activated carbon and its application as precursor for citronellal-scented aromatic briquette. Rasayan Journal of Chemistry. 2022;15(3):1608-18.

9. El-Sayed SA, Mostafa ME. Thermal pyrolysis and kinetic parameter determination of mango leaves using common and new proposed parallel kinetic models. RSC Advances. 2020;10(31):18160-79.
10. Thommes M, Kaneko K, Neimark A, Olivier J, Rodriguez-Reinoso F, Rouquerol J, et al. Physisorption of gases, with special reference to the evaluation of surface area and pore size distribution (IUPAC Technical Report). Pure and Applied Chemistry. 2015;87.
11. Sing KSW, Williams RT. Physisorption Hysteresis Loops and the Characterization of Nanoporous Materials. Adsorption Science & Technology. 2004;22(10):773-82.
12. Rouquerol J, Llewellyn P, Rouquerol F. Is the BET Equation Applicable to Microporous Adsorbents? Studies in Surface Science and Catalysis. 2007;160:49-56.
13. Gonçalves GdC, Nakamura PK, Furtado DF, Veit MT. Utilization of brewery residues to produces granular activated carbon and bio-oil. Journal of Cleaner Production. 2017;168:908-16.
14. Nandiyanto A, Oktiani R, Ragadhita R. How to Read and Interpret FTIR Spectroscope of Organic Material. Indonesian Journal of Science and Technology. 2019;4:97-118.
15. Jackowski M, Niedźwiecki Ł, Jagiełło K, Uchańska O, Trusek A. Brewer's Spent Grains-Valuable Beer Industry By-Product. Biomolecules. 2020;10(12):1669.
16. Silbir S, Göksungur MY. Natural Red Pigment Production by Monascus Purpureus in Submerged Fermentation Systems Using a Food Industry Waste: Brewer's Spent Grain. 2019;8:161.
17. Borel LDMS, Lira TS, Ribeiro JA, Ataíde CH, Barrozo MAS. Pyrolysis of brewer’s spent grain: Kinetic study and products identification. Industrial Crops and Products. 2018;121:388-95.
18. Ravindran R, Jaiswal S, Abu-Ghannam N, Jaiswal AK. A comparative analysis of pretreatment strategies on the properties and hydrolysis of brewers’ spent grain. Bioresource Technology. 2018;248:272-9.
19. Jacobsen SE, Wyman CE. Xylose Monomer and Oligomer Yields for Uncatalyzed Hydrolysis of Sugarcane Bagasse Hemicellulose at Varying Solids Concentration. Industrial & Engineering Chemistry Research. 2002;41(6):1454-61.
20. Vanreppelen K, Vanderheyden S, Kuppens T, Schreurs S, Yperman J, Carleer R. Activated carbon from pyrolysis of brewer's spent grain: Production and adsorption properties. Waste Manag Res. 2014;32(7):634-45.
21. Teixeira S, Delerue-Matos C, Santos L. Application of experimental design methodology to optimize antibiotics removal by walnut shell based activated carbon. Science of The Total Environment. 2019;646:168-76.
22. Cao W, Xu H, Zhang X, Xiang W, Qi G, Wan L, et al. Novel post-treatment of ultrasound assisting with acid washing enhance lignin-based biochar for CO2 capture: adsorption performance and mechanism. Chemical Engineering Journal. 2023;471:144523.
23. Hao X, Quach L, Korah J, Spieker W, Regalbuto JR. The control of platinum impregnation by PZC alteration of oxides and carbon. Journal of Molecular Catalysis A: Chemical. 2004;219(1):97-107.

24. Tran HN, You S-J, Chao H-P. Effect of pyrolysis temperatures and times on the adsorption of cadmium onto orange peel derived biochar. Waste Management & Research. 2016;34(2):129-38.
25. Zafar S, Bukhari DA, Rehman A. Azo dyes degradation by microorganisms–An efficient and sustainable approach. Saudi Journal of Biological Sciences. 2022;29(12):103437.
26. Qiu H, Shen F, Yin A, Liu J, Wu B, Li Y, et al. Biodegradation and detoxification of azo dyes by halophilic/halotolerant microflora isolated from the salt fields of Tibet autonomous region China. Front Microbiol 13: 877151. 2022.
27. Chung K, Fulk G, Andrews A. The mutagenicity of methyl orange and metabolites produced by intestinal anaerobes. Mutat Res. 1978;58(2-3):375-9.
28. Ajslev JZ, Møller JL, Andersen MF, Pirzadeh P, Lingard H. The hierarchy of controls as an approach to visualize the impact of occupational safety and health coordination. International journal of environmental research and public health. 2022;19(5):2731.
29. ÇAĞLAR E, Donar YO, SINAĞ A, BİROĞUL İ, Bilge S, Aydincak K, et al. Adsorption of anionic and cationic dyes on biochars, produced by hydrothermalcarbonization of waste biomass: effect of surface functionalization and ionicstrength. Turkish Journal of Chemistry. 2018;42(1):86-99.
30. Zhang B, Wu Y, Cha L. Removal of methyl orange dye using activated biochar derived from pomelo peel wastes: performance, isotherm, and kinetic studies. Journal of Dispersion Science and Technology. 2020.
31. Yu J, Zhang X, Wang D, Li P. Adsorption of methyl orange dye onto biochar adsorbent prepared from chicken manure. Water Science and Technology. 2018;77(5):1303-12.
32. Islam MS, Ang BC, Gharehkhani S, Afifi ABM. Adsorption capability of activated carbon synthesized from coconut shell. Carbon letters. 2016;20:1-9.
33. Khaniabadi YO, Heydari R, Nourmoradi H, Basiri H, Basiri H. Low-cost sorbent for the removal of aniline and methyl orange from liquid-phase: aloe vera leaves wastes. Journal of the Taiwan institute of chemical engineers. 2016;68:90-8.

6. Optimisation of Biochar Synthesis Parameters

6.1 Design of Experiments Planning

6.1.1 Central Composite Design Choice

As stated in Chapter 5, a two-factor optimisation design of experiments is required for the optimisation of the washed biochars produced from BSG, with hold time and temperature the parameters of interest. As outlined in Chapter 1, there are typically 3 different central composite designs to choose from: CCC, CCI and CCF. A central composite circumscribed design was deemed a poor choice for this system, as the axial points would require to be far outside the design space leading to temperatures and times impractical to the running of the experiments. For example, the maximum hold time would be approximately 2.9 h, causing issues with scheduling. This is due to local lab guidelines on cooling of equipment and leaving equipment of elevated temperatures unsupervised as discussed in Section 1.5.7.2 in the discussion of how the screening ranges were selected. The choice was then to be made between central composite inscribed and central composite face centred designs. Ultimately, CCF was chosen as the design regime going forward due to the inability of CCI to accurately model the responses outside of the design space encompassed by the data points, and the fact that the highest adsorption uptakes and surface areas were found in this region of the design space at coded values of x_1=1, x_2=1 or a hold temperature of 900 °C and a hold time of 2.5 h in the screening studies. A CCF has the drawback of poorly estimating the quadratic effects of the model equation after computation. This was deemed as an acceptable shortcoming to avoid the faults of the other two options.

6.1.2 Other Parameters

The other design parameters, which would be kept constant in this optimisation, must also be considered before moving on with the experimental phase. In keeping with the green chemistry principles of this project, and due to the lack of effects on the responses investigated, all of the variables would be set to the lowest or highest tested value to minimise environmental and economic impact. The ramp rate was set to the highest value tested (20 °C min-1) to minimise experimental time in the ramp phase and reduce the amounts of gas reagents used. The gas flowrates of both the inert and activating gases were chosen to be at the lowest level tested in the screening design (i.e. 60ml min-1). This allowed the volume of gases used to be minimised, reducing both costs and waste gas

stream output, which included the greenhouse gas CO2. This also increased the atom economy of the process by reducing the reagents required, and minimising by-products.

6.1.3 Central Composite Face Centred Design

Shown in Table 6.48 is the experimental design table outlining the 4 factorial points, 4 axial points and 5 repetitions of the centre point.

Table 6.48: CCF experimental design table

Sample	Type of point	Temperature (°C)	x_1 coded value	Hold time (h)	x_2 coded value
O1	Factorial	500	-1	0.5	-1
O2	Factorial	900	1	0.5	-1
O3	Factorial	500	-1	2.5	1
O4	Factorial	900	1	2.5	1
O5	Axial	500	-1	1.5	0
O6	Axial	900	1	1.5	0
O7	Axial	700	0	0.5	-1
O8	Axial	700	0	2.5	1
O9	Centre	700	0	1.5	0
O10	Centre	700	0	1.5	0
O11	Centre	700	0	1.5	0
O12	Centre	700	0	1.5	0
O13	Centre	700	0	1.5	0

The matrix equations shown below allow for the calculation of the coefficients in matrix b to determine the model equation.

$$\begin{bmatrix} y_1 \\ y_2 \\ y_3 \\ y_4 \\ y_5 \\ y_6 \\ y_7 \\ y_8 \\ y_9 \\ y_{10} \\ y_{11} \\ y_{12} \\ y_{13} \end{bmatrix} = \begin{bmatrix} 1 & -1 & -1 & 1 & 1 & 1 \\ 1 & 1 & -1 & 1 & 1 & -1 \\ 1 & -1 & 1 & 1 & 1 & -1 \\ 1 & 1 & 1 & 1 & 1 & 1 \\ 1 & -1 & 0 & 1 & 0 & 0 \\ 1 & 1 & 0 & 1 & 0 & 0 \\ 1 & 0 & -1 & 0 & 1 & 0 \\ 1 & 0 & 1 & 0 & 1 & 0 \\ 1 & 0 & 0 & 0 & 0 & 0 \\ 1 & 0 & 0 & 0 & 0 & 0 \\ 1 & 0 & 0 & 0 & 0 & 0 \\ 1 & 0 & 0 & 0 & 0 & 0 \\ 1 & 0 & 0 & 0 & 0 & 0 \end{bmatrix} \begin{bmatrix} b_0 \\ b_1 \\ b_2 \\ b_{11} \\ b_{22} \\ b_{12} \end{bmatrix}$$

6.2 Yield Optimisation

The yields detailed below are the overall yields after both pyrolysis and the acid washing process.

The yields of each of the samples produced according to the design of experiments outlined above are detailed in Table 6.49 below.

Table 6.49: Overall yield data for optimisation design of experiments biochar samples

Sample	Overall yield (% dried BSG basis)
O1	28.5
O2	20.4
O3	29.5
O4	8.2
O5	28.6
O6	11.0
O7	25.7
O8	24.8
O9	24.7
O10	23.9
O11	25.0
O12	23.5
O13	26.9

The model equation for the overall yield can be seen in Equation 6.1:

$$y = 24.6 - 7.8x_1 - 2x_2 - 4.3{x_1}^2 + 1.1{x_2}^2 - 3.3x_1x_2 \quad (6.1)$$

The model was used to acquire a surface response plot, showing both the model data and the experimental points. This can be seen from two angles in Figure 6.78.

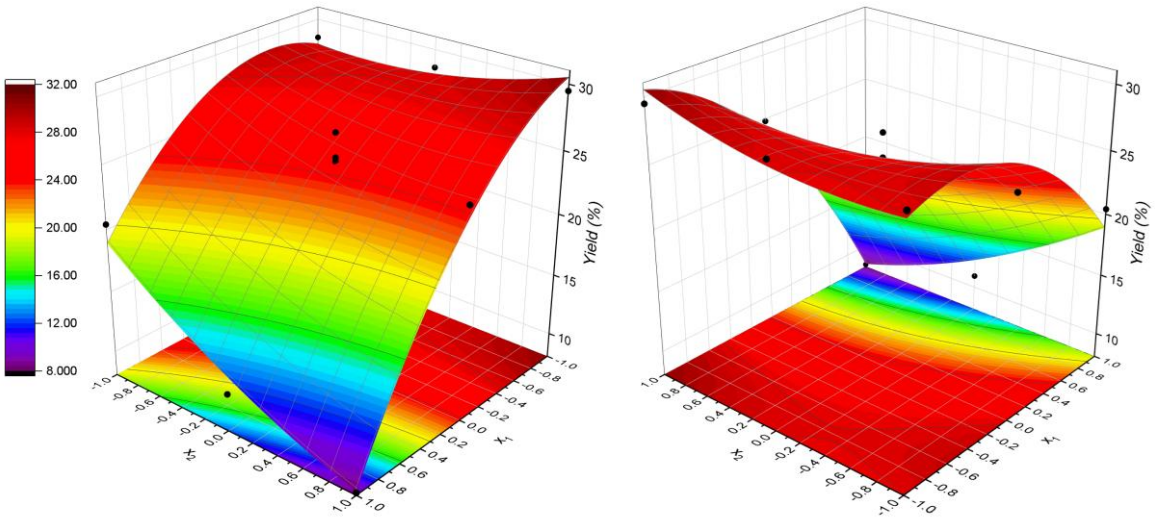

Figure 6.78: Yield surface response plots as a function of hold temperature and hold time, front face (left), back face (right)

The model predicts a minimum yield of 8.3% at the factorial point where hold temperature is 900 °C and hold time is 2.5 h. This logically makes sense, as pyrolysis and gasification will be most complete under these conditions. This is in very close agreement with the experimental point obtained under these conditions, with a yield of 8.2%. The model predicts a maximum yield of 30.5% at the factorial point where the hold temperature is 500 °C and the hold time is 2.5 h. This is also close to the experimental point, O3, with a yield of 29.5%. This is an unexpected result as it could reasonably be predicted that the highest yield would be produced at the lowest temperature and shortest hold time. This unexpected result may be down to natural variation in the feedstock, which is known to be less homogenous at higher yields, due to the different levels of macromolecules in the material and/or due to the washing process. It could also be down to the poor estimation of the quadratic effects giving rise to inaccurate results, as discussed before in Section 6.1.

6.3 Surface Area Optimisation

The BET surface area data obtained for the biochars produced in the optimisation design of experiments are shown in Table 6.50.

Table 6.50: BET surface areas of optimisation design of experiments biochar samples[11]

Sample	BET Surface area ($m^2\ g^{-1}$)
O1	18 ± 0
O2	446 ± 0
O3	1 ± 0
O4	1273 ± 5
O5	20 ± 0
O6	1064 ± 3
O7	106 ± 0
O8	92 ± 0
O9	78 ± 0
O10	111 ± 0
O11	98 ± 1
O12	25 ± 1
O13	54 ± 0

The model equation for the BET surface area is shown in Equation 6.2:

$$y = 91.6 + 457.3x_1 + 132.7x_2 + 404.4{x_1}^2 - 38.6{x_2}^2 + 211.0x_1x_2 \qquad (6.2)$$

The surface response plots describing this model for BET surface area can be seen in Figure 6.79[12].

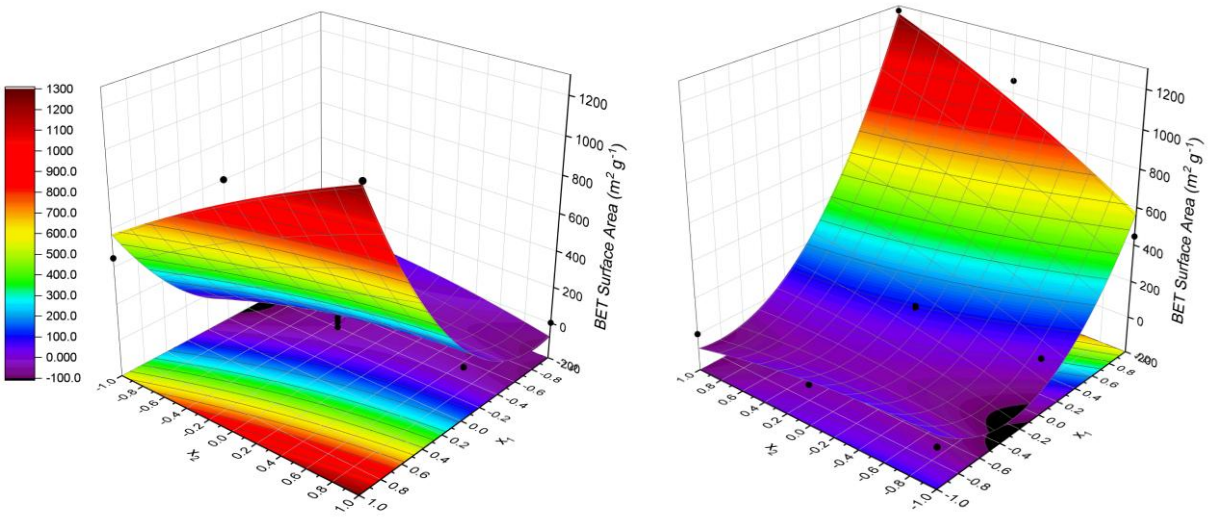

Figure 6.79: BET surface area model response plot as a function of hold temperature and hold time, front face (left), back face (right)

[11] Errors calculated from regression error on BET isotherm fits, the error propagation equations are detailed in Appendix D

[12] It should be noted that the plots represent the mathematical models determined through design of experiments and consequently show negative values, which have no physical meaning. This is discussed later within the analysis.

The model predicts a maximum surface area of 1258 $m^2 g^{-1}$ at the factorial point of a hold temperature of 900 °C and a hold time of 2.5 h. This is close to the experimental value obtained at this point (O4) with a BET surface area value of 1273 $m^2 g^{-1}$, but still lies outside of the reported error value for this experimental point. This coincides with the lowest yield, as seen in Section 6.2 and is a logical result, as with more pyrolysis, more volatile material is removed and leaves behind void spaces, opening up more of the porous matrix of the material, and creating a greater number of sites for nitrogen adsorption. The model predicts a surface area minimum of -90 $m^2 g^{-1}$, at a hold temperature of 535 °C and a hold time of 2.5 h. While a negative surface area is an impossible result, the preclusion of non-positive values cannot be accounted for in this model; it is, thus, assumed that the material created under these conditions would have a BET surface area within the margin of error of 0 $m^2 g^{-1}$. The observed global minimum is likely a false minimum, a plateau of multiple minima would be expected. This cannot be modelled using the quadratic model equation employed in this work. As the quadratic model equation contains only one turning point, the model equation attempts to globally average this expected plateau area around zero, giving rise to the large negative area seen. Where the surface response plot shows a large negative area can be assumed to be an error of the model equation; in reality, these would be surface areas of zero. The biochars produced under these conditions would be non-porous, having multiple minima on the response plot. This would fit better with the results seen in the screening design of experiments, with all of the biochars of group ***α***, produced at 500 °C, showing no porosity. By choosing a 'useful' porosity threshold of 100 $m^2 g^{-1}$, the response plot and model equation show that for a hold time of 0.5 h, a temperature of at least 786 °C is required, and for a hold time of 2.5 h a lower temperature of 672 °C is required. This shows the trade-off required in the relationship between residence time and temperature to ensure porosity is created within the synthesised biochars.

An unexpected trend is, however, shown in the model, as it also produces some anomalous results, at low hold times and low temperatures. Higher surface areas than would be expected around factorial point O1, produced at 500 °C and 0.5 h, are projected by the model. The model predicts a surface area of 78 $m^2 g^{-1}$ at factorial point O1, while the experimental data shows a surface area of 18 $m^2 g^{-1} \pm 0$, showing the model predicts far outside of the calculated error range. Logically this point would have the lowest level of pyrolysis, as it is produced at the lowest temperature and hold time investigated, giving the lowest surface area and smallest pore volume. This anomaly is an artefact of the symmetric

property of parabolic quadratic functions used in this study, increasing after the minima giving this anomalous result. The model incorrectly predicts an increase in surface areas in some chars produced at temperatures lower than 532 °C. The introduction of the 'useful' porosity limit designated above still has these chars lower than the 100 $m^2 g^{-1}$ limit and, therefore, they are still designated as non-porous in this work.

6.4 Short Residence Time Kinetics Optimisation

The adsorption uptakes obtained for methyl orange after 1 h of adsorption, for each of the samples produced according to the optimisation design of experiments, are shown in Table 6.4 below.

Table 6.51: Methyl orange adsorption uptakes on optimisation design of experiments biochar samples after 1 h[13]

Sample	Methyl Orange uptake (mg g^{-1})
O1	1 ± 0
O2	3 ± 0
O3	0 ± 0
O4	86 ± 0
O5	0 ± 0
O6	49 ± 0
O7	1 ± 0
O8	0 ± 0
O9	0 ± 0
O10	2 ± 0
O11	1 ± 0
O12	0 ± 0
O13	1 ± 0

The model equation for the 1 h residence time adsorption experiments is shown in Equation 6.3:

$$y = 1 + 22.8x_1 + 13.5x_2 + 22.9{x_1}^2 - 1.1{x_2}^2 + 21.0x_1x_2 \qquad (6.3)$$

The surface response plots describing this model for the 1 h methyl orange adsorption experiments can be seen in Figure 6.80[14].

[13] Errors calculated from propagation of error in Beer-Lambert fit, the error propagation equations are detailed in Appendix D

[14] It should be noted that the plots represent the mathematical models determined through design of experiments and consequently show negative values, which have no physical meaning. This is discussed later within the analysis.

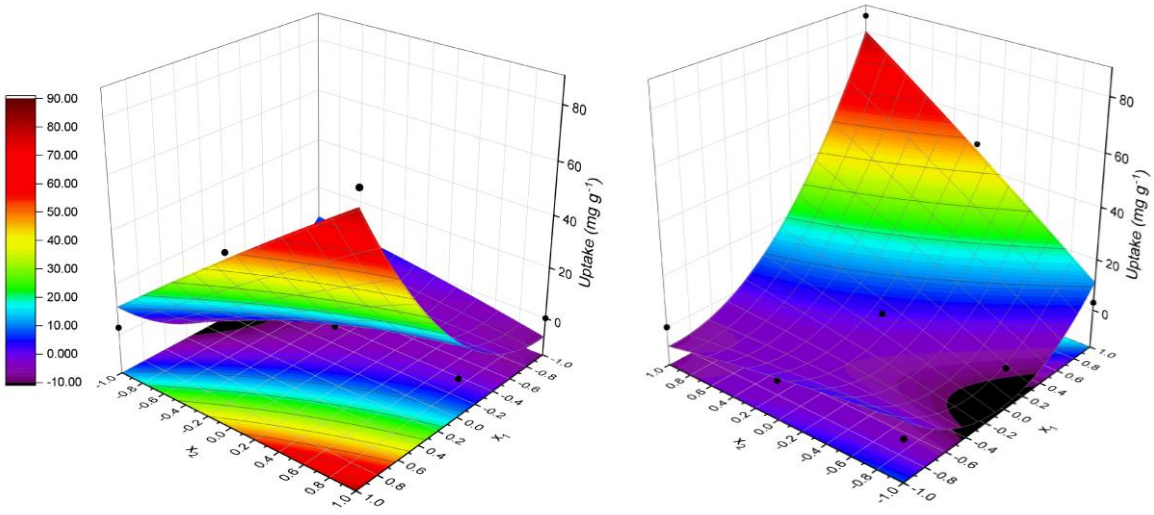

Figure 6.80: 1 h methyl orange liquid phase adsorption experiment surface response plot as a function of hold temperature and hold time, front face (left), back face (right)

The model predicts a maximum uptake of 80 mg g^{-1}, occurring at a pyrolysis temperature of 900 °C and a hold time of 2.5 h, coinciding with the maximum surface area and minimum yield synthesis conditions. The model prediction shows good agreement with the experimental point O4, which demonstrated an uptake of 86 mg g^{-1}. The model predicts a minimum of -8 mg g^{-1}, at a hold temperature of 508 °C a hold time of 2.5 h. The negative value implies an increase in methyl orange concentration in the bulk, which is not possible when using clean, unadsorbed adsorbents. This inaccuracy in the model is down to the inability of the model to have multiple minima, as described by the data, with many experimental points showing uptakes of 0 mg g^{-1}, which is the practical minimum uptake expected in this experimental set up. Similar to the case described in Section 6.3, all negative uptake values should be recorded as 0 mg g^{-1} during analysis.

6.5 Long Residence Time Kinetics Optimisation

The adsorption uptakes of methyl orange on each of the samples produced according the optimisation design of experiments, after 7 days exposure, are shown in Table 6.52 below.

Table 6.52: Methyl orange adsorption uptakes on optimisation design of experiments biochar samples after 7 days[15]

Sample	Methyl Orange uptake (mg g^{-1})
O1	0 ± 0
O2	11 ± 0
O3	0 ± 0
O4	97 ± 0
O5	0 ± 0
O6	97 ± 0
O7	0 ± 0
O8	0 ± 0
O9	0 ± 0
O10	0 ± 0
O11	0 ± 0
O12	0 ± 0
O13	0 ± 0

The model equation for the 7-day residence time adsorption experiments is shown in Equation 6.4:

$$y = 3.0 + 34.2x_1 + 14.3x_2 + 38.1{x_1}^2 - 10.4{x_2}^2 + 21.5x_1x_2 \qquad (6.4)$$

The surface response plots describing this model can be seen in Figure 6.81[16].

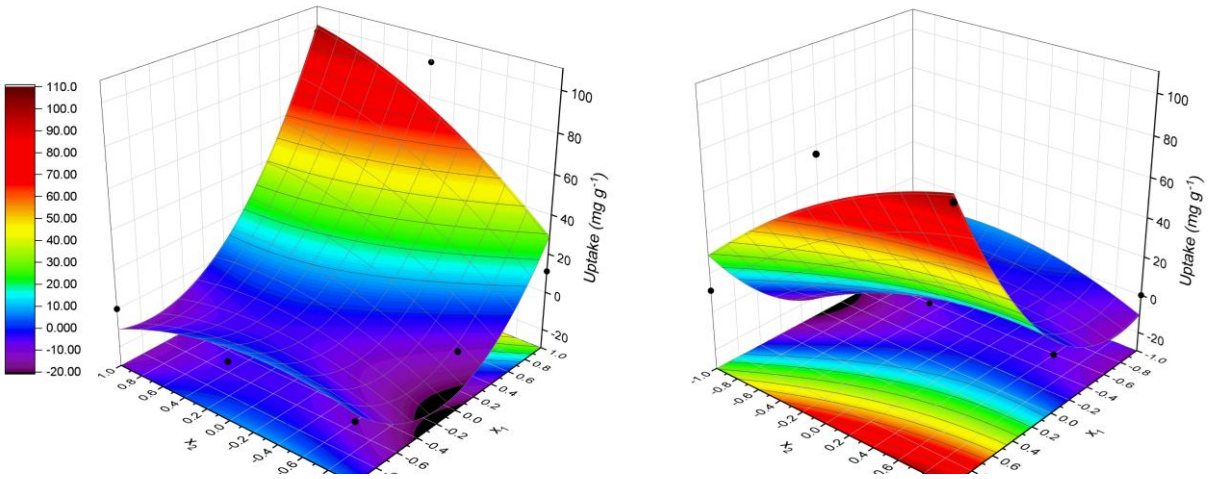

Figure 6.81: 7-day methyl orange adsorption experiments surface response plot as a function of hold temperature and hold time, front face (left), back face (right)

[15] Errors calculated from propagation of error in Beer-Lambert law fit, the error propagation equations are detailed in Appendix D

[16] It should be noted that the plots represent the mathematical models determined through design of experiments and consequently show negative values, which have no physical meaning. This is discussed later within the analysis.

The model predicts a maximum uptake of 101 mg g^{-1}, at a hold temperature of 900 °C and a hold time of 2.5 h, coinciding with the maximum surface area, maximum uptake after 1 h, and minimum yield. While an uptake of 101 mg g^{-1} is not possible, as the theoretical maximum is 100 mg g^{-1} due to the volume concentration and mass of adsorbent used, the value is in close agreement with the experimental value observed for point O4 of 97 mg g^{-1}. The model predicts a minimum uptake of -13 mg g^{-1} at a hold temperature of 554 °C and a hold time of 2.5 h. Similar to the discussion in Section 6.4, these negative uptakes are not possible in this system and are an artefact of the quadratic model equation being unable to have multiple minima. These negative values should be taken as 0 mg g^{-1} for the purpose of analysis.

In the actual calculation of the methyl orange uptake, some of the above values, reported as 0 mg g^{-1}, were in fact calculated as negative uptakes ranging from -3 to -11 mg g^{-1}. As the biochars were fresh and contained no methyl orange to desorb and increase the concentration of methyl orange in the system, the reason given for the greater concentration was loss of water from these flasks through evaporation. While parafilm and aluminium foil were used to seal the flasks and prevent temperature effects, evidently this was insufficient to prevent evaporation of the aqueous phase of the methyl orange solutions. Extra care was taken in future work to perfectly seal the flasks with multiple layers of parafilm, especially during temperature elevated studies where evaporation would be enhanced.

As the theoretical maximum uptake of the experiments is 100 mg g^{-1}, samples O4 and O6 also showed the necessity for increasing the total mass of adsorbent in the flasks to allow for saturation of the adsorbents to occur. To ensure maximum comparability with the literature standard, i.e. 100 mg L^{-1} concentrations, the increase in adsorptive mass was achieved by increasing the volume of the methyl orange solution. Trial studies with samples O4 and O6 were carried out with 20 mL and 30 mL volumes of 100 mg L^{-1} methyl orange solution at 7 days residence time. The results obtained are shown below in Table 6.53.

Table 6.53: Adsorption uptake of MO on O4 and O6 at varying solution volumes[17]

Volume of 100 mg L^{-1} MO solution	Uptake on O4 (mg g^{-1})	Uptake on O6 (mg g^{-1})
10	97 ± 0	97 ± 0
20	184 ± 0	155 ± 0
30	240 ± 0	191 ± 0

The 20 mL experiment using O4 showed a value of 184 mg g^{-1}, close to maximum value of 200 mg g^{-1} with a percentage uptake of 92%. This is still very near completion, while the 30 mL studies showed uptakes much farther away from the theoretical maximum of 300 mg g^{-1}, with percentage uptakes of 80% and 54% for O4 and O6, respectively. The volume of solution in the flasks was therefore increased to 30 mL for all future liquid phase adsorption experiments.

Once again it should be noted that the above values are from single batch adsorption experiments without repetition. These samples will have full liquid phase isotherm studies described in Chapter 7.

Table 6.54 below compares the maximum uptakes of methyl orange dye of the highly adsorbing materials from this work with other carbonaceous adsorbents reported in the literature.

Table 6.54: Comparison of O4 and O6 with other methyl orange adsorbents from literature

Sample	q_{max} (mg g^{-1})	Reference
O4	240	This work
O6	191	This work
Biochar from Hazelnut Shell	182	(173)
Biochar from Cellulose	167	(173)
Biochar from Glucose	147	(173)
Biochar from Pomelo Peel	163	(174)
Biochar from Chicken Manure	41.5	(175)
Activated Carbon from Coconut Shell	3	(176)
Activated Carbon from Aloe Vera	196	(177)

[17] Errors calculated from propagation of error in Beer-Lambert law fit, , the error propagation equations are detailed in Appendix D

The uptake reported for O6 is comparable with the highest performing materials from the literature, such as the biochar derived from hazelnut shell and activated carbon derived from aloe vera, indicating it as a viable candidate for methyl orange removal in water treatment applications. However, the optimal sample, O4, vastly outperforms the other materials shown here. Sample O4 outperforms the best material from the literature, the activated carbon from aloe vera by approximately 22% indicating it may be an exceptionally effective adsorbent for the remediation of organic dyes.

It is important to note that the q_{max} values from the literature reported above were obtained through Langmuir isotherm modelling, whereas the values for O4 and O6 were determined from a single sample with an initial concentration of 100 mg L^{-1}. Consequently, the true q_{max} values for O4 and O6 may be even greater than those reported here.

6.6 Optimisation ANOVA

Analysis of variance (ANOVA) was carried out on the 4 models obtained above using Minitab 22 software. The ANOVA analysis was used to determine the significance of the factors, the curvature and the interactions within the models. The ANOVA table is shown with Table 6.55 below.

Table 6.55: Optimisation ANOVA data

Source	DF	Adj SS	Adj MS	F-Value	P-Value
Yield					
Model	5	488.649	97.73	37.02	0.000
x_1	1	368.167	368.167	139.47	0.000
x_2	1	24.402	24.402	9.24	0.019
x_1*x_1	1	51.643	51.643	19.56	0.003
x_2*x_2	1	3.501	3.501	1.33	0.287
x_1*x_2	1	43.56	43.56	16.5	0.005
Lack-of-Fit	3	11.518	3.839	2.21	0.23
Pure Error	4	6.96	1.74		
Total	12	507.128			
Surface Area					
Model	5	2033514	406703	32.32	0.000
x_1	1	1254923	1254923	99.73	0.000
x_2	1	105603	105603	8.39	0.023
x_1*x_1	1	451788	451788	35.91	0.001
x_2*x_2	1	4105	4105	0.33	0.586

x_1*x_2	1	178084	178084	14.15	0.007
Lack-of-Fit	3	83320	27773	23.34	0.005
Pure Error	4	4759	1190		
Total	12	2121593			
Short Residence Time Kinetics					
Model	5	7617.8	1523.56	17.74	0.001
x_1	1	3128.17	3128.17	36.43	0.001
x_2	1	1093.5	1093.5	12.73	0.009
x_1*x_1	1	1445.75	1445.75	16.84	0.005
x_2*x_2	1	3.47	3.47	0.04	0.846
x_1*x_2	1	1764	1764	20.54	0.003
Lack-of-Fit	3	598.33	199.44	284.92	0.000
Pure Error	4	2.8	0.7		
Total	12	8218.92			
Long Residence Time Kinetics					
Model	5	14154.8	2830.97	12.77	0.002
x_1	1	7004.2	7004.17	31.6	0.001
x_2	1	1232.7	1232.67	5.56	0.05
x_1*x_1	1	4013.6	4013.56	18.11	0.004
x_2*x_2	1	297.5	297.54	1.34	0.285
x_1*x_2	1	1849	1849	8.34	0.023
Lack-of-Fit	3	1551.5	517.15	*	*
Pure Error	4	0	0		
Total	12	15706.3			

Significant at p-value <0.05

Model summaries were also obtained to help describe how well the models predict the responses. The model summaries are shown in Table 6.56 below.

Table 6.56: Optimisation ANOVA model summaries

Model	**S**	**R^2**	**R^2 (Adjusted)**	**R^2 (Predicted)**
Yield	1.62474	96.36%	93.75%	75.77%
Surface Area	112.173	95.85%	92.88%	61.63%
Short Residence Time Kinetics	9.26689	92.69%	87.46%	25.91%
Long Residence Time Kinetics	14.8875	90.12%	83.07%	6.26%

6.6.1 Yield

The yield model shows strong overall significance, with a very low model p-value. Both main effects (x_1 and x_2) are highly significant, and their interaction is also significant, indicating that the factors influence each other. The ANOVA results show clear curvature in x_1, while curvature in x_2 is not detected. This makes the x_2^2 term statistically non-significant, its presence may be introducing noise but it does not cause instability in the model. Importantly, the lack-of-fit test is not significant ($p = 0.23$), meaning the quadratic model adequately captures the shape of the response surface. As a result, the model achieves high R^2 and adjusted R^2 values that are close together indicating a stable model. The strong predicted R^2, indicates that the yield model is reliable for predicting new values.

6.6.2 Surface Area

The surface area model also shows strong overall significance ($p=0.000$). The main effect x_1 is highly significant, and x_2 and the interaction term are also significant contributors. As with yield, the model detects curvature in x_1 but not in x_2, making the x_2^2 term non-significant and a likely source of noise. Unlike the yield model, however, the ANOVA indicates a significant lack-of-fit. The relatively low pure error mean square compared with the much larger lack-of-fit mean square shows that the model predictions deviate from the real data more than can be explained by random variation alone. This suggests that the quadratic model form does not fully capture the true response behaviour for surface area and may require additional or alternate terms to accurately represent the data. Although the model achieves high R^2 and adjusted R^2 values, the significant lack-of-fit results in a much lower predicted R^2, meaning the model performs poorly when predicting new points. Future work could improve this model by removing the non-significant x_2^2 term and refitting the model.

6.6.3 Short Residence Time Kinetics

The short residence time kinetics model is statistically significant overall, with a high F-value and low model p-value. The main effects x_1 and x_2, as well as the interaction term, are significant. Curvature is detected in x_1, but not in x_2, as shown by the extremely high p-value for x_2^2 (0.846). The lack-of-fit is highly significant, and the combination of a very low pure error mean square with a very large lack-of-fit mean square indicates that the overall shape of the modelled surface deviates substantially from the underlying response behaviour. The model summary shows high R^2 and adjusted R^2 values, but a very low predicted R^2, meaning

the model fits the existing data well but does not generalise well and performs poorly when predicting new values. Removing the non-significant x_2^2 term in future work may help reduce overfitting and noise.

6.6.4 Long Residence Time Kinetics

The long residence time kinetics model shows strong overall significance, with a low model p-value and high F-value. The main effect x_1, the interaction term $x_1 \cdot x_2$, and the quadratic term x_1^2 were all shown to be significant by ANOVA. The main effect x_2 shows borderline significance ($p = 0.05$), but due to the significant interaction term, it must remain in the model. As with the other responses, the quadratic term x_2^2 is non-significant, indicating no curvature in x_2 and contributing unnecessary noise. The lack-of-fit test cannot be computed because the pure error mean square is zero, caused by identical centre-point replicates. However, the large lack-of-fit mean square suggests that the model would likely show significant lack-of-fit if the test were calculable. The model achieves high R^2 and adjusted R^2 values, but the very low predicted R^2 indicates the model will be poor at predicting new points. Removing the non-significant x_2^2 term in future work would help reduce overfitting.

6.6.5 ANOVA Summary

Across all four models, the quadratic term for hold time (x_2^2) is consistently non-significant, indicating that hold time behaves linearly across the experimental range. Removing x_2^2 in future modelling would reduce noise and help improve lack-of-fit. All models show high R^2 and adjusted R^2 values, but only the yield and surface area models achieve satisfactory predicted R^2 values, meaning only these two are suitable for predicting responses outside the measured data points. However, the optimal synthesis conditions of 900 °C and 2.5 hours lie directly on an experimental point within the design space. Because this point is part of the dataset, the model accurately describes it, and it can be considered a reliable optimum for the purposes of this work.

6.7 Optimisation Conclusions

The optimisation design of experiments was successfully employed to determine biochars with high efficacy of removing methyl orange dye molecules from solution. The chars produced showed a reciprocal relationship between yield and adsorption capacity and adsorption kinetic performance, and a proportional relationship between surface area and adsorption capacity and adsorption kinetic performance.

The optimisation design of experiments did however come with some draw backs. Unphysical and impossible results like negative surface areas and negative adsorption uptakes were noted due to the simplicity and choice of model used. The model also only allowed for a single global minimum also giving rise to unexpected and incorrected results, this was also assigned as a shortcoming of the model employed in this work. As the optimal biochar, sample O4, was found in the upper corner of the design space at the maximum hold time and maximum temperature investigated, if future work was to be carried out, a widening of the design space is advised. This may lead to chars with higher surface areas and better adsorption performance, but will likely further reduce the yield of the biochars which must be taken into account. Model term reduction to remove the x_2^2 term in all four optimisation models is also advised from the outcome of ANOVA to remove noise in future work.

However, despite the shortcomings of the model, it did allow for the identification of the optimal points and for the optimal biochar within the range investigated to be found in a reduced number of experiments. The chars O4 and O6 were both identified as having significant adsorption performance to remove methyl orange from aqueous solutions, and so will both be fully characterised through composition, gas adsorption analysis, surface chemistry, morphology and liquid phase adsorption tests. This is not only to determine their effectiveness but also to study the differences between the two in closer detail.

6.8 References

1. ÇAĞLAR E, Donar YO, SINAĞ A, BİROĞUL İ, Bilge S, Aydincak K, et al. Adsorption of anionic and cationic dyes on biochars, produced by hydrothermalcarbonization of waste biomass: effect of surface functionalization and ionicstrength. Turkish Journal of Chemistry. 2018;42(1):86-99.
2. Zhang B, Wu Y, Cha L. Removal of methyl orange dye using activated biochar derived from pomelo peel wastes: performance, isotherm, and kinetic studies. Journal of Dispersion Science and Technology. 2020.
3. Yu J, Zhang X, Wang D, Li P. Adsorption of methyl orange dye onto biochar adsorbent prepared from chicken manure. Water Science and Technology. 2018;77(5):1303-12.
4. Islam MS, Ang BC, Gharehkhani S, Afifi ABM. Adsorption capability of activated carbon synthesized from coconut shell. Carbon letters. 2016;20:1-9.
5. Khaniabadi YO, Heydari R, Nourmoradi H, Basiri H, Basiri H. Low-cost sorbent for the removal of aniline and methyl orange from liquid-phase: aloe vera leaves wastes. Journal of the Taiwan institute of chemical engineers. 2016;68:90-8.

7. Optimal Biochar Characterisation

7.1 Sample Composition and Synthesis

7.1.1 Yield and Proximate Analysis

The optimal sample O4 (synthesised at 900 °C, 2.5 h hold time, 20 °C min^{-1} ramp rate and nitrogen and carbon dioxide gas flowrates of 100 mL min^{-1}) and O6 (synthesised at 900 °C, 1.5 h hold time, 20 °C min^{-1} ramp rate and nitrogen and carbon dioxide gas flowrates of 100 mL min^{-1}) from Chapter 6, were reproduced in order to provide sufficient sample for full characterisation, this duplicate synthesis also allowed for error analysis of the obtained yields. The samples from Chapter 6 will be referred to as O4.1 and O6.1; the samples synthesised for the full characterisation will be referred to as O4.2 and O6.2. All characterisation and analysis, unless otherwise stated, was carried out on samples O4.2 and O6.2. The average yields, with errors and proximate analysis data, are shown in Table 7.57.

Table 7.57: Average yields for O4 and O6 and proximate analysis data for samples O4.2 and O6.2

Sample	*Total Yield[18] (% dry basis)*	*Moisture (%)*	*Volatiles (%)*	*Fixed carbon (%)*	*Ash (%)*
O4	7.6 ± 0.4	4.6	15.7	67.8	11.9
O6	10.8 ± 0.1	1.6	39.7	50.6	8.1

The samples both exhibit compositions close to the 10 % ash content consent limit, which this was deemed acceptable for the current study but should be noted for future studies and/or potential commercialisation of these and related materials.

A chart of the proximate compositions of the synthesised materials per 100g of BSG feedstock is shown in Figure 7.82. The samples have consistent amounts of ash and fixed carbon with only the amount of volatile carbon and water varying between the samples. While O4 and O6 were both produced at 900 °C, O4 was subject to a longer hold time (2.5 h compared to 1.5 h for O6), which resulted in a decrease in the mass of volatile carbon and an increase in fixed carbon. This is consistent with the pattern shown in the proximate analysis data obtained within the screening investigation, reported in Section 5.1.1, where a higher degree of pyrolysis increases the fixed carbon fraction of the synthesised biochars,

[18] Samples were synthesized in duplicate for the purpose of error calculation, the standard error equation is detailed in Appendix D

affecting the surface chemistry, which can lead to varying water adsorption on the surface of the materials.

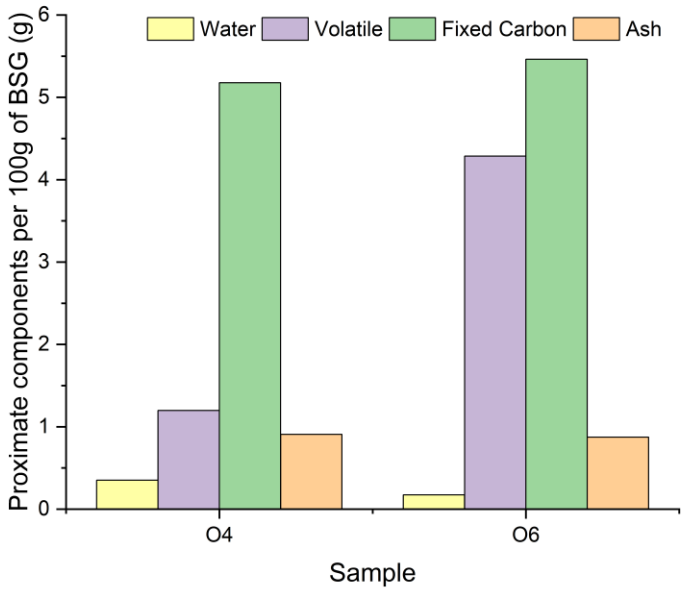

Figure 7.82: Proximate components per 100g of BSG of samples O4 and O6

7.1.2 CHN Elemental Analysis

Carbon, hydrogen and nitrogen elemental analysis was carried out on both of the optimised samples in duplicate; the results can be seen in Table 7.58.

Table 7.58: CHN elemental analysis of samples O4 and O6[19]

Sample	*Carbon (%)*	*Hydrogen (%)*	*Nitrogen (%)*	*Other (%)*
O4	68.8 ± 2.0	0.5 ± 0.1	3.0 ± 0.1	27.7. ± 2.2
O6	73.7 ± 0.0	0.2 ± 0.0	3.2 ± 0.0	22.9. ± 0.0

A chart of the elemental compositions of the synthesised materials per 100 g of BSG feedstock is shown in Figure 7.83. Again, viewing the data in terms of the greater degree of pyrolysis, moving from O6 to O4, the data shows a slight decrease in the masses of nitrogen and 'other' elements, however, there is a significant decrease in the relative mass of carbon within the sample. The decrease is still relevant when considering the comparative yields

[19] Errors calculated in duplicate from two samples of O4.2 and O6.2, the standard error equation is detailed in Appendix D

obtained for the two samples, with the reduction in carbon mass likely due to removal of the lignin macromolecular structure making up the volatile fraction, which is primarily comprised of carbon. The nitrogen decreases slightly due to the higher degree of pyrolysis removing surface nitrogen groups – notably, the protein fraction contained within the matrix of the material is left unpyrolysed. As was found from EDS analysis in Section 5.4.4.5, the 'other' elements in the biochars were found to be predominantly silicon and oxygen, with trace amounts of other metal and non-metal elements found. Some of these 'other' elements can be removed during a washing process, with higher ash removal levels seen for the materials synthesised using higher degrees of pyrolysis. This is further investigated for samples O4 and O6 in Section 7.3.4 and Section 7.3.5.

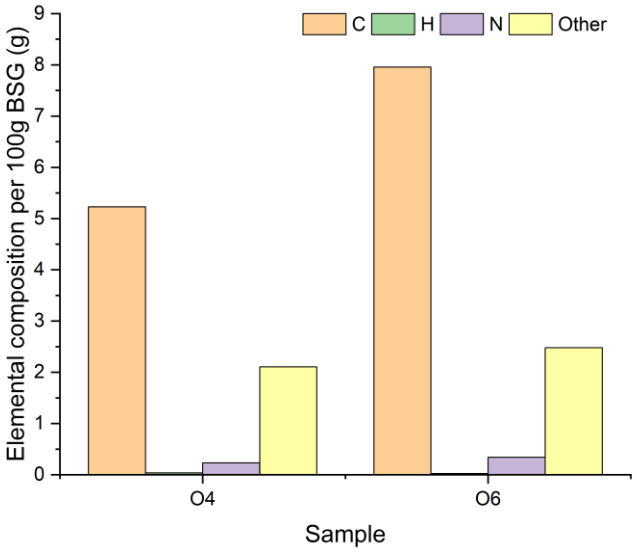

Figure 7.83: Elemental composition of samples per 100 g of BSG

7.2 Gas Adsorption Isotherms

7.2.1 Nitrogen Adsorption Isotherms

7.2.1.1 BET and Isotherm Analysis

Nitrogen adsorption isotherms (at 77.4 K) were obtained for the newly re-synthesised O4 and O6 samples. This data, in tandem with the nitrogen isotherms carried out to determine the surface areas of materials created in Chapter 6 (see Section 6.3) were used as duplicates to determine the average nitrogen adsorption characteristics of these samples. All isotherms can be categorised within the IUPAC classification system as Type I(b) with

Type H4 hysteresis, indicating that the materials contain wide micropores and small mesopores, similar in character to the 900 °C samples discussed in Section 5.2.1. All four newly acquired isotherms can be seen in Figure 7.84.

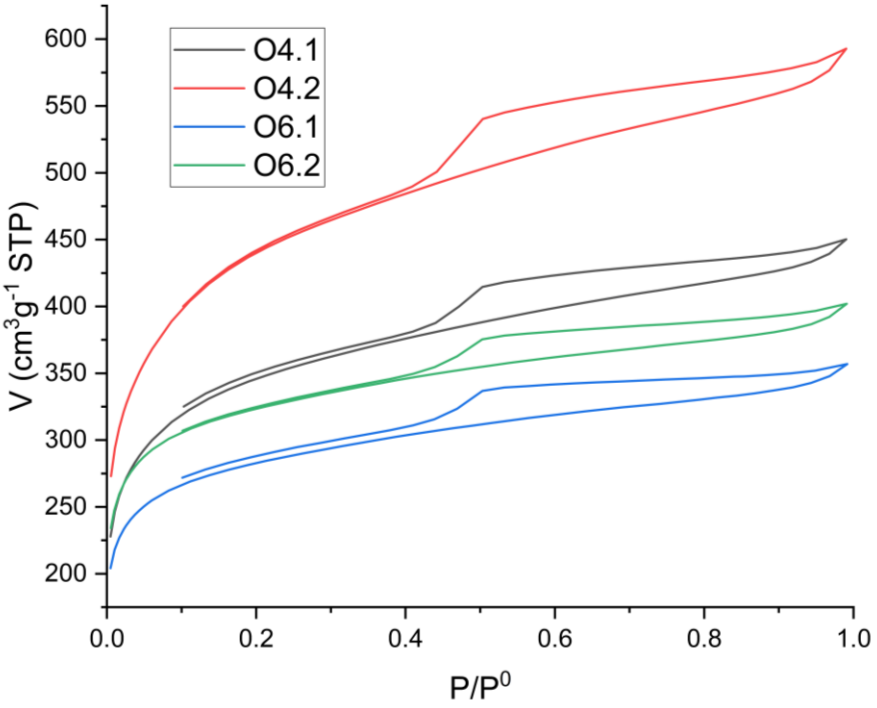

Figure 7.84: Nitrogen adsorption isotherms for both samples of O4 and O6

The data obtained was analysed using the BET isotherm model, employing the Rouquerol correction for calculation of the surface area of microporous materials. The monolayer capacity, BET constant, surface area, enthalpy of adsorption, IUPAC isotherm classification and hysteresis type are summarised in Table 7.59.

Table 7.59: BET parameters calculated from nitrogen adsorption isotherms on optimal biochar samples.[20]

Sample	*Monolayer capacity (cm^3g^{-1})*	*BET constant*	*BET Surface area (m^2g^{-1})*	*Enthalpy of adsorption($kJmol^{-1}$)*	*IUPAC isotherm classification*	*Hysteresis Type*
O4.1	292 ± 1	412 ± 35	1273 ± 5	9.4 ± 0.1	I(b)	H4
O4.2	366 ± 2	285 ± 24	1594 ± 7	9.2 ± 0.1	I(b)	H4
O4 Average	329 ±26	349 ± 45	1433 ± 114	9.3 ± 0.1	I(b)	H4
O6.1	244 ± 1	694 ± 52	1064 ± 3	9.7 ± 0.0	I(b)	H4
O6.2	278 ± 1	829 ± 120	1212 ± 4	9.9 ± 0.1	I(b)	H4
O6 Average	261 ± 12	762 ± 48	1138 ± 52	9.8 ± 0.0	I(b)	H4

The results show marked variation between the samples synthesised in the optimisation runs reported in Section 6.3 and the resynthesized samples for further characterisation. This is contrary to the very similar sample adsorption characteristics seen in the screening experiments in Section 5.2 which were also synthesised and tested in duplicate. One reason for the large variation in the samples could be due to aging effects in the BSG precursor material, which was stored in a frozen state, to preserve the 'as received' condition, prior to use. In the field of soil remediation, significant effects on biochar adsorption performance have been noted when studying sample aging, due to effects such as freeze/thaw action, leaching of soluble fractions through to rainfall or via biological degradation (178, 179). These processes have been shown to alter the pore volume, pore structure and surface functional groups of biochars, and often lead to an increase in surface area of the materials (180). Such an increase in surface area is demonstrated in the change from both O4.1 to O4.2, and O6.1 to O6.2, demonstrating an increase in available surface area for the samples synthesised from the precursor material which was kept frozen for longer. It is thought that the freezing process may not be a good long-term storage method, and that some form of aging has occurred between the two times for the sample syntheses, possibly as a consequence of raw material degradation. This may, however, be an advantage to the application of these biochars. As stated before, both aged samples exhibited higher surface

[20] Single sample errors found through regression error propagation, average sample error found through standard error formula. Standard error formula and error propagation equations are shown in Appendix D.

areas and monolayer capacities, while still maintaining the same highly microporous character, as shown through the isotherm shape and hysteresis type. This suggests that beneficial sample degradation may occur during storage, producing enhanced materials post-freezing. The high error in the averaged samples for O4 and O6 is thought to be a consequence of the associated storage method and aging effects. It should be noted that all the samples listed above in Table 7.59 show greater surface areas than the physically activated biochars derived from BSG listed in the literature and discussed in Section 1.4.4. In previous studies, the maximum surface area exhibited for a physically activated BSG carbon materials, produced using carbon dioxide, is 551 $m^2 g^{-1}$ (87).

7.2.1.2 Mesopore Size Characterisation

The isotherm data was analysed using the installed Micromeritics ASAP 2420 software, to determine the pore size distribution, using the BJH method. This allowed the pore size distribution within the mesopore range to be determined for both original and repeat samples of O4 and O6, showing dominant peaks in the distributions at 3 nm. The resulting BJH plots can be seen in Figure 7.85.

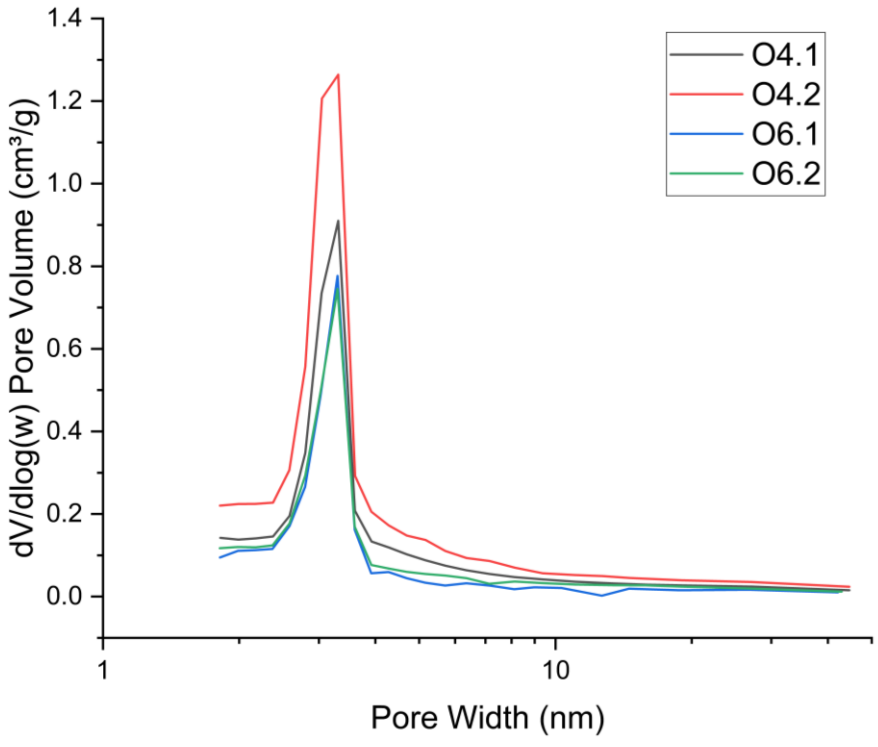

Figure 7.85: Mesopore size distributions for optimal biochars

The mesopore size distributions of the optimal biochars show good agreement with the mesopore size distributions of the biochars produced at 900 °C, as shown in Section 5.2.2.1, showing once again that the mesopore size distributions for the BSG biochars at 900°C are not possible to control based on the process parameters investigated in this work. This may imply that the mesopore size is inherent to the combination of precursor material and activation method used.

7.2.1.2 Micropore Size Characterisation

The Dubinin-Radushkevich equation was used to determine the microporous character of the optimal biochar samples, and the resulting Dubinin-Radushkevich plots can be seen in Figure 7.86. The data shows an upwards deviation in the high-pressure region, indicating a larger proportion of super micropores, greater than 1.4 nm in size, than would be expected from a Gaussian distribution in micropore sizes (as used to develop the Dubinin-Radushkevich equation).

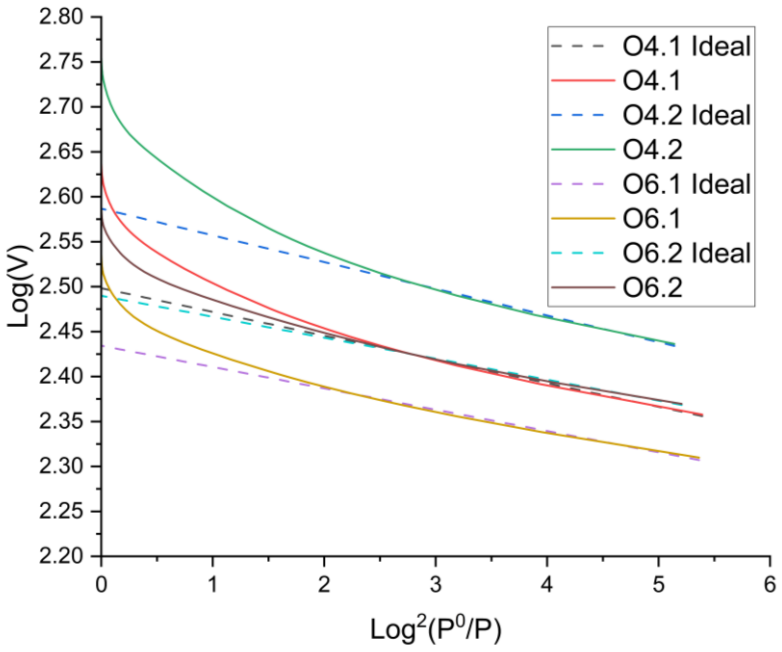

Figure 7.86: Dubinin-Radushkevich plots for O4 and O6

The data obtained from the Dubinin-Radushkevich plots were used to calculate the micropore area and percentage of the pore volume attributed to microporosity. The data is shown in Table 7.60 below.

Table 7.60: Dubinin-Radushkevich results for O4 and O6 samples[21]

Sample	*Micropore surface area (m^2g^{-1})*	*Percentage pore volume attributed to micropores (%)*
O4.1	1372 ± 12	69.9 ± 0.6
O4.2	1682 ± 18	65.1 ± 0.7
O4 Average	1527 ± 110	67.5 ± 1.7
O6.1	1184 ± 7	76.2 ± 0.5
O6.2	1345 ± 9	76.8 ± 0.5
O6 Average	1264 ± 57	76.5 ± 0.2

The samples show high micropore surface areas and high percentage pore volumes attributed to micropores, this is the same trend as the washed microporous biochars discussed in Section 5.4.3, with micropore surface area increasing with hold time from O6 to O4, but the percentage pore volume decreasing with increasing hold time. This, along with the surface area data shown in Table 7.59, indicates not just an increase in microporous surface area but an increase in mesopore volume with increase hold time and pyrolysis. This increase in mesopore volume is important for application in water treatment systems, due to the importance of such sub-structure sizes in transport of liquids through pores. It is worth noting that this may be partially responsible for the increased maximum adsorption capacity and speed of adsorption reported in Sections 6.4 and 6.5.

7.3 Surface Characterisation

7.3.1 Point of Zero Charge

The point of zero charge provides insight into the surface polarity of tested materials, and was determined using the salt addition method for both O4 and O6. The results obtained are summarised below in Table 7.61:

Table 7.61: Point of zero charge results for samples O4 and O6

Sample	*PZC (pH)*	*Net charge at pH 7*
O4	5.9	**Negative**
O6	6.4	Neutral

[21] Single sample errors found through regression error propagation, average sample errors found through standard error formula. Standard error formula and error propagation equations are shown in Appendix D.

The point of zero charge for these samples follows the same pattern reported in Section 5.4.4, where the more porous biochars, which had greater surface areas, demonstrated lower points of zero charge. This is thought to be due to the presence of a greater number of surface functional groups available for protonation, as the larger surface area gives greater contact between surface functional groups and the adsorptive solution. Sample O6 has a point of zero charge between that of sample S14W, produced at 900 °C and 0.5 h hold time (pH= 6.8), and samples S16W and O4, produced at 900 °C and 2.5 h hold time (pH=5.5 and pH 5.9, respectively). This follows the logic that longer hold times and, therefore, a higher degree of pyrolysis leads to a higher surface area and a lower point of zero charge. However, both samples S16W and O4, which were produced at the same temperature and hold time, have varying points of zero charge, which may be a result of other varying synthesis conditions for these chars. The synthesis conditions of O4 and S16W are detailed briefly in Table 7.62 below.

Table 7.62: Comparison of samples S16W and O4

Sample	Hold temperature (°C)	Hold time (h)	Ramp rate (°C min^{-1})	CO_2 flowrate (mL min^{-1})	N_2 flowrate (mL min^{-1})	Acid washing	PZC	Surface Area ($m^2 g^{-1}$)
S16W[22]	900	2.5	20	**600**	**600**	Yes	**5.5**	**1776 ± 12**
O4[23]	900	2.5	20	**100**	**100**	Yes	**5.9**	**1433 ± 114**

It can be seen from the data shown within the table that, while the chars only vary in process parameters deemed to be statistically insignificant to the response variables tested in Chapter 5, the response variables do show significant deviation. While it was shown, in Section 5.3.3, that the point of zero charge was independent of the five pyrolysis process parameters used in the study, and that, in Section 5.4.4.1, acid washing was successful at altering the point of zero charge, there may be a relationship previously not investigated between the pyrolysis process gas flowrates and the response variables after washing with the acid solution. For example, an increased carbon dioxide gas flowrate may lead to a

[22] Surface area error calculated through regression error propagation, the error propagation equations are shown in Appendix D.
[23] Surface area error calculated through standard error formula, the standard error formula is shown in Appendix D.

greater number of oxygen functional groups on the surface of the internal pores of the biochar, these oxygen functional groups contain lone pairs of electrons, which act as binding sites for protons, leading to a lower point of zero charge, and a more negative charge at pH 7. This increase of oxygen surface functional groups, alongside an increase in surface area, may have a synergistic effect, leading to greater proton adsorption during acid washing and a lower subsequent point of zero charge. However, due to the screening design of experiments being carried out prior to the acid washing experiments, it has not been possible, in the current study, to determine if either of the pyrolysis gas flowrates have a significant impact on the point of zero charge after washing, or if point of zero charge is purely a linked variable of surface area, which is, in turn, only dependent on hold temperature and hold time, as shown in Section 5.2.1. This should be investigated through further experiments.

Regardless, the biochars optimised in this work both show a positive point of zero charge at the acidic pH values of methyl orange solutions, making them ideal candidates for methyl orange adsorption.

7.3.2 Attenuated Total Reflectance Fourier Transform Infrared Spectroscopy

The ATR-FTIR spectra of samples O4 and O6, were measured as outlined in Section 4.5.4, and are shown in Figure 7.87.

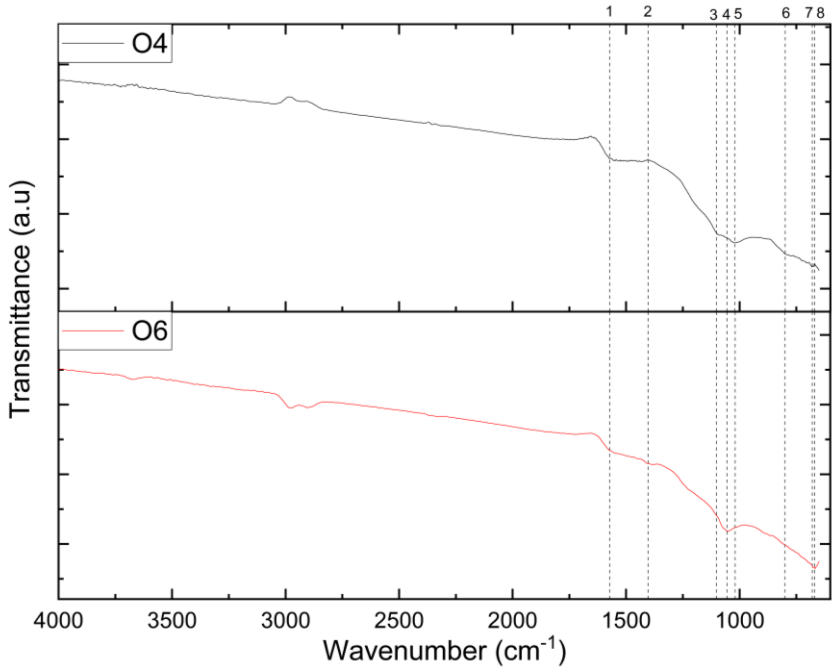

Figure 7.87: ATR FTIR spectra of samples O4 and O6

Table 7.63: Potential surface functional groups attributed to absorbance bands

Peak	Wavenumber (cm^{-1})	Present in O4	Present in O6	Potential functional group			
1	1572	Yes	Yes	C=C-C aromatic ring stretch	Secondary amine, >N-H bend		
2	1403	No	Yes	Phenol or tertiary alcohol, OH bend			
3	1102	Yes	No	Secondary alcohol, C-O stretch	Organic siloxane or silicone (Si-O-C)	Alkyl-substituted ether, C-O stretch	Skeletal C-C vibrations
4	1055	No	Yes	Organic siloxane or silicone (Si-O-Si)	Alkyl-substituted ether, C-O stretch	Primary amine, CN stretch	
5	1020	Yes	No	Organic siloxane or silicone (Si-O-Si)	Primary alcohol, C-O stretch	Primary amine, CN stretch	
6	800	Yes	No	Aromatic C-H out-of-plane bend	Skeletal C-C vibrations		
7	680	Yes	No	Alcohol, OH out-of-plane bend	Aromatic C-H out-of-plane bend		
8	670	No	Yes	Alcohol, OH out-of-plane bend	Aromatic C-H out-of-plane bend		

Table 7.63 details the absorbance peaks exhibited within the two spectra and potential functional groups to which they are ascribed. The peaks at approximately 3000 cm^{-1} were

not included in the analysis, as these were thought to be due to residual acetone used to clean the ATR crystal between runs.

The ATR-FTIR results show significant distortion of the peaks, similar to the samples reported in Section 5.3.2. These distortions are thought to be due to the highly absorbing nature of the black coloured biochar materials, their resulting high refractive index, and the nature of ATR-FTIR measurement principles. Due to this issue, significant difficulty was encountered during this analysis of these measurements and should be cross validated with other surface characterisation methods.

Sample O4 showed five absorbance bands, denoted as peaks 1, 3, 5, 6 and 7 in Table 7.63. Peaks 1, 6 and 7 could be attributed to the aromatic ring structures present in the material, arising from the polyphenolic lignin material that remains unpyrolysed post-synthesis. Peaks 1 and 5 may be attributed to amine groups, which could be present due to the known high protein content of the BSG precursor material, which is confirmed by the high nitrogen content determined from CHN measurements shown in Section 7.1.2. Peak 3 could be indicative of an oxygen containing functional group, such as a secondary alcohol or ether C-O stretch, or possibly indicative of a silicon and oxygen containing group such as siloxane and silanol on the surface of the material.

Sample O6 showed four absorbance bands, designated as peaks 1, 2, 4 and 8 in Table 7.63. Peaks 1 and 8 are indicative of the aromatic rings structures resulting from lignin, as described above. Peak 2 is indicative of a phenolic alcohol group, also known to be present in the polyphenolic lignin structures present in the materials, peak 8 could also be the OH out of plane bend resulting from these phenol groups. Peak 4 may be attributed to an amine stretch, an ether or the silicon and oxygen containing surface functional groups similar to those observed for O4.

Both samples show evidence of aromatic carbon, oxygen and nitrogen containing surface functional groups typical of an activated carbon while also presenting evidence of inorganic silicon containing functional groups like those identified through EDS in Chapter 5. These different chemical moieties should provide a wide variety of sites for the adsorption of methyl orange dye through a wide variety of intermolecular interactions. These findings will be helpful in determining the mechanism of adsorption in future work.

7.3.3 X-ray Photoelectron Spectroscopy

The relative atomic concentrations of the functional groups found on the surface of samples O4 and O6 were determined at three separate analysis spots on the surface, and are shown in Table 7.64. An example of the three XPS scans curves with deconvoluted peaks for sample O4 Point 1 and fitting data can be seen in Appendix F.

Table 7.64: XPS atomic functional group percentages for optimised samples[24]

Binding energy (eV)		284.6	285.5	288	398.2	400.8	402.8	532.4	533.2	535.5
Functional Group		C=C	C-C	C=O	N6	N-Q	N-X	O-I	O-II	O-III
Sample	Point	Relative atomic concentration (%)								
O4	1	32	27	20	2	7	3	2	6	1
	2	29	27	20	1	9	3	2	7	1
	3	28	28	21	1	8	2	2	8	1
O6	1	26	28	24	2	8	4	1	6	1
	2	25	27	18	3	14	2	2	7	1
	3	29	27	20	2	10	3	2	5	2

Sample O4 showed good consistency across all 3 analysis spots investigated, with relatively similar percentages found for all functional groups present on the sample surface. It showed 28-32 % C=C, 27-28 % C-C, and 20-21 % C=O. This almost 1:1 ratio of C=C to C-C is consistent with the expected lignin structure thought to be present within the material. The N1s scan also shows good consistency with 1-2 % N6 pyridine groups, 7-9 % quaternary nitrogen, and 2-3 % pyridine-N-oxide functional groups. This large percentage of nitrogen functional groups (11-13 % of the total) could provide adsorption sites for specific target molecules, utilising the lone pair of electrons on the nitrogen atoms in electron donor-acceptor (EDA) interactions. The analysed sites also showed good consistency in the O1s scan, with 2 % of the functional groups being attributed to C=O quinone groups, 6-8 % phenolic groups and 1 % attributed to physisorbed water or carboxylic acid groups. This

[24] C-O, O-C=O and N5 functional groups were omitted due to none being detected during the analysis of O4 and O6

high proportion of oxygen functional groups (9-11 % total) also provides useful sites for adsorption processes to take place.

Sample O6 also showed global consistency across the 3 analysis spots, although less than that of sample O4. This is thought to be due to localised spots of varying degrees of pyrolysis, leading to increased inconsistency between spots in the less pyrolysed sample, O6. Sample O6 showed the same approximate 1:1 ratio of C=C to C-C functional groups as O4, with C=C at 26-29 % and C-C at 27-28 %. The results show a quite inconsistent C=O functional group range of 18-24 %, while the N1s scan showed a pyridine concentration of 2-3 %, and pyridine-n-oxide concentration of 2-4 %. The quaternary nitrogen was the most inconsistent functionality, with a range of 8-14 %,which was, on average, higher than that of sample O4. This may be due to residual protein from the BSG precursor material being under-pyrolysed, or may be due to the N substituted surface polyphenol material being more greatly pyrolyzed in sample O6, as compared to O4. Sample O6 has an overall higher percentage of nitrogen functional groups (14-19 % total) than that of O4, which may provide an advantage in adsorption performance for some applications. The O1s scan showed good consistency across the 3 analysis spots with a quinone group concentration of 1-2 %, phenol concentration of 5-6 % and carboxylic acid or water concentration of 1-2 %. This showed good agreement with the O4 O1s scan, with a total oxygen functional group percentage of 8-10 % total.

As outlined above, XPS analysis has been employed effectively to show several differences in the global surface characteristics of samples O4 and O6, and to determine the potential sites for adsorption process to occur. The first difference is in the homogeneity of the samples, with O4 being more consistent across all 3 analysis spots than O6. Secondly, sample O6 shows a greater number of nitrogen functional groups on the surface than that of O4, due to the shorter pyrolysis time of the former. Both samples show highly heterogenous surfaces on a global scale, with many types of surface sites for adsorption. This will be tested later with further adsorption experiments. Both samples show evidence of carboxylic acid functional groups or water on the surfaces. If the OIII peaks are present from water this indicates a hydrophilic nature, which is important for the effective passage of liquid through the pores of the material and imperative to liquid phase adsorption media.

7.3.4 Scanning Electron Microscope Imaging

Scanning electron microscope secondary electron detector (SEM SED) images for the optimised samples were obtained. Both showed the same two distinct morphologies exhibited on the washed screening samples shown in Section 5.4.4.4, one exhibiting the glassy bead-like structures and an amorphous region. The SEM SED images for sample O4 are shown in Figure 7.88 and sample O6 are shown in Figure 7.89.

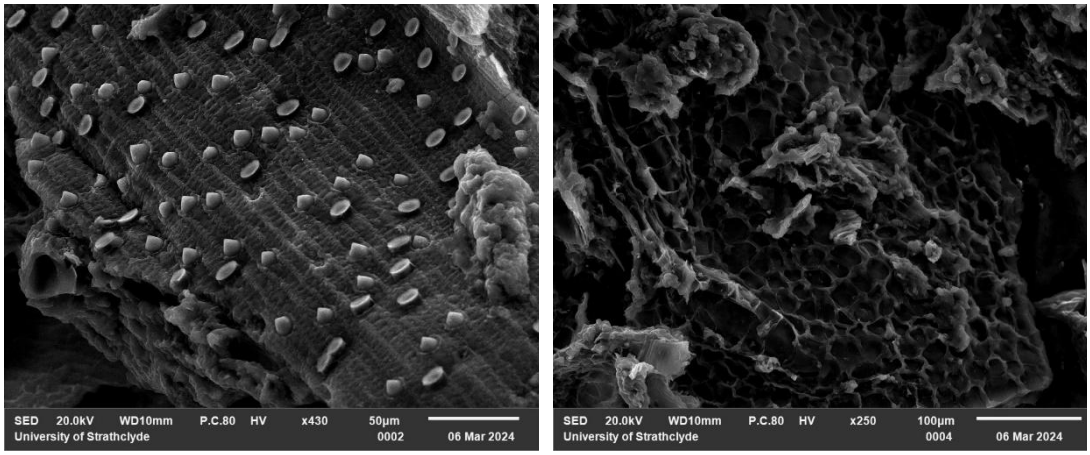

Figure 7.88: O4 scanning electron microscope secondary electron detector images, glassy bead sites (left), amorphous structure (right)

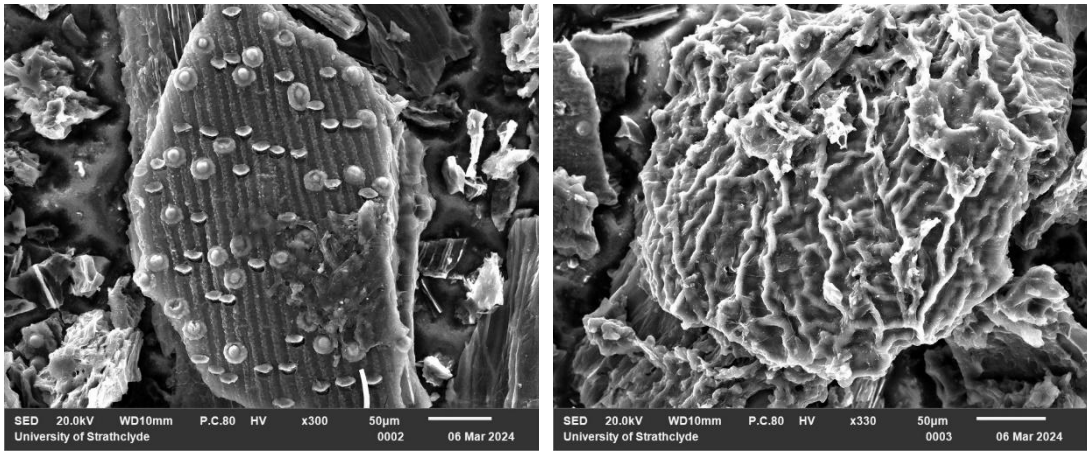

Figure 7.89: O6 scanning electron microscope secondary electron detector images, glassy beads (left), amorphous structure (right)

The glassy bead site images for both O4 and O6 show the same glassy beads which were shown to be concentrations of silicon oxides on the surface of the material through EDS mapping in Section 5.4.4.5. Results for samples O4 and O6, using EDS mapping, are presented in Section 7.3.5. The amorphous regions on both samples show indications of porosity, with openings penetrating deeper into the material indicative of a hierarchical pore structure.

7.3.5 Energy Dispersive Spectroscopy

Energy Dispersive spectroscopy was used to determine the percentage mass of the elements present on the surfaces of the samples. The two different sites observed during SEM imaging were investigated. The percentage mass results for both the glassy bead sites and the amorphous region of O4 are shown in Table 7.65.

Table 7.65: Percentage mass EDS results for sample O4

Element	O4 glassy bead sites (%mass)	O4 amorphous region (%mass)
C	73.83	82.43
O	21.99	14.68
Si	2.60	0.62
P	1.20	1.40
S	0.11	0.26
Fe	0.14	0.31
Cu	0.13	0.30
Ash	4.18	2.89
Non-Si Ash	1.58	2.27

The EDS analyses show a distinct difference in elemental composition between the two different sites found on the sample. Both show carbon as the most prevalent element, with oxygen as a marked second. The glassy bead sites showed the third most prevalent element as silicon, while the amorphous region showed phosphorus as the third most prevalent element. The glass bead sites also exhibited a higher concentration of ash present on the surface as compared to the amorphous region, but in the amorphous region much more of the ash was attributed to non-silicon elements.

The EDS maps of these samples were also investigated to see the distribution of the elements across the surfaces of the materials. The EDS maps for the O4 glassy bead sites are shown in Figure 7.90 and the O4 amorphous region is shown in Figure 7.91.

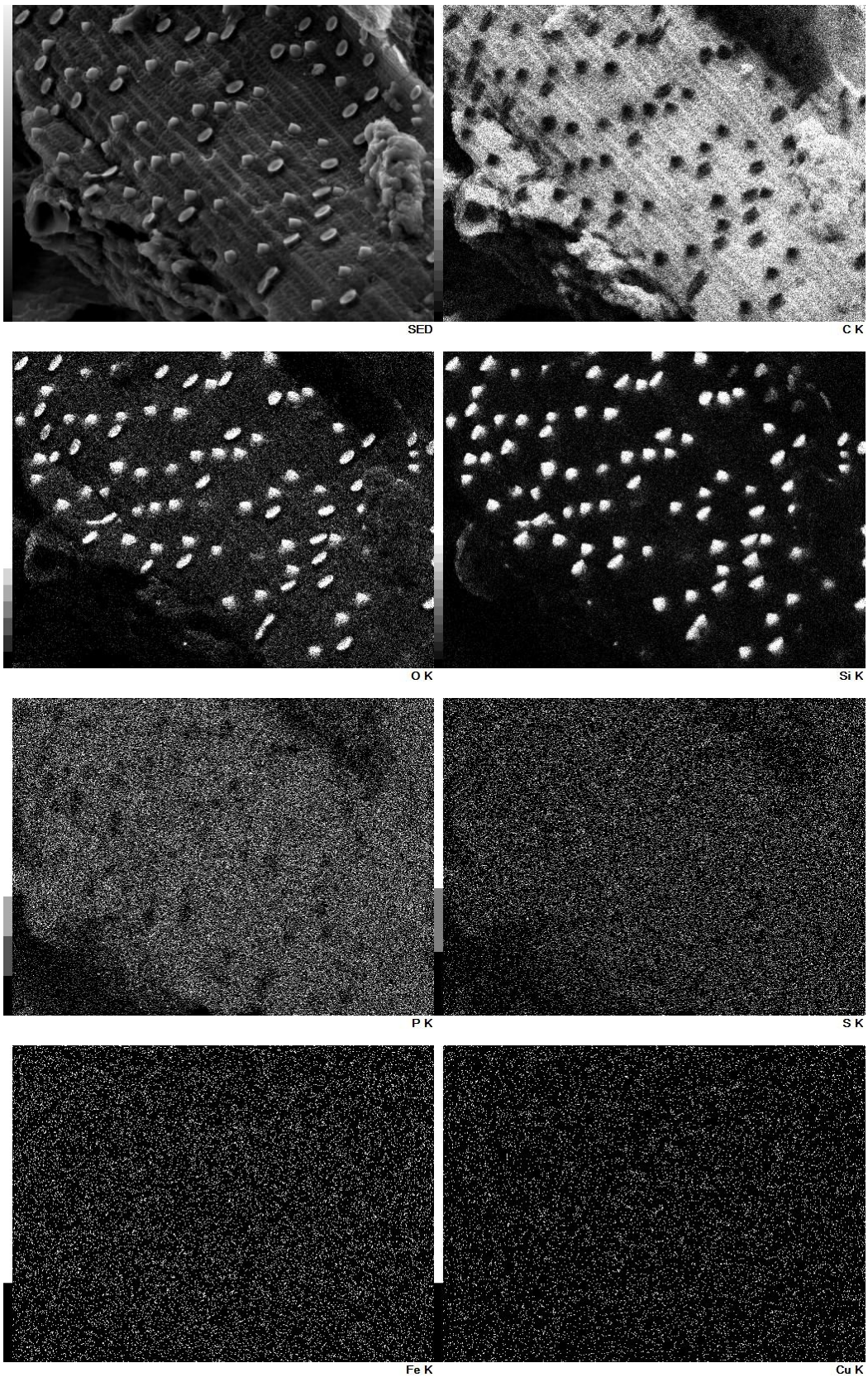

Figure 7.90: EDS elemental mapping of O4 glassy bead sites

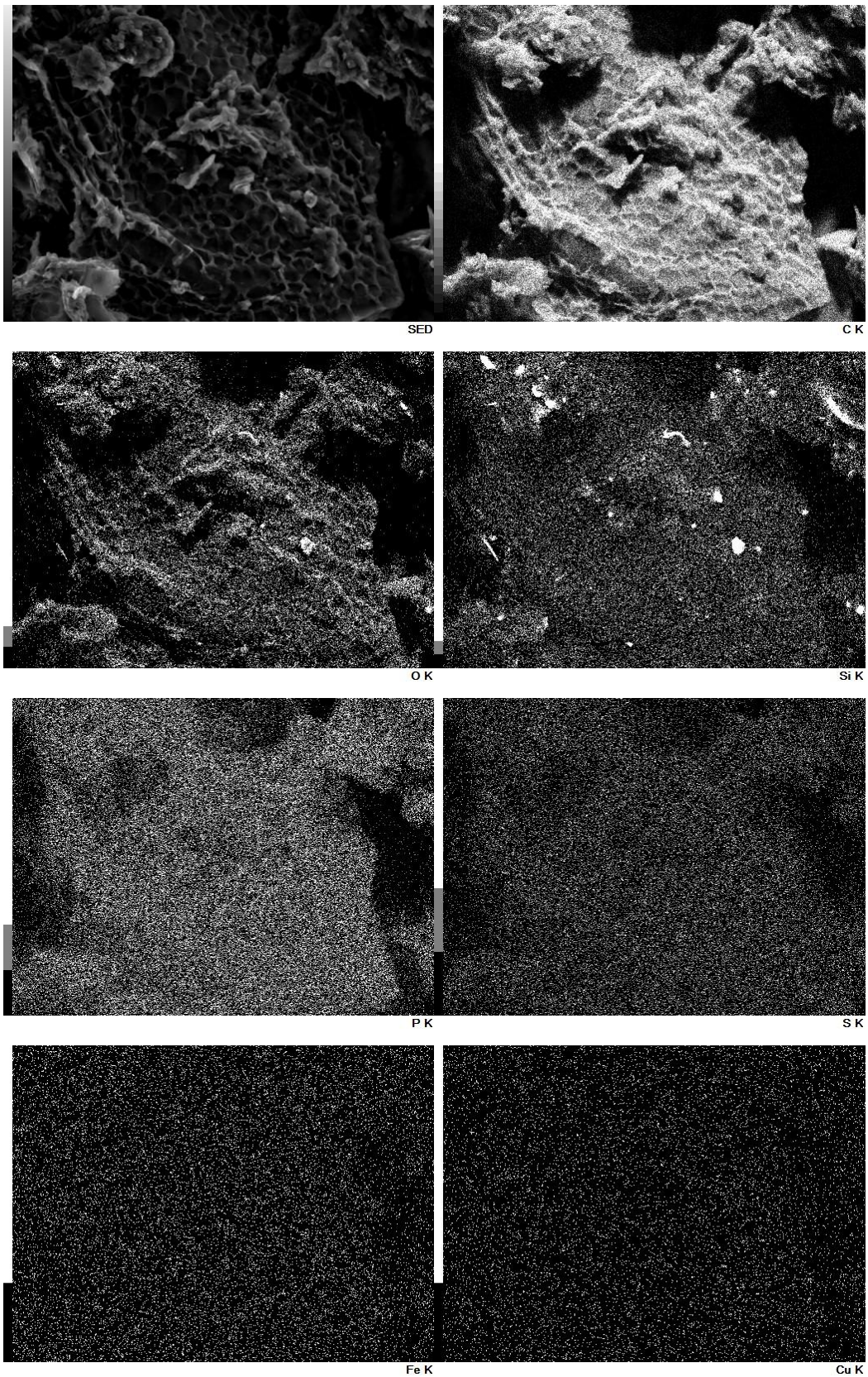

Figure 7.91: EDS elemental mapping of O4 amorphous region

The EDS maps of the glassy bead sites clearly show concentrated regions of silicon and oxygen localised at the glassy bead structures seen in the SED images. With carbon dominating the vast majority of the surrounding biochar surface, the non-silicon ash elements are evenly distributed throughout the biochar but absent at the silicon-oxygen complex sites.

The EDS map of the amorphous region shows a more typical biochar distribution with carbon and oxygen dominating almost the entire surface. While not obvious from the SED image, there are some small concentrations of silicon and oxygen present, likely of the same nature as for the glassy bead sites, just lower in number. Once again, the non-silicon ash elements are homogenously distributed across the surface of the biochar material.

The percentage mass results for the glassy bead sites and amorphous region for O6 are shown in Table 7.66.

Table 7.66: Mass % EDS results for sample O6

Element	O6 glassy bead sites (%mass)	O6 amorphous region (%mass)
C	76.66	82.21
O	19.53	15.05
Na	0.19	-
Si	2.26	0.98
P	0.91	1.23
S	0.22	0.16
Cl	0.06	0.05
Ca	-	0.05
Fe	0.07	0.11
Cu	0.11	0.16
Ash	3.82	2.74
Non-Si Ash	1.56	1.76

The EDS results again show a distinct difference in the two sites, with the amorphous region showing a greater concentration of carbon, and the glassy bead sites showing a greater concentration of silicon and oxygen. The glassy bead sites show the third most prevalent element as silicon, while the amorphous region shows the third most prevalent element as

phosphorous, exactly like the sample for O4 above. The glassy bead sites have a greater proportion of ash overall, with the majority of that ash coming from silicon. The presence of chlorine in both sites indicates the sample may retain chloride ions from the hydrochloric acid washing process, which was not observed for sample O4; this may mean that O6 requires a more intensive washing procedure to remove the chlorine from the surface of the material, or that O6 has a greater affinity for anions, like chloride ions. This may indicate a fundamental change in surface chemistry between O4 and O6 brought on by the varying residence time and greater degree of pyrolysis for sample O4.

The EDS maps for O6 were also obtained to investigate the distribution of the elements across the surfaces of the materials. The EDS maps for the O6 glassy bead sites are shown in Figure 7.92 and the O6 amorphous region is shown in Figure 7.93.

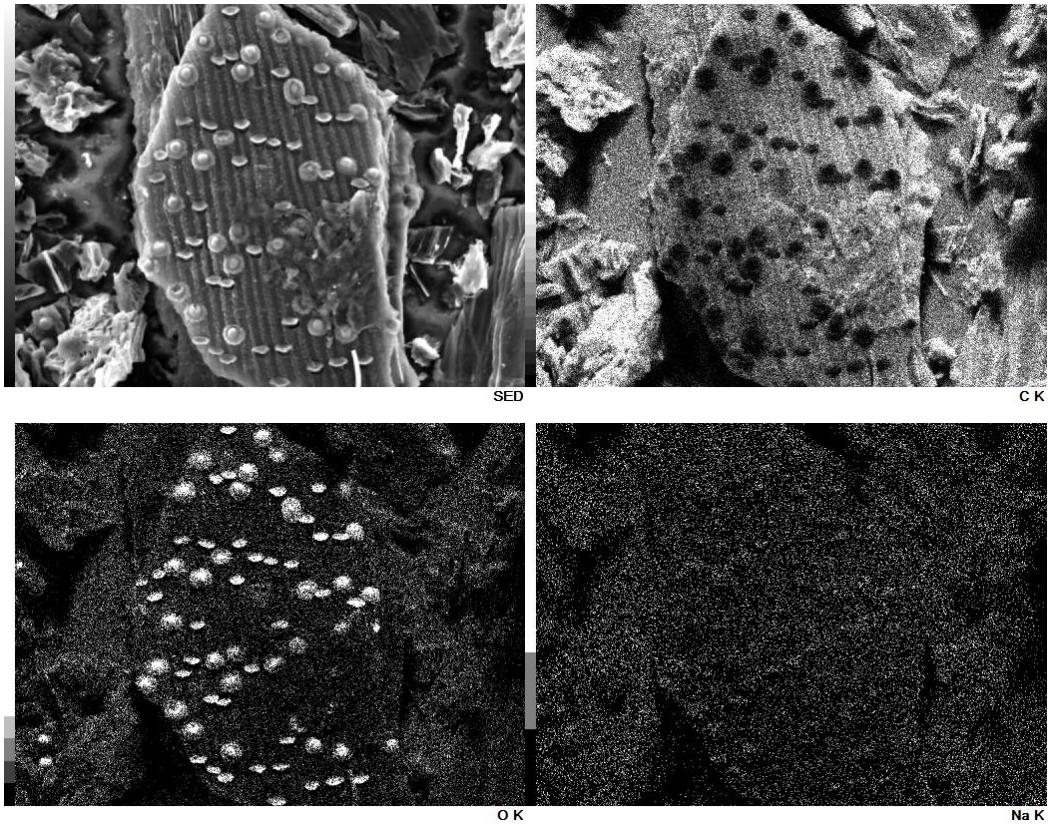

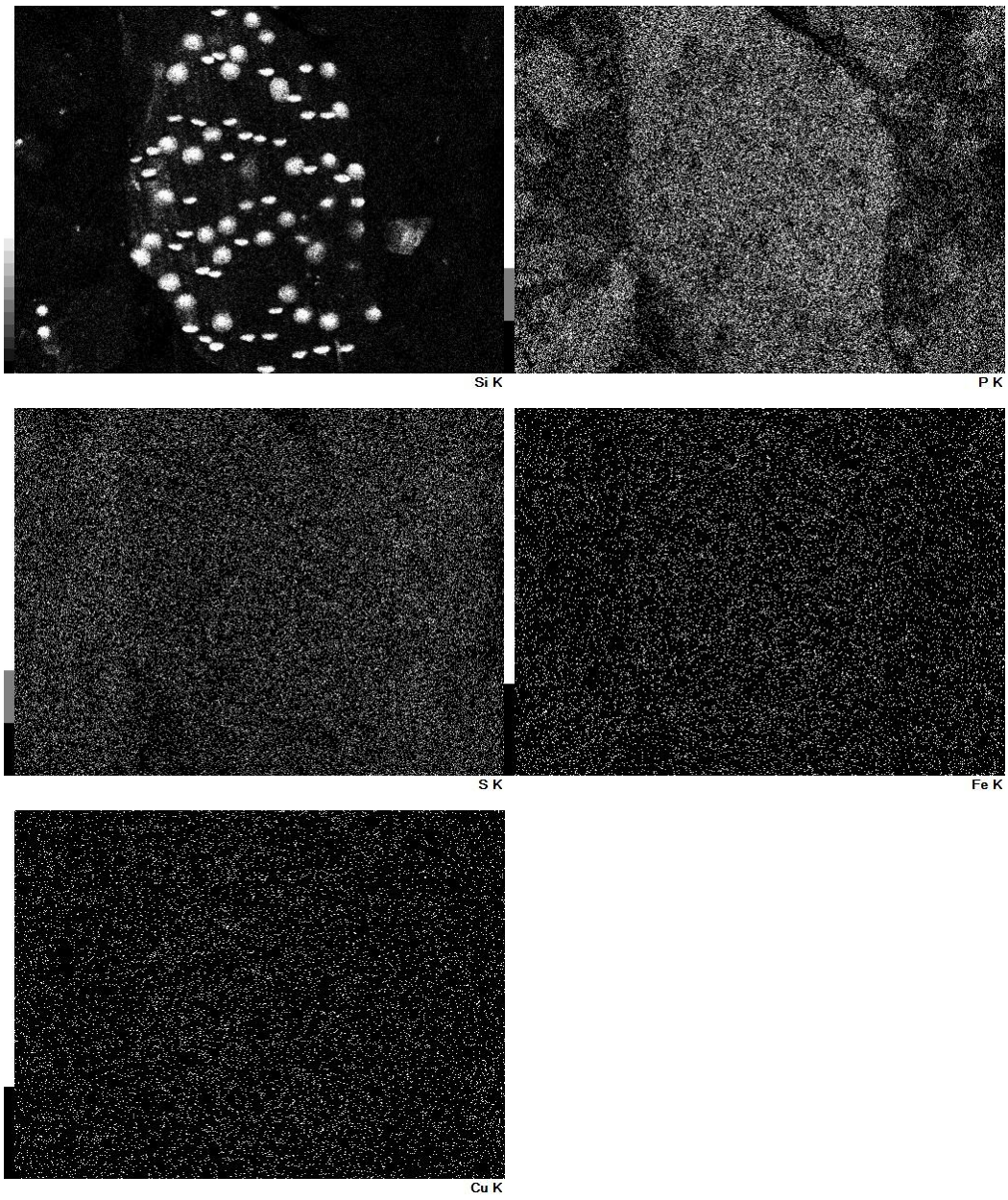

Figure 7.92: EDS elemental mapping of O6 glassy bead sites

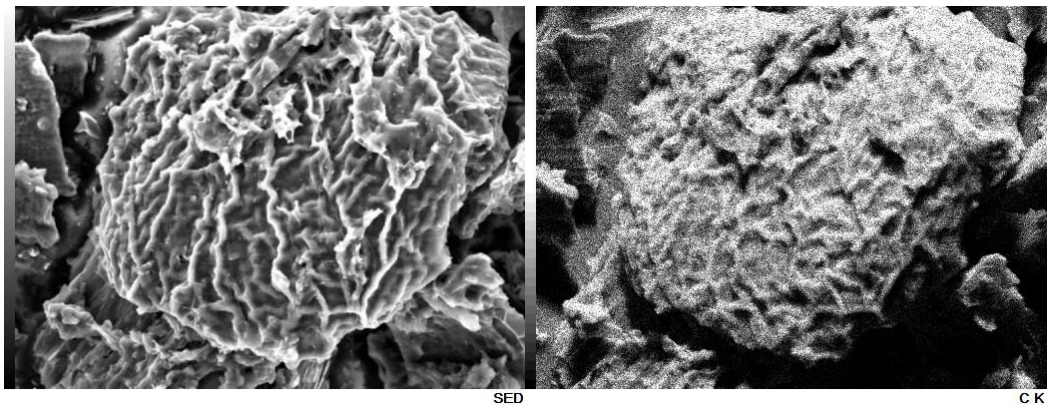
SED
C K

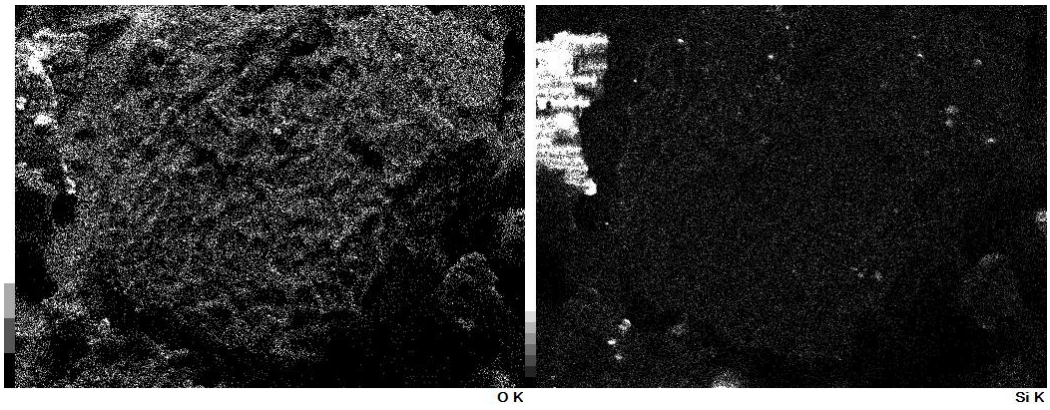
O K
Si K

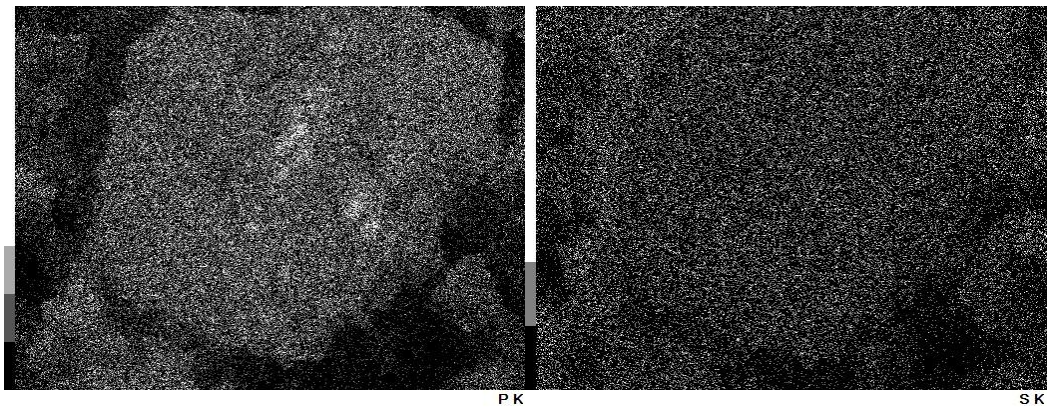
P K
S K

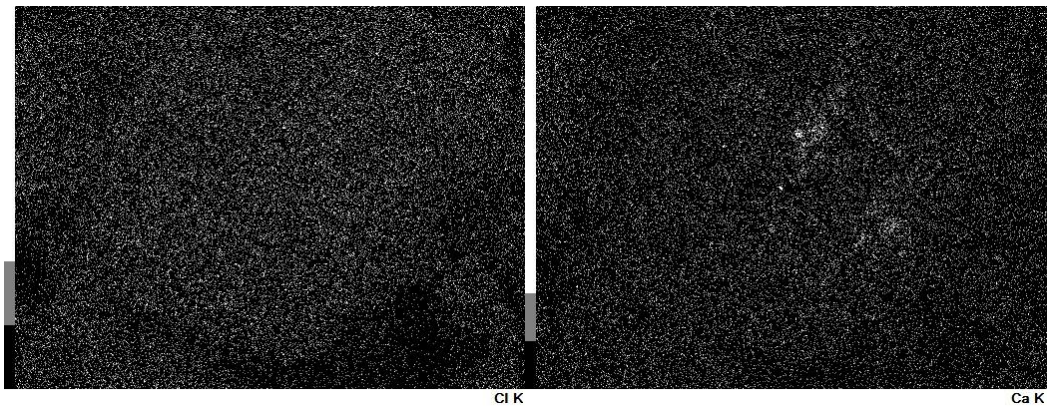
Cl K
Ca K

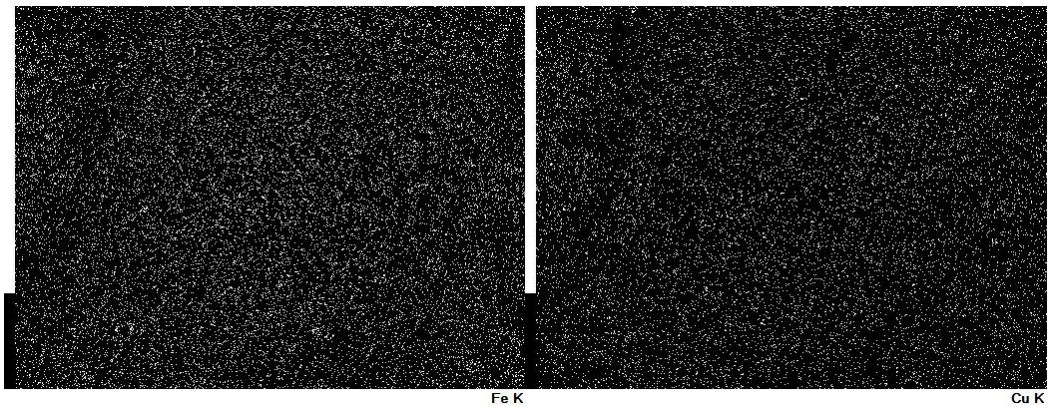

Figure 7.93: EDS elemental mapping of O6 amorphous region

The EDS map of the glassy bead sites show localised concentrations of silicon and oxygen at the glassy bead sites seen in the SED images. The amorphous sample also shows a localised concentration of silicon and oxygen in the top left corner of the analysis window, this is likely from a site with a similar nature to the one seen in the glassy bead sites image. Possibly due to the inclusion of this other site, the values obtained for the silicon and oxygen percentage masses in Table 7.66 for the amorphous region site may not be representative of the pure amorphous material and should be treated with caution. As expected, the surfaces of both sites are primarily comprised of carbon and oxygen, and all non-silicon ash is distributed relatively homogenously across the surface of both types of sites. The amorphous region for O6 also shows an area with increased phosphorous and calcium concentrations at the centre of the particle, lending further evidence to the fact that the O6 samples may require further washing to remove ash, due to differences in surface chemistry or composition from sample O4.

7.3.6 Silica Investigation

The high silicon content observed for all of the materials tested in Sections 5.4.4.5 and 7.3.5, and the unusual glassy bead formations found on the surfaces of these samples, warranted an investigation into the nature and origin of these structures. Four additional samples were analysed using SEM imaging and EDS analysis, each used to elucidate and better understand the formation and nature of these glassy bead structures. These samples were: i) a sample of dried BSG precursor material; ii) BSG ash recovered from TGA analysis of the BSG precursor material following the experimental procedure described in Section 4.3.1; iii) a sample of biochar synthesised from BSG at a temperature 1100 °C, a ramp rate of 20 °C min^{-1} under a nitrogen atmosphere, a hold time of 1 h under a carbon dioxide

atmosphere, and cooled under nitrogen; and iv) a sample of ash from the TGA analysis of sample O4, following the experimental procedure described in Section 4.3.1.

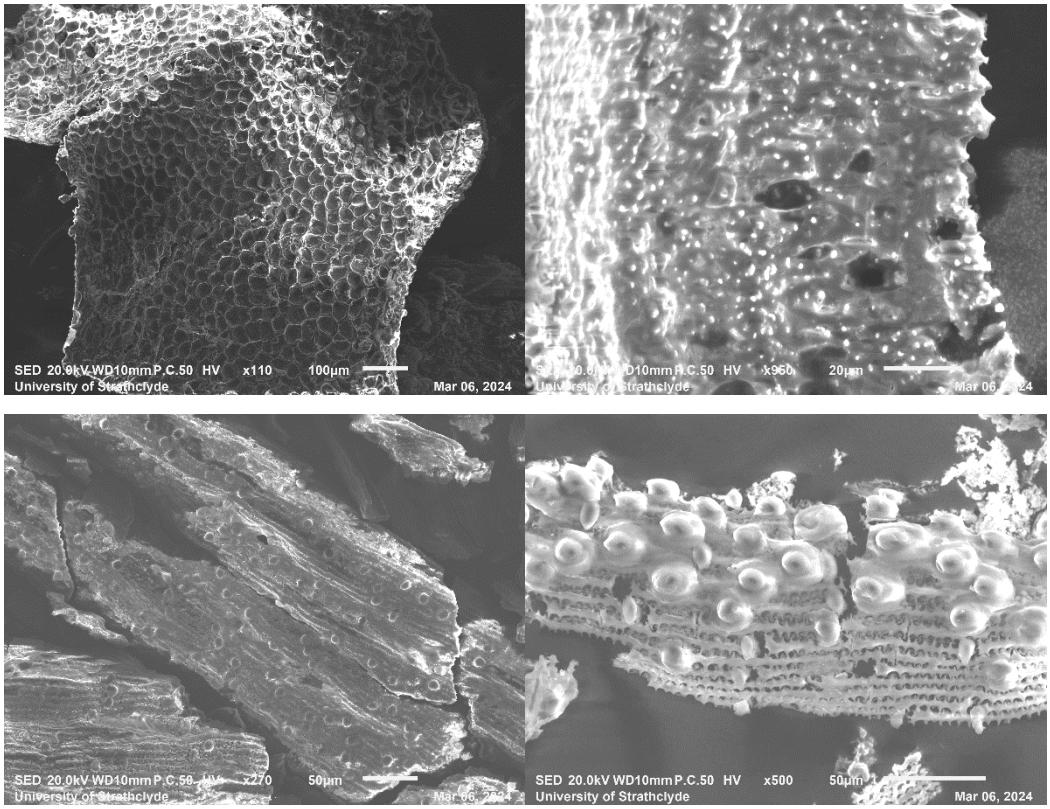

Figure 7.94: SED SEM images of BSG (top left), BSG ash (top right), 1100 °C biochar (bottom left), O4 ash (bottom right)

From the SEM micrographs shown in Figure 7.94, only the 1100 °C biochar and the O4 ash show the distinctive glassy beads on the surface of the materials, indicating that the glassy beads are not inherent to the material, nor are they produced in the simple heating of the BSG. The presence of the glassy beads is dependent on the synthesis procedure under the specific conditions outlined in the biochar production.

EDS was used to determine the percentage mass of the elements present on the surface of the samples. The percentage mass results for all 4 of the new sites are shown in Table 7.67. Please note that the 1100 °C Biochar and O4 ash samples were zoomed in as compared to SED SEM images above for the purposes of EDS analysis to minimise the EDS signal from the carbon tape used to adhere the samples to the analysis stubs.

Table 7.67: Percentage mass results for silica investigation samples obtained using EDS analysis

Element	BSG (%mass)	BSG Ash (%mass)	1100°C Biochar (%mass)	O4 Ash (%mass)
C	51.68	39.81	-	17.71
N	1.21	-	-	-
O	46.00	33.92	51.17	52.84
Na	0.13	0.97	-	-
Mg	0.16	3.22	10.41	-
Al	0.30	-	-	-
Si	0.04	4.09	18.96	27.54
P	0.26	8.42	14.23	1.43
S	0.13	-	-	-
K	-	6.37	1.64	0.49
Ca	0.08	1.79	3.59	-
Fe	-	0.68	-	-
Cu	0.01	0.74	-	-
Ash[25]	1.11	26.28	48.83	29.46
Non-Si ash[26]	1.07	22.19	29.87	1.92

EDS analysis of the BSG sample shows that there is a very small, but not insignificant, amount of silicon contained on the surface of the material, showing that the silicon is inherent to the BSG material and not introduced to the material in some way through the synthesis procedure. This is backed up by the results obtained for the BSG ash sample, which shows that the silicon surface concentration is increased after combustion, indicating more of the silicon is uncovered and shown on the surface of the material.

The EDS maps for the four new samples were also obtained to investigate the distribution of the elements across the surfaces of the materials. The EDS elemental maps for BSG are shown in Figure 7.95, those for BSG ash are shown in Figure 7.96, analogous maps for 1100 °C Biochar are shown in Figure 7.97 and finally, the results obtained for O4 ash are shown in Figure 7.98.

[25] Ash is defined as all elements that are not carbon or oxygen
[26] Non-Si Ash is defined as all elements that are not carbon, oxygen or silicon

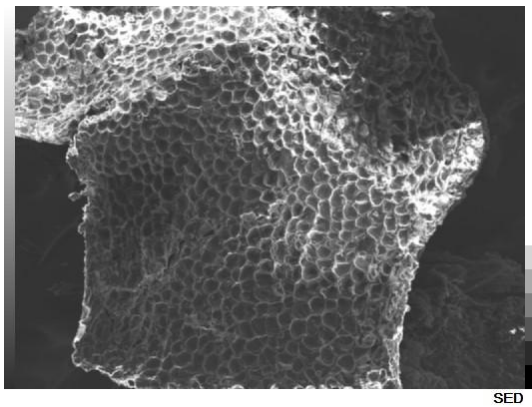

SED

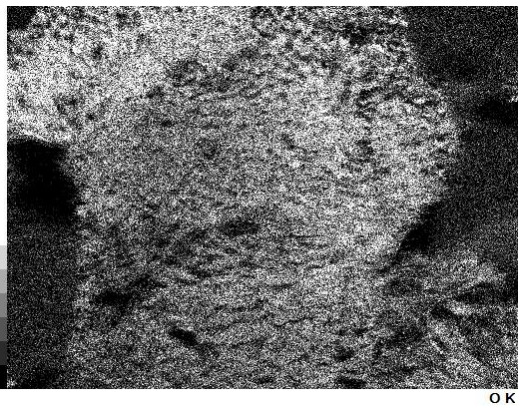

O K

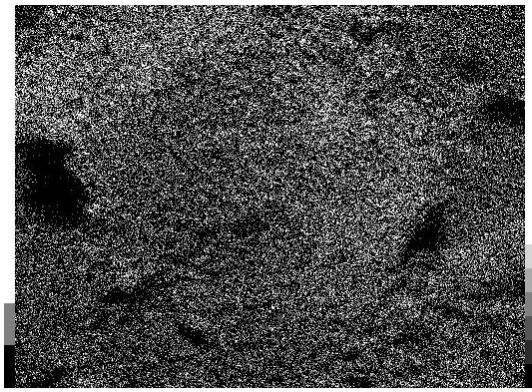

N K

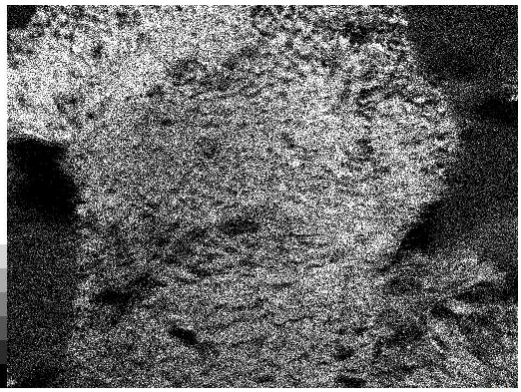

O K

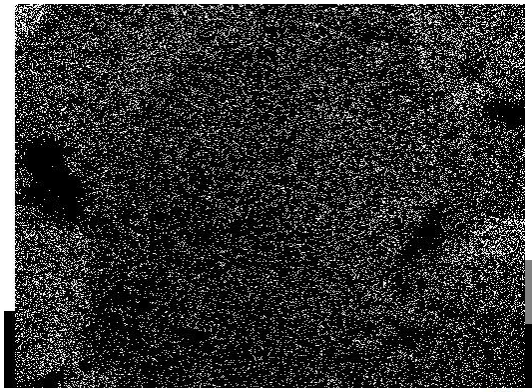

Na K

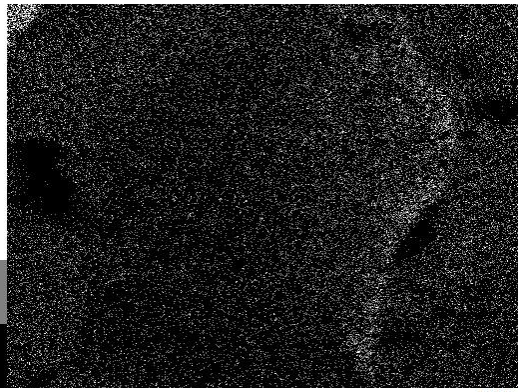

Mg K

Al K

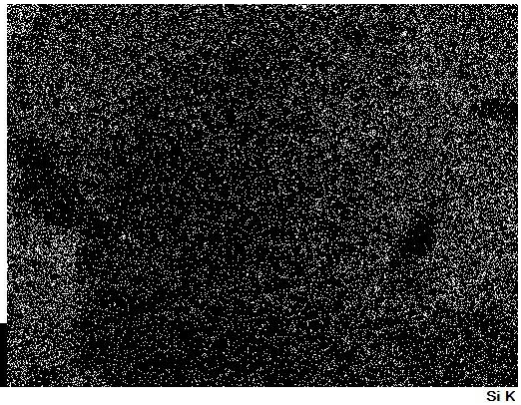

Si K

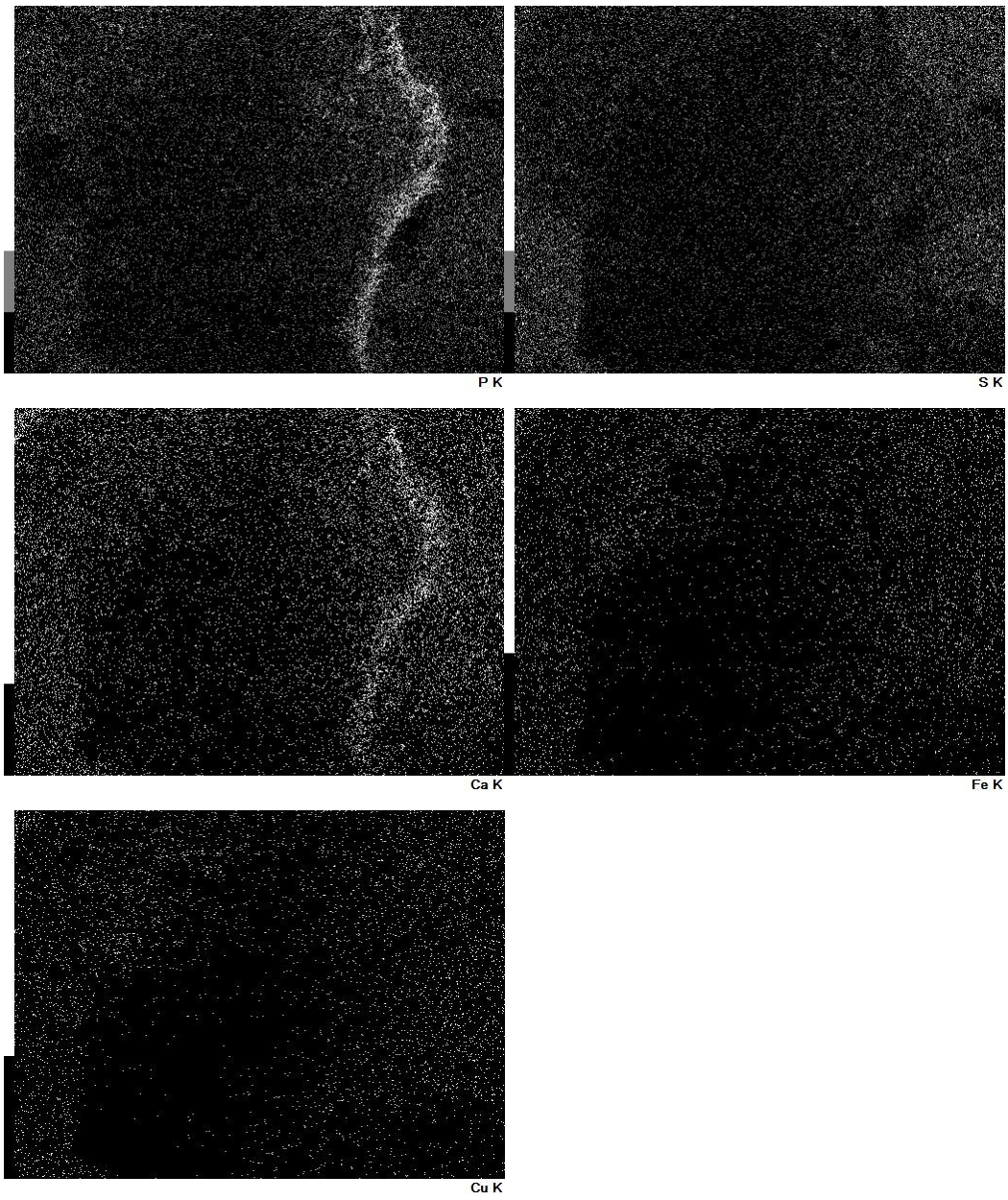

Figure 7.95: EDS elemental mapping of BSG

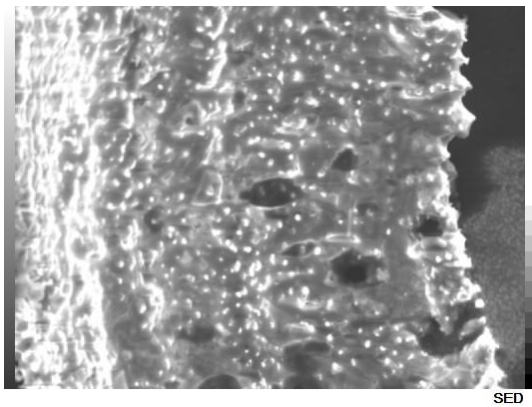

SED

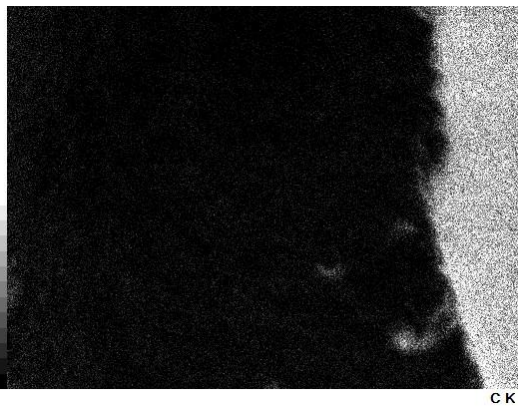

C K

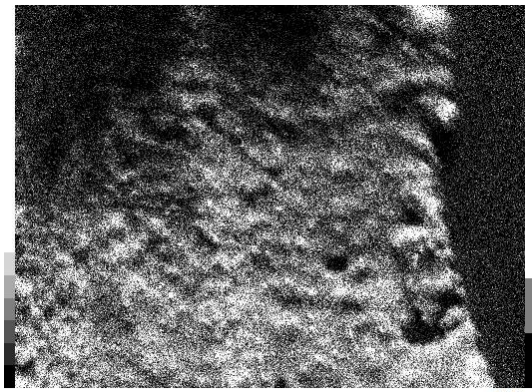

O K

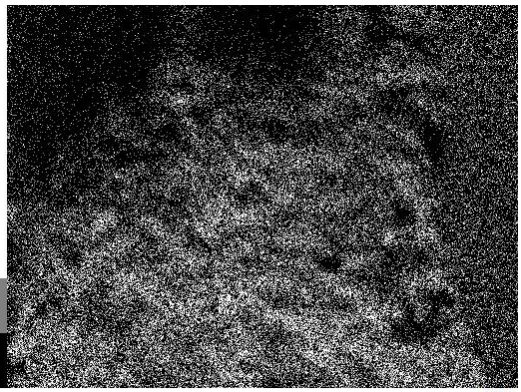

Na K

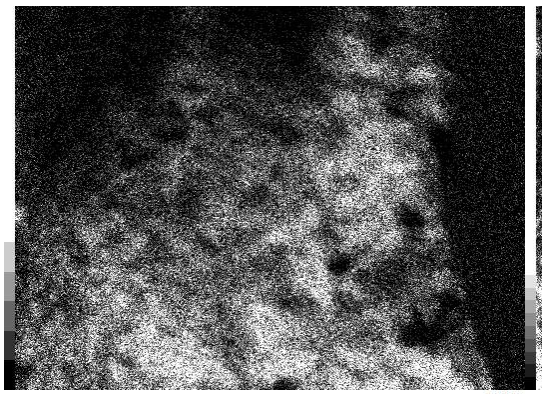

Mg K

Si K

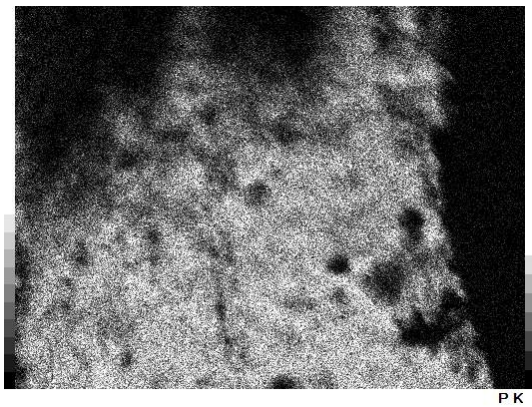

P K

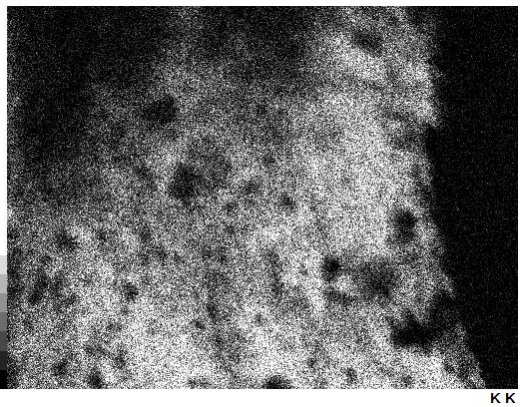

K K

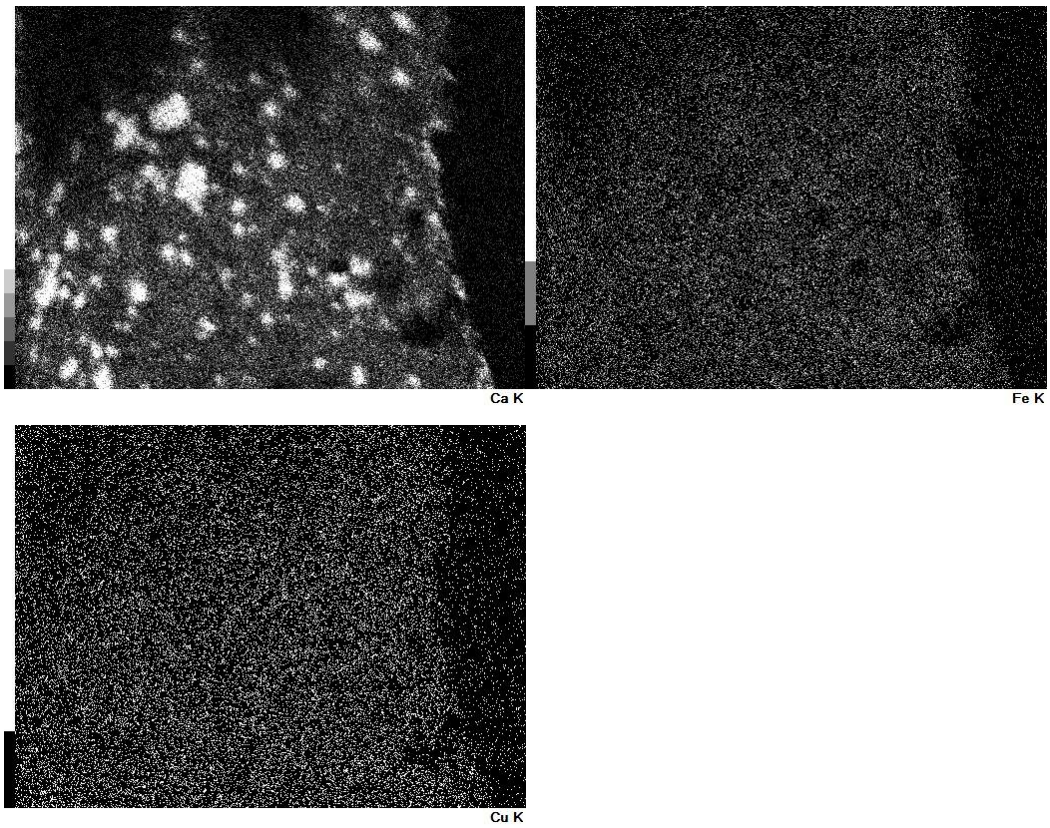

Figure 7.96: EDS elemental mapping of BSG ash

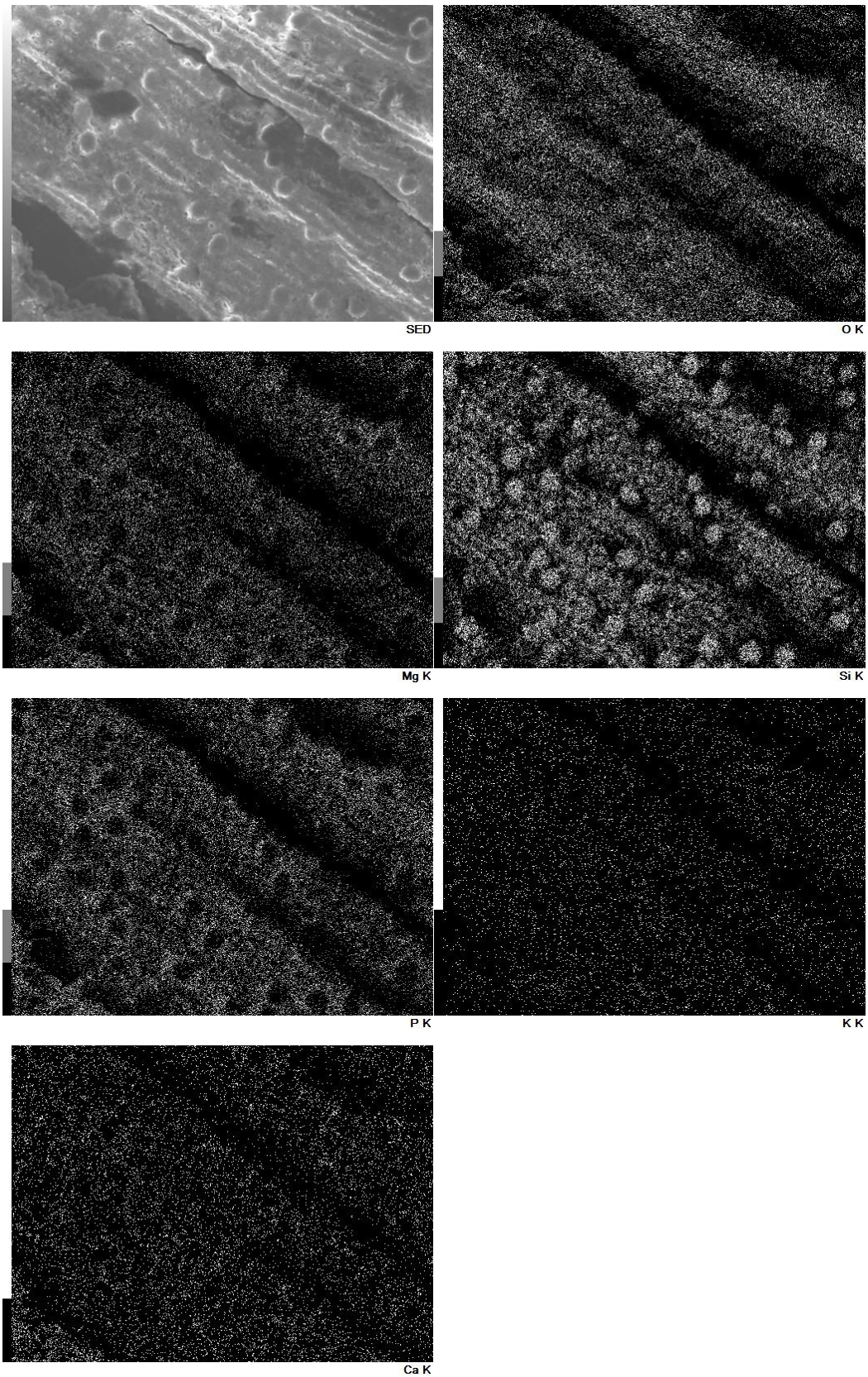

Figure 7.97: EDS elemental mapping of 1100 °C biochar

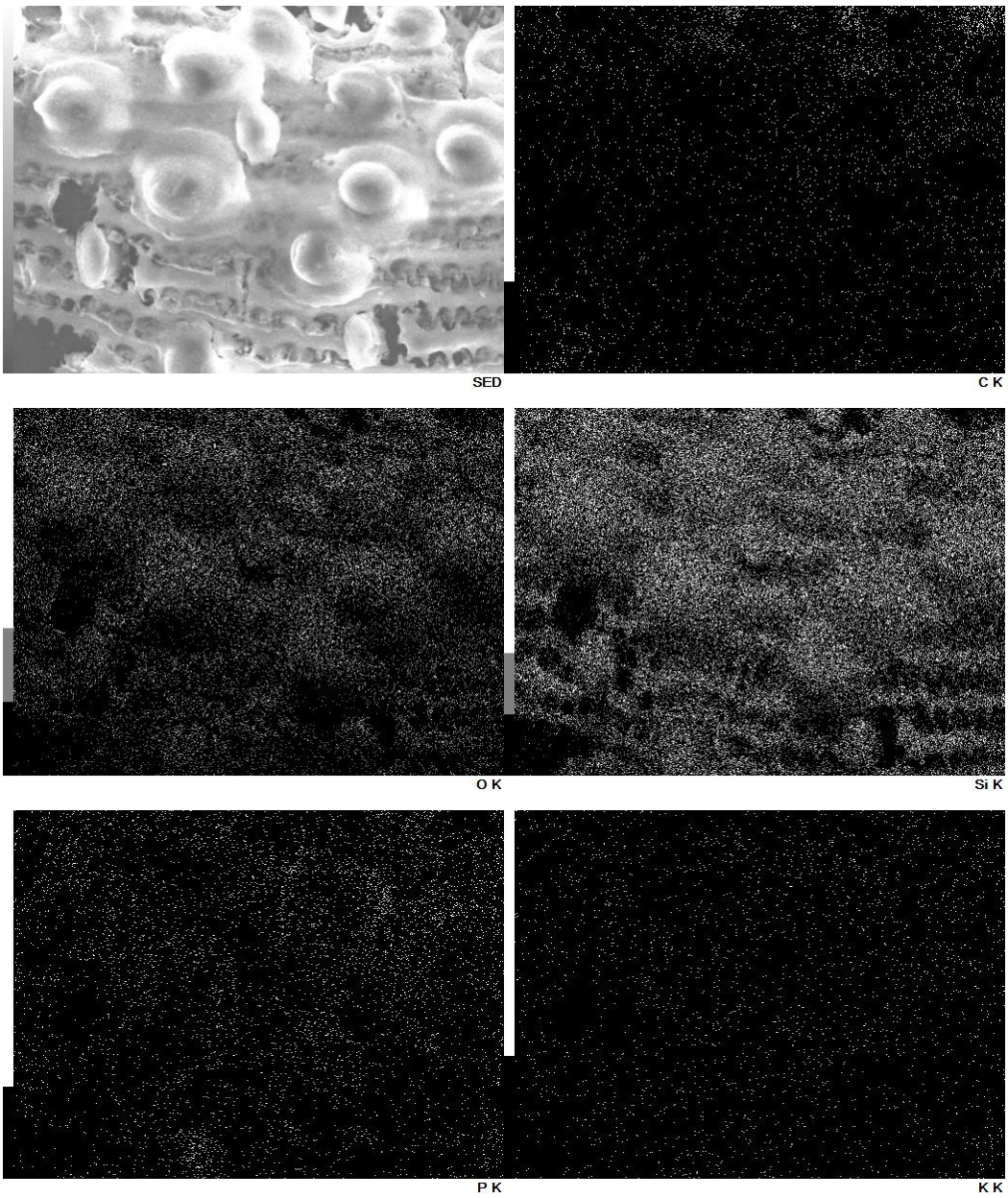

Figure 7.98: EDS elemental mapping of O4 ash

The EDS map of the BSG sample shows that all of the ash, including silicon, is relatively homogenously distributed across the surface of the material. The BSG ash sample shows some local concentrations of silicon but no presence of the glassy bead like structures observed previously. The 1100 °C biochar and O4 ash samples both show the characteristic silicon and oxygen concentrations around glassy bead structures. Notably, the O4 ash sample shows a very small amount of carbon that was not combusted during TGA analysis, while the 1100 °C biochar sample exhibited no carbon signal, indicating complete removal

of carbon during synthesis at this higher temperature. The O4 ash sample shows the characteristic glassy bead structures in the foreground of the sample, indicating that the silica species were present on the surface prior to combustion in the TGA procedure, but also shows a silica backbone present in the background of the image. This demonstrates the mechanism through which the glassy bead structures are formed during synthesis. In summary, the BSG material has a silica backbone present in all of the samples, which is hidden within the structure of the material; during sustained pyrolysis under anoxic conditions this silica backbone begins to form a mesophase, as the carbonaceous layers separating it pyrolyse and are wicked away by the gas flow in the tube furnace. This mesophase cools and is left behind as the glassy beads seen in a number of the biochar SEM micrographs shown in this work. The silica may also go through a polymorph transition during the synthesis process, which explains the different appearances observed for the pyrolysed and unpyrolysed samples. The most common, and likely initial form, of the silica in the BSG is α-quartz, which has a melting point of 573 °C, at atmospheric pressure; this melting may cause polymorph transition into β-quartz, which can undergo a further transition into tridymite at 870 °C, again at atmospheric pressure (181). It would be valuable to understand the transitions between these three polymorphs in more detail and a suggestion is for researchers to investigate this in future work.

The high silica content of the biochars suggests the availability of another surface functionality for intermolecular interactions with target pollutant molecules. The siloxane (Si-O-Si) functional groups offer lone pairs of electrons for EDA interactions, while the silanol (Si-OH) functional groups on the edges of the silica structures provide groups for dipole interactions, as well as protonation and deprotonation giving rise to anionic and cationic charges. Silicon biochars (SiChars) are an area of research for both water remediation and soil amendment applications. One study utilising fly-ash, a high silica content waste product from coal fired power stations and biomass(182), indicated an enhanced surface area and adsorption capacity for methylene blue dye using a silica composited biochar, as compared to only biomass derived biochars. This was attributed to the additional surface functionalities, and variety of inter-molecular interactions, in the silica-doped materials.

A review carried out on silica rich biochars, for use in the controlled release of fertiliser materials for use in soil amendment applications (183), highlighted the potential of these

materials to be used as composite adsorbent materials, utilising the inherent chemical make-up of these materials rather than doping biochars with high silicon content additives. It indicated that cereal crops, such as rice, corn, and wheat, exhibit high silica contents, and offer good potential for upcycling into SiChar materials. Barley, from which the BSG used in this work is derived, also falls in this family of cereal crops, giving rise to the inherent silica content of the biochar materials synthesised in this work. The review also indicates that silica-rich adsorbent materials derived from silica rich biomass demonstrate higher surface charge densities and have a greater tendency to chemically react on their surface than more carbon-rich biochar materials (184). In an adsorption context, this suggests that the silica functionalities on the surface of the biochar may tend to chemisorb target species rather than exhibit intermolecular physisorptive interactions.

A study in which a high silica content biochar composite material, obtained using red-mud derived silica and oil palm derived biochar, was used for dye adsorption, also showed increased surface and dye adsorption than for adsorption on the constituent parts (185). The study purposefully set out to maximise silica content on the surface of the biochar to encourage n-π interactions between the siloxane lone pairs and the aromatic rings on the rhodamine B dye. The study showed a silicon content of 0.36% on the surface of the material, through EDS analysis. This is in comparison to the 2.60% of silica measured for the glassy bead sites and 0.62% for the amorphous region of sample O4, equating to between 2 and 8 times as much silica on the sample surface. While this work has not purposefully attempted to encourage the promotion of silica functional groups on the synthesised biochars, they are an attractive gain, and offer another surface functionality for use in adsorption of pollutant material.

7.4 Liquid Phase Adsorption

7.4.1 Adsorption Kinetic Modelling

7.4.1.1 Pseudo First Order & Pseudo Second Order Modelling

The kinetic performance of the two adsorbents O4 and O6 were tested by measuring the uptake of methyl orange dye at various contact times, using an initial solution concentration of 100 mg g^{-1} and an adsorptive solution volume of 30 mL. The data was then fitted to four kinetic models: pseudo first order (PFO), pseudo second order (PSO), Elovich and intraparticle diffusion models. The model parameters obtained for fits using the PFO

and PSO models can be seen below, in Table 7.68. These models, and the experimental points, are shown graphically in Figure 7.99 for sample O4, and Figure 7.100 for sample O6.

Table 7.68: Model coefficients and R^2 for pseudo first and pseudo second order kinetic models

Sample	PFO			PSO		
	K_1 (min^{-1})	q_e (mg g^{-1})	R^2	K_2 (g mg^{-1} min^{-1})	q_e (mg g^{-1})	R^2
O4	$2.25x10^{-2}$	241	0.9795	$1.07x10^{-4}$	271	0.9898
O6	$8.34x10^{-3}$	179	0.9376	$5.08x10^{-5}$	199	0.9720

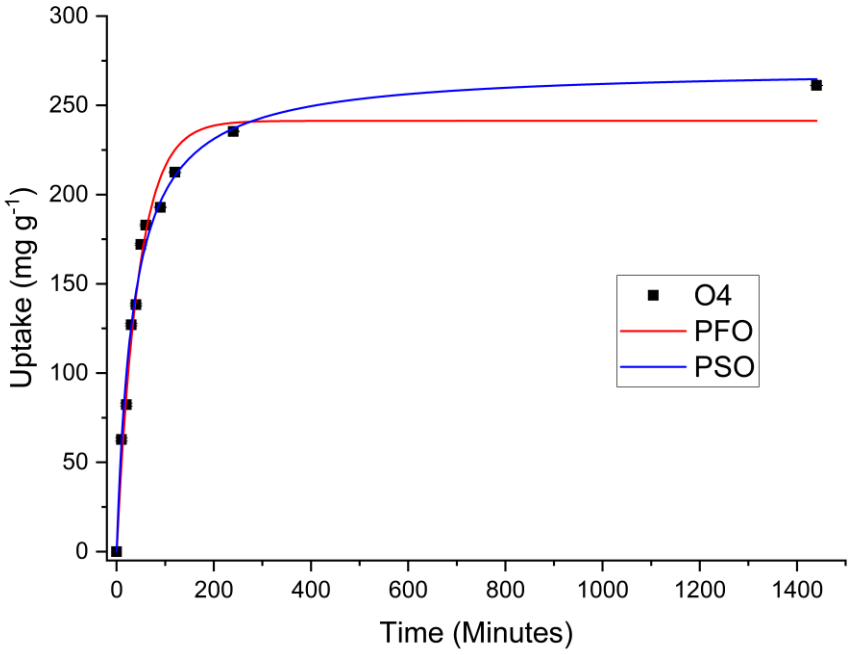

Figure 7.99: Pseudo first and second order fits for methyl orange adsorption on sample O4 (dye initial concentration 100 mg g^{-1}; solution volume 30 mL)

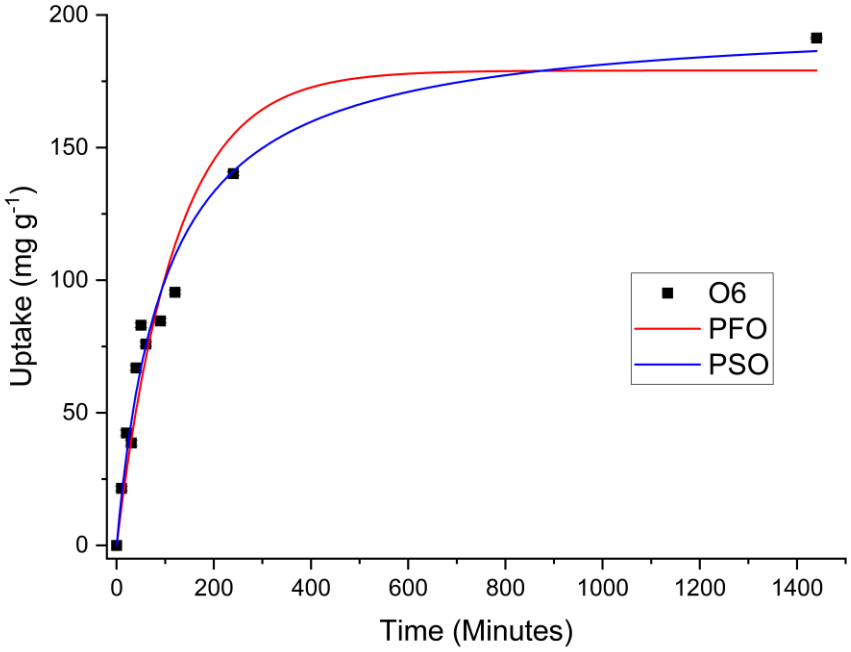

Figure 7.100: Pseudo first and second order fits for methyl orange adsorption on sample O6 (dye initial concentration 100 mg g^{-1}; solution volume 30 mL)

Both samples show a better fit using the PSO model, as shown through the higher R^2 values obtained for this model. Both models fit the data well at low contact times, but the PFO model then overestimates uptakes for moderate contact times, and underestimates uptake at contact times approaching equilibrium. The PSO model fits the data better across the whole range of contact times tested. The kinetic constant K_2 for sample O4 is larger than that of the O6, meaning that the rate of adsorption of methyl orange is greater for sample O4. The PSO model also predicts a greater uptake of methyl orange on sample O4 as compared to sample O6, which corroborates the findings of the optimisation experiments carried out in Chapter 6. As stated in Chapter 3, the PSO model may imply that the interaction between the adsorbent and adsorptive is chemisorptive in nature. However, further investigations must be carried out to verify the mechanism of the interaction.

7.4.1.2 Elovich Kinetic Modelling

The data was also fitted to the Elovich model, however, the initial state point (i.e. zero uptake at 0 min) was removed from the regression, due to a breakdown of the Elovich model at low contact times. The model coefficients, and R^2 values, obtained are shown in

Table 7.69. The plots of the Elovich model fit for the experimental data is shown in Figure 7.101.

Table 7.69: Elovich kinetic model fitting parameters for methyl orange adsorption onto samples O4 and O6

Sample	Elovich		
	a ($mg\ g^{-1}\ min^{-1}$)	b ($g\ mg^{-1}$)	R^2
O4	29.8	$2.32x10^{-2}$	0.8772
O6	5.42	$2.81x10^{-2}$	0.9693

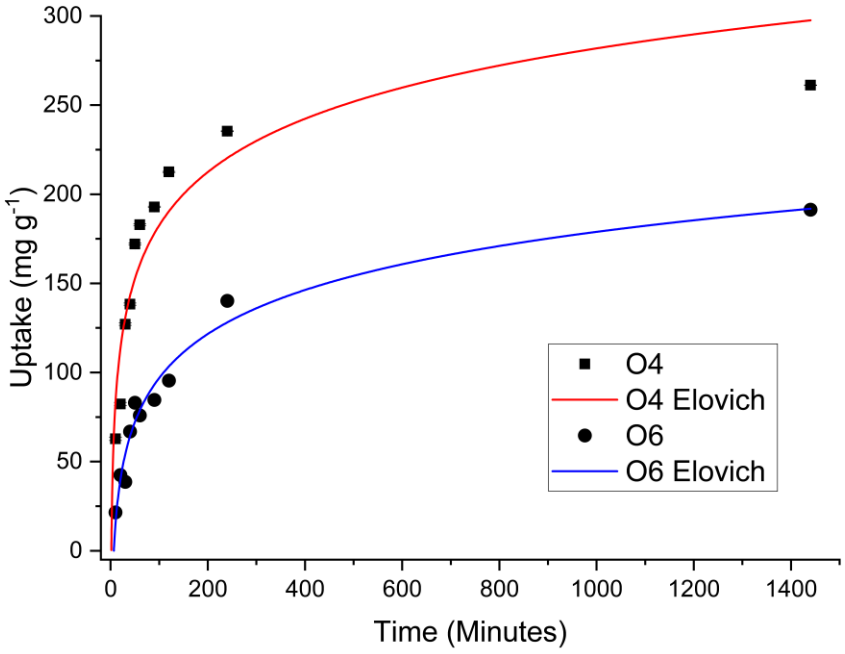

Figure 7.101: Elovich model plots for samples O4 and O6

The Elovich model breaks down when used to fit the data obtained for sample O4, at times below 1.44 min, while the model for O6 breaks down at times below 6.59 min. While the Elovich model provided a relatively poor fit for sample O4, in comparison to the PSO model, the Elovich model fitted the kinetic data for sample O6 very well, shown through the high R^2 value of 0.9693. This could indicate that the mechanism of methyl orange adsorption onto the surface of O6 is chemisorptive in nature. This difference in mechanism could also explain why the kinetic behaviour of O4 is, in general, faster than for O6, as physisorptive processes are commonly much quicker than those of chemisorptive processes.

7.4.1.3 Intra-Particle Diffusion Kinetic Modelling

The kinetic data obtained for methyl orange adsorption on both samples was fitted to the intraparticle diffusion model. Plots of uptake vs $t^{0.5}$ were created and two linear sections were identified within the plots for both samples. The model coefficients obtained for each sample and the resulting R^2 values are detailed in Table 7.70. The experimental plots and linear fits are shown in Figure 7.102.

Table 7.70: Intra-particle diffusion model coefficients for both linear sections for samples O4 and O6

Sample	Region 1			Region 2		
	$k_{int,1}$ (mg $g^{-1}min^{-0.5}$)	$C_{int,1}$ (mg g^{-1})	R^2	$k_{int,2}$ (mg $g^{-1}min^{-0.5}$)	$C_{int,2}$ (mg g^{-1})	R^2
O4	20.1	9.29	0.9235	1.15	218	-
O6	9.13	0.868	0.9554	2.28	105	-

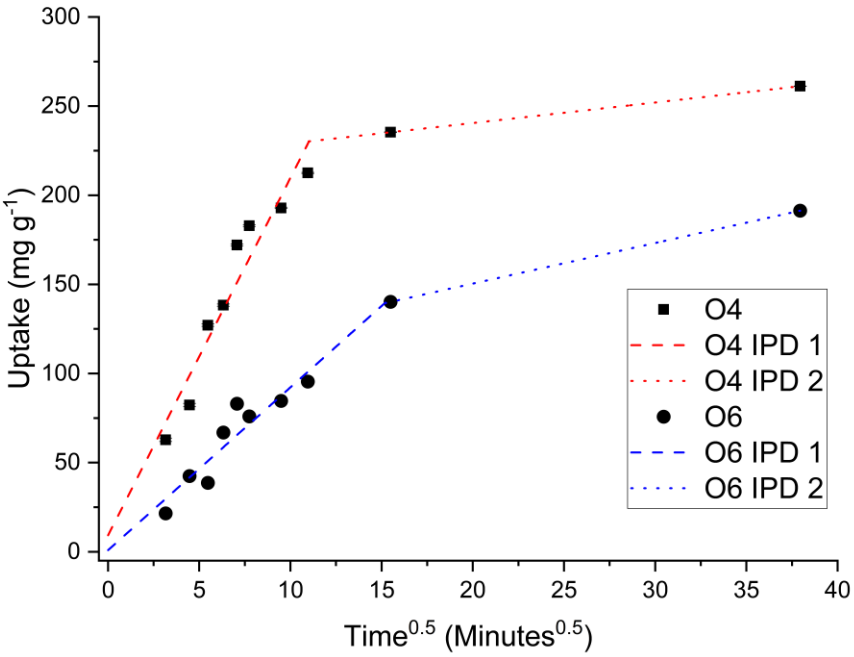

Figure 7.102: Intra-particle diffusion model experimental plots and fitting lines for samples O4 and O6

Both samples show an initial, steep linear section with y-axis intercepts close to the origin. The regime indicated by IPD 1 for both of the samples is the step in which diffusion across the boundary layer to the surface of the adsorbent is the rate limiting step. The diffusion rate for the boundary layer diffusion step for O4 is greater than that for O6, as indicated by

$k_{int,1}$ in Table 7.70 and by the gradient of the lines in Figure 7.102. This may be due to a greater attraction between the adsorptive molecules and the surface of O4 as compared to O6, allowing for faster diffusion of adsorptive molecules through the larger pores of the material.

The second regime, IPD 2 for both samples likely relates to both the intra-particle diffusion step where the rate of diffusion slows due to the entering of pores and the equilibrium phase of the adsorption process, where the adsorption of dye molecules slows down due to the decrease in bulk dye concentration. While it is certain that this is a different regime from the section identified as the boundary layer diffusion rate limiting step section in IPD 1, the rate constants and R^2 values should be treated with caution due to the low number of experimental points within this section and inability to differentiate between the intra particle diffusion and equilibrium stages. In future studies, additional experimental points should be obtained in the longer contact times region to ascertain the adsorption rates of these sections with greater accuracy.

7.4.2 Adsorption Isotherm Modelling

Adsorption experiments using varying initial solution concentrations of methyl orange dye were carried out to obtain adsorption isotherms for both samples O4 and O6. The experiments were carried out at three fixed temperatures: 25 °C, 35 °C and 45 °C. The adsorbate uptakes vs equilibrium concentration of adsorptive in the solution were plotted and the data fitted to the Langmuir, Freundlich and Temkin isotherm models. The relevant model parameters are summarised in Table 7.71 for sample O4 and Table 7.72 for sample O6. The model plots for both samples O4 and O6 at all temperatures investigated are shown in Appendix C.

Table 7.71: Isotherm modelling parameters for sample O4 with methyl orange dye

Model	Parameters	Temperature (°C)		
		25	35	45
Langmuir	q_{max} (mg g^{-1})	347	368	400
	K_L (L mg^{-1})	0.477	0.258	0.108
	R^2	0.9186	0.9181	0.9022
Freundlich	n_F	6.03	5.36	4.48
	K_F ($mg^{(n-1)/n}L^{1/n}g^{-1}$)	150	140	121
	R^2	0.9116	0.9370	0.9586
Temkin	n_T (mg g^{-1})	42.9	48.8	55.7
	K_T (L mg^{-1})	22.5	11.1	5.26
	R^2	0.9579	0.9786	0.9687

For all three temperatures studied, the Temkin isotherm model fit the data the closest, as shown through the R^2 values presented in Table 7.71. This indicates that adsorption onto sample O4 is heterogenous in nature, either through varying adsorption sites on the surface of O4 or through interactions between the adsorptive and adsorbate molecules.

Table 7.72: Isotherm modelling parameters for sample O6 with methyl orange dye

Model	Parameters	Temperature (°C)		
		25	35	45
Langmuir	q_{max} (mg g^{-1})	247	261	292
	K_L (L mg^{-1})	0.346	0.475	0.192
	R^2	0.7874	0.8818	0.872
Freundlich	N_F	6.17	6.92	5.79
	K_F ($mg^{(n-1)/n}L^{1/n}g^{-1}$)	107	124	116
	R^2	0.9078	0.8762	0.9065
Temkin	n_T (mg g^{-1})	29.3	29.8	36.4
	K_T (L mg^{-1})	27.6	40.4	14.4
	R^2	0.9181	0.9267	0.9430

Similar to sample O4, the Temkin isotherm showed the best fit to the isotherm data for all three temperatures for sample O6. This similarly indicates a heterogenous adsorption process for this sample.

The relatively poor fitting of the data to the Langmuir isotherm model for either sample could indicate that one or more of the assumptions underpinning the Langmuir model did not apply for these systems. This could either be the assumption of monolayer coverage, the assumption of homogeneity of adsorption sites across the surface, or the assumption that there are no interactions between adsorbed molecules. While the Freundlich and Temkin isotherm models share many of the same assumptions: heterogeneity in adsorption sites, interactions between adsorbed molecules is possible, and multilayer formation is allowed; the key distinction is the variation in the enthalpy of adsorption with varying surface coverage. In the Temkin isotherm model this is assumed to linearly decrease with increasing coverage, while in the Freundlich isotherm model this is assumed to exponentially decrease with increasing surface coverage. The accuracy of this assumption will be checked later in Section 7.4.3, and the applicability of the Temkin isotherm model assessed in more detail.

7.4.3 Adsorption Thermodynamics of Sample O4

The Temkin isotherm equilibrium constants K_T stated in Table 7.71 and Table 7.72 were used to calculate the maximum Gibbs free energy of the adsorption systems at the various temperatures of study, which occurs when the surface is pristine, prior to any adsorption taking place. This data was then used to calculate the maximum enthalpy and entropy of the system to better understand the nature of the adsorption mechanism taking place. The results are summarised in Table 7.73 for both samples O4 and O6.

Table 7.73: Thermodynamic quantities calculated for samples O4 and O6

Sample	ΔH_{max}^{θ} (kJ mol^{-1})	ΔS^{θ} (J mol^{-1}K^{-1})	ΔG_{max}^{θ} (kJ mol^{-1})		
			25°C	35°C	45°C
O4	-57.2	-60.5	-39.2	-38.7	-38.0
O6	-25.1	51.0	-39.7	-42.0	-40.6

Sample O4 shows an exothermic enthalpy and a negative entropy, indicative of a physisorption process. It also shows an increase in Gibbs free energy with increasing temperature, another hallmark of physisorption, becoming less spontaneous with increasing temperature. Sample O6, however, shows a different behaviour, with an exothermic enthalpy but a positive entropy. This is indicative of an exothermic chemisorption process with a dissociative step leading to the increase in entropy of the

system. The Gibbs free energy does not follow any distinct pattern with the temperature change of the system. This is atypical of an entropic system where one would expect lower temperatures to be more spontaneous and therefore have a lower Gibbs free energy as discussed in Section 3.3.

The trend in isotherm shape was investigated to corroborate the thermodynamic properties found. The Temkin isotherm fits for sample O4 at all three temperatures studied are shown in Figure 7.103.

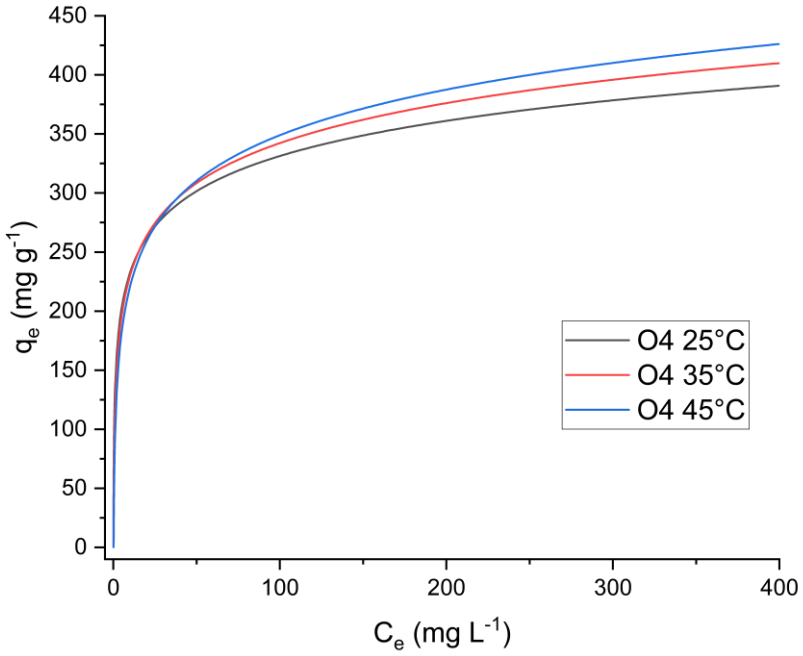

Figure 7.103: Temkin isotherm fits for sample O4 at 25 °C, 35 °C and 45 °C

Contrary to the thermodynamic data discussed above, the isotherm curves show an increase in uptake with increasing temperature. This is counter to both the expected behaviour of a negentropic system but also the Gibbs free energy trend shown in Table 7.73. A truncated view of the isotherms between equilibrium concentrations of 0 and 60 mg L^{-1} can be seen in Figure 7.104.

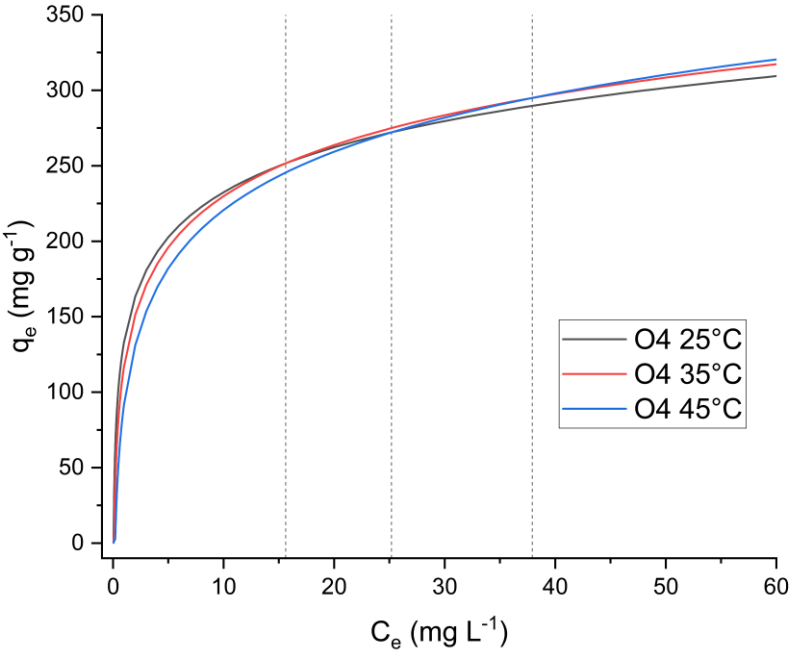

Figure 7.104: Truncated view of Temkin isotherm fits for sample O4 at 25 °C, 35 °C and 45 °C

From Figure 7.104, we see the characteristic negentropic behaviour at low equilibrium concentrations, less than 16 mg L^{-1}, with uptake increasing with decreasing temperature. There is then a transition phase where the isotherms intersect each other: 25 °C and 35 °C intersect at an equilibrium concentration of 16 mg L^{-1} and uptake of 252 mg g^{-1}; 25 °C and 45 °C intersect at 25 mg L^{-1} and 272 mg g^{-1}; and 35 °C and 45 °C intersect at 38 mg L^{-1} and 295 mg g^{-1}. Above an equilibrium concentration of 38 mg L^{-1} we see the entropic behaviour in which uptake increases with increasing temperature which is visible in the expanded view of the whole isotherm (Figure 7.103).

At lower uptakes and equilibrium concentrations, the isotherms show the behaviour predicted by the thermodynamic properties calculated in Table 7.73, which, as highlighted earlier, indicates the initial pristine state prior to adsorption. The vastly different thermodynamic behaviour indicated by the isotherms suggest a system with multiple different mechanisms taking place, both entropic and negentropic in nature. To further understand the mechanism of adsorption, the van't Hoff isochore was employed to determine how the enthalpy varies with uptake of adsorbate. The plot of how enthalpy of adsorption varies with adsorbate uptake for the Temkin isotherm fits of sample O4 is shown in Figure 7.105.

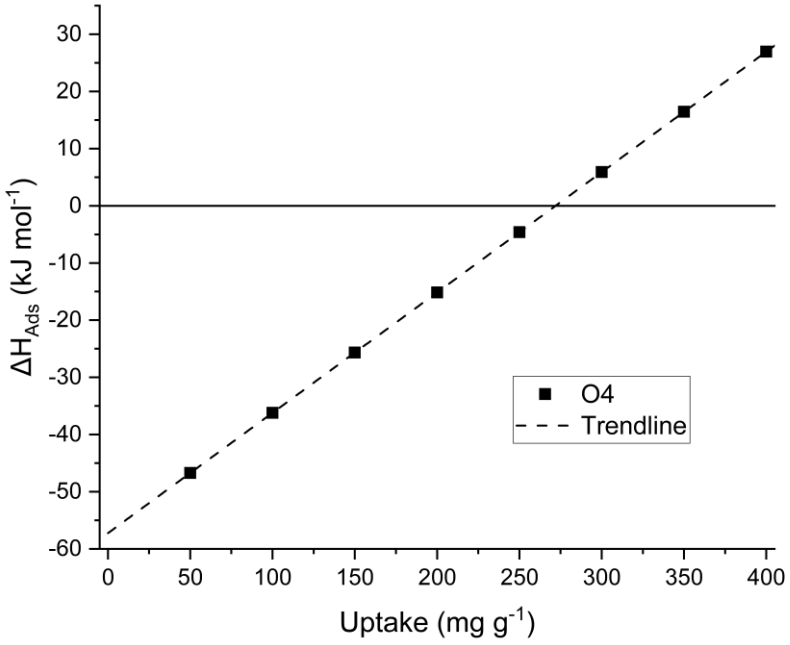

Figure 7.105: Enthalpy of adsorption vs uptake plot for sample O4

Figure 7.105 shows a linear increase in enthalpy, as assumed by the Temkin isotherm model, indicating further merit to the application of the model in this work. The plot also shows an increase in enthalpy with increasing uptake, moving from an exothermic process to an endothermic one, while remaining a spontaneous adsorption process. The switch in behaviour from exothermic to endothermic corresponds to a mass uptake of approximately 270 mg g^{-1}, which is in the region of the isotherm where the entropy trend switches from negentropic (increasing with decreasing temperature) to entropic (increasing with increasing temperature). This indicates that at lower uptakes there is an exothermic and negentropic physisorptive interaction occurring with certain surface sites interacting with the adsorbate. After these sites are filled, an endothermic and entropic process takes place with formal chemical bonds being formed between the dye molecules and other sites on the adsorbent surface. Both of these processes are spontaneous and occur sequentially and on separate sites. It is likely that the physisorption process offers a more favourable interaction to the adsorptive molecules, as it appears to complete before chemisorption occurs. It is believed that these two different sites are what give rise to the heterogeneous nature of the interactions between the adsorbate and adsorbent, which manifests as Temkin isotherm behaviour.

To investigate the different sites for adsorption available on the surface, Scatchard analysis was carried out, and the Scatchard plots for sample O4 can be seen in Figure 7.106, Figure 7.107 and Figure 7.108, at 25 °C, 35 °C, and 45 °C, respectively.

A table of the Scatchard model parameters obtained for sample O4 are shown in Table 7.74.

Table 7.74: Scatchard parameters for favourable and unfavourable sites for sample O4 isotherms at 25 °C, 35 °C and 45 °C

Temperature	Favourable sites		Unfavourable sites		Intersection
°C	q_s (mg g^{-1})	K_b (L mg^{-1})	q_s (mg g^{-1})	K_b (L mg^{-1})	(mg g^{-1})
25	287	0.792	412	0.0437	280
35	262	0.780	427	0.0456	252
45	232	0.849	472	0.0298	224

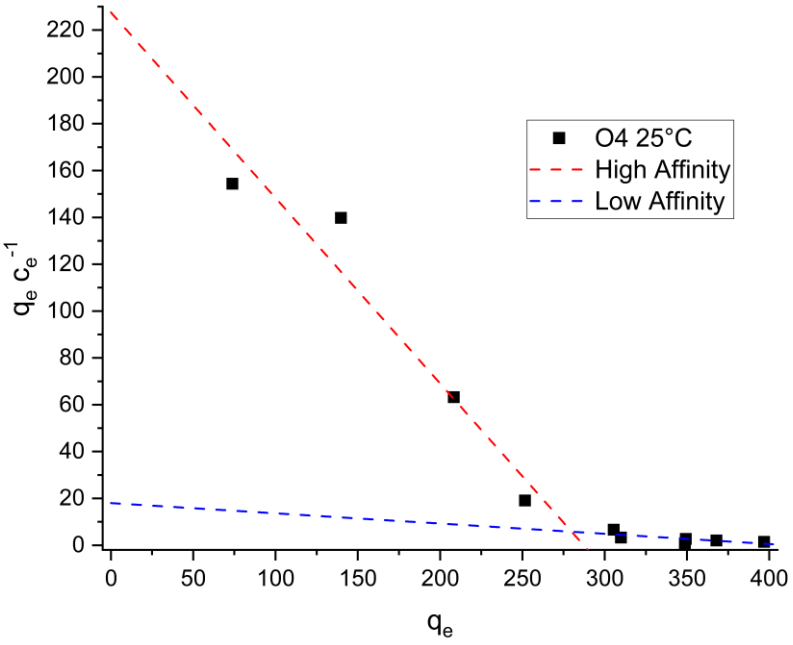

Figure 7.106: Scatchard plot for sample O4 at 25°C

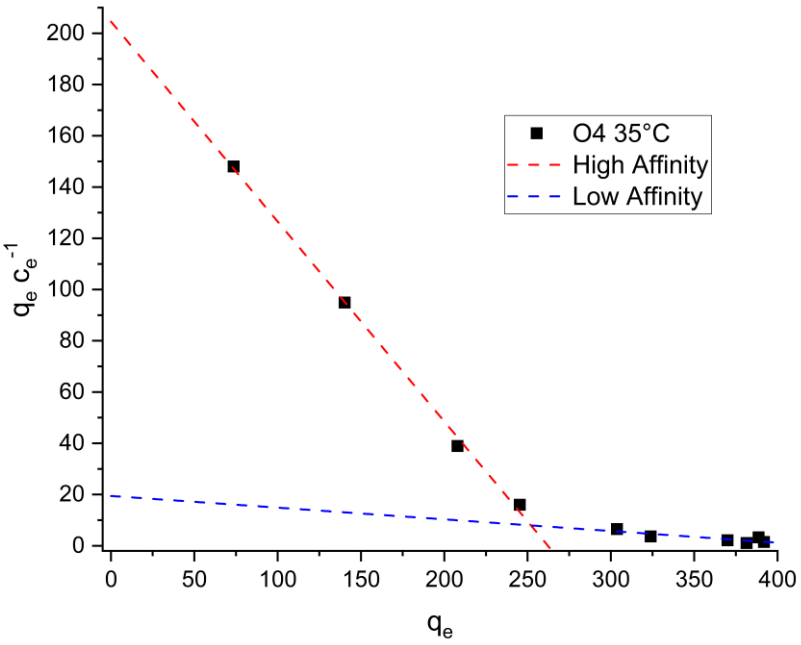

Figure 7.107: Scatchard plot for sample O4 at 35°C

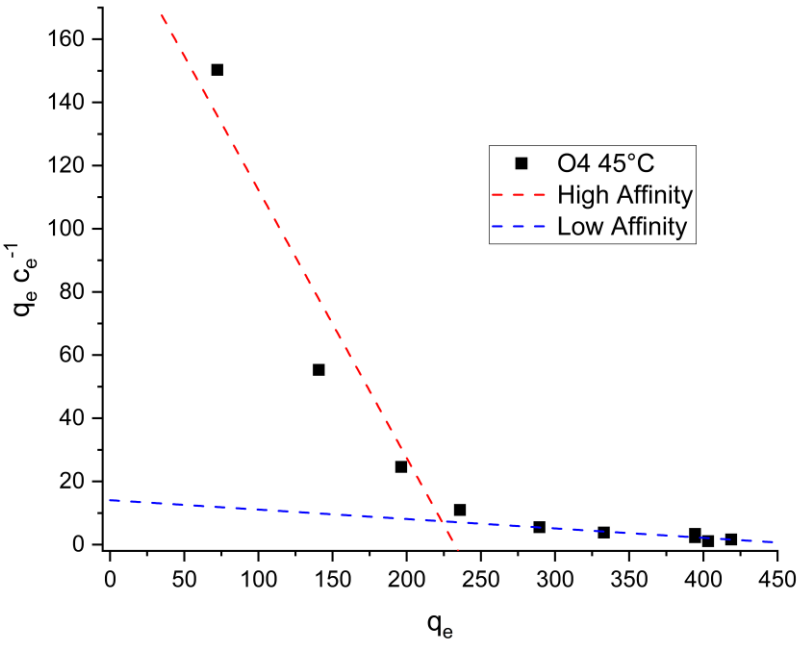

Figure 7.108: Scatchard plot for sample O4 at 45°C

The Scatchard plots for all three isotherms clearly show two linear zones, the first is for more favourable sites with higher kinetic constants K_b, and the second is for more unfavourable sites with a lower kinetic constant. The intersections of the two trendlines for the favourable and unfavourable sites lines occur approximately around the regime change from exothermic and negentropic to endothermic and entropic behaviour, i.e. at around 270 mg g^{-1}, as shown in the van't Hoff plot in Figure 7.105. The two different sites also exhibit comparable kinetic constants for each temperature, indicating a similar mechanism occurs. The uptakes for each site, however, change with temperature - following the trend for the assumed entropic process taking place: at the favourable sites, the uptake increases with increasing temperature, indicative of a negentropic process, while at the less favourable sites, the uptake increases with increasing temperature, indicative of an entropic process. This is further corroboration for two different adsorption mechanisms taking place at low and high uptakes of adsorbent on the surface.

7.4.4 Adsorption Thermodynamics of Sample O6

The Temkin isotherm plots for sample O6 in Figure 7.109 show an agreement with the entropic thermodynamic behaviour discussed above, i.e. an increase in uptake is observed as temperature increases. A truncated view of the isotherms between equilibrium concentrations of 0 and 20 mg L^{-1} can be seen in Figure 7.110.

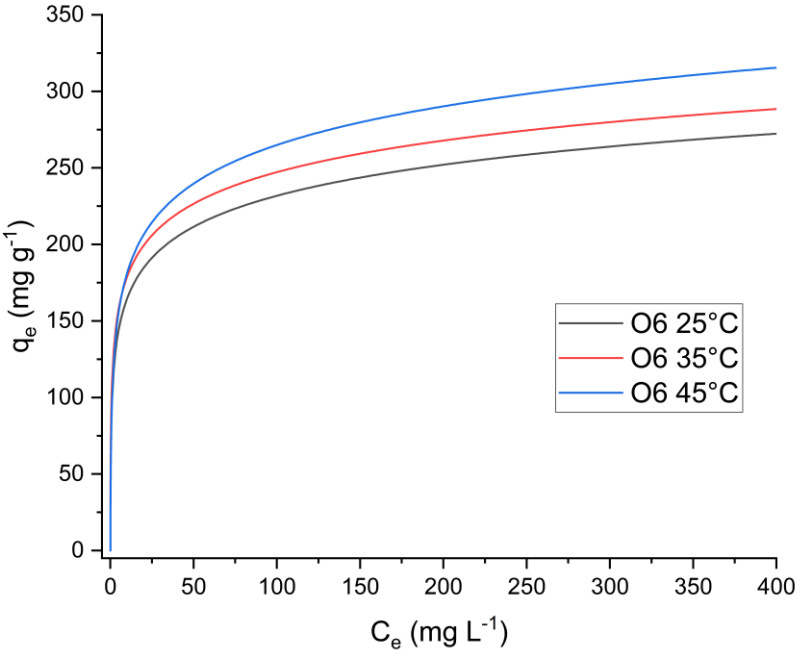

Figure 7.109: Temkin isotherm fits for sample O6 at 25°C, 35°C and 45°C

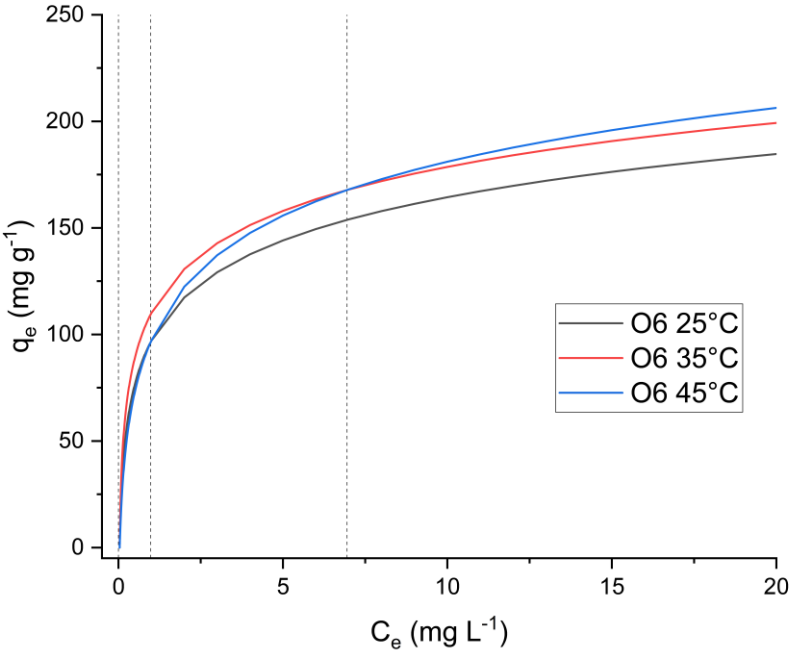

Figure 7.110: Truncated view of Temkin isotherm fits for sample O6 at 25°C, 35°C and 45°C

A similar intersecting of the lines can be seen at low equilibrium concentrations on the Temkin isotherm fits for sample O6, as previously seen for sample O4. At equilibrium concentrations above 7 mg L^{-1}, the isotherms show characteristic entropic behaviour where the uptake increases with increasing temperature. Below 7 mg L^{-1}, there is a similar transition stage where the isotherms intercept: 45 °C and 35 °C intercept at 7 mg L^{-1} and 168 mg g^{-1}; 25 °C and 45 °C intercept at 1 mg L^{-1} and 97 mg g^{-1}; and 25 °C and 35 °C intercept at very close to 0 mg L^{-1} and 0 mg g^{-1}. The plot of how enthalpy of adsorption varies with adsorbate uptake for the Temkin isotherm fits of sample O6 can be seen in Figure 7.111.

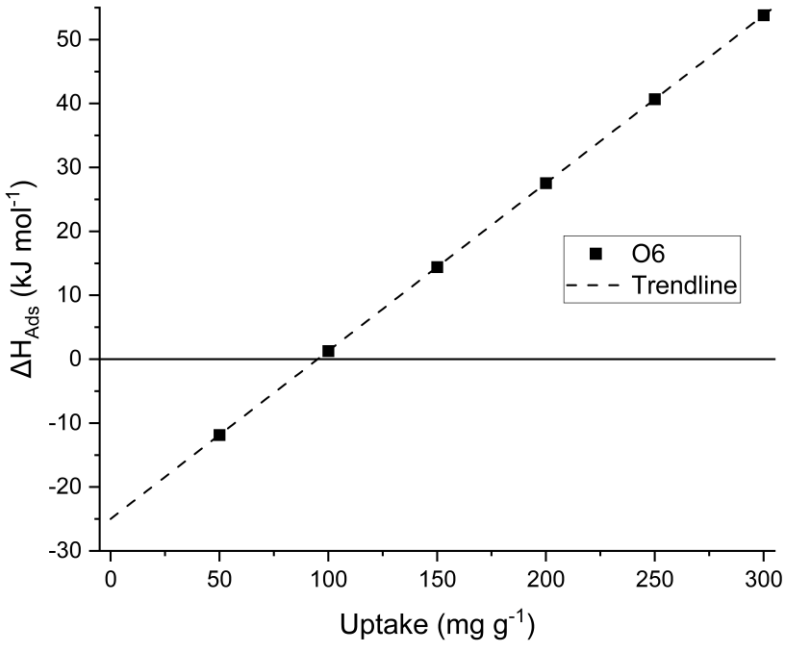

Figure 7.111: Enthalpy of adsorption vs uptake for sample O6

The O6 van't Hoff plot above shows a similar trend to the earlier O4 plot. The highly linear trend of increasing adsorption enthalpy with uptake further displays the applicability of the Temkin isotherm. Sample O6 shows a similar switch from an exothermic process to an endothermic process, with the switch occurring at approximately 100 mg g^{-1}. This is within the intermediate intersection zone highlighted on Figure 7.110 which was from uptakes of 0- 168 mg L^{-1}.

If adsorption on sample O6 follows the same mechanism as that for sample O4, then it can be assumed that, in the transitional intersection zone between uptakes of 0 and 168 mg L^{-1},

the adsorption process taking place switches from a negentropic and exothermic physisorptive process to an entropic, endothermic chemisorptive process. The reduced uptake of this physisorptive process for sample O6, as compared to sample O4, is likely linked to the reduced surface area of sample O6 compared to sample O4 (1527 $m^2 g^{-1}$ to 1264 $m^2 g^{-1}$).

This initial negentropic and exothermic process is, however, counter to the thermodynamic parameters found for the initial pristine surface, which indicates an initial adsorption process that is exothermic but entropically positive. This, coupled with the unusual lack of pattern to the Gibbs free energy variation with temperature, leads us to believe that one or more of the fits for one of the isotherms for sample O6 is incorrect. This is thought to be due to the inconsistency between samples of O6 used for the adsorption isotherms. The generally lower R^2 values obtained for the adsorption isotherms of sample O6, as compared to sample O4, as well as the large spot-to-spot variation in oxygen and nitrogen functional groups, shown in the XPS analysis of sample O6, corroborate this hypothesis. The global variation in sample O6 is thought to be due to the lower furnace residence time used in the synthesis of this biochar. The longer hold time of a sample like O4 reduces the effect of natural variation between different samples of BSG, homogenising the final product.

To further investigate the different adsorption sites available on sample O6, Scatchard analysis was carried out, and the Scatchard plots for sample O6 can be seen in Figure 7.112, Figure 7.113 and Figure 7.114, at 25 °C, 35 °C, and 45 °C, respectively.

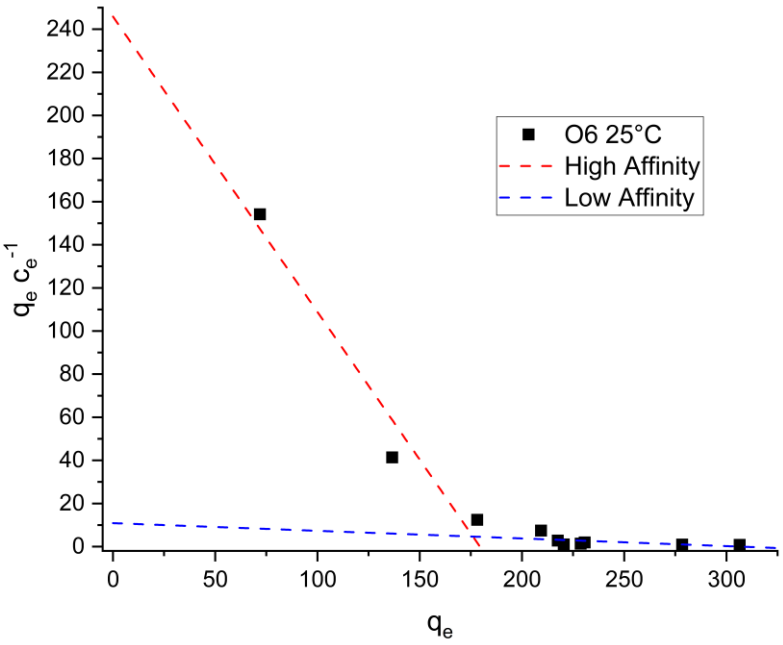

Figure 7.112: Scatchard plot for sample O6 at 25 °C

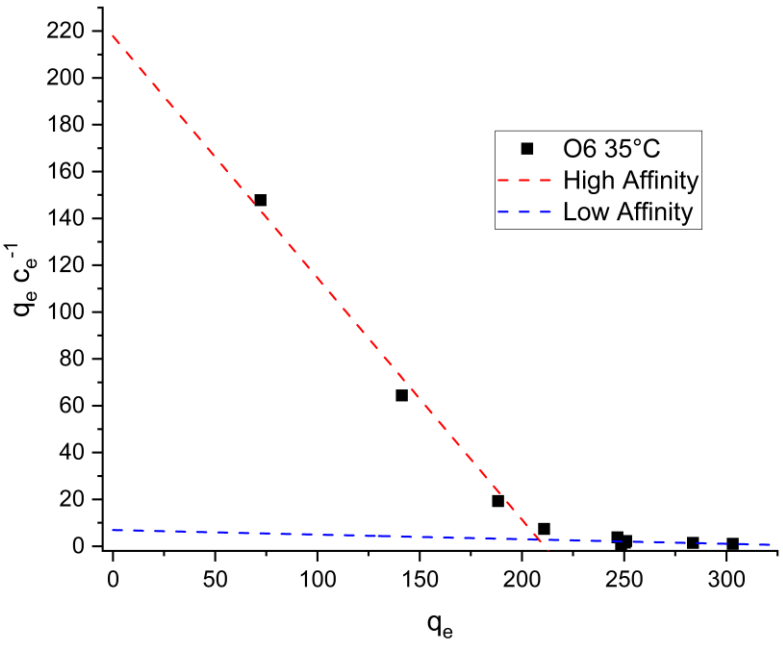

Figure 7.113: Scatchard plot for sample O6 at 35 °C

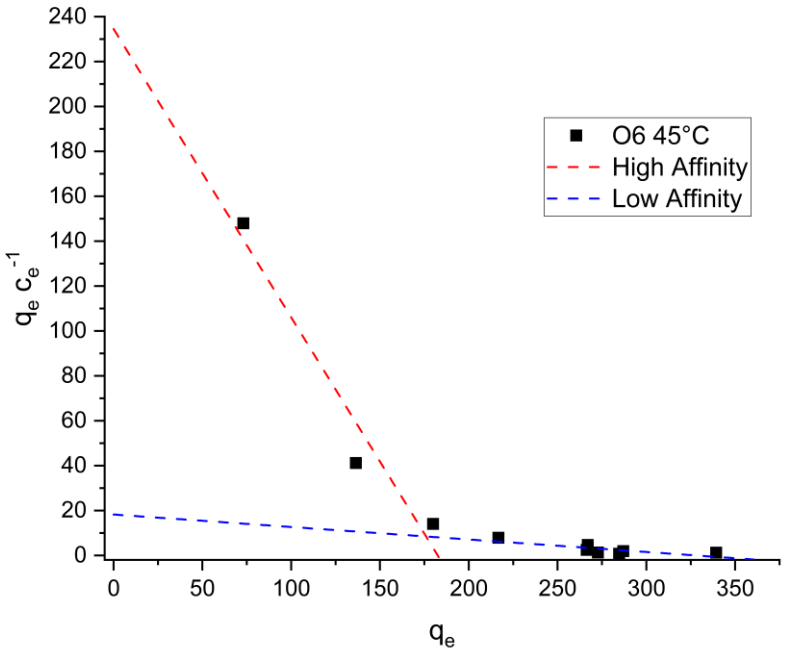

Figure 7.114: Scatchard plot for sample O6 at 45 °C

The Scatchard parameters obtained for both the favourable and unfavourable sites on the surface of sample O6 can be seen in Table 7.75.

Table 7.75: Scatchard parameters for favourable and unfavourable sites for sample O6 isotherms at 25°C, 35°C and 45°C

Temperature (°C)	Favourable sites		Unfavourable sites		Intersection
	q_s (mg g^{-1})	K_b (L mg^{-1})	q_s (mg g^{-1})	K_b (L mg^{-1})	(mg g^{-1})
25	179	1.37	306	0.0356	176
35	203	1.11	299	0.0598	198
45	183	1.28	328	0.0556	176

If sample O6 exhibits a similar mechanism as sample O4 then, at the favourable physisorptive sites, on which the negentropic exothermic process takes place, we would expect the capacity q_s to increase with decreasing temperature, while at the unfavourable chemisorptive entropic and endothermic sites, we would expect the capacity to increase with elevated temperature. The behaviour of the 25 °C isotherm Scatchard does not follow this pattern for either of the favourable or unfavourable sites. Additionally, the magnitudes of the kinetic constants for 25 °C are both dissimilar to the other temperatures, which are

in good agreement, further lending evidence that it is the 25 °C isotherm for which an error has been obtained in the experimental data.

Due to the possibility that the isotherm for sample O6 is inaccurate, the thermodynamic data for sample O6 can be assumed to not be fully accurate and should be treated with caution. As it is suspected that these systems exhibit chemisorption, it is not feasible to regenerate and reuse samples within a suite of isotherm experiments. In future work, isotherms at more temperatures should be carried out, where possible, and greater homogenisation of biochar samples should be carried out to avoid batch variation issues, as seen here.

7.4.5 Error Analysis of Isotherm Fits

Error analysis of the Temkin fits for each isotherm were carried out. The isotherm parameter values and associated margin of error are shown in Table 7.76 below.

Table 7.76: Temkin isotherm parameters with associated margin of error

Sample	Parameters	Temperature (°C)		
		25	35	45
O4	n_T (mg g^{-1})	42.9 ± 3.18	48.8 ± 2.56	55.7 ± 3.54
	K_T (L mg^{-1})	22.5 ± 11.4	11.1 ± 3.59	5.26 ± 1.86
	R^2	0.9579	0.9786	0.9687
O6	n_T (mg g^{-1})	29.3 ± 3.09	29.8 ± 2.96	36.4 ± 3.17
	K_T (L mg^{-1})	27.6 ± 21.6	40.4 ± 30.9	14.4 ± 8.41
	R^2	0.9181	0.9267	0.9430

The plots of this data for each sample and associated upper and lower bound curves are shown in Appendix G.

Despite the high R^2 values, the relative error in some of the isotherm fitting parameters is quite large, particularly K_T. This is reflected in the curves shown in Appendix G which show large error bands for each of the isotherms for both samples and all 3 temperature curves lie within each other's error envelopes. Statistically, this indicates that the difference between each of the isotherms at 25, 35 and 45°C are small relative to the uncertainty in the fitted parameters.

As a result, the apparent separation and intersection of the isotherms cannot be considered robust. This may indicate that the error in the system is too large to draw meaningful conclusions around the relative shape of the isotherms and therefore thermodynamic data derived using the van't Hoff isochore may be inaccurate. For this reason the values and conclusions should be treated with caution. Future work to add more points to the isotherms and additional isotherms at more temperatures should be carried out to validate or refute the thermodynamic claims made above.

Despite these limitations, the mechanistic analysis that follows is based on the absolute values for the isotherm fitting parameters and the thermodynamic conclusions made from their analysis. These values remain informative for interpreting the adsorption behaviour, provided the above considerations are acknowledged.

7.4.6 Physisorption Mechanism

The effect of solution pH on the adsorption uptake was investigated for both samples O4 and O6. Sample solutions were prepared at 100 mg L^{-1} with a solution volume of 30 mL. The solution pH was subsequently altered to pH 3, 5, 7, 9 and 11 using sodium hydroxide and hydrochloric acid. These results are also compared to the 100 mg L^{-1} samples from the 25 °C isotherm experiments and 24 h hold time samples from the kinetics experiments, these were used as references to the unaltered 'natural' pH of the adsorptive solution, which was found to be approximately pH= 5.6 at a concentration of 100 mg L^{-1}. The results obtained for samples O4 and O6 are shown in Figure 7.115 and Figure 7.116 respectively.

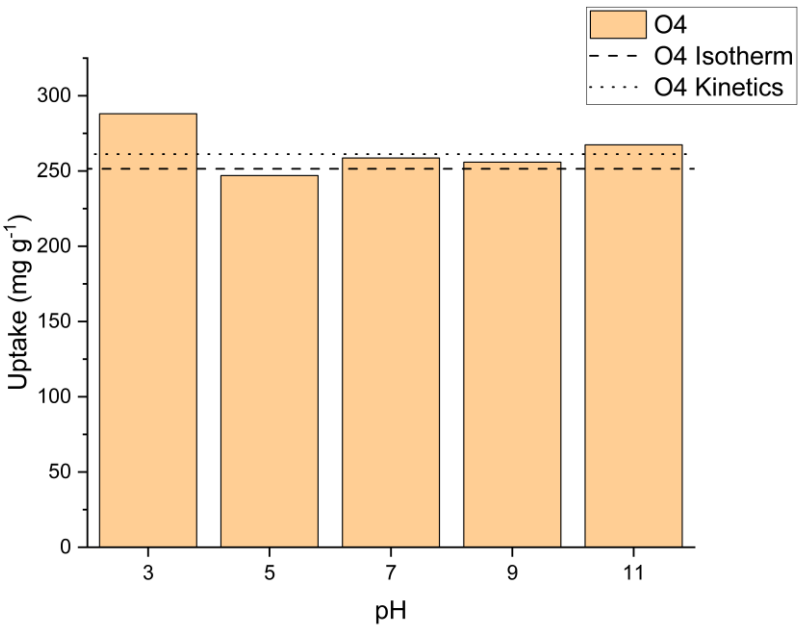

Figure 7.115: Effect of pH on uptake of methyl orange on sample O4

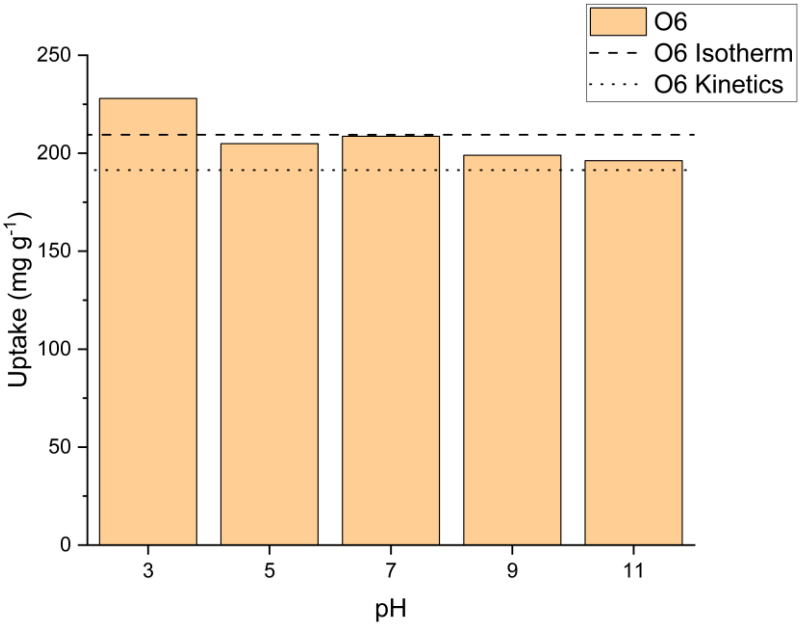

Figure 7.116: Effect of pH on uptake of methyl orange on sample O6

Both samples showed enhanced uptake at pH 3, the pH below the quoted literature range of values at which methyl orange switches from the yellow in colour benzenoid structure to its red in colour acidified quinonoid structure. The reason for a greater degree of adsorption may be two-fold. The first is alteration of the chemistry of the methyl orange

dye molecules to the quinonoid structure of methyl orange (as shown in Table 7.77), which has two fixed charges in its structure, the negative charge at the sulphonate functional group, and the positive charge at one of the nitrogen atoms, either in the protonated azo group or the tertiary amine group, depending on the resonance structure. As stated in the discussion on point of zero charge, the acidic PZCs of the materials indicate that there is a greater number of positive charged surface functional groups - this does not, however, mean that there are no negatively charged functional groups to be found on the surface. This was corroborated by the XPS results that showed quinone and aromatic ring structures, which, as areas of high electron density, form intermolecular bonds readily with fixed positive charges. The increase in uptake could be explained by the new intermolecular interactions taking place between the positive charges on the quinonoid form of methyl orange and these functional groups, known to exist on both samples.

The second potential reason for the uptake is the alteration of the adsorbent surface through protonation of the lone pairs existing on the surface of the biochar materials such as the nitrogen and oxygen containing functional groups. This would alter the structures from areas of high electron density to permanent dipoles with potential to form hydrogen bonds with areas of electron density like the lone pairs on the sulfonate group, lone pairs on the tertiary amine, π electrons of the aromatic rings or π electrons of the azo group. It is likely a combination of both of these effects which gives rise to the increase in uptake of methyl orange dye on the biochar materials.

The uptake of methyl orange on the surface of both samples, at solution pHs when only the benzenoid structure is exhibited, is relatively constant and remains close to behaviour observed for the 'natural' pH values from the isotherm and kinetic experiments. There was no noticeable decrease or enhancement of adsorption uptake below or above the point of zero charge (pH=5.9 and pH= 6.4 for O4 and O6, respectively). This leads to the conclusion that the adsorption mechanism is not significantly controlled by the interactions between the electron donor groups, such as those identified by XPS, such as quinone, carbonyl or aromatic nitrogen groups nor by sites for hydrogen bonding, such as phenol, protonated aromatic nitrogen or pyridinic-N oxide. The physisorption mechanism is controlled more by sites that are not affected by protonation or deprotonation, such as the graphitic carbon structures that were identified as the most prevalent functional group using XPS. This also makes sense, as the biochar materials are derived from BSG material, which comprises a

significant lignin component - a large polyphenolic network comprising of aromatic rings (186, 187). The prevalent adsorption mechanism is, therefore, likely to be π-π interactions from the aromatic rings of the methyl orange structure or π-π interactions between the azo group π electrons or sulphone π electrons with the π electrons of the adsorbent aromatic rings. If the physisorption mechanism was controlled strongly by electrostatic interactions between functional groups on the surface that are easily affected by the protonation or deprotonation of lone pairs of electrons, we would expect a vast difference in uptake on the surface as the pH of the adsorptive solution surrounding the adsorbent changes from above to below the point of zero charge.

Table 7.77 describes the functional groups found for methyl orange in its various forms and their role in intermolecular interactions.

Table 7.77: Methyl orange forms and functional groups

Species	Structure	Amine group	Ring groups	Azo group	Sulfone group
Benzenoid methyl orange	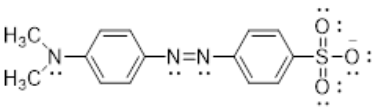	Lone pair	Pi and Pi* orbitals	Lone pairs	Anionic charge, lone pair
Quinonoid methyl orange resonance 1	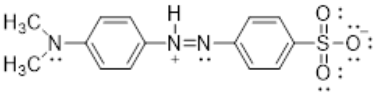	Lone pair	Pi and Pi* orbitals	Cationic charge	Anionic charge, lone pair
Quinonoid methyl orange resonance 2	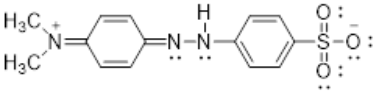	Cationic charge	Pi and Pi* orbitals	Lone pair and hydrogen bond donor	Anionic charge, lone pair

Table 7.78 shows the organic groups identified through XPS analysis, their chemical environment, potential intermolecular interactions, and role in those interactions.

Table 7.78: Functional groups identified and potential adsorption mechanism with methyl orange

Species	Structure	Mechanism
Aromatic carbon	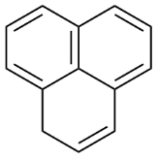	π-electrons and orbitals: n-π* acceptor, π-π stacking, cation- pi interaction, Yoshida hydrogen bond acceptor
Quinone (OI)	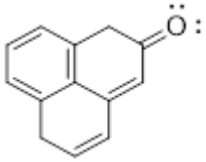	Lone pair: hydrogen bond acceptor, lone pair-cation interaction
Ketone (OI)	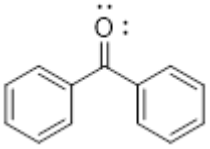	Lone pair: hydrogen bond acceptor, lone pair-cation interaction
Phenol (OII)	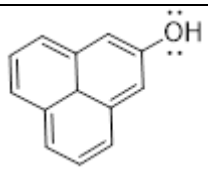	Hydrogen-oxygen dipole: hydrogen bond donator
Ether (OII)	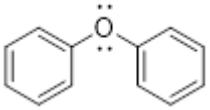	Lone pair: hydrogen bond acceptor, lone pair-cation interaction
Carboxylic acid (OIII)	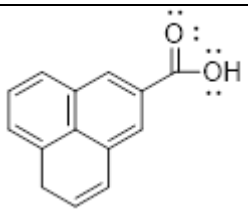	Lone pair: hydrogen bond acceptor, lone pair-cation interaction Hydrogen-oxygen dipole: hydrogen bond donator
Physisorbed water (OIII)	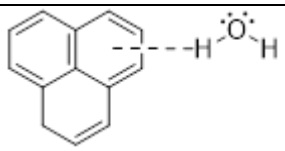	Hydrogen-oxygen dipole: hydrogen bond donator
Pyridinic nitrogen (N6)	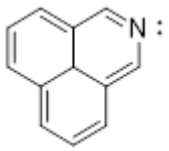 or	Lone pair: hydrogen bond acceptor, lone pair-cation interaction

	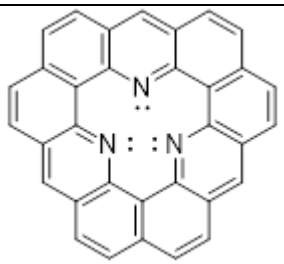	
Quaternary nitrogen (NQ)	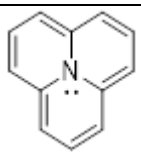	Lone pair: hydrogen bond acceptor, lone pair-cation interaction
Pyridinic-N Oxide (N-X)	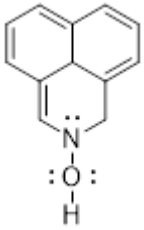	Lone pair: hydrogen bond acceptor, lone pair-cation interaction Hydrogen-oxygen dipole: hydrogen bond donator
Silica	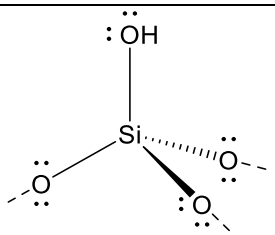	Lone pair: hydrogen bond acceptor, lone pair-cation interaction Hydrogen-oxygen dipole at edge defects: hydrogen bond donator

Note than in an acidified environment each of the lone pairs in the structures described in Table 7.78 above can become protonated, creating a fixed cationic charge. These positively charged cations will form intermolecular bonds with lone pairs, delocalised electrons in aromatic rings, and any anionic fixed charges present in the system.

7.4.7 Chemisorption Mechanism

7.4.7.1 Photocatalytic Degradation Investigation

The endothermic and entropically positive adsorption of methyl orange dye onto sample O4 was initially investigated to determine if the process was a photocatalytic degradation reaction, as suggested by previous work where photocatalytic degradation was observed in a system using fullerenes functionalised onto a silica support in an acidic environment (188). This mechanism proposes that the visible light promotes the fullerene/ SiO_2 complex to an excited state, with electron transfer from the complex to the quinoid form of the

methyl orange cleaving the azo bond, leading to sulphanilic acid and N, N-dimethyl-p-phenylenediamine products. Within that study, the silica support was stated to not play a role in the reaction and only existed as a support for the fullerene active sites. It could be postulated that the role of fullerene, as a carbonaceous material containing delocalised electrons, may be replicated, in this work, by the basal plane graphene structures noted to be present in both samples O4 and O6. While silica was not explicitly stated to have a role in the mechanism, it is also present on the surface of the materials synthesised in this work.

To test the hypothesis that photocatalytic effects may contribute to methyl orange reduction for sample O4, two experiments were proposed, batch adsorption in complete darkness with no light irradiation and an experiment under constant controlled visible light exposure. A reduced points isotherm experiment was carried out using initial methyl orange concentrations of 100, 200, 300 and 500 mg L^{-1}. These were chosen to conserve material while giving two points expected to be above and below the transition from an exothermic and entropically negative to an endothermic and entropically positive adsorption mechanism, expected at an uptake of approximately 270 mg g^{-1} on sample O4.

The experiments were carried out at room temperature with a flask volume of 30 mL and a contact time of 24 h. Due to the size of the dark-box available, the orbital shaker used for other batch liquid phase adsorption experiments could not be used. Instead, a magnetic stirrer, set at 350 rpm, was used to provide constant agitation of the vessel contents. The light source used was a Wolezek 80-LED lamp, consisting of 28 white 5000 K, 40 warm white 3000 K, and 12 red 660 nm LEDs. This lamp provides the full spectrum (380-800 nm) of visible light, simulating the visible band of sunlight. The LEDs were suspended 10 cm above the stirring plate and were used on full power at 40 W. A lux meter reading was taken prior to the experiment, the site of the flask read 4740 ±180 lux. Note that LEDs were specifically chosen due to their low heat production, minimising the potential effects of temperature on the experiments. The removal of methyl orange using sample O4, was determined using residual concentrations, and the data were fitted using the Temkin isotherm. The results are summarised in Table 7.79.

Table 7.79: Comparison of Temkin fitting parameters of methyl orange adsorption onto O4 for darkness and continuous light

Experiment	n_T (mg g^{-1})	K_T (L mg^{-1})	R^2
Dark	45.0	3.92	0.8323
Light	44.2	3.98	0.8478

The comparison plots of these two isotherms can be seen in Figure 7.117.

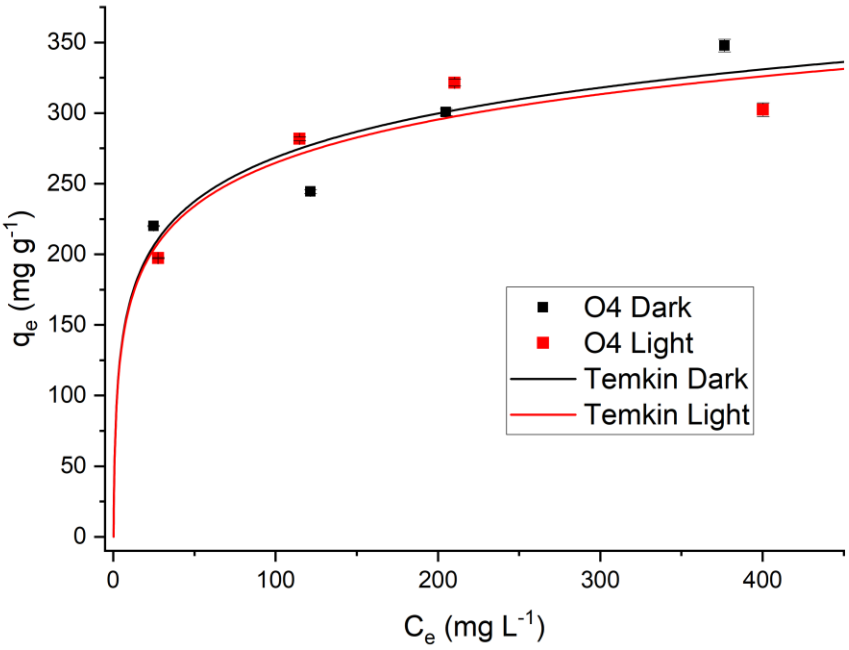

Figure 7.117: Isotherm comparisons of methyl orange adsorption onto O4 in darkness and constant light[27]

As can be seen from both the plots and the resulting isotherm fitting parameters, there is very little difference in the adsorption behaviour at the two sets of conditions. For this reason, it was deemed that the endothermic and entropically positive mechanism taking place is not photocatalytic and, therefore, chemisorptive in nature. While there is some variation in the fits for the two sets of conditions, the variation is significantly lower in magnitude than the difference between the Temkin isotherm fitting parameters shown in Table 7.71. The variation here is thought to be due to sample variation, or minute

[27] Errors are included in the data points for these plots but are too small to be seen at this resolution but were calculated through propagation of Beer-Lambert regression error. The error propagation equations can be seen in appendix D.

differences in temperature between the two experiments. The coefficient of determination for the model fittings are much lower than those found previously in Table 7.71- this is likely due to the much lower number of data points used in the regression for these experiments.

7.4.7.2 Chemisorption Mechanisms in Literature

As both carbonaceous and silica groups have been identified on the surface of the biochar materials, both were investigated as potential sites for chemisorption with methyl orange.

A chemisorption mechanism of methyl orange adsorption using magnetic core-shell Fe_3O_4@ SiO_2 (189) has been observed. The researchers in that study ascribe a physisorption mechanism to the interaction, but show thermodynamics indicative of a chemisorption process: a positive entropy and enthalpy, and an inversely proportional relationship between Gibbs free energy and temperature. To further confuse the situation, they also report a reusability study in which, after 5 cycles, a 20% reduction in adsorption capacity was observed. This reduction in adsorption capacity may be due to incomplete desorption processes or may, possibly, be due to chemisorption taking place. This hints at the adsorption process in the reported study also being a hybrid process, with both physisorption and chemisorption taking place, similar to observations made in this work. The mechanism presented in that study suggests a strong hydrogen bonding interaction between the silanol groups, on the silica nanoparticles, with the sulfone anionic group, on the methyl orange molecules, which may create a formal chemical bond.

A study of methyl orange adsorption utilising Finger-Citron residue activated carbon (190) also reported a positive enthalpy and positive entropy in calculation of the thermodynamic parameters. They also however, incorrectly, presume a physisorptive mechanism for the interaction, which cannot be the case based on the data presented. There is unfortunately no surface characterisation carried out in that study to potentially corroborate the findings carried out in that work. Similarly, in a study carried out where methyl orange dye was adsorbed onto birchwood pellet derived activated carbon (191), the predominant mechanism and rate-limiting step was determined to be chemisorption due to the close fit with the Elovich kinetic model. That study similarly showed an increase in uptake at low pH, when the methyl orange was in the quinoid form, perhaps indicating a relationship between the chemisorptive mechanism and the presence of the cationic charge on the adsorptive molecules. The biochar also presented a zeta potential point of zero charge -

analogous to the salt addition method- of approximately a pH of 5.5, similar to sample O4. This indicated a net positive surface charge on the surface of the material and a greater number of positively charged functional groups such as phenol groups and other hydrogen bond donors. These would form strong interactions with the fixed anionic charge on the sulphone group end of the methyl orange molecules. Unfortunately, no other surface characterisation of the biochars was presented to develop a better picture of the adsorbent surface sites.

7.4.7.3 Proposed Chemisorption Mechanism

In this work, two potential chemisorption mechanisms are proposed. The first is related to the negative charge on the sulfone group at one end of the adsorptive molecule. This cationic centre will form strong interactions with any positively charged areas on the adsorbent surface. These could arise from hydrogen bonding on a dipole on a phenolic -OH or silanol edge defect on silica, or from a protonated lone pair on a quaternary nitrogen group for example. These strong interactions may lead to a formal covalent bond being formed.

The second involves the anionic charge that forms on the quinoid form of the methyl orange adsorptive at low pH. The low point of zero charge of the adsorbent, which is a result of the acid washing procedure during synthesis, may lead to local areas of high proton concentration while in solution. These may reduce the benzenoid structure to the quinoid one allowing for interactions with the cationic nitrogen. The hydrazine cation resonance form is highly sterically hindered, so the resonance form with the tertiary amine cation is more likely to be the form that bonds with the adsorbent. The positively charged cation will form strong interactions with any negatively charged areas on the adsorbent surface. These could be negatively charged ends of dipoles, such as carbonyl or quinone, or lone pairs of electrons present on any nitrogen- or oxygen-containing functional groups. The electrophilic cation may also undergo electrophilic aromatic substitution by attacking the delocalised π-electrons of the aromatic ring structures forming covalent bonds. The first case would also occur at low pH, as the sulfone anion is unaffected by the change in pH of the adsorptive solution; this may be one reason for the increased uptake seen at low pH (shown in Figure 7.115 and Figure 7.116).

7.4.7.4 Desorption Tests

For each sample, dye-loaded biochars were recovered from an adsorption experiment, as described in Section 4.7.3, with an initial dye concentration of 500 mg L^{-1}, a flask volume of 30 mL, and a mass loading of 10 mg. A sample of the biochar was recovered and dried, denoted as 'unwashed'. Some of this sample was taken and washed with 500 mL water, mixed for 10 min to encourage desorption from the surface. This step was repeated until the filtrate water ran clear, the biochars were then recovered and denoted as 'washed'. These two biochar samples were tested, alongside a sample of virgin 'clean' biochar, using Ge ATR FTIR to identify any shifts in the spectral peaks obtained during analysis. The spectra for all three samples, at various levels of dye loading, are shown in Figure 7.118 for sample O4 and Figure 7.119 for sample O6.

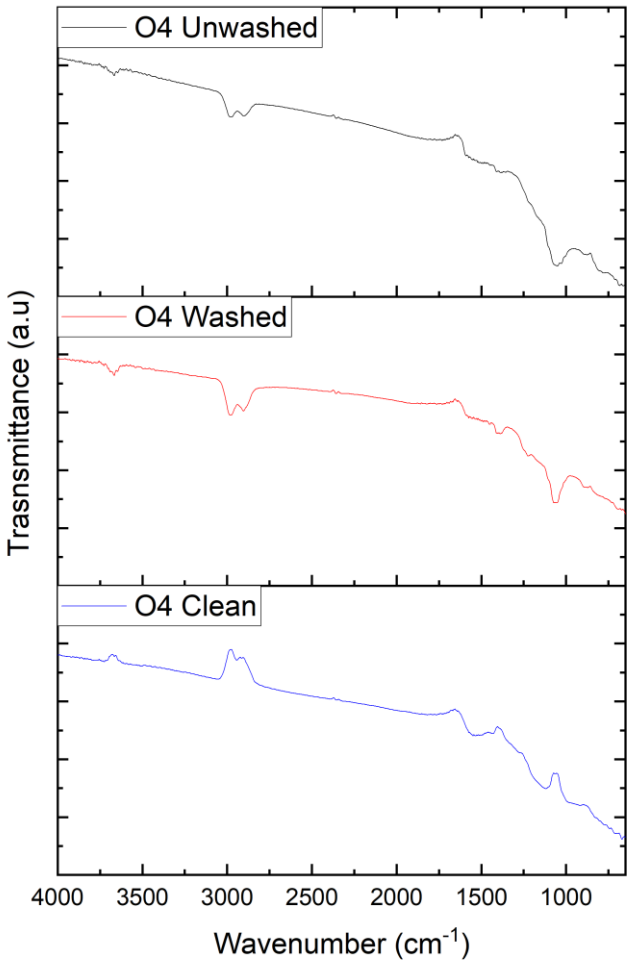

Figure 7.118: ATR FTIR spectra of sample O4 with various levels of methyl orange adsorbed

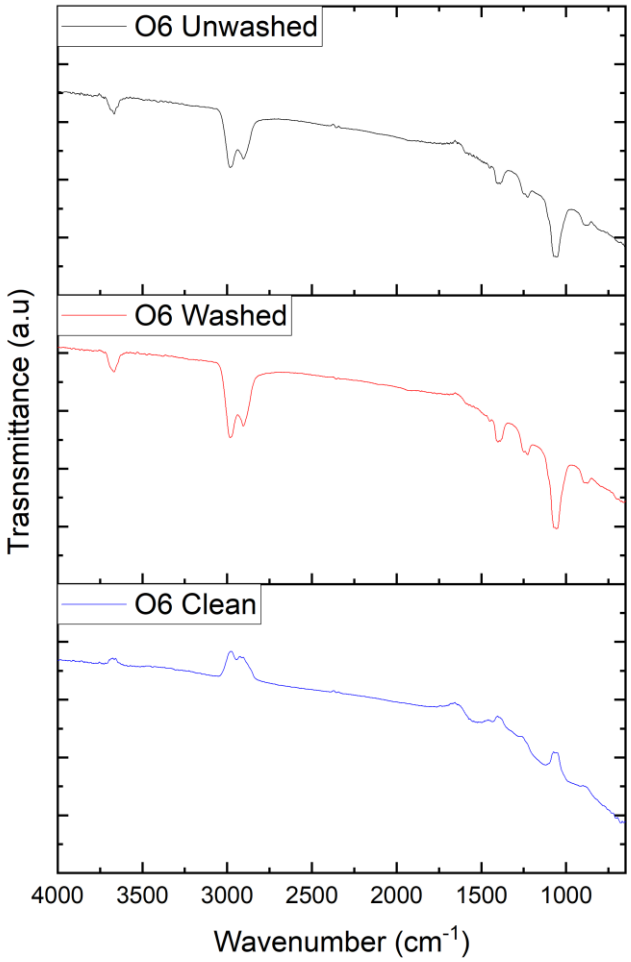

Figure 7.119: ATR FTIR spectra of sample O6 with various levels of methyl orange adsorbed

For both samples, both the washed and unwashed spectra exhibit very similar traces, indicating that either full desorption of the physisorbed material had not been completed during the washing process, or that an irreversible chemisorption process had taken place and so, after washing, dye molecules were still bonded to the biochar surface. Due to the thermodynamic results discussed earlier, the latter was assumed to be more plausible. The large, well-defined peaks at approximately 1050 cm^{-1} and 1400 cm^{-1} were identified as an organic sulphate peak arising from the sulfone functional group on the methyl orange dye, the presence of this on both the 'washed' and 'unwashed' samples indicates its presence both pre- and post-desorption, adding further evidence to the presence of chemisorbed methyl orange on the surface.

A small peak shift from approximately 916 cm^{-1} to 880 cm^{-1} was noted on moving from the dye-loaded sample to the clean samples. This peak is attributed to skeletal C-C vibrations and indicates there may be an intermolecular interaction taking place on the basal aromatic carbon plane (192, 193). This fits with the observation found in the previously discussed investigation into pH influence on uptake, as pH and, therefore, protonation/deprotonation of functional groups did not greatly impact the amount of adsorption observed. A π-π stacking interaction between the aromatic rings on the methyl orange adsorptive and the basal aromatic plane of the biochar materials is likely a major interaction in this system.

7.5 Summary

Sample O4 was synthesised and fully characterised for use in liquid phase adsorption applications, being produced from brewers spent grain biomass feedstock in a tube furnace at 900 °C, at a hold time of 2.5 h, a ramp rate of 20°C min^{-1}, nitrogen and CO_2 gas flows of 100 mL min^{-1}, and subsequently washed with 0.1M hydrochloric acid. Sample O4 had a yield of 7.6 ± 0.4 %, with a carbon content of 68.8 ± 2.0 %. With a high surface area of 1433 ± 114 m^2 g^{-1}, a supermicroporous micropore distribution and a pore size in the mesopore range of 3 nm. The material showed an acidic point of zero charge at pH=5.9, with high concentrations of nitrogen (11-13%) and oxygen (9-11 %) surface functional groups as potential sites for adsorption. Scanning electron microscopy and energy dispersive spectroscopy indicated a hierarchical pore structure and heterogenous sites for adsorption: a carbonaceous site and a site with silicon and oxygen surface functionalities. Methyl orange adsorption studies showed a good fit with the Temkin isotherm model indicating heterogenous adsorption. Through a thorough thermodynamic investigation, both physical and chemical adsorption mechanisms were proposed on the surface of the material, with an initial entropically negative and exothermic physisorption process taking place at low surface coverage and an entropically positive and endothermic chemisorption process taking place after surface coverages of approximately 270 mg g^{-1}, presumably once physisorptive adsorption sites are saturated. The initial enthalpy of adsorption on a clean sample of O4 was found to be -57.2 kJ mol^{-1}.

The physisorption mechanism is believed to involve many intermolecular interactions, such as hydrogen bonding, Yoshida hydrogen bonding (where the proton acceptor is the π electrons of an aromatic ring), and dipole interactions, but mainly π-π stacking of the aromatic basal plane of the biochar with the aromatic rings of the methyl orange. The

chemisorption mechanism is attributed to strong interactions with the fixed anionic charge on the methyl orange with protonated lone pairs, positive dipoles and cationic charge of the methyl orange dye in its quinoid form with negatively charged electron dense dipoles, or reactions with the delocalised electrons in the aromatic carbon basal plane.

7.6 References

1. Gleick PH. Water in crisis: New York: Oxford University Press; 1993.
2. DESA U. The Sustainable Development Goals Report: Special edition. UN, New York, USA. 2023.
3. Leonard AJ. War in Kyrgyzstan and Tajikistan: Freshwater Scarcity and the Path to Peace. 2025.
4. Matthews R, Vivoda V. 'Water Wars': strategic implications of the grand Ethiopian Renaissance Dam. Conflict, Security & Development. 2023;23(4):333-66.
5. Al-Shamaa M. Ethiopia's plan to fill reservoir opposed by Egypt at UN. ARAB NEWS [Internet]. 2022 [cited 2025 20/5]. Available from: https://www.arabnews.com/node/2132831/middle-east.
6. UNESCO. The United Nations world water development report 2024: Water for prosperity and peace: UN; 2024.
7. Connor R, Economic UN, Asia SCfW, Economic, Asia SCf, Pacific t, et al. The united nations world water development report 2017. wastewater: the untapped resource. 2017.
8. Helwig K, Cooper A, Pagaling E, Henderson F, Avery L, Roberts J, et al. Emerging Contaminants: Informing Scotland's strategic monitoring and policy approaches on substances of increasing concern. 2024.
9. Vieira L, Soares A, Freitas R. Caffeine as a contaminant of concern: a review on concentrations and impacts in marine coastal systems. Chemosphere. 2022;286:131675.
10. Raza'i TS, Amrifo V, Pardi H, Putra IP, Febrianto T, Ilhamdy AF. Accumulation of essential (copper, iron, zinc) and non-essential (lead, cadmium) heavy metals in Caulerpa racemosa, sea water, and marine sediments of Bintan Island, Indonesia. F1000Research. 2022;10:699.
11. Islam T, Repon MR, Islam T, Sarwar Z, Rahman MM. Impact of textile dyes on health and ecosystem: a review of structure, causes, and potential solutions. Environmental Science and Pollution Research. 2023;30(4):9207-42.
12. Richardson SD. Disinfection by-products and other emerging contaminants in drinking water. TrAC Trends in Analytical Chemistry. 2003;22(10):666-84.
13. Aus der Beek T, Weber FA, Bergmann A, Hickmann S, Ebert I, Hein A, et al. Pharmaceuticals in the environment—Global occurrences and perspectives. Environmental toxicology and chemistry. 2016;35(4):823-35.
14. Tovar-Sánchez A, Sánchez-Quiles D, Basterretxea G, Benedé JL, Chisvert A, Salvador A, et al. Sunscreen products as emerging pollutants to coastal waters. PLoS One. 2013;8(6):e65451.
15. Jagini S, Konda S, Bhagawan D, Himabindu V. Emerging contaminant (triclosan) identification and its treatment: a review. SN Applied Sciences. 2019;1:1-15.
16. Alberti S, Sotiropoulou M, Fernández E, Solomou N, Ferretti M, Psillakis E. UV-254 degradation of nicotine in natural waters and leachates produced from cigarette butts and heat-not-burn tobacco products. Environmental Research. 2021;194:110695.
17. Adeel M, Song X, Wang Y, Francis D, Yang Y. Environmental impact of estrogens on human, animal and plant life: A critical review. Environment international. 2017;99:107-19.

18. Dueñas-Moreno J, Vázquez-Tapia I, Mora A, Cervantes-Avilés P, Mahlknecht J, Capparelli MV, et al. Occurrence, ecological and health risk assessment of phthalates in a polluted urban river used for agricultural land irrigation in central Mexico. Environmental Research. 2024;240:117454.
19. Vale F, Sousa CA, Sousa H, Santos L, Simões M. Parabens as emerging contaminants: Environmental persistence, current practices and treatment processes. Journal of Cleaner Production. 2022;347:131244.
20. Yang J, Zhao Y, Li M, Du M, Li X, Li Y. A review of a class of emerging contaminants: the classification, distribution, intensity of consumption, synthesis routes, environmental effects and expectation of pollution abatement to organophosphate flame retardants (OPFRs). International journal of molecular sciences. 2019;20(12):2874.
21. Lippold A, Harju M, Aars J, Blévin P, Bytingsvik J, Gabrielsen GW, et al. Occurrence of emerging brominated flame retardants and organophosphate esters in marine wildlife from the Norwegian Arctic. Environmental Pollution. 2022;315:120395.
22. Stoiber T, Evans S, Naidenko OV. Disposal of products and materials containing per- and polyfluoroalkyl substances (PFAS): A cyclical problem. Chemosphere. 2020;260:127659.
23. Ford AT, Ginley F. Insights into PFAS contaminants before and after sewage discharges into a marine protected harbour. Chemosphere. 2024;366:143526.
24. Tang KHD. Per-and polyfluoroalkyl substances (PFAS) in wastewater streams: occurrence and current treatment. Academia Engineering. 2023;1(1).
25. Sanzana S, Fenti A, Iovino P, Panico A. A review of PFAS remediation: Separation and degradation technologies for water and wastewater treatment. Journal of Water Process Engineering. 2025;74:107793.
26. Authority EFS. Pesticides [Available from: https://www.efsa.europa.eu/en/topics/topic/pesticides.
27. Praveena SM, Cheema MS, Guo H-R. Non-nutritive artificial sweeteners as an emerging contaminant in environment: A global review and risks perspectives. Ecotoxicology and environmental safety. 2019;170:699-707.
28. Yu Z, Xu X, Guo L, Jin R, Lu Y. Uptake and transport of micro/nanoplastics in terrestrial plants: Detection, mechanisms, and influencing factors. Science of the Total Environment. 2024;907:168155.
29. Liu W, Liao H, Wei M, Junaid M, Chen G, Wang J. Biological uptake, distribution and toxicity of micro (nano) plastics in the aquatic biota: a special emphasis on size-dependent impacts. TrAC Trends in Analytical Chemistry. 2024;170:117477.
30. Li Y, Tao L, Wang Q, Wang F, Li G, Song M. Potential health impact of microplastics: a review of environmental distribution, human exposure, and toxic effects. Environment & Health. 2023;1(4):249-57.
31. Singh G, Thakur N, Kumar R. Nanoparticles in drinking water: Assessing health risks and regulatory challenges. Science of The Total Environment. 2024:174940.
32. Carballa M, Omil F, Lema JM, Llompart Ma, García-Jares C, Rodríguez I, et al. Behavior of pharmaceuticals, cosmetics and hormones in a sewage treatment plant. Water research. 2004;38(12):2918-26.
33. Ray S, Gusain R, Kumar N. Water purification using various technologies and their advantages and disadvantages. Carbon nanomaterial-based adsorbents for water purification. 2020:37-66.
34. Varjani SJ, Chaithanya Sudha M. Treatment technologies for emerging organic contaminants removal from wastewater. Water remediation. 2018:91-115.
35. Lee A, Elam JW, Darling SB. Membrane materials for water purification: design, development, and application. Environmental Science: Water Research & Technology. 2016;2(1):17-42.

36. AlSawaftah N, Abuwatfa W, Darwish N, Husseini G. A comprehensive review on membrane fouling: Mathematical modelling, prediction, diagnosis, and mitigation. Water 2021, 13, 1327.
37. Malaeb L, Ayoub GM. Reverse osmosis technology for water treatment: State of the art review. Desalination. 2011;267(1):1-8.
38. Mohammed HA, Sachit DE, Al-Furaiji M. Applications and challenges of the reverse osmosis membrane process: a review. Journal of Engineering and Sustainable Development. 2023;27(5):630-46.
39. Judd SJ. Membrane technology costs and me. Water research. 2017;122:1-9.
40. Çeçen F, Aktaş Ö. Water and wastewater treatment: Historical perspective of activated carbon adsorption and its integration with biological processes. Activated carbon for water and wastewater treatment: integration of adsorption and biological treatment. 2011;1.
41. Jonnalagadda S, Nadupalli S. Chlorine dioxide for bleaching, industrial applications and water treatment. Indian Chemical Engineer. 2014;56(2):123-36.
42. EPA U. Wastewater Technology Fact Sheet: Chlorine Disinfection. 1999.
43. Verma AK, Dash RR, Bhunia P. A review on chemical coagulation/flocculation technologies for removal of colour from textile wastewaters. Journal of environmental management. 2012;93(1):154-68.
44. Duan J, Gregory J. Coagulation by hydrolysing metal salts. Advances in colloid and interface science. 2003;100:475-502.
45. Lee CS, Robinson J, Chong MF. A review on application of flocculants in wastewater treatment. Process safety and environmental protection. 2014;92(6):489-508.
46. Ali A, Sadia M, Azeem M, Ahmad MZ, Umar M, Abbas ZU. Ion Exchange Resins and their Applications in Water Treatment and Pollutants Removal from Environment: A Review: Ion Exchange Resins and their Applications. Futuristic Biotechnology. 2023:12-9.
47. Bożęcka A, Orlof-Naturalna M, Sanak-Rydlewska S. Removal of lead, cadmium and copper ions from aqueous solutions by using ion exchange resin C 160. Gospodarka Surowcami Mineralnymi. 2016;32(4):129-39.
48. Rengaraj S, Yeon K-H, Moon S-H. Removal of chromium from water and wastewater by ion exchange resins. Journal of hazardous materials. 2001;87(1-3):273-87.
49. Lehman SG, Badruzzaman M, Adham S, Roberts DJ, Clifford DA. Perchlorate and nitrate treatment by ion exchange integrated with biological brine treatment. Water research. 2008;42(4-5):969-76.
50. Levchuk I, Màrquez JJR, Sillanpää M. Removal of natural organic matter (NOM) from water by ion exchange–a review. Chemosphere. 2018;192:90-104.
51. Miklos DB, Remy C, Jekel M, Linden KG, Drewes JE, Hübner U. Evaluation of advanced oxidation processes for water and wastewater treatment–A critical review. Water research. 2018;139:118-31.
52. Dong S, Feng J, Fan M, Pi Y, Hu L, Han X, et al. Recent developments in heterogeneous photocatalytic water treatment using visible light-responsive photocatalysts: a review. Rsc Advances. 2015;5(19):14610-30.
53. Fenton HJH. LXXIII.—Oxidation of tartaric acid in presence of iron. Journal of the Chemical Society, Transactions. 1894;65:899-910.
54. Khamparia S, Jaspal DK. Adsorption in combination with ozonation for the treatment of textile waste water: a critical review. Frontiers of Environmental Science & Engineering. 2017;11:1-18.
55. Adityosulindro S, Barthe L, González-Labrada K, Haza UJJ, Delmas H, Julcour C. Sonolysis and sono-Fenton oxidation for removal of ibuprofen in (waste) water. Ultrasonics sonochemistry. 2017;39:889-96.

56. Villegas LGC, Mashhadi N, Chen M, Mukherjee D, Taylor KE, Biswas N. A short review of techniques for phenol removal from wastewater. Current Pollution Reports. 2016;2:157-67.
57. Zou LY, Li Y, Hung Y-T. Wet air oxidation for waste treatment: Springer; 2007.
58. Gusain R, Kumar N, Ray SS. Recent advances in carbon nanomaterial-based adsorbents for water purification. Coordination Chemistry Reviews. 2020;405:213111.
59. Sathya R, Arasu MV, Al-Dhabi NA, Vijayaraghavan P, Ilavenil S, Rejiniemon T. Towards sustainable wastewater treatment by biological methods–A challenges and advantages of recent technologies. Urban Climate. 2023;47:101378.
60. Talaiekhozani A. A review on different aerobic and anaerobic treatment methods in dairy industry wastewater. Goli A, Shamiri A, Khosroyar S, Talaiekhozani A, Sanaye R, Azizi K A review on different aerobic and anaerobic treatment methods in dairy industry wastewater Journal of Environmental Treatment Techniques. 2019;7(1):113-41.
61. Garcia-Segura S, Ocon JD, Chong MN. Electrochemical oxidation remediation of real wastewater effluents—A review. Process Safety and Environmental Protection. 2018;113:48-67.
62. Moreno-Casillas HA, Cocke DL, Gomes JA, Morkovsky P, Parga J, Peterson E. Electrocoagulation mechanism for COD removal. Separation and purification Technology. 2007;56(2):204-11.
63. Chen X, Chen G. Electroflotation. Electrochemistry for the Environment: Springer; 2009. p. 263-77.
64. Chang J-H, Ellis AV, Yan C-T, Tung C-H. The electrochemical phenomena and kinetics of EDTA–copper wastewater reclamation by electrodeposition and ultrasound. Separation and Purification Technology. 2009;68(2):216-21.
65. Zhu Y, Fan W, Zhou T, Li X. Removal of chelated heavy metals from aqueous solution: A review of current methods and mechanisms. Science of the Total Environment. 2019;678:253-66.
66. Singh N, Goldsmith BR. Role of electrocatalysis in the remediation of water pollutants. Acs Catalysis. 2020;10(5):3365-71.
67. Martínez-Huitle CA, Andrade LS. Electrocatalysis in wastewater treatment: recent mechanism advances. Quimica Nova. 2011;34:850-8.
68. Zhang S, Fu J, Xing G, Zhu W, Ben T. Porous Materials for Atmospheric Water Harvesting. ChemistryOpen. 2023;12(5):e202300046.
69. Anastas PT, Zimmerman JB. Peer reviewed: design through the 12 principles of green engineering. ACS Publications; 2003.
70. Jackowski M, Niedźwiecki Ł, Jagiełło K, Uchańska O, Trusek A. Brewer's Spent Grains—Valuable Beer Industry By-Product. Biomolecules. 2020;10(12).
71. Mussatto SI, Dragone G, Roberto IC. Brewers' spent grain: generation, characteristics and potential applications. Journal of Cereal Science. 2006;43(1):1-14.
72. Arnison R, Carrick R. Sector Study on Beer, Whisky and Fish. 2015.
73. Weegels PL, Courtin CM, Arrachid A, Silvestri M. Abstracts: Technology Track: Posters. Consumer Driven Cereal Innovation: AACC International Press; 2008. p. 177-86.
74. Vanreppelen K, Vanderheyden S, Kuppens T, Schreurs S, Yperman J, Carleer R. Activated carbon from pyrolysis of brewer's spent grain: Production and adsorption properties. Waste Management & Research. 2014;32(7):634-45.
75. Cacace C, Cocozza C, Traversa A, Coda R, Rizzello CG, Pontonio E, et al. Potential of native and bioprocessed brewers' spent grains as organic soil amendments. Frontiers in Sustainable Food Systems. 2022;6:1010890.

76. Yoo J-H, Luyima D, Lee J-H, Park S-Y, Yang J-W, An J-Y, et al. Effects of brewer's spent grain biochar on the growth and quality of leaf lettuce (Lactuca sativa L. var. crispa.). Applied biological chemistry. 2021;64:1-10.
77. Paz A, Outeiriño D, Guerra NP, Domínguez JM. Enzymatic hydrolysis of brewer's spent grain to obtain fermentable sugars. Bioresource technology. 2019;275:402-9.
78. Meneses NG, Martins S, Teixeira JA, Mussatto SI. Influence of extraction solvents on the recovery of antioxidant phenolic compounds from brewer's spent grains. Separation and purification technology. 2013;108:152-8.
79. Liguori R, Soccol CR, Vandenberghe LPdS, Woiciechowski AL, Faraco V. Second generation ethanol production from brewers' spent grain. Energies. 2015;8(4):2575-86.
80. Pejin J, Radosavljević M, Kocić-Tanackov S, Djukić-Vuković A, Mojović L. Lactic acid fermentation of brewer's spent grain hydrolysate by Lactobacillus rhamnosus with yeast extract addition and pH control. Journal of the Institute of Brewing. 2017;123(1):98-104.
81. Czubaszek A, Wojciechowicz-Budzisz A, Spychaj R, Kawa-Rygielska J. Baking properties of flour and nutritional value of rye bread with brewer's spent grain. LWT. 2021;150:111955.
82. Shih YT, Wang W, Hasenbeck A, Stone D, Zhao Y. Investigation of physicochemical, nutritional, and sensory qualities of muffins incorporated with dried brewer's spent grain flours as a source of dietary fiber and protein. Journal of Food Science. 2020;85(11):3943-53.
83. Petrović JS, Pajin BS, Kocić TSD, Pejin JD, Fišteš AZ, Bojanić NĐ, et al. Quality properties of cookies supplemented with fresh brewer's spent grain. Food and Feed research. 2017;44(1):57-63.
84. He Y, Dietrich AM, Jin Q, Lin T, Yu D, Huang H. Cellulose adsorbent produced from the processing waste of brewer's spent grain for efficient removal of Mn and Pb from contaminated water. Food and Bioproducts Processing. 2022;135:227-37.
85. Stjepanović M, Velić N, Lončarić A, Gašo-Sokač D, Bušić V, Habuda-Stanić M. Adsorptive removal of nitrate from wastewater using modified lignocellulosic waste material. Journal of molecular liquids. 2019;285:535-44.
86. Wu J, Zhang Z, Xu J, Lu X, Wang C, Xu H, et al. Brewer's grains with different pretreatments used as bio-adsorbents for the removal of Congo red dye from aqueous solution. BioResources. 2020;15(3):6928-40.
87. Jagiełło K, Hińcz W, Kaczorowska W, Jackowski M, Bartman M, Kaczmarczyk J. Properties of activated carbon obtained from brewers spent grains. Biomass Conversion and Biorefinery. 2024;14(5):6475-93.
88. Vanderheyden S, Van Ammel R, Sobiech-Matura K, Vanreppelen K, Schreurs S, Schroeyers W, et al. Adsorption of cesium on different types of activated carbon. Journal of Radioanalytical and Nuclear Chemistry. 2016;310:301-10.
89. de Araújo TP, Quesada HB, Dos Santos DF, da Silva Fonseca BC, Barbieri JZ, Bergamasco R, et al. Acetaminophen removal by calcium alginate/activated hydrochar composite beads: Batch and fixed-bed studies. International Journal of Biological Macromolecules. 2022;203:553-62.
90. Xi X, Yan J, Quan G, Cui L. Removal of the pesticide pymetrozine from aqueous solution by biochar produced from brewer's spent grain at different pyrolytic temperatures. BioResources. 2014;9(4):7696-709.
91. Su Y, Böhm W, Wenzel M, Paasch S, Acker M, Doert T, et al. Mild hydrothermally treated brewer's spent grain for efficient removal of uranyl and rare earth metal ions. RSC advances. 2020;10(73):45116-29.

92. Olajire A, Abidemi J, Lateef A, Benson N. Adsorptive desulphurization of model oil by Ag nanoparticles-modified activated carbon prepared from brewer's spent grains. Journal of environmental chemical engineering. 2017;5(1):147-59.
93. Castro'º LEN, Mançano RR, Battocchio DAJ. Adsorption of food dye using activated carbon from brewers' spent grains. Acta Scientiarum Technology. 2023;45:e60443.
94. Su Y, Wenzel M, Paasch S, Seifert M, Böhm W, Doert T, et al. Recycling of brewer's spent grain as a biosorbent by nitro-oxidation for uranyl ion removal from wastewater. ACS omega. 2021;6(30):19364-77.
95. Lee HW, Jeon HG, Kim K-W. Removal of cobalt and strontium by adsorption using Brewer's spent grain formed by pyrolysis. Environmental Geochemistry and Health. 2023;45(10):7131-44.
96. Mussatto SI, Fernandes M, Rocha GJ, Órfão JJ, Teixeira JA, Roberto IC. Production, characterization and application of activated carbon from brewer's spent grain lignin. Bioresource technology. 2010;101(7):2450-7.
97. de Oliveira Fontoura CR, Dutra LV, Guezgüan SM, Nascimento MA, de Oliveira AF, Lopes RP. Optimization of one-pot H3PO4-activated hydrochar synthesis by Doehlert design: Characterization and application. Journal of Analytical and Applied Pyrolysis. 2022;168:105775.
98. Kukić DV, Vasić VM, Panić SN, Radosavljević MS, Šćiban MB, Prodanović JM, et al. Adsorption kinetics of Cr (VI) ions onto biochar from brewer's spent grain. Acta Periodica Technologica. 2019(50):134-42.
99. Nadolny B, Heineck RG, Bazani HAG, Hemmer JV, Biavatti ML, Radetski CM, et al. Use of brewing industry waste to produce carbon-based adsorbents: paracetamol adsorption study. Journal of Environmental Science and Health, Part A. 2020;55(8):947-56.
100. De Araújo TP, Quesada HB, Bergamasco R, Vareschini DT, De Barros MASD. Activated hydrochar produced from brewer's spent grain and its application in the removal of acetaminophen. Bioresource technology. 2020;310:123399.
101. Geremias R, Pelissari C, Libardi N, Carpiné D, Ribani RH. Chromium adsorption studies using brewer's spent grain biochar: kinetics, isotherm and thermodynamics. Ciência Rural. 2023;53:e20210914.
102. Bachmann SAL, Nunes KGP, Calvete T, Féris LA. Low-cost adsorbents prepared from brewer's spent grain for pollutants removal. Emergent Materials. 2023;6(2):741-53.
103. Anastas P, Eghbali N. Green chemistry: principles and practice. Chemical Society Reviews. 2010;39(1):301-12.
104. Schaubeder JB, Guizani C, Selinger J, Mautner A, Hummel M, Spirk S. Design of experiments as a tool to guide the preparation of tailor-made activated carbons. Scientific Reports. 2023;13(1):3977.
105. Heckert NA, Filliben JJ, Croarkin CM, Hembree B, Guthrie WF, Tobias P, et al. Handbook 151: Nist/sematech e-handbook of statistical methods. 2002.
106. Lenth RV. L enth's Method for the Analysis of Unreplicated Experiments. Wiley StatsRef: Statistics Reference Online. 2014.
107. Safety Data Sheet Carbon BLack [Internet]. 2021. Available from: https://www.birlacarbon.com/wp-content/uploads/hse/AUS-GHS-RCB-ENGLISH.pdf.
108. Pourhakkak P, Taghizadeh A, Taghizadeh M, Ghaedi M, Haghdoust S. Fundamentals of adsorption technology. Interface science and technology. 33: Elsevier; 2021. p. 1-70.
109. Wiśniewski M, Moszczyńska J, Liu X. Room-Temperature Oxygen Dissociative Chemisorption on Carbon Surface–Experimental Evidence. Langmuir. 2023;40(1):193-200.
110. Haghseresht F, Nouri S, Lu GM. Effects of carbon surface chemistry and solution pH on the adsorption of binary aromatic solutes. Carbon. 2003;41(5):881-92.

111. Lee G, Ahmed I, Lee HJ, Jhung SH. Adsorptive removal of organic pollutants with a specific functional group from water by using metal–organic frameworks (MOFs) or MOF-derived carbons: A review. Separation and Purification Technology. 2024:127602.
112. Paso KG. Constructing thermodynamic models of toxic metal biosorption. Microbial biodegradation and bioremediation: Elsevier; 2022. p. 109-43.
113. Zhao X, Xiao B, Fletcher A, Thomas K. Hydrogen adsorption on functionalized nanoporous activated carbons. The Journal of Physical Chemistry B. 2005;109(18):8880-8.
114. Langmuir I. The constitution and fundamental properties of solids and liquids. Part I. Solids. Journal of the American chemical society. 1916;38(11):2221-95.
115. Brunauer S, Emmett PH, Teller E. Adsorption of gases in multimolecular layers. Journal of the American chemical society. 1938;60(2):309-19.
116. Freundlich H. Kapillarchemie: eine Darstellung der Chemie der Kolloide und verwandter Gebiete: akademische Verlagsgesellschaft; 1922.
117. Temkin M. Kinetics of ammonia synthesis on promoted iron catalysts. Acta physiochim URSS. 1940;12:327-56.
118. Daniels R. Adsorption—Theory, Modelling, and Analysis, József Tóth (Ed.), Marcel Dekker, New York (2002), p. 878, pp $188.50; ISBN 0-8247-0747-8. Elsevier; 2005.
119. Chen T, Da T, Ma Y. Reasonable calculation of the thermodynamic parameters from adsorption equilibrium constant. Journal of Molecular Liquids. 2021;322:114980.
120. Madaeni S, Salehi E. Adsorption of cations on nanofiltration membrane: Separation mechanism, isotherm confirmation and thermodynamic analysis. Chemical Engineering Journal. 2009;150(1):114-21.
121. Thakur A, Assad H, Kaya S, Kumar A. Plant extracts as environmentally sustainable corrosion inhibitors II. Eco-Friendly Corrosion Inhibitors: Elsevier; 2022. p. 283-310.
122. Rowley H, Innes W, editors. Application of the Van't Hoff Equation to Adsorption Equilibria. Proceedings of the Iowa Academy of Science; 1940.
123. Ayar A, Gezici O, Küçükosmanoğlu M. Adsorptive removal of Methylene blue and Methyl orange from aqueous media by carboxylated diaminoethane sporopollenin: On the usability of an aminocarboxilic acid functionality-bearing solid-stationary phase in column techniques. Journal of hazardous materials. 2007;146(1-2):186-93.
124. Lagergren S. Zur theorie der sogenannten adsorption geloster stoffe. 1898.
125. Revellame ED, Fortela DL, Sharp W, Hernandez R, Zappi ME. Adsorption kinetic modeling using pseudo-first order and pseudo-second order rate laws: A review. Cleaner Engineering and Technology. 2020;1:100032.
126. Low M. Kinetics of chemisorption of gases on solids. Chemical Reviews. 1960;60(3):267-312.
127. Alkan M, Demirbaş Ö, Doğan M. Adsorption kinetics and thermodynamics of an anionic dye onto sepiolite. Microporous and mesoporous materials. 2007;101(3):388-96.
128. Sahoo TR, Prelot B. Chapter 7 - Adsorption processes for the removal of contaminants from wastewater: the perspective role of nanomaterials and nanotechnology. In: Bonelli B, Freyria FS, Rossetti I, Sethi R, editors. Nanomaterials for the Detection and Removal of Wastewater Pollutants: Elsevier; 2020. p. 161-222.
129. Wang J, Guo X. Adsorption kinetic models: Physical meanings, applications, and solving methods. Journal of Hazardous Materials. 2020;390:122156.
130. Sha'arani SAW, Khudri MAMRS, Othman AR, Halmi MIE, Yasid NA, Shukor MYA. Kinetic Analysis of the Adsorption of the Brominated Flame Retardant 4-bromodiphenyl Ether onto Biochar-immobilized Sphingomonas sp. Bioremediation Science and Technology Research. 2019.
131. Vareda JP. On validity, physical meaning, mechanism insights and regression of adsorption kinetic models. Journal of Molecular Liquids. 2023;376:121416.

132. Qiu H, Lv L, Pan B-c, Zhang Q-j, Zhang W-m, Zhang Q-x. Critical review in adsorption kinetic models. Journal of Zhejiang University-Science A. 2009;10(5):716-24.
133. Wu F-C, Tseng R-L, Juang R-S. Initial behavior of intraparticle diffusion model used in the description of adsorption kinetics. Chemical engineering journal. 2009;153(1-3):1-8.
134. Thommes M, Kaneko K, Neimark A, Olivier J, Rodriguez-Reinoso F, Rouquerol J, et al. Physisorption of gases, with special reference to the evaluation of surface area and pore size distribution (IUPAC Technical Report). Pure and Applied Chemistry. 2015;87.
135. Rouquerol J, Avnir D, Fairbridge CW, Everett DH, Haynes J, Pernicone N, et al. Recommendations for the characterization of porous solids (Technical Report). Pure and applied chemistry. 1994;66(8):1739-58.
136. Mikhail RS, Brunauer S. Surface area measurements by nitrogen and argon adsorption. Journal of Colloid and Interface Science. 1975;52(3):572-7.
137. Barrett EP, Joyner LG, Halenda PP. The determination of pore volume and area distributions in porous substances. I. Computations from nitrogen isotherms. Journal of the American Chemical society. 1951;73(1):373-80.
138. Micromeritics. ASAP 2020 Accelerated Surface Area and Porosimetry System Operator's Manual2011.
139. Dubinin M, Radushkevich L. Equation of the characteristic curve of acti vated charcoal: Proe. A cad Sei USSR, Phys Chem Sec. 1974:55,331-3.
140. Marsh H. Adsorption methods to study microporosity in coals and carbons—a critique. Carbon. 1987;25(1):49-58.
141. Materials ASfT. Standard Test Method for Moisture Analysis of Particulate Wood Fuels. Procedure 1996.
142. Pandia S, Hutagalung A, Siahaan A. Utilization of Cocoa Peel as Biosorbent for Oil and Color Removal in Palm Oil Mill Effluent (POME). IOP Conference Series: Materials Science and Engineering. 2018;300:012066.
143. Ojeda J, Dittrich M. Fourier Transform Infrared Spectroscopy for Molecular Analysis of Microbial Cells. Methods in molecular biology (Clifton, NJ). 2012;881:187-211.
144. Medalia A, Richards L. Tinting strength of carbon black. Journal of Colloid and Interface Science. 1972;40(2):233-52.
145. Spectral Systems L. Ge ATR Optical Elements 2024 [Available from: https://www.spectral-systems.com/products/ge-atr-optical-elements/.
146. Kumar KV, Sivanesan S. Selection of optimum sorption kinetics: Comparison of linear and non-linear method. Journal of Hazardous Materials. 2006;134(1):277-9.
147. Mathias TRdS, Alexandre VMF, Cammarota MC, de Mello PPM, Sérvulo EFC. Characterization and determination of brewer's solid wastes composition. Journal of the Institute of Brewing. 2015;121(3):400-4.
148. Buffington J. The Economic Potential of Brewer's Spent Grain (BSG) as a Biomass Feedstock. Advances in Chemical Engineering and Science. 2014;04:308-18.
149. Coronado Ortega M, Montero G, Montes DG, valdez salas B, Ayala Bautista J, Garcia C, et al. Physicochemical Characterization and SEM-EDX Analysis of Brewer's Spent Grain from the Craft Brewery Industry. Sustainability. 2020;12.
150. Machado RM, Rodrigues RAD, Henriques CMC, Gameiro MLF, Ismael MRC, Reis MTA, et al. Dewatering of brewer's spent grain using an integrated membrane filter press with vacuum drying capabilities. Separation Science and Technology. 2016;51(4):692-700.
151. Becidan M, Skreiberg Ø, Hustad JE. Products distribution and gas release in pyrolysis of thermally thick biomass residues samples. Journal of Analytical and Applied Pyrolysis. 2007;78(1):207-13.
152. Xiros C, Christakopoulos P. Biotechnological Potential of Brewers Spent Grain and its Recent Applications. Waste and Biomass Valorization. 2012;3(2):213-32.

153. Efiyanti L, Darmawan S, Saputra N, Wibisono H, Hendra D, Pari G. Quality evaluation of coconut shell activated carbon and its application as precursor for citronellal-scented aromatic briquette. Rasayan Journal of Chemistry. 2022;15(3):1608-18.
154. El-Sayed SA, Mostafa ME. Thermal pyrolysis and kinetic parameter determination of mango leaves using common and new proposed parallel kinetic models. RSC Advances. 2020;10(31):18160-79.
155. Sing KSW, Williams RT. Physisorption Hysteresis Loops and the Characterization of Nanoporous Materials. Adsorption Science & Technology. 2004;22(10):773-82.
156. Rouquerol J, Llewellyn P, Rouquerol F. Is the BET Equation Applicable to Microporous Adsorbents? Studies in Surface Science and Catalysis. 2007;160:49-56.
157. Gonçalves GdC, Nakamura PK, Furtado DF, Veit MT. Utilization of brewery residues to produces granular activated carbon and bio-oil. Journal of Cleaner Production. 2017;168:908-16.
158. Nandiyanto A, Oktiani R, Ragadhita R. How to Read and Interpret FTIR Spectroscope of Organic Material. Indonesian Journal of Science and Technology. 2019;4:97-118.
159. Jackowski M, Niedźwiecki Ł, Jagiełło K, Uchańska O, Trusek A. Brewer's Spent Grains-Valuable Beer Industry By-Product. Biomolecules. 2020;10(12):1669.
160. Silbir S, Göksungur MY. Natural Red Pigment Production by Monascus Purpureus in Submerged Fermentation Systems Using a Food Industry Waste: Brewer's Spent Grain. 2019;8:161.
161. Borel LDMS, Lira TS, Ribeiro JA, Ataíde CH, Barrozo MAS. Pyrolysis of brewer’s spent grain: Kinetic study and products identification. Industrial Crops and Products. 2018;121:388-95.
162. Ravindran R, Jaiswal S, Abu-Ghannam N, Jaiswal AK. A comparative analysis of pretreatment strategies on the properties and hydrolysis of brewers’ spent grain. Bioresource Technology. 2018;248:272-9.
163. Jacobsen SE, Wyman CE. Xylose Monomer and Oligomer Yields for Uncatalyzed Hydrolysis of Sugarcane Bagasse Hemicellulose at Varying Solids Concentration. Industrial & Engineering Chemistry Research. 2002;41(6):1454-61.
164. Vanreppelen K, Vanderheyden S, Kuppens T, Schreurs S, Yperman J, Carleer R. Activated carbon from pyrolysis of brewer's spent grain: Production and adsorption properties. Waste Manag Res. 2014;32(7):634-45.
165. Teixeira S, Delerue-Matos C, Santos L. Application of experimental design methodology to optimize antibiotics removal by walnut shell based activated carbon. Science of The Total Environment. 2019;646:168-76.
166. Cao W, Xu H, Zhang X, Xiang W, Qi G, Wan L, et al. Novel post-treatment of ultrasound assisting with acid washing enhance lignin-based biochar for CO2 capture: adsorption performance and mechanism. Chemical Engineering Journal. 2023;471:144523.
167. Hao X, Quach L, Korah J, Spieker W, Regalbuto JR. The control of platinum impregnation by PZC alteration of oxides and carbon. Journal of Molecular Catalysis A: Chemical. 2004;219(1):97-107.
168. Tran HN, You S-J, Chao H-P. Effect of pyrolysis temperatures and times on the adsorption of cadmium onto orange peel derived biochar. Waste Management & Research. 2016;34(2):129-38.
169. Zafar S, Bukhari DA, Rehman A. Azo dyes degradation by microorganisms–An efficient and sustainable approach. Saudi Journal of Biological Sciences. 2022;29(12):103437.
170. Qiu H, Shen F, Yin A, Liu J, Wu B, Li Y, et al. Biodegradation and detoxification of azo dyes by halophilic/halotolerant microflora isolated from the salt fields of Tibet autonomous region China. Front Microbiol 13: 877151. 2022.

171. Chung K, Fulk G, Andrews A. The mutagenicity of methyl orange and metabolites produced by intestinal anaerobes. Mutat Res. 1978;58(2-3):375-9.
172. Ajslev JZ, Møller JL, Andersen MF, Pirzadeh P, Lingard H. The hierarchy of controls as an approach to visualize the impact of occupational safety and health coordination. International journal of environmental research and public health. 2022;19(5):2731.
173. ÇAĞLAR E, Donar YO, SINAĞ A, BİROĞUL İ, Bilge S, Aydincak K, et al. Adsorption of anionic and cationic dyes on biochars, produced by hydrothermalcarbonization of waste biomass: effect of surface functionalization and ionicstrength. Turkish Journal of Chemistry. 2018;42(1):86-99.
174. Zhang B, Wu Y, Cha L. Removal of methyl orange dye using activated biochar derived from pomelo peel wastes: performance, isotherm, and kinetic studies. Journal of Dispersion Science and Technology. 2020.
175. Yu J, Zhang X, Wang D, Li P. Adsorption of methyl orange dye onto biochar adsorbent prepared from chicken manure. Water Science and Technology. 2018;77(5):1303-12.
176. Islam MS, Ang BC, Gharehkhani S, Afifi ABM. Adsorption capability of activated carbon synthesized from coconut shell. Carbon letters. 2016;20:1-9.
177. Khaniabadi YO, Heydari R, Nourmoradi H, Basiri H, Basiri H. Low-cost sorbent for the removal of aniline and methyl orange from liquid-phase: aloe vera leaves wastes. Journal of the Taiwan institute of chemical engineers. 2016;68:90-8.
178. Yang X, Wang L, Guo J, Wang H, Mašek O, Wang H, et al. Aging features of metal (loid) s in biochar-amended soil: effects of biochar type and aging method. Science of the Total Environment. 2022;815:152922.
179. Liu Y, Chen J. Effect of ageing on biochar properties and pollutant management. Chemosphere. 2022;292:133427.
180. Liu Y, Sohi SP, Jing F, Chen J. Oxidative ageing induces change in the functionality of biochar and hydrochar: Mechanistic insights from sorption of atrazine. Environmental Pollution. 2019;249:1002-10.
181. Roney N, Faroon O, Williams M, Jones DG, Klotzbach JM, Kawa M, et al. Toxicological profile for silica. 2019.
182. Wang K, Peng N, Sun J, Lu G, Chen M, Deng F, et al. Synthesis of silica-composited biochars from alkali-fused fly ash and agricultural wastes for enhanced adsorption of methylene blue. Science of the total environment. 2020;729:139055.
183. Nguyen MN. Potential use of silica-rich biochar for the formulation of adaptively controlled release fertilizers: A mini review. Journal of Cleaner Production. 2021;307:127188.
184. Mai NT, Nguyen NH, Tsubota T, Shinogi Y, Dultz S, Nguyen MN. Fern Dicranopteris linearis-derived biochars: Adjusting surface properties by direct processing of the silica phase. Colloids and Surfaces A: Physicochemical and Engineering Aspects. 2019;583:123937.
185. Sari L, Shofiyani A, Sapar A. Synthesis and Characterization of Silica-Biochar Composite as Rhodamine B Dye Adsorbent. Jurnal Kimia Sains dan Aplikasi. 2024;27(6):284-92.
186. Gbenebor OP, Olanrewaju OA, Usman MA, Adeosun SO. Lignin from Brewers' Spent Grain: Structural and Thermal Evaluations. Polymers. 2023;15(10):2346.
187. Okonkwo CE, Hussain SZ, Onyeaka H, Adeyanju AA, Nwonuma CO, Bashir AA, et al. Lignin polyphenol: From biomass to innovative food applications, and influence on gut microflora. Industrial Crops and Products. 2023;206:117696.

188. Wakimoto R, Kitamura T, Ito F, Usami H, Moriwaki H. Decomposition of methyl orange using C60 fullerene adsorbed on silica gel as a photocatalyst via visible-light induced electron transfer. Applied Catalysis B: Environmental. 2015;166:544-50.
189. Li H, Jin H, Li R, Hua J, Zhang Z, Li R. Magnetic Fe3O4@ SiO2 study on adsorption of methyl orange on nanoparticles. Scientific Reports. 2024;14(1):1217.
190. Gong R, Ye J, Dai W, Yan X, Hu J, Hu X, et al. Adsorptive removal of methyl orange and methylene blue from aqueous solution with finger-citron-residue-based activated carbon. Industrial & Engineering Chemistry Research. 2013;52(39):14297-303.
191. Lee H, Fiore S, Berruti F. Adsorption of methyl orange and methylene blue on activated biocarbon derived from birchwood pellets. Biomass and Bioenergy. 2024;191:107446.
192. Al-Ghouti M, Khraisheh M, Allen S, Ahmad M. The removal of dyes from textile wastewater: a study of the physical characteristics and adsorption mechanisms of diatomaceous earth. Journal of environmental management. 2003;69(3):229-38.
193. Rytwo G, Tropp D, Serban C. Adsorption of diquat, paraquat and methyl green on sepiolite: experimental results and model calculations. Applied Clay Science. 2002;20(6):273-82.

8. Conclusions and Future Work

8.1 Conclusions

This work set out to develop a pathway to upcycle brewer's spent grain waste biomass into value added biochar adsorbent materials for use in water remediation applications. These biochar materials were identified as a potential wastewater treatment technology to remove emerging contaminants through a low energy, ambient process. Design of experiments was employed to better understand the synthesis process and efficiently optimise the development of these materials.

A screening design of experiments was employed to determine the factors of significance to the response variables yield, surface area and point of zero charge. Yield and surface area were found to only be influenced by hold temperature and hold time of the pyrolysis process, while point of zero charge was not found to be influenced by any of the synthesis variables tested. For this reason, a chemical activation step was introduced to include a surface chemical tunability in the synthesis process. Introduction of the washing step allowed for the lowering of the point of zero charge, indicating a modification of the surface chemistry of the material.

Through initial investigation of the surface chemistry of the washed biochar materials through point of zero charge, Fourier transform infrared spectroscopy, X-ray photoelectron spectroscopy, scanning electron microscopy and energy dispersive spectroscopy, methyl orange dye was chosen as a proxy pollutant molecule for investigation in liquid phase adsorption studies.

A 2-factor central composite face centred optimisation design of experiments was developed using hold time and hold temperature as the synthesis variables. All other process variables were set to their most environmentally and economically efficient values. Yield, surface area, methyl orange uptake after 1 hour of contact and methyl orange uptake after 7 days were chosen as the response variables to capture both adsorbent performance and production efficiency. Model equations and surface response plots for each response variable were found and the optimal synthesis conditions for each found. The optimal biochar synthesis conditions were chosen to be hold temperature of 900°C and hold time of 2.5 hours due to the exceptional adsorption capacities for both short and long residence times. Yield and adsorption capacity were found to be inversely proportional, and a low

yield was found at these synthesis conditions, which may be a barrier to process commercialisation in the future.

The optimal biochar was resynthesised and its composition, surface chemistry, topology, surface area porosity were fully characterised. The optimal biochar sample O4, was found to have a yield of 7.6 ± 0.4%, with high carbon content of 68.8% and an ash content of 11.9%. Surface area was found to be 1433 ± 114 $m^2 g^{-1}$ with a mesopore size of 3 nm. The sample displayed a high micropore volume of 67.5 ± 1.7% and a highly supermicroporous micropore distribution.

The sample showed an acidic point of zero charge of 5.9 indicating a large proportion of positively charged surface functional groups. Oxygen and nitrogen containing surface functional groups as well as aromatic carbon were identified on the surface through a combination of XPS and FTIR. Scanning electron microscopy showed two separate surface sites: a typical carbonaceous site indicating a hierarchical pore structure; and a region with small glass-like beads present on the surface. EDS identified these small glassy beads as silicon and oxygen containing compounds, likely silica which is present in grassy materials like the barley from which the BSG this biochar was synthesised from is derived. Further investigation identified these silica sites as a product of the synthesis process, and not inherent to BSG itself. The silica sites were identified as a potential site for adsorption.

Liquid phase kinetic adsorption studies with methyl orange dye showed optimal fit with the pseudo second order kinetic model. Equilibrium liquid phase adsorption studies with methyl orange and the optimised biochar showed Temkin isotherm behaviour at all three temperatures investigated, indicating heterogenous adsorption on the surface. The enthalpy and entropy of adsorption onto the pristine surface were determined to be -57.2 kJ mol^{-1} and -60.5 J mol^{-1} K^{-1}, respectively. The isotherm shapes, van't Hoff plot and Scatchard analysis indicated a multi-mechanism adsorption taking place, with an initial exothermic and negentropic physisorption phase followed by an endothermic and entropic chemisorption phase which switches at an uptake of approximately 270 mg g^{-1}. The physisorption mechanism has been attributed to intermolecular interactions such as hydrogen bonding, Yoshida hydrogen bonding, dipole interactions and π-π stacking of the aromatic rings of the biochar and those on the adsorptive. The chemisorption mechanism has been attributed to the strong interactions between the anionic charge on the methyl orange molecules and the positively charged functional groups such as protonated lone

pairs or positive dipoles, or due to the cationic charge of the methyl orange in its acidified form and negatively charged functional groups such as negative dipoles or delocalised electrons on the aromatic rings of the biochar.

The interactions taking place and wide variety of surface functional groups make this biochar likely to be capable of adsorbing many different types of target emerging contaminants.

From the work conducted here, it is proposed that the methodology developed is broadly applicable for the screening, optimisation, and validation of biochar derived from any carbonaceous feedstock. While the specific synthesis parameters, response variables, and validation approaches will inevitably depend on the experimental set-up and intended application, following the general framework outlined—together with the guiding principles of green chemistry and engineering—provides a systematic route to identifying an optimal material based on the selected key performance indicators.

8.2 Future Work

This study has shown the applicability in utilisation and upcycle of brewer's spent grain into biochar materials for adsorbent applications. However, this work is presented as a launching off point for further investigation into these materials, with many applications and variations in synthesis routes available for research. For this reason, several areas for future work are suggested before commercialisation and implementation can be carried out.

Most adsorbent wastewater treatment systems operate in flowing systems in columns or packed beds. As all adsorption tests carried out in this work were carried out in batch tests at small volumes, scale up in continuous systems is required to simulate real world operation.

The small yield of the optimal biochar is another barrier to process commercialisation, as much larger amounts of biochar will be required for continuous column tests. For this reason, transfer from a small volume tube furnace to a larger volume furnace such as a muffle furnace is suggested for future production. Investigation into how the change in synthesis procedure affects adsorbent characteristics such as porosity, surface area, surface chemistry and adsorption capacity must all be closely monitored to maintain adsorbent effectiveness.

While the activating acid hydrochloric acid was used in this work to tailor the surface chemistry of the biochars synthesised in this work and lower the PZC, other activating agents could also be investigated. Basic solutions like sodium hydroxide can also be used to raise the PZC and make the surface contain more negatively charged functional groups making the material more applicable for the adsorption of cations. This should be investigated to broaden the range of pollutant molecules and tailor the surface chemistry to different applications.

This work set out to avoid using chemical activating agents in the interest of sustainability and cost saving. Substitution of the mineral acid for a renewable organic acid such as ethanoic acid, which can be derived from sustainable synthesis, could be a way to better align the synthesis of the materials in this work with the principles of green chemistry and engineering. If not feasible, recycling and recovery of the spent hydrochloric acid could also be an avenue for future research.

The π-π stacking interactions exhibited by the materials synthesised in this work make it an ideal candidate for adsorption of aromatic pharmaceuticals and personal care products like oestradiol, estrone and paracetamol. The suspected strong interaction between the anionic sulphone group and the adsorbent makes it potentially a good adsorbent for per fluoroalkyl sulphonic acids (PFSA) substances, an emerging contaminant class in the PFAS family. PFSA substances present a similar sulphone functional group to the methyl orange dyes studied here. However, full investigation of the adsorption capacity on these substances must be tested before any full conclusions can be drawn.

Regeneration and reusability of the spent biochar is also an important next step in the commercialisation of the materials from this work. While this may not be possible after the adsorption of methyl orange due to the chemisorptive interactions which may be irreversible, the renewable capacity should be investigated to further argue the case of these materials as a commercially viable adsorbent.

The optimisation model ANOVA analysis indicated that model reduction by removal of the quadratic term for hold time may be beneficial for all 4 models but especially the short and long residence time kinetics models. Carrying out this work would help to remove noise, improve lack-of-fit and increasing the reliability of the models in predicting new values.

The formulation of an objective function utilising all of the key performance indicators of the biochar to consider the trade-off between different key material characteristics (as seen in this work with yield and surface area) could be beneficial. This objective function could also be tailored to different applications by assigning appropriate weightings to each response variable, ensuring that the optimisation reflects the performance requirements of the intended use case. This would allow for a more holistic approach utilising multiple criteria that balance functionality, sustainability and productivity in the design of these new materials.

Further exploration into the silicon and oxygen containing glassy bead structures found on the surface of the biochars should be investigated. Their isolation and testing should be carried out to determine their true chemical nature and to help evaluate their role in any adsorption interactions. Work utilising X-ray diffraction to determine the amorphous or crystalline nature of the glassy bead structures is currently ongoing. This may also help to identify specialised applications where the adsorbents synthesised here would demonstrate enhanced performance, as with the SiChar materials reviewed previously.

Finally, further investigation into the mechanism taking place on the surface of the biochars should be carried out. Isotherms at other temperatures should be carried out to see if the suspected dual physisorption and chemisorption mechanism continues to take place and to improve the quality of the isotherm regressions. Other adsorbates such as methylene blue dye could be used to determine the mechanism taking place with a cationic azo-dye. This would help to elucidate the intermolecular and/or chemical bonding taking place common to both adsorbate molecules. Furthermore, utilisation of techniques such as XPS and BET nitrogen adsorption on adsorbents saturated with dye would also help to determine the functional groups which the dye molecules are interacting with and also any changes to pore size distribution will indicate the type of pores within the pore structure the dye has adsorbed onto.

Appendices

Appendix A: Duplicate Screening Samples Isotherms and BET Parameters

Table A80 shows the BET parameters calculated from the Nitrogen adsorption isotherms shown in Chapter 5. These experiments were carried out by myself and are denoted below as SJX (Screening Jordan Sample X). Table A81 shows the BET parameters calculated from the Nitrogen adsorption isotherms shown in Figure A120, Figure A121, Figure A122 and Figure A123. These experiments were carried out by Mathis Bornand, a visiting Erasmus trainee, and are denoted below as SMX (Screening Mathis Sample X). These parameters were averaged and the error calculated by the standard error formula and reported in Table 5.27 in the main body of this work.

Table A80: Yield and BET parameters calculated from nitrogen adsorption isotherms on biochar samples of screen sample set 1[28]

Sample	*Yield (%)*	*Monolayer capacity (cm^3g^{-1})*	*BET constant*	*BET Surface area (m^2g^{-1})*	*Enthalpy of adsorption ($kJmol^{-1}$)*	*IUPAC isotherm classification*	*Hysteresis Type*
SJ1	29.8	0 ± 0	348 ± 47	1 ± 0	9.3 ± 0.1	II	-
SJ2	20.8	129 ± 0	2595 ± 127	560 ± 0	10.6 ± 0.0	I(b)	H4
SJ3	28.0	6 ± 0	348 ± 29	28 ± 0	9.3 ± 0.1	II	-
SJ4	6.6	268 ± 2	202 ± 21	1169 ± 8	9.0 ± 0.1	I(b)	H4
SJ5	26.7	2 ± 0	86 ± 3	8 ± 0	8.4 ± 0.0	II	-
SJ6	17.9	140 ± 0	2388 ± 136	609 ± 1	10.5 ± 0.0	I(b)	H4
SJ7	27.0	5 ± 0	48 ± 6	22 ± 1	8.0 ± 0.1	II	-
SJ8	8.9	284 ± 2	271 ± 25	1236 ± 7	9.1 ± 0.1	I(b)	H4
SJ9	28.8	1 ± 0	40 ± 1	3 ± 0	7.9 ± 0.1	II	-
SJ10	18.2	141 ± 0	2107 ± 117	615 ± 1	10.5 ± 0.0	I(b)	H4
SJ11	26.5	4 ± 0	41 ± 9	16 ± 2	7.9 ± 0.1	II	-
SJ12	9.2	281 ± 1	299 ± 27	1223 ± 6	9.2 ± 0.1	I(b)	H4
SJ13	26.8	2 ± 0	167 ± 24	7 ± 0	8.8 ± 0.1	II	-
SJ14	19.0	133 ± 0	2298 ± 96	581 ± 0	10.5 ± 0.0	I(b)	H4
SJ15	28.1	2 ± 0	173 ± 15	9 ± 0	8.9 ± 0.1	II	-

[28] Errors calculated from propagation of error in BET isotherm fit, the error propagation equations are detailed in Appendix D

SJ16	5.8	252 ± 2	185 ± 18	1099 ± 7	8.9 ± 0.1	I(b)	H4

Table A81: Yield and BET parameters calculated from nitrogen adsorption isotherms on biochar samples of screen sample set 2[29]

Sample	*Yield (%)*	*Monolayer capacity (cm^3g^{-1})*	*BET constant*	*BET Surface area (m^2g^{-1})*	*Enthalpy of adsorption ($kJmol^{-1}$)*	*IUPAC isotherm classification*	*Hysteresis Type*
SM1	29.1	6 ± 0	98 ± 24	28 ± 2	8.5 ± 0.2	II	-
SM2	20.9	128 ± 0	2538 ± 120	559 ± 0	10.6 ± 0.0	I(b)	H4
SM3	26.7	1 ± 0	197 ± 26	2 ± 0	8.9 ± 0.1	II	-
SM4	6.8	269 ± 2	183 ± 19	1171 ± 10	8.9 ± 0.1	I(b)	H4
SM5	29.2	1 ± 0	126 ± 17	5 ± 0	8.7 ± 0.1	II	-
SM6	19.4	142 ± 0	2435 ± 151	619 ± 1	10.6 ± 0.0	I(b)	H4
SM7	28.0	10 ± 0	100 ± 17	43 ± 2	8.5 ± 0.1	II	-
SM8	8.9	283 ± 1	290 ± 26	1232 ± 6	9.2 ± 0.1	I(b)	H4
SM9	28.7	6 ± 0	50 ± 7	26 ± 2	8.1 ± 0.1	II	-
SM10	19.7	134 ± 0	2160 ± 98	585 ± 0	10.5 ± 0.0	I(b)	H4
SM11	28.1	13 ± 0	218 ± 29	58 ± 1	9.0 ± 0.1	II	-
SM12	8.8	285 ± 2	274 ± 26	1242 ± 7	9.2 ± 0.1	I(b)	H4
SM13	28.3	10 ± 0	133 ± 24	43 ± 1	8.7 ± 0.1	II	-
SM14	19.3	133 ± 0	2571 ± 154	578 ± 0	10.6 ± 0.0	I(b)	H4
SM15	28.0	15 ± 0	164 ± 34	64 ± 2	8.8 ± 0.1	II	-
SM16	6.3	260 ± 2	161 ± 16	1134 ± 9	8.8 ± 0.1	I(b)	H4

[29] Errors calculated from propagation of error in BET isotherm fit, the error propagation equations are detailed in Appendix D

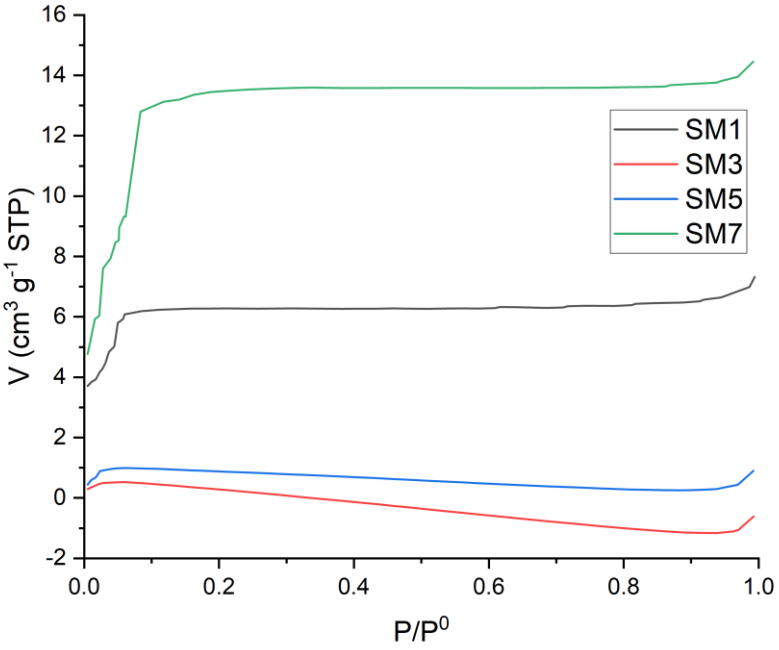

Figure A120: Screening isotherms SM1, SM3, SM5 and SM7 from sample set 2

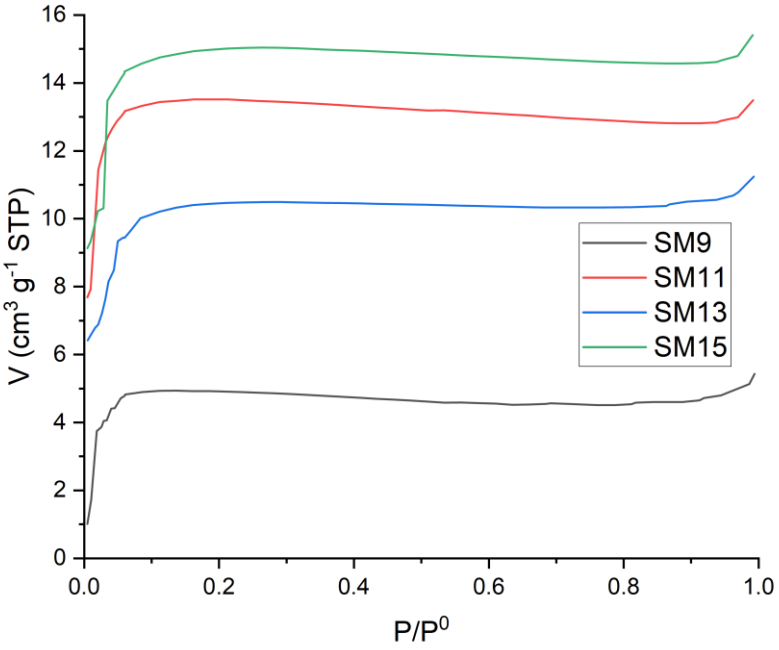

Figure A121: Screening isotherms SM9, SM11, SM13 and SM15 from sample set 2

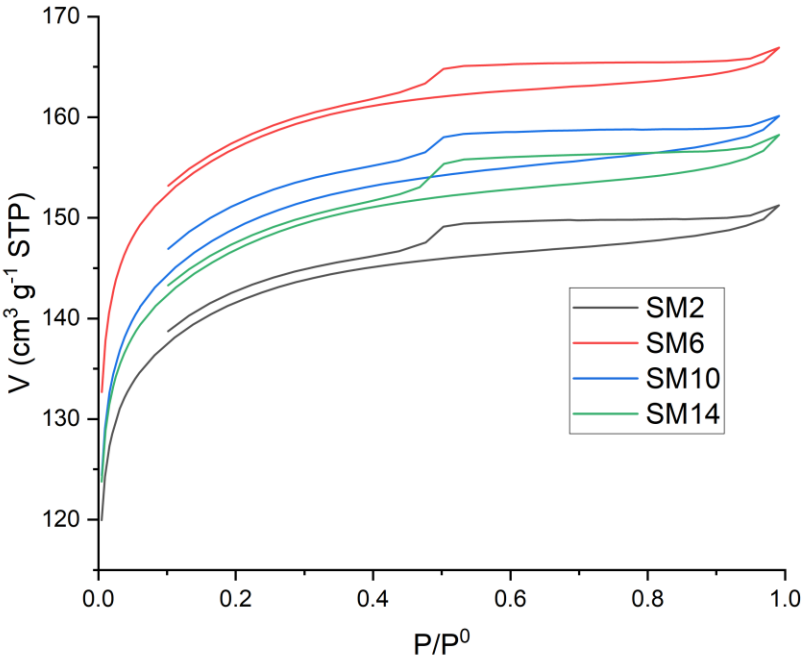

Figure A122: Screening isotherms SM2, SM6, SM10 and SM14 from sample set 2

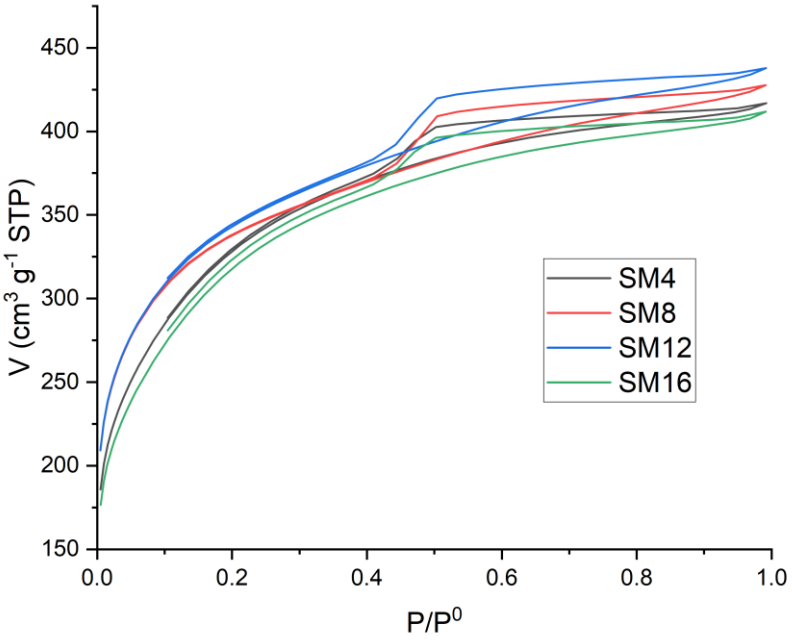

Figure A123: Screening isotherms SM4, SM8, SM12 and SM16 from sample set 2

Appendix B: Methyl Orange Beer-Lambert Calibration

Figure A124 shows the UV-Vis spectra for the various concentrations of methyl orange dye in water.

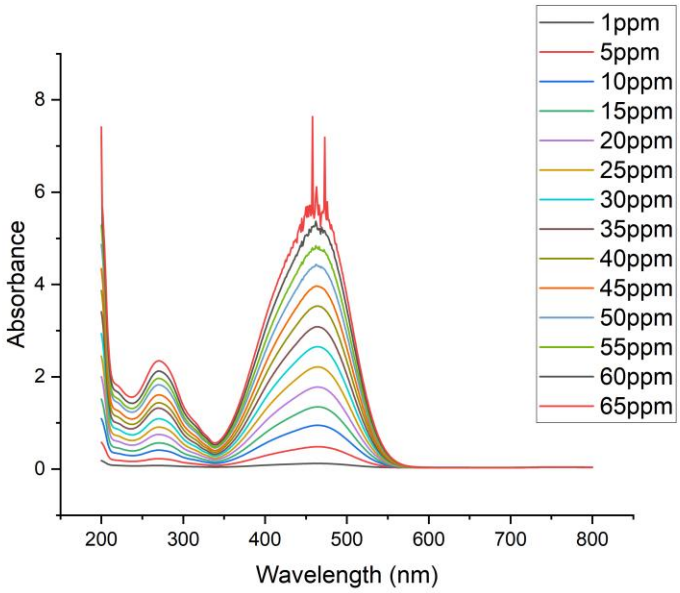

Figure A124: UV-Vis spectra for MO calibration

Figure A125 shows the Beer-Lambert line fitting for the absorbance peaks shown in Figure A124.

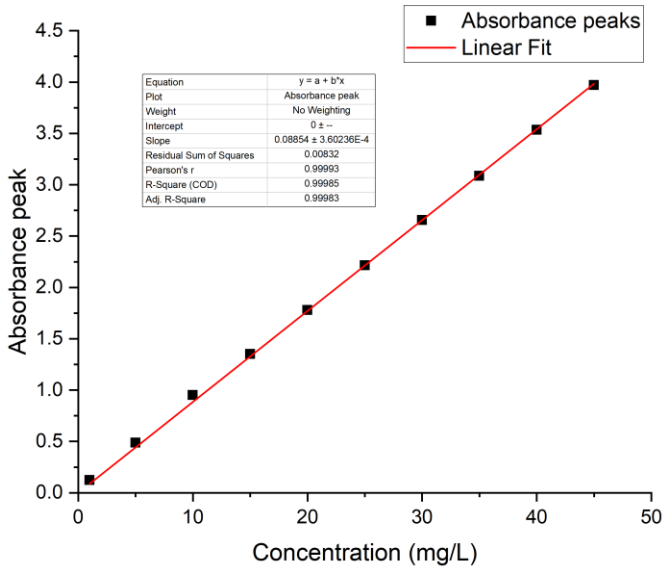

Figure A125: Methyl orange calibration curve

Appendix C: Methyl Orange Isotherms

Figures A124- A129 show the various isotherm model fits for both sample O4 and O6 at 25°C, 35°C and 45°C.

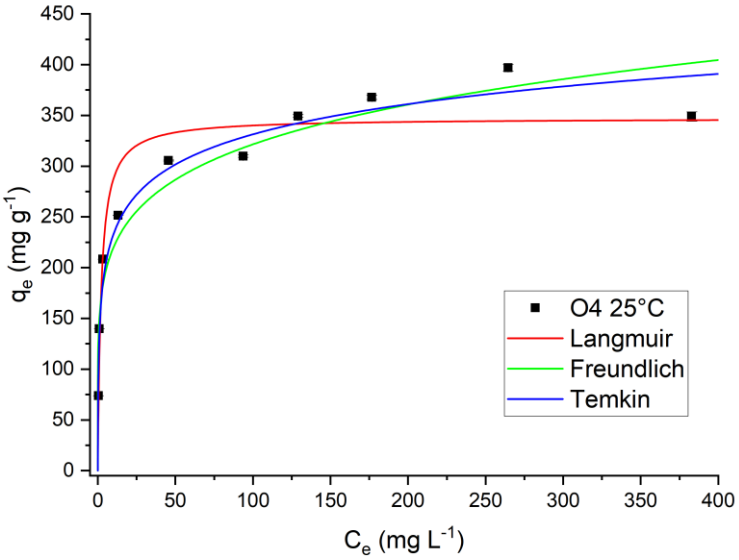

Figure A126: MO adsorption Langmuir, Freundlich and Temkin isotherm fits for O4 at 25°C

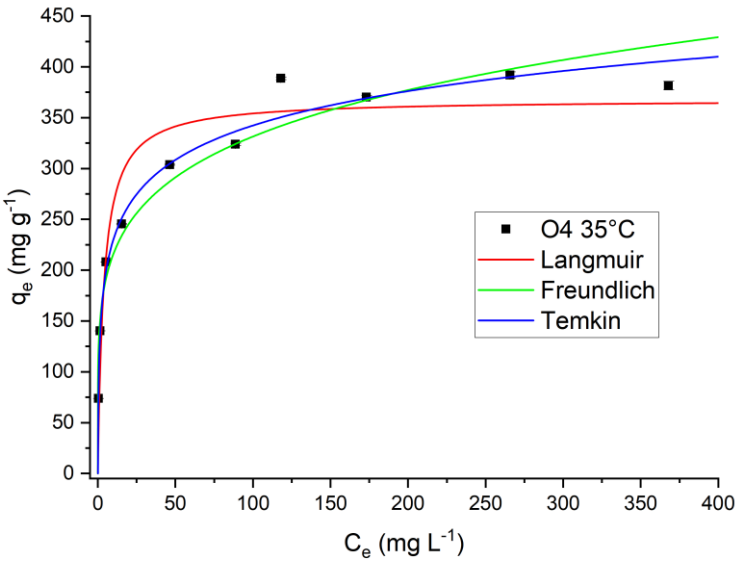

Figure A127: MO adsorption Langmuir, Freundlich and Temkin isotherm fits for O4 at 35°C

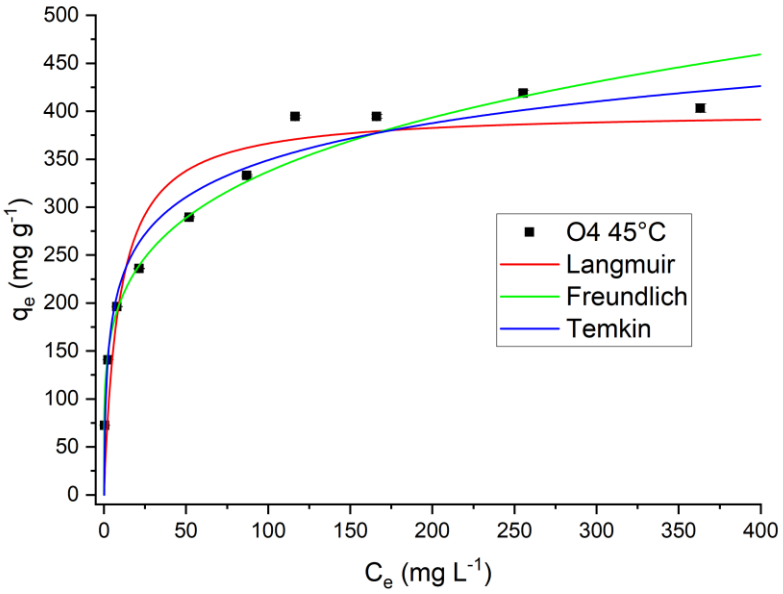

Figure A128: MO adsorption Langmuir, Freundlich and Temkin isotherm fits for O4 at 45°C

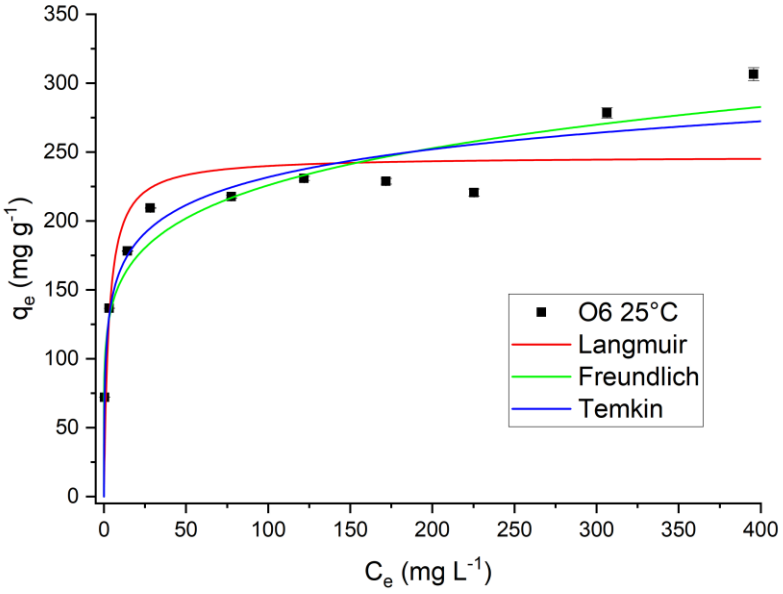

Figure A129: MO adsorption Langmuir, Freundlich and Temkin isotherm fits for O6 at 25°C

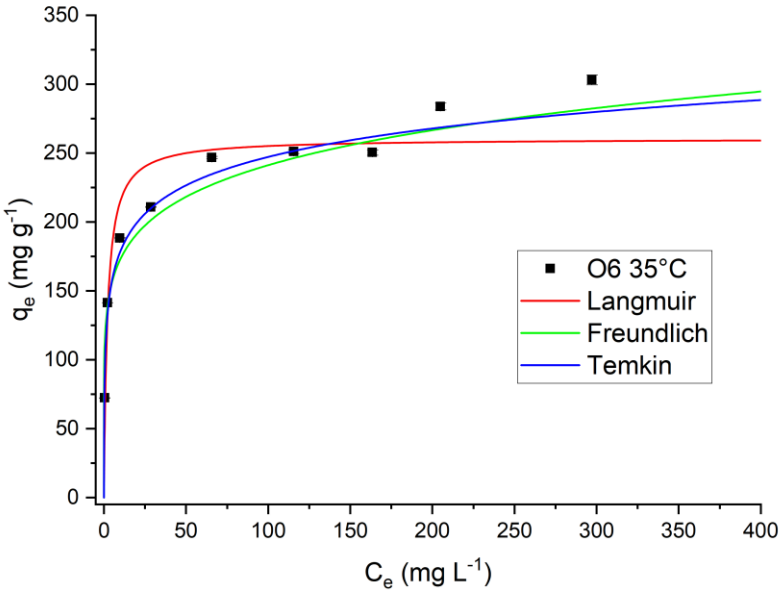

Figure A130: MO adsorption Langmuir, Freundlich and Temkin isotherm fits for O4 at 35°C

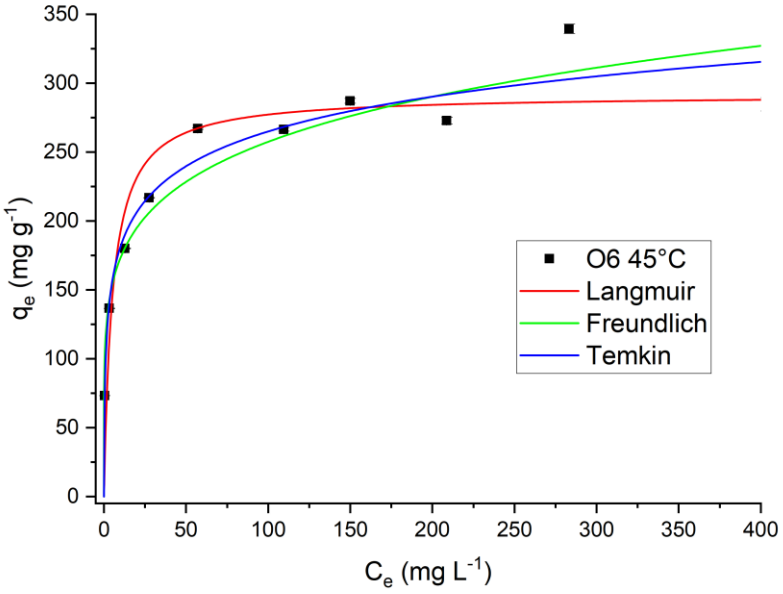

Figure A131: MO adsorption Langmuir, Freundlich and Temkin isotherm fits for O4 at 45°C

Appendix D: Error Propagation

Error calculation through duplicates utilised the standard error formula shown below

$$Standard\ error = \sqrt{\frac{Standard\ deviation}{sample\ size}}$$

Individual sample errors were calculated by propagating error from the fitting parameters. The excel function =LINEST was used to determine the error in the gradient (m) and y-intercept (b) for any linear fitting calculated.

Propagation of the error for each of the calculated parameters is shown below.

Monolayer Capacity v_m

$$v_m = \frac{1}{(slope + intercept)}$$

$$v_m = \frac{1}{(m + b)}$$

$$\sigma_{v_m}^2 = \left(\frac{\partial v_m}{\partial m}\right)^2 \sigma_m^2 + \left(\frac{\partial v_m}{\partial b}\right)^2 \sigma_b^2$$

$$\sigma_{v_m}^2 = \left(\frac{-1}{(b+m)^2}\right)^2 \sigma_m^2 + \left(\frac{-1}{(b+m)^2}\right)^2 \sigma_b^2$$

$$\sigma_{v_m}^2 = \left(\frac{-1}{(b+m)^2}\right)^2 \sigma_m^2 + \left(\frac{-1}{(b+m)^2}\right)^2 \sigma_b^2$$

$$\sigma_{v_m} = \sqrt{\frac{\sigma_m^2 + \sigma_b^2}{(b+m)^4}}$$

BET Constant c

$$c = \frac{m}{b} + 1 \qquad (3.52)$$

$$\sigma_c^2 = \left(\frac{\partial c}{\partial m}\right)^2 \sigma_m^2 + \left(\frac{\partial c}{\partial b}\right)^2 \sigma_b^2$$

$$\sigma_c^2 = \left(\frac{1}{b}\right)^2 \sigma_m^2 + \left(\frac{-m}{b^2}\right)^2 \sigma_b^2$$

$$\sigma_c^2 = \frac{\sigma_m^2}{b^2} + \frac{m^2}{b^4}\sigma_b^2$$

$$\sigma_c = \sqrt{\frac{b^2\sigma_m^2 + m^2\sigma_b^2}{b^4}}$$

BET Surface Area

$$Pv_m = n_m RT$$

$$\sigma_{v_m}^2 = \left(\frac{\partial v_m}{\partial m}\right)^2 \sigma_m^2 + \left(\frac{\partial v_m}{\partial b}\right)^2 \sigma_b^2 + \left(\frac{\partial v_m}{\partial P}\right)^2 \sigma_P^2 + \left(\frac{\partial v_m}{\partial R}\right)^2 \sigma_R^2 + \left(\frac{\partial v_m}{\partial T}\right)^2 \sigma_T^2$$

P, R and T are all constants with no error

$$\sigma_P = \sigma_R = \sigma_T = 0$$

$$\sigma_{n_m} = \frac{P}{RT}\sigma_{v_m}$$

Then,

$$S = n_m \cdot N_A \cdot A_m \tag{3.54}$$

N_A and A_m are constants with no error

$$\sigma_{A_m} = \sigma_{N_A} = 0$$

So,

$$\sigma_S = N_A A_m \, \sigma_{n_m}$$

Enthalpy of Adsorption ΔH_A

$$c = e^{\left[\frac{|\Delta H_A| - |\Delta H_L|}{RT}\right]} \tag{3.55}$$

$$|\Delta H_A| = |\Delta H_L| + RTlnc$$

$$|\Delta H_A| = |\Delta H_L| + RTln\left(\frac{m}{b} + 1\right)$$

$$\sigma_{|\Delta H_A|}^2 = \left(\frac{\partial|\Delta H_A|}{\partial m}\right)^2 \sigma_m^2 + \left(\frac{\partial|\Delta H_A|}{\partial b}\right)^2 \sigma_b^2 + \left(\frac{\partial|\Delta H_A|}{\partial|\Delta H_L|}\right)^2 \sigma_{|\Delta H_L|}^2 + \left(\frac{\partial|\Delta H_A|}{\partial R}\right)^2 \sigma_R^2 + \left(\frac{\partial|\Delta H_A|}{\partial T}\right)^2 \sigma_T^2$$

$$\sigma_{|\Delta H_L|} = \sigma_R = \sigma_T = 0$$

$$\sigma_{|\Delta H_A|}^2 = \left(\frac{\partial|\Delta H_A|}{\partial m}\right)^2 \sigma_m^2 + \left(\frac{\partial|\Delta H_A|}{\partial b}\right)^2 \sigma_b^2$$

$$\sigma_{|\Delta H_A|}^2 = \left(\frac{RT}{m+b}\right)^2 \sigma_m^2 + \left(\frac{-RTm}{b(b+m)}\right)^2 \sigma_b^2$$

$$\sigma_{|\Delta H_A|}^2 = \frac{R^2T^2}{(m+b)^2}\sigma_m^2 + \frac{R^2T^2m^2}{b^2(m+b)^2}\sigma_b^2$$

$$\sigma_{|\Delta H_A|} = RT\sqrt{\frac{b^2\sigma_m^2 + m^2\sigma_b^2}{b^2(m+b)^2}}$$

Micropore Area

$$V_0 = 10^b$$

$$\sigma_{V_0}^2 = \left(\frac{\partial V_0}{\partial b}\right)^2 \sigma_b^2$$

$$\sigma_{V_0}^2 = \left(\ln(10)\, 10^b\right)^2 \sigma_b^2$$

$$\sigma_{v_0} = \ln(10)\sqrt{10^{2b}}\sigma_b$$

$$n_0 = \frac{PV_0}{RT}$$

$$n_0 = \frac{P\, 10^b}{RT}$$

$$\sigma_{n_0}^2 = \left(\frac{\partial n_0}{\partial b}\right)^2 \sigma_b^2 + \left(\frac{\partial n_0}{\partial P}\right)^2 \sigma_P^2 + \left(\frac{\partial n_0}{\partial R}\right)^2 \sigma_R^2 + \left(\frac{\partial n_0}{\partial T}\right)^2 \sigma_T^2$$

$$\sigma_P = \sigma_R = \sigma_T = 0$$

$$\sigma_{n_0}^2 = \left(\frac{\partial n_0}{\partial b}\right)^2 \sigma_b^2$$

$$\sigma_{n_0} = \frac{\ln(10)\, P\, \sqrt{10^{2b}}}{RT}\sigma_b$$

$$S = n_0 \cdot N_A \cdot A_m \tag{3.54}$$

N_A and A_m are constants with no error

$$\sigma_{A_m} = \sigma_{N_A} = 0$$

So,

$$\sigma_S = N_A A_m\, \sigma_{n_0}$$

$$\sigma_S = \frac{\ln(10)\, N_A A_m P\, \sqrt{10^{2b}}}{RT}\sigma_b$$

Percentage Volume Attributed to Micropores

$$Micropore\ volume\ \% = \frac{v_0}{MQA} * 100$$

$$\sigma_{Micropore\ volume\ \%} = \frac{100 * \ln(10)\ \sqrt{10^{2b}}}{MQA}\sigma_b$$

Liquid Phase Adsorption Uptake

$$Uptake = \frac{V(C_0 \varepsilon l - A.Dilution\ factor)}{Mass * \varepsilon l}$$

All except ε are constant and have no error,

$$\sigma_{Uptake}^2 = \left(\frac{\partial Uptake}{\partial \varepsilon}\right)^2 \sigma_\varepsilon^2$$

$$\sigma_{Uptake}^2 = \left(\frac{AV.Dilution\ factor}{Mass.l.\varepsilon^2}\right)^2 \sigma_\varepsilon^2$$

$$\sigma_{Uptake} = \frac{AV.Dilution\ factor}{Mass.l.\varepsilon^2}\sigma_\varepsilon$$

Appendix E: Data Availability Statement

All data underpinning this publication are openly available from the University of Strathclyde KnowledgeBase at https://doi.org/10.15129/1550527d-538d-416a-bfdb-cd1151edc78e

Appendix F: XPS Examples

In Figure A132, Figure A133 and Figure A134 below are the Fityk curve deconvolution software fits for the C1s, N1s and O1s scans of sample S9W point 1 respectively.

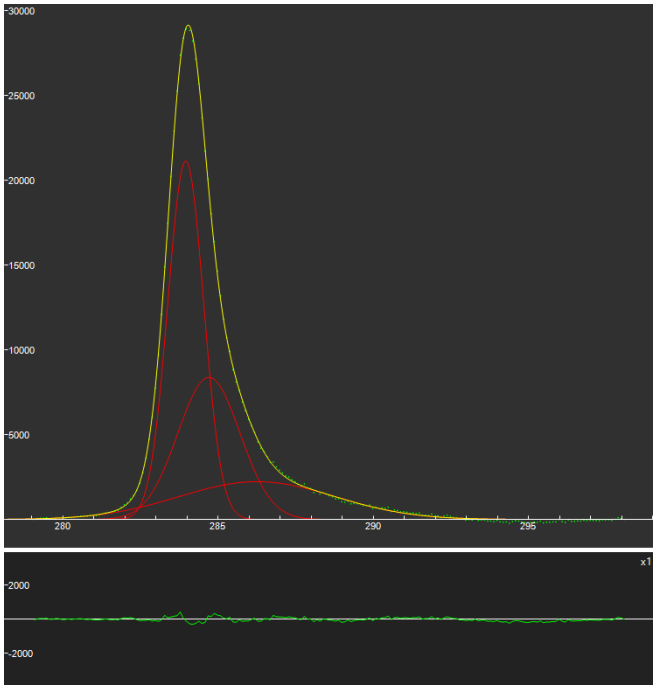

Figure A132: C1s scan of S9W point 1 with deconvoluted peaks

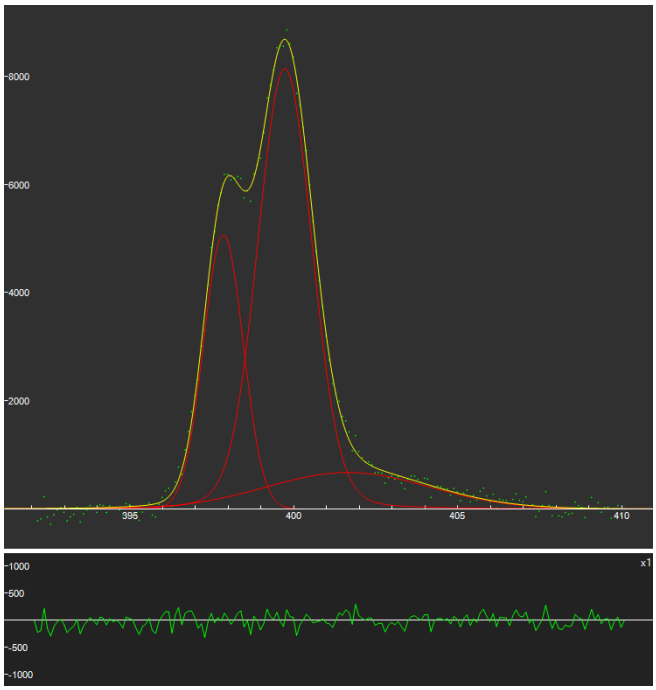

Figure A133: N1s scan of S9W point 1 with deconvoluted peaks

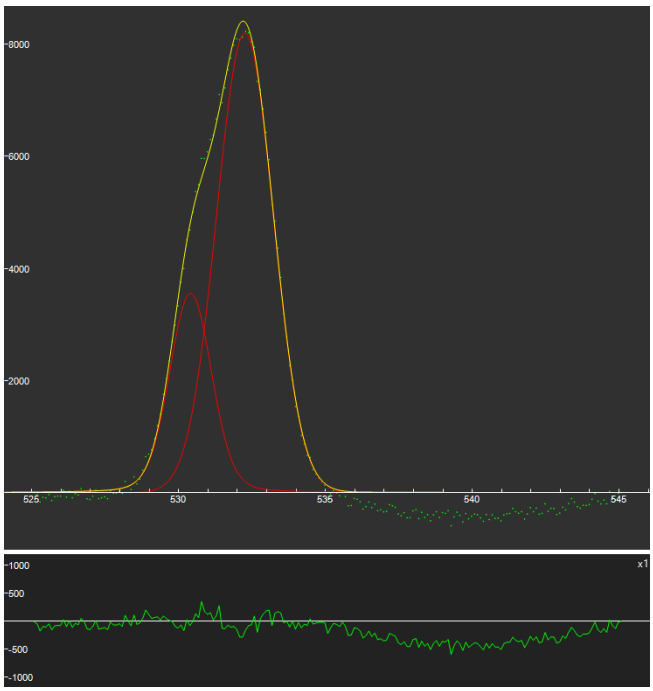

Figure A134: O1s scan of S9W point 1 with deconvoluted peaks

Table A82 details the fitting parameters of the Voigt curves used to deconvolute the scans.

Table A82: Voigt fitting parameters for S9W point 1

Scan	C1s			N1s			O1s	
Peak	1	2	3	1	2	3	1	2
Centre	283.956	286.557	284.679	399.724	397.847	401.652	532.259	530.408
Area	29713	11560.5	24535.2	17603	7692.27	4206.33	19775.1	6780.85
Height	20802.9	1937.34	9099.77	8140.07	5068.44	676.9	8202.17	3555.08

Figure A135, Figure A136 and Figure A137 below are the Fityk curve deconvolution software fits for the C1S, N1S and O1S scans of sample O4 point 1 respectively .

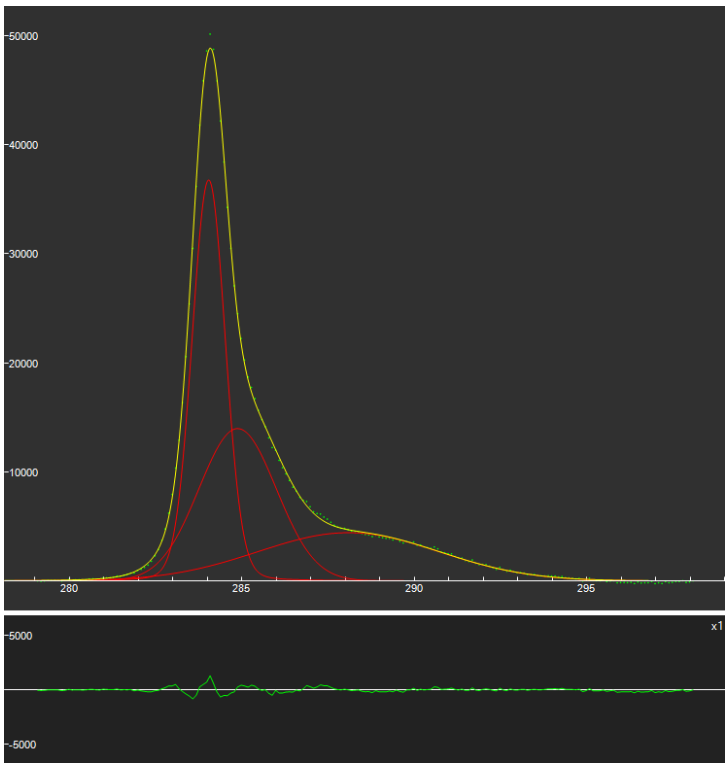

Figure A135: C1s scan of O4 point 1 with deconvoluted peaks

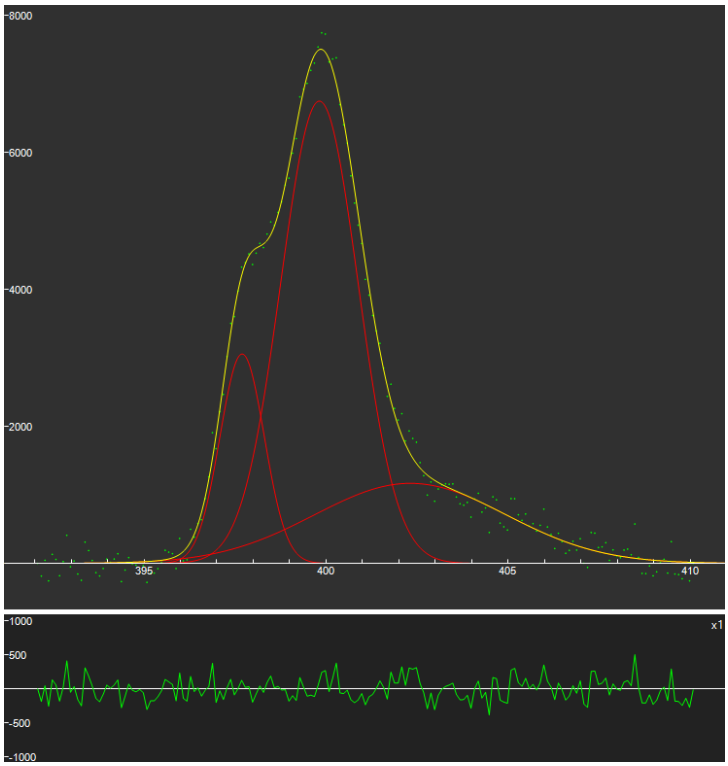

Figure A136: N1s scan of O4 point 1 with deconvoluted peaks

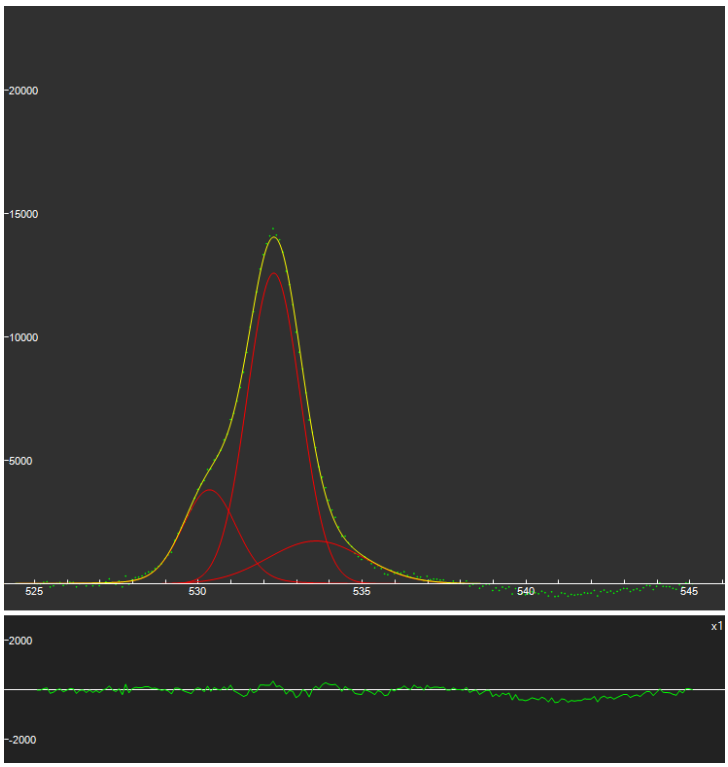

Figure A137: O1s scan of O4 point 1 with deconvoluted peaks

Table A83 details the fitting parameters of the Voigt curves used to deconvolute the scans.

Table A83: Voigt fitting parameters for O4 point 1

Scan	C1s			N1s			O1s		
Peak	1	2	3	1	2	3	1	2	3
Centre	284.040	288.089	284.878	399.817	397.695	402.315	532.230	530.327	533.680
Area	45781.7	29077	39198.9	17996.5	4666.01	7717.93	26031.3	8117.18	5969.46
Height	36773	4421.41	13969	6750.77	3057.98	1169.3	12773.4	3811.17	1674.56

Appendix G: Temkin Isotherm Error Analysis Curves

Figure A138 and Figure A139 show the Temkin isotherms for all three temperatures with their upper and lower bounds calculated from their margin of error for Sample O4 and O6 respectively.

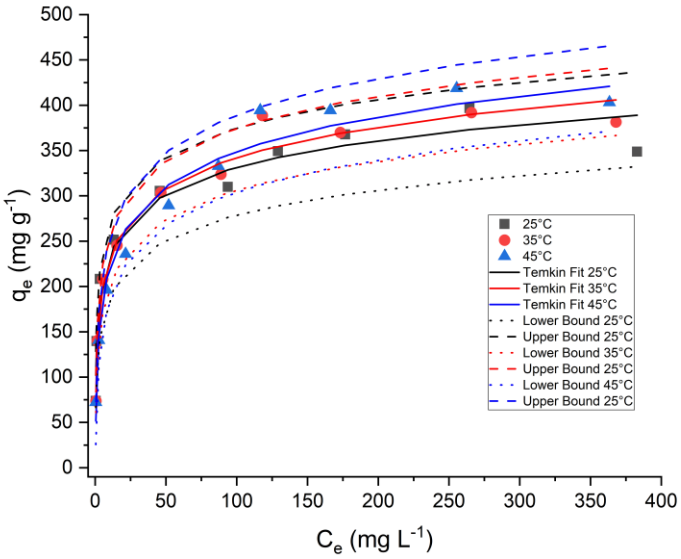

Figure A138: Temkin isotherm fits for sample O4 with upper and lower bound from error analysis

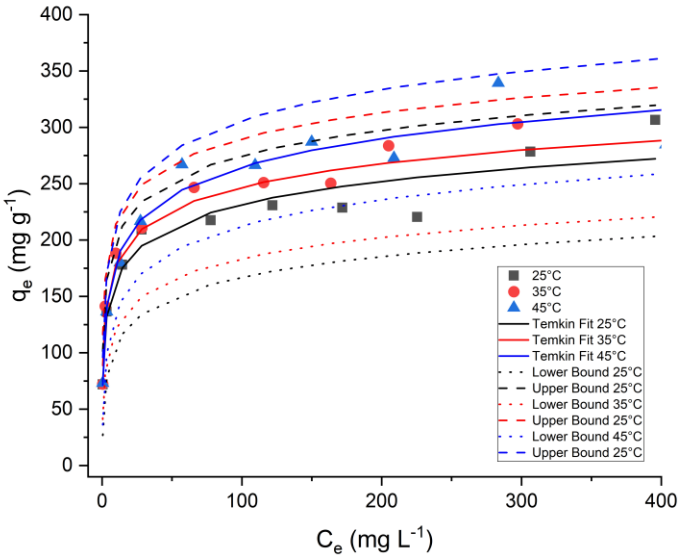

Figure A139: Temkin isotherm fits for sample O4 with upper and lower bound from error analysis